

Duyang Zang *Editor*

Acoustic Levitation

From Physics to Applications



Springer

Acoustic Levitation

Duyang Zang
Editor

Acoustic Levitation

From Physics to Applications



Springer

Editor

Duyang Zang

School of Physical Science and Technology

Northwestern Polytechnical University

Chang'an Campus

Xi'an, Shaanxi, China

ISBN 978-981-32-9064-8

ISBN 978-981-32-9065-5 (eBook)

<https://doi.org/10.1007/978-981-32-9065-5>

© Springer Nature Singapore Pte Ltd. 2020

This work is subject to copyright. All rights are reserved by the Publisher, whether the whole or part of the material is concerned, specifically the rights of translation, reprinting, reuse of illustrations, recitation, broadcasting, reproduction on microfilms or in any other physical way, and transmission or information storage and retrieval, electronic adaptation, computer software, or by similar or dissimilar methodology now known or hereafter developed.

The use of general descriptive names, registered names, trademarks, service marks, etc. in this publication does not imply, even in the absence of a specific statement, that such names are exempt from the relevant protective laws and regulations and therefore free for general use.

The publisher, the authors and the editors are safe to assume that the advice and information in this book are believed to be true and accurate at the date of publication. Neither the publisher nor the authors or the editors give a warranty, expressed or implied, with respect to the material contained herein or for any errors or omissions that may have been made. The publisher remains neutral with regard to jurisdictional claims in published maps and institutional affiliations.

This Springer imprint is published by the registered company Springer Nature Singapore Pte Ltd.
The registered company address is: 152 Beach Road, #21-01/04 Gateway East, Singapore 189721,
Singapore

Foreword

The famous science fiction writer Arthur C. Clark once said, “Any sufficiently advanced technology is indistinguishable from magic”. I have been showing acoustic levitation to the public and prospective students for many years now and the effect is consistently one of amazement. People’s instant reaction is that I am showing them some kind of magic trick. But, as this book demonstrates, acoustic levitation is a well-understood scientific fact and not magic at all. For this reason, the quote is perfect. Even non-scientists think they understand sound due to it being ever present in our everyday lives. Indeed, sound, in the form of music, can affect us emotionally, to the extent that it feels like a physical force. But this emotional force is not the subject of this book. Rather, this book concerns the very real physical phenomena that happen when the sound intensity is sufficiently high that the momentum of a propagating soundwave becomes significant.

The field of acoustic levitation, like much in acoustics, was born with the work of Lord Rayleigh [1] that spanned the late nineteenth and early twentieth centuries. He was the first to describe the basic equations that govern the acoustic radiation force on large planar objects. This work was perhaps inspired by the experimental work of August Kundt [2] some years earlier who had shown that dust in an acoustically excited tube formed into patterns, with the dust collecting at the low-intensity nodal regions. In the now famous Kundt’s tube experiment, the objective was to measure the wavelength of the sound and thereby deduce the speed of sound. Unknowingly, he also sowed the seeds for the field of acoustic levitation. These ideas remained a scientific curiosity for many years, arguably, until the bright sparks at NASA saw applications in space science. In the 1980s and 1990s, NASA and their collaborators developed a multitude of levitators [3], both to hold objects in place during experiments in space and to mimic microgravity on earth. This explosion of interest kick-started the field and started it on a path to becoming what it is today.

For an object to be levitated on earth, we must overcome the forces on the object due to gravity. The classic experiment to achieve this is to use a high-power transducer and a reflector to establish a standing wave. This standing wave consists of a repeating pattern of low and high intensities (i.e. the nodes and antinodes respectively). In this book, and the vast majority of the research on acoustic

levitation, the levitated object is significantly smaller than the wavelength—the well-named Rayleigh regime—objects are trapped stably at the nodes and conversely repelled from the antinodes. Operation in the Rayleigh regime also dramatically simplifies the mathematics as the potential theory of Gor'kov [4] can be used to predict the forces. In this theory, the acoustic radiation force is governed by the local first-order acoustic pressure and the properties of the particle and host fluid, typically air. This represents a dramatic simplification as the first-order acoustic pressure can be obtained from linear acoustic modelling approaches, such as superposition of point sources or the finite element method. But whilst this is an incredibly powerful approach, it is only an approximation of reality.

This book describes this classic standing wave levitator experiment and the Gor'kov potential theory, but then goes on to cover the advanced theories that explain the flow phenomena that happen alongside acoustic radiation forces at high acoustic intensities. These flow phenomena, known as acoustic streaming, occur as the momentum of the acoustic wave is transferred to the host fluid. In many of the experiments where positioning and manipulation are the aims, acoustic streaming is an unwanted side effect. In such situations, the streaming still needs to be understood, from the perspective of minimising its effects. However, in other situations the streaming itself can be useful as it leads to the formation of unique conditions within levitated liquid droplets. This allows the exciting possibility of controlled flow to facilitate effects such as centrifugation and mixing within a levitated droplet.

Although this book restricts itself to acoustically manipulating matter in air, the phenomena it describes are generally applicable to almost any combination of particle and host fluid. There is a particularly strong parallel line of research into the manipulation of matter in liquid media, often with the aim of manipulating cells. Because of the small size of cells, these waterborne acoustic devices typically operate at megahertz frequencies to generate wavelengths of hundreds of micrometres. Experiments have recently demonstrated the ultrasonic radiation force devices that can sort different cell types for medical diagnostics as well as seeding cells for tissue engineering. Despite the obvious practical differences between the water and airborne devices, they share much in common and workers in each field should endeavour to remain up to date with each other's work.

What does the future hold for acoustic levitation? After acoustic levitation burst onto the scene in the 1980s and 1990s, spurred on by space applications, the basic techniques were refined, and interest plateaued. However, recent years have seen an explosion of interest driven by emerging applications in biomedicine and materials science. One factor that is enabling this new progress is the dramatic reduction in cost of the levitation devices themselves. Now, almost any laboratory, anywhere in the world can build a basic working acoustic levitator from off-the-shelf parts and powered by relatively simple and easily available electronics. We can expect this trend to continue, meaning that even the most advanced, re-programmable levitators become available at similarly low costs.

In the small wavelength regime, density is the governing parameter and it has already been demonstrated that dense solids such as iridium (density of 22.6 g/cm³) can be levitated [5]. However, the size of the levitated object is currently still a

restriction as the objects must currently be small compared to the wavelength. Reducing the frequency to the audible range is problematic as the high sound levels required would make such devices obviously loud, so this appears to set a practical upper limit on the size of object that can be levitated to a couple of millimetres. However, recent results show that this limit can be overcome using either acoustic vortices [6] or boundary holograms [7]. In both cases, only low-density objects have so far been levitated, but this breaking of the wavelength limit could open a much wider range of future applications. The other end of the length scale increasing the frequency to manipulate smaller objects is a distinct possibility. But this cannot be achieved without limit due to the attenuation in air which increases sharply with frequency. So, perhaps, this sets a threshold on the smallest objects that can be stably acoustically levitated.

An exciting direction described in this book that seems set to continue is the incorporation of acoustic levitators in chemical and biological processing work streams and physical production lines. Here, the levitators might work, much like a production line in the automotive industry, collectively performing a task, such as delicately assembling consumer electronics or constructing a new generation of pharmaceutical products. As acoustic levitators can position, move, rotate and deform liquid droplets in a controllable way, they meet the dictionary definition of a robot—an acoustic robot. Unlike physical robots, the acoustic robot has no moving parts, is completely non-contact and can handle liquids just as easily as solids. Viewed from this perspective, the greater the functionality of the acoustic robot, the more versatile it is and the larger the range of applications. For this reason, one of the recurring themes of this book is to explore the range of functions that acoustic robots can perform. As the chapters progress, it is shown that each new function of the acoustic robot expands the range of applications yet further.

December 2019

Bruce W. Drinkwater
University of Bristol, Bristol, UK

References

1. L. Rayleigh, XLII. On the momentum and pressure of gaseous vibrations, and on the connexion with the virial theorem. *Lond. Edinb. Dublin Phil. Mag. J. Sci.* **10**(57), 364–374 (1905)
2. A. Kundt, Acoustic experiments. *Lond. Edin. Dublin Phil. Mag. J. Sci.* **35**(4), 41–48 (1868)
3. L. Gorkov, On the forces acting on a small particle in an acoustical field in an ideal fluid. *Sov. Phys. Dokl.* **6**, 773–775 (1962)
4. T.G. Wang, E.H. Trinh, A.P. Croonquist, D.D. Elleman, Shapes of rotating free drops: spacelab experimental results. *Phys. Rev. Lett.* **56**(5), 452–455 (1986)
5. W.J. Xie, C.D. Cao, Y.J. Lu, B. Wei, Levitation of iridium and liquid mercury by ultrasound. *Phys. Rev. Lett.* **89**(10), 104304 (2002)

6. A. Marzo, M. Caleap, B.W. Drinkwater, Acoustic virtual vortices with tunable orbital angular momentum for trapping of MIE particles. *Phys. Rev. Lett.* **120**(4), 044301 (2018)
7. S. Inoue, S. Mogami, T. Ichiyama, A. Noda, Y. Makino, H. Shinoda, Acoustical boundary hologram for macroscopic rigid-body levitation. *J. Acoust. Soc. Am.* **145**(1), 328–327 (2019)

Preface

It is really a fruitful combination when soft matter/complex fluids meet acoustic levitation. The first idea was flashed into my mind when I did a conjoint (between China and France) Ph.D. project in Prof. Dominique Langevin's group at Orsay, where I started to learn the science of soft matter. My knowledge of acoustic levitation was benefited from my supervisor Prof. Bingbo Wei who has guided and generously helped me to start my career as a scientist. I got rich ideas when the knowledge from the two different groups interacts.

In the past decade, our group (Soft Matter and Complex Fluids group in NPU) has studied the dynamic of complex drops under acoustic levitation. We have focused on how drops respond to acoustic stimulus and tried to link drop dynamics with liquid rheology. We have found plenty of new phenomena in acoustically levitated drops ranging from coalescence, internal flow, to drop evaporation and the associated phase behaviours.

The experiments of acoustic levitation are not boring, not at all. It is really a promising and exciting experience when you look at how a liquid drop responds to sound field. It is amazing that the drop can “hear” in its own manner. The open issue is how can we understand what the drop had heard.

Acoustic levitation is an old but still active research filed. The technique is ready to be incorporated into other fields including materials science, fluid physics and bio/chemical analysis. It is highly desirable to stimulate further study on acoustic levitation, particularly to arouse researchers from different disciplines. For this purpose, the book is organized and be written by active researchers in this field. The book is constructed of nine chapters.

Chapter 1, written by the editor, is a brief introduction to acoustic levitation and other levitation techniques, which is in the form of dialogues. Dr. Marzo and Dr. Andrade present respectively in Chaps. 2 and 3 the general theory of standing wave acoustic levitation and the design of various acoustic levitators. These two chapters describe the scientific foundations and technical details of acoustic levitation, both theoretically and experimentally. In Chap. 4, Prof. Chen reviews the numerical simulation of sound field, particularly for standing wave field. He has discussed the utilization of Lattice Boltzmann method for acoustic levitation.

Chapters 5–9 are related to the detailed applications of acoustic levitation. In Chap. 5, Prof. Zang et al. have reviewed the dynamics of drops under acoustic levitation. Prof. Hasegawa has reviewed in Chap. 6 the flow fields, both internal flows and external ones associated with acoustically levitated drops. In Chap. 7, Prof. Wei mainly focuses on evaporation of the levitated drops. Due to the advantage of non-contact with solid substrate, acoustic levitation provides an ultra-clean environment for crystallization. Therefore, in Chap. 8, Prof. Yin et al. have reviewed the crystallization in acoustically levitated drops of both solutions and melts (i.e. liquid alloys). In Chap. 9, Prof. Tsujino has summarized the bio/chemical applications of acoustic levitation, which represents one of the more promising directions for the future exploration of acoustic levitation.

I would like to thank all the authors for their great contribution and nice cooperation in preparing the book; I appreciate my students: Zehui Zhang, Kangqi Liu, Wenli Di who had helped me a lot on materials collection, and Mr. Chandra Sekaran for his great patience and generous help.

I hope that you enjoy the book.

Xi'an, China
January 2020

Yours sincerely,
Duyang Zang

Contents

1 Dialogues on Levitation Techniques and Acoustic Levitation	1
Duyang Zang	
2 Standing Waves for Acoustic Levitation	11
Asier Marzo	
3 Design of Single-Axis Acoustic Levitators	27
Marco A. B. Andrade	
4 Lattice Boltzmann Method for Acoustics Levitation	57
Xiao-Peng Chen	
5 Dynamics of Acoustically Levitated Drops	79
Zehui Zhang, Kangqi Liu, and Duyang Zang	
6 Flow Fields and Heat Transfer Associated with an Acoustically Levitated Droplet	97
Koji Hasegawa	
7 Droplet Evaporation Under Acoustic Levitation	121
Yanju Wei	
8 Crystallization in Acoustically Levitated Drops	131
Da-Chuan Yin and Duyang Zang	
9 Applications of Acoustic Levitation in Chemical Analysis and Biochemistry	151
Soichiro Tsujino and Takashi Tomizaki	

Chapter 1

Dialogues on Levitation Techniques and Acoustic Levitation



Duyang Zang

This chapter is in the form of dialogues which took place at three different scenarios. In the dialogues, the fundamental principle, applications and future directions of acoustic levitation as well as the comparison with other levitation techniques are discussed.

1.1 Scenario I

Today is the opening day of the lab. A class of school kids are visiting the lab. One kid (K) walks to a master student (S) who is preparing to do acoustic levitation experiments.

K: I heard that sound can levitate objects, really?

S: Yeah, that's true.

K: Can you show me how sound can do that? I'm eager to see.

S: Sure.

After a few seconds, the master student levitated a drop of water in the acoustic levitator [1] (Fig. 1.1).

K: Amazing, the drop is levitated there, like our planet in the universe.

S: Yes, the phenomena are similar. But the underlying mechanism is quite different. For our planet as well as other celestial bodies, they are levitated in the universe dominated by gravity.

K: Is the drop blown by something? Like a bubble in wind.

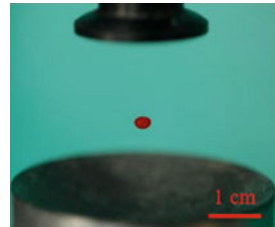
D. Zang (✉)

Soft Matter and Complex Fluids Group, School of Physical Science and Technology,

Northwestern Polytechnical University, 710129 Xi'an, China

e-mail: dyzang@nwpu.edu.cn

Fig. 1.1 Levitation of a drop of water by ultrasound [1]



- S: No, wind is a strong flow of air, in which all the air molecules move together in a certain direction. In the acoustic levitation, however, the air molecules vibrate round their original position. Their average velocity will be zero. Even though the molecules do have a nonzero net velocity (acoustic streaming, arising from the non-linear effect of ultrasound), there is no strong flows, like wind, in the levitator.
- K: If not wind that blows the drop, could it be said that sound has hands that hold the drop?
- S: This is really a pretty analogy. You know, when a drop is positioned in the sound field, sound can exert an additional pressure on the drop surface, which is called acoustic radiations pressure P_A . This pressure is not homogenous distributed on the surface (Fig. 1.2), usually being positive at the upper and bottom surface whereas negative at the equator area. This is quite like your analogy that sound extends many hands onto the levitated sample, some of the hands push it upwards, some push it downwards, whereas some try to pull it [2]. It is the integral of P_A that balances the gravitational force of the sample.
- K: Wonderful, I seems understand why sound can levitate objectives. But I wonder if a drop can be levitated by the sound when we speak?
- S: This is a good question. I must say that it's quite difficult to levitate a objective by walking sound waves, like the voices when we speak. On the contrary, we need standing sound waves. That's why you usually see both a sound emitter and a reflector are arranged together in a levitator. The main purpose is to form a standing wave filed in between them [3] (Fig. 1.3). As a result, small objectives,

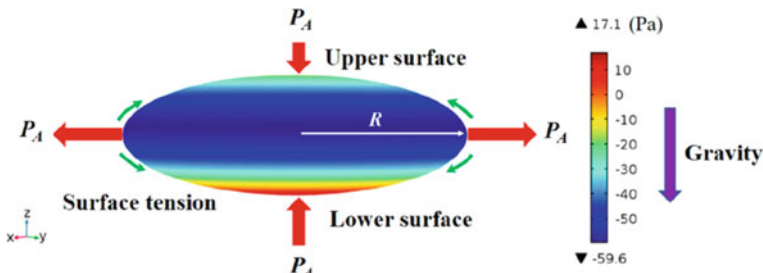


Fig. 1.2 Acoustic radiation pressure on the surface of an acoustically levitated drop [2]

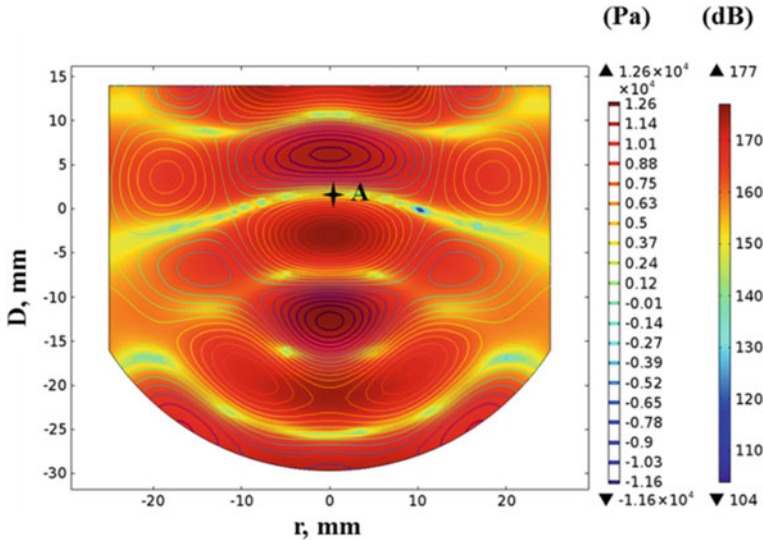


Fig. 1.3 Standing sound wave field in an acoustic levitator [3]

generally smaller than a half of sound wave length, can be trapped in one of the potential wells of the sound field.

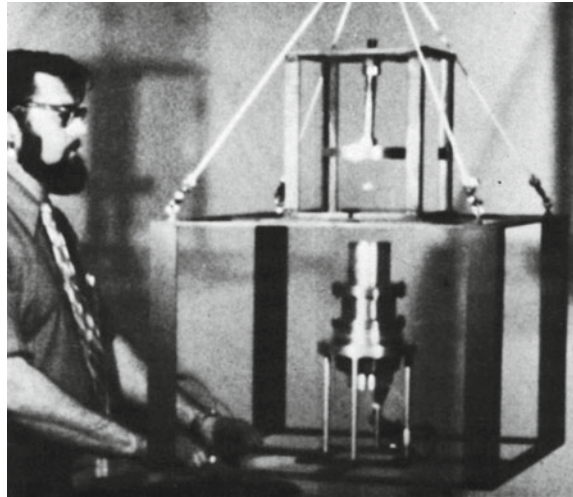
- K: I got it. Ultrasound can generate surface force on levitated objective which balance its gravitational force. Thank you for tell me so many on acoustic levitation.
- S: It's my pleasure.

1.2 Scenario II

A undergraduate student named Lei Li, who is studying applied physics for the second year. He is planning to apply a research project (National innovation experiment program for university students) on acoustic levitation. To gain a deeper understanding, he visit a professor (P) in the department of physics, who works in this field.

- Li: Professor, first thank you for agreeing the discussion. I'm very interested in acoustic levitation and have many questions.
- P: I'm happy to hear that and glad to share what I know with you.
- Li: I've read several papers, including a review article. At the moment, I know that acoustic levitation is one of the most important techniques for container-free processing of materials. The fundamental principle is the acoustic radiation force, caused by the nonlinear effect of ultrasound, can act against sample's gravity. But I wonder how this technique appear and become important in scientific research?

Fig. 1.4 Acoustic levitator used in space station for materials positioning [6]



- P: The first phenomenon was reported by Kundt in 1866. He found that the particle of dust can be trapped at certain positions in a resonant tube [4]. In 1933, a Polish scientist Bücks et al. successfully levitated droplets of water of 1–2 mm in diameter, opening the drop dynamics study via acoustic levitation [5]. In 1975, Whymark, a USA scientist developed the acoustic levitator which could be applied in space because of its excellent trapping ability [6] (Fig. 1.4).
- Li: So the most important application of acoustic levitation is sample trapping and positioning in space experiments.
- P: I agree sample positioning in space station is one of the most important applications of acoustic levitation. However, I would like to say acoustic levitation plays a more important role on the earth. As far as I know, for acoustic levitation, more researches have been carried out on the earth rather than in space station. For instance, rapid solidification of liquid alloys [7, 8], salt crystallization [9].
- Li: I got it, But why scientist so eager to levitate the materials?
- P: A good question. One of the main advantages of levitation is the avoidance of contact with solid surface. This is of great importance for the study of material science requiring ultra-clean condition which could bring the levitated samples to the state of non-equilibrium. In addition, because of the complete suppression of contact lines, it is also favorable to study the drop dynamics [10].
- Li: Beside acoustic levitation, there are also some other levitation techniques, such as magnetic levitation [11], electrostatic levitation [12], electromagnetic levitation [13], and optical levitation [14]. I knew Prof Andrey Geim had levitated a hazelnut(even an alive frog) using magnetic levitation [11] (Fig. 1.5). My question is what are the advantages of acoustic levitation over others?
- P: Yes, there are indeed many levitated techniques. Researchers tried different physical fields to generate the force which balances gravity, as illustrated in Fig. 1.6. Compared with other levitation techniques, acoustic levitation does

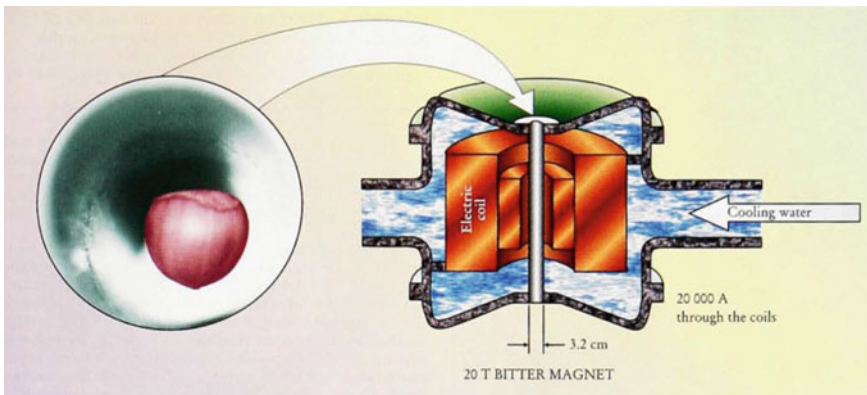


Fig. 1.5 Levitating nuts in magnetic field [11]

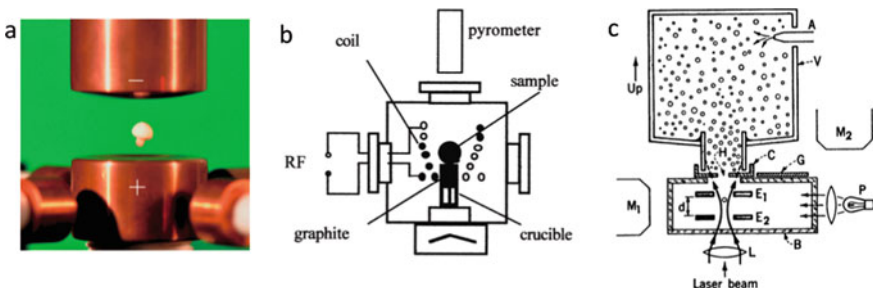


Fig. 1.6 Different levitation techniques. **a** magnetic levitation [11], **b** electrostatic levitation [12], **c** optical levitation [14]

not require the electro/magnetic properties of the sample. Moreover, it is gentle, i.e., does not ruin the sample.

- Li: So it indicates that acoustic levitation is suitable for the study of biological specimens.
- P: Exactly. For instance, Prof. Xie et al. have studied the levitation of small animals via a single-axis levitator [15] (Fig. 1.7).
- Li: Professor, I'm planning to apply a research project, namely the national innovation experiment program for university students. I intend to study liquid surface tension via the acoustic levitation of liquid drops. Do you have any suggestions?
- P: There already exist surface tension studies via the acoustic levitation approach, which are usually based on two different theories. One is based on Laplace equation through which surface tension can be extracted from the shape profile of the levitated drop [16, 17]. The other is based on the oscillation dynamics [18]. However, both methods, are complex and not sufficiently accurate. It would be valuable to develop a more simple theory which link surface tension with the drop dynamic behaviors.

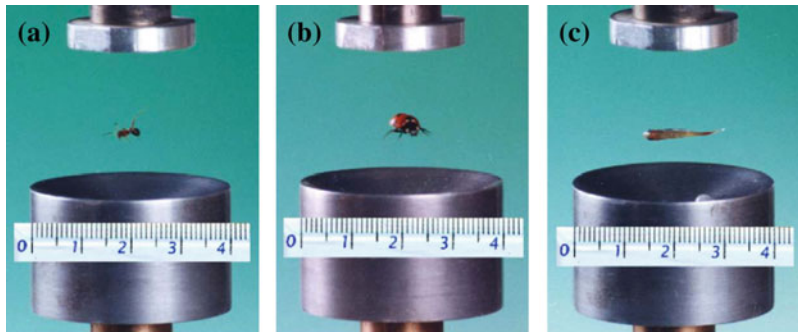


Fig. 1.7 Acoustic levitation of small animals [15]. **a** ant **b** ladybug **c** fish

1.3 Scenario III

A Ph.D. student, Meimei Han, has done a thorough literature review on acoustic levitation. To start her research project, she will give a presentation to the Supervisor Committee. To prepare it, she meets her supervisor professor Z for a deep discussion.

Han: Professor, I understand clearly that ultrasound can levitate small objectives because of the trapping effect of the pressure wells of the standing sound waves. But recently, I read a paper which showed that acoustic levitation could be used for sample transportation [19] (Fig. 1.8). I wonder whether the standing sound wave is really good at transportation.

Z: I believe sample manipulation, including transportation, is just one of the powerful and promising applications of acoustic levitation. As you know, it is the sound pressure wells that “hold” the samples, either solid balls or liquid drops. If one can shift/manipulate the pressure wells, the transportation/manipulation of levitated sample can be accomplished [20]. The problem is the accurate control of sound field.

Han: Yes, that can be realized by adjusting the phase of the transducers or via tuning the emitter reflector distance. But I know and have observed in the experiment, there always acoustic streaming in the levitator associating with levitation. Does this affect the sample manipulation?

Z: You are right. The acoustic streaming is intrinsically inevitable because of the nonlinear effect of ultrasound, which may bring instability to the levitated sample. This side effect is stronger for the levitation of smaller sample where the shear stress caused by acoustic streaming is comparable to the acoustic radiation. However, it should be noted that acoustic streaming has another side. For instance, it is favorable to tissue engineering via 3-dimensional assembly of cells [21] (Fig. 1.9).

Han: Yesterday, I levitated a sheet of paper ($\text{Ca. } 10 \times 10 \text{ mm}^2$). I noted once the paper was levitated in the sound field, it always rotated round the vertical axis. The rotation has also been evidenced in the levitation of liquid drops [22].

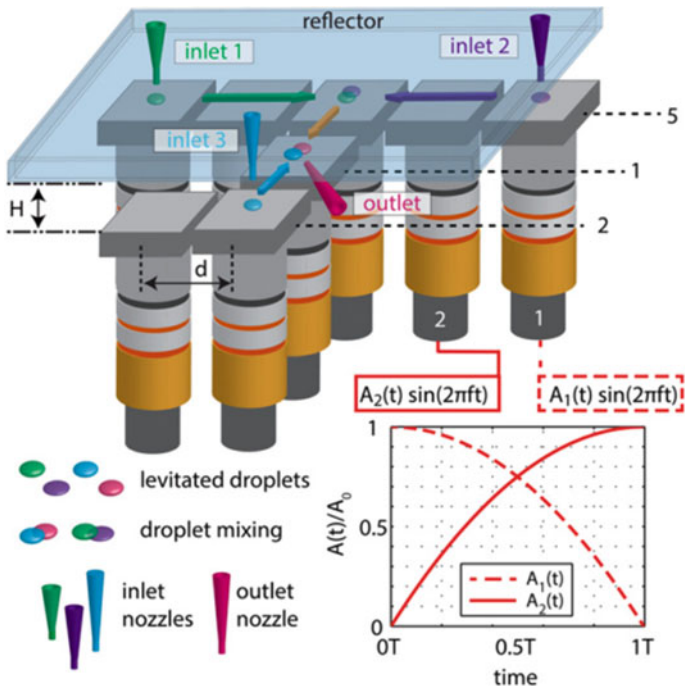


Fig. 1.8 Transportation of objectives via acoustic levitation [19]

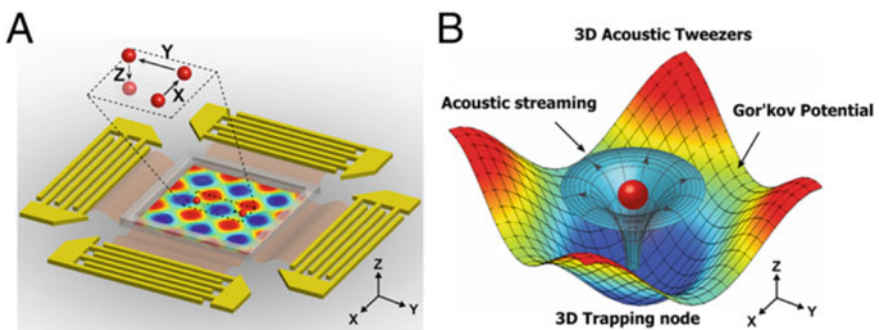


Fig. 1.9 Illustration of the 3D acoustic tweezers [21]. **a** Configuration of the planar surface acoustic wave generators, **b** Numerical simulation results mapping the acoustic field around a particle that shows the physical operating principle for the 3D acoustic tweezers

Z: In acoustic levitation, sample rotation is really frequently observed. This is largely arising from acoustic streaming which is inevitable for the utilization of ultrasound. For the rotation of liquid drops, the underlying mechanism would be more complex. On one hand, acoustic streaming, which exerts shear to drop surface, plays an important role. On the other hand, the capillary wave

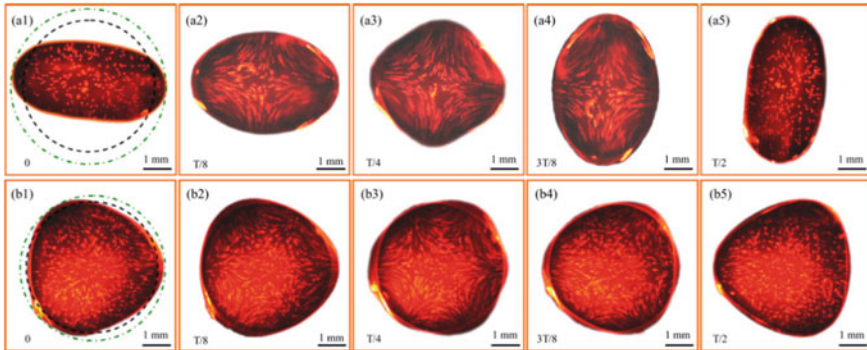


Fig. 1.10 Internal flows of drops undergoing sectorial oscillations [23]. **a1–a5** the second mode; **b1–b5** the third mode

caused by acoustic radiation pressure may bring complex internal flows to the drop (Fig. 1.10), which may couple with the sectorial oscillation of the levitated drop as well as sample rotation [23].

- Han: It is well known that the container-free condition provided by acoustic levitation plays important role in material science. But, besides levitation of sample, what else can this technique do?
- Z: This is a good question. Container-free condition provides an ultraclean environment which is important not only for materials process but also for bio/chemistry analysis. For instance, cell culturing or tissue engineering. Meanwhile, acoustic levitation is an excellent technique to deform a liquid drops, avoiding the influence of solid substrate. If one can stimulate different dynamic behaviors of levitated drops in a contact-free manner, it is possible to study/measure the liquid rheology provided one uncovers the relationship between response (drop dynamics) and external stimulus (acoustic radiation force or streaming).
- Han: So there would be plenty of opportunities for fluid physics study via acoustic levitation.
- Z: Yes, but this requires accurate control of the sound field. At the same time the size of the levitated sample is limited by the sound wavelength, typically $<\lambda/2$. Therefore, the first challenge is to construct potential well of expected size to trap sample of larger size. Moreover, in order to accomplish controlled drop deformation and dynamics, it is necessary to accurately control the sound field, which can be realized by controlling the phase of transducer patterns.
- Han: It is also need multidisciplinary effort to develop novel instruments based on acoustic levitation.
- Z: Definitely. One promising direction would be the integration of artificial intelligence (AI) with acoustic levitation, which may leads to the developing of acoustic robots and acoustic rheometer as well.

References

1. W. Di, Z. Zhang, L. Li, K. Lin, J. Li, X. Li, B.P. Binks, X. Chen, D. Zang, Shape evolution and bubble formation of acoustically levitated drops. *Phys. Rev. Fluids.* **3** (2018)
2. Q. Shi, W. Di, D. Dong, L.W. Yap, L. Li, D. Zang, W. Cheng, A general approach to free-standing nanoassemblies via acoustic levitation self-assembly. *ACS Nano* **13**, 5243–5250 (2019)
3. D. Zang, J. Li, Z. Chen, Z. Zhai, X. Geng, B.P. Binks, Switchable opening and closing of a liquid marble via ultrasonic levitation. *Langmuir. The ACS J. Surf. Colloids* **31**, 11502–11507 (2015)
4. A. Kundt, *Annu. Phys.* **84**, 497 (1886)
5. K. Bücks, H. Müller, Über einige Beobachtungen an schwingenden Piezoquarzen und ihrem Schallfeld. *Zeitschrift für Physik* **84**, 75–86 (1933)
6. R.R. Whymark, Acoustic field positioning for containerless processing. *Ultrasonics* **13**, 251–261 (1975)
7. N. Yan, Z.Y. Hong, D.L. Geng, W.L. Wang, B. Wei, Phase separation and structure evolution of ternary Al–Cu–Sn immiscible alloy under ultrasonic levitation condition. *J. Alloy. Compd.* **544**, 6–12 (2012)
8. N. Yan, Z.Y. Hong, D.L. Geng, B. Wei, A comparison of acoustic levitation with microgravity processing for containerless solidification of ternary Al–Cu–Sn alloy. *Appl. Phys. A* **120**, 207–213 (2015)
9. H.L. Cao, D.C. Yin, Y.Z. Guo, X.L. Ma, J. He, W.H. Guo, X.Z. Xie, B.R. Zhou, Rapid crystallization from acoustically levitated droplets. *J. Acoust. Soc. Am.* **131**, 3164–3172 (2012)
10. D. Zang, Y. Yu, Z. Chen, X. Li, H. Wu, X. Geng, Acoustic levitation of liquid drops: Dynamics, manipulation and phase transitions. *Adv. Coll. Interface. Sci.* **243**, 77–85 (2017)
11. A. Geim, Everyone's Magnetism. *Phys. Today* **51**, 36 (1998)
12. L. Hu, H. Wang, L. Li, B. Wei, Electrostatic levitation of plant seeds and flower buds. *Chin. Phys. Lett.* **29**, 064101 (2012)
13. R.P. Liu, T. Volkmann, D.M. Herlach, Undercooling and solidification of Si by electromagnetic levitation. *Acta Mater.* **49**, 439–444 (2001)
14. A. Ashkin, J.M. Dziedzic, Optical levitation of liquid drops by radiation pressure. *Science* **187**, 1073–1075 (1975)
15. W. Xie, C. Cao, Y. Lü, Z. Hong, B. Wei, Acoustic method for levitation of small living animals. *Appl. Phys. Lett.* **89**, 214102 (2006)
16. Y. Bayazitoglu, G.F. Mitchell, Experiments in acoustic levitation-surface tension measurements. *J. Thermophys. Heat Transfer* **9**, 694–701 (1995)
17. Y. Tian, R.G. Holt, R.E. Apfel, A new method for measuring liquid surface tension with acoustic levitation. *Rev. Sci. Instrum.* **66**, 3349 (1995)
18. C. Shen, W. Xie, B. Wei, Digital image processing of sectorial oscillations for acoustically levitated drops and surface tension measurement. *Sci China Phys. Mech. Astrono* **53**, 2260–2265 (2010)
19. D. Foresti, M. Nabavi, M. Klingauf, A. Ferrari, D. Poulikakos, Acoustophoretic contactless transport and handling of matter in air. *Proc. Natl. Acad. Sci. U S A* **110**, 12549–12554 (2013)
20. A. Marzo, S.A. Seah, B.W. Drinkwater, D.R. Sahoo, B. Long, S. Subramanian, Holographic acoustic elements for manipulation of levitated objects. *Nat. Commun.* (2015)
21. F. Guo, Z. Mao, Y. Chen, Z. Xie, J.P. Lata, P. Li, L. Ren, J. Liu, J. Yang, M. Dao, S. Suresh, T.J. Huang, Three-dimensional manipulation of single cells using surface acoustic waves. *Proc. Natl. Acad. Sci. U S A* **113**, 1522–1527 (2016)
22. A. Biswas, E.W. Leung, E.H. Trinh, Rotation of ultrasonically levitated glycerol drops. *J. Acoust. Soc. Am.* **90**, 1502–1507 (1991)
23. C.L. Shen, W.J. Xie, Z.L. Yan, B. Wei, Internal flow of acoustically levitated drops undergoing sectorial oscillations. *Phys. Lett. A* **374**, 4045–4048 (2010)

Chapter 2

Standing Waves for Acoustic Levitation



Asier Marzo

Abstract Standing waves are the most popular method to achieve acoustic trapping. Particles with greater acoustic impedance than the propagation medium will be trapped at the pressure nodes of a standing wave. Acoustic trapping can be used to hold particles of various materials and sizes, without the need of a close-loop controlling system. Acoustic levitation is a helpful and versatile tool for biomaterials and chemistry, with applications in spectroscopy and lab-on-a-droplet procedures. In this chapter, multiple methods are presented to simulate the acoustic field generated by one or multiple emitters. From the acoustic field, models such as the Gor'kov potential or the Flux Integral are applied to calculate the force exerted on the levitated particles. The position and angle of the acoustic emitters play a fundamental role, thus we analyse commonly used configurations such as emitter and reflector, two opposed emitters, or arrangements using phased arrays.

2.1 Introduction

Sound is a mechanical wave that transports momentum capable of exerting forces on objects as a consequence of the acoustic radiation force [1–4]. If the forces that act on an object are converging and sufficiently strong, the objects can be suspended and trapped in mid-air [5] or other propagation media. The trapping of particles using soundwaves is referred to as acoustic levitation, acoustic trapping, acoustic tweezers or acoustophoresis.

Acoustic trapping can be used to hold particles of various materials and sizes. This is in contrast with optical trapping in which the trapped objects have to be of micrometric scale and the particle should be optically transparent or dielectric [6]. Acoustic trapping is also more efficient in terms of input power to exerted forces [7]. Other types of contactless trapping, such as electrostatic levitation [8], require closed-loop control and the range of materials that can be trapped is also limited; on the other hand, aerodynamic levitation [9] stirs and disturbs the samples. Magnetic

A. Marzo (✉)

UpnaLab, Public University of Navarre, 31006 Pamplona, Spain

e-mail: asier.marzo@unavarra.es

levitation is a popular method to hold objects in mid-air [10]; however, it works only on ferromagnetic materials; diamagnetic materials can also be employed [11, 12], but due to the much weaker diamagnetic effect, the required amount of power is only accessible to a couple of research laboratories.

The flexibility of mid-air acoustic levitation has made it a valuable apparatus for containerless transportation [13, 14], pharmaceutics [15], nano-assemblies [16], the levitation of biological samples [17], little animals [18, 19] and food [20]. Acoustic levitation of liquid droplets can be employed to explore novel liquid dynamics [21], measure surface tension [22, 23] or rheological properties [24]. Other applications are the formation of suspended ice flakes [25], growing crystals in liquid metals [26], evaporation of solutions [27], phase transitions [28], the fast crystallization [29] or ionization [30] of samples and the creation of bubbles for coverings [31]. Samples held with acoustic levitation are not in physical contact with a container; this provides benefits in mass [32] and Raman [33] spectroscopies, e.g., in algae [34] or blood cell [17] characterization. In general, acoustic levitation is a helpful and adaptable tool in biomaterials research [35], chemistry [36] and enables lab-on-a-drop procedures [37].

Single-axis levitators [38] are the most typical device for producing acoustic traps. They are composed of an acoustic emitter and a reflector opposed to it. A standing wave is generated between the emitter and the reflector. The nodes of the standing wave act as an acoustic trap for spherical particles smaller than half-wavelength and with positive acoustic contrast (i.e., the acoustic impedance of the particle is larger than that of the propagation medium). When the medium is water based, it is also possible to have particles with negative contrast; in this case, the particles go to the anti-nodes [39]. A simple single-axis levitator is presented in Fig. 2.1 as well as the simulated amplitude field that generates and the forces that exert on a 1 mm diameter spherical particle.

Standing waves are the most common method to trap particles given its trapping strength but present some limitations such as particle size (it has to be smaller than half-wavelength) and spherical shape for the particles. Some of these limitations have been overcome in the past years. Particles larger than half-wavelength can be levitated close to an emitter using near-field levitation [40, 41]. Also, special types of acoustic vortices can trap objects larger than the wavelength in the far-field [42, 43]; however, they require high power and only very light objects have been trapped. Non-spherical particles can be steadily trapped using the acoustic lock technique [44], but extra control on the emission of the fields is needed.

Apart from standing waves, acoustic beams emitted from a single-sided device are capable of trapping particles in three dimensions [7, 45–47]; these beams are also referred to as tractor beams since they can attract particles toward the source, i.e., generate negative forces along the propagation direction of the beam. However, complex equipment or high power is required for generating functional tractor beams. Consequently, standing-wave trapping remains as the most common method to trap samples in mid-air. A more detailed description of the acoustic levitation methods can be found in these reviews [48, 49].

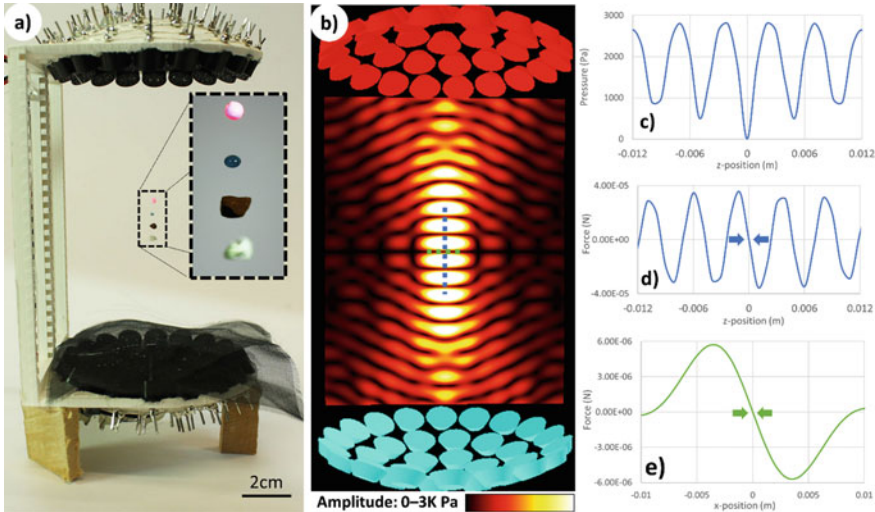


Fig. 2.1 **a** TinyLev, a single-axis levitator, trapping plastic, water, soil and paper. **b** The amplitude pressure field generated by the levitator. **c** The amplitude pressure distribution across the vertical axis z . **d** The force acting on a particle of 1 mm diameter depending on its position along the z -axis and **e** x -axis. Note that both forces are converging toward the center

We have covered the trapping of one or a series of particles along the static nodes of a standing wave, but it is also possible to generate multiple standing waves with nodes at user-specified positions. Multi-emitter arrays arranged in an opposed configuration enable the trapping of multiple particles that can be moved independently; these traps are named holographic acoustic tweezers [50].

In the second section of the chapter, we will review the main models employed to calculate the acoustic field generated by acoustic levitators and how to determine the exerted forces on the objects that are contained in these fields. In the third section, we analyse the most common configurations used for standing-wave levitators.

2.2 Principle Governing Equations

In this section, we describe the most common models used to calculate the generated acoustic field by acoustic emitters and the forces that this field exerts on objects. When the models operate in the frequency domain at a single frequency, the acoustic pressure (p) is represented as a complex scalar field: The magnitude represents the amplitude in pascals and the argument is the phase in radians. When the models operate in the time domain, the pressure is a real scalar field. The particle velocity of the medium (v) is a vector field that also appears in the calculations; it can be obtained from the model or as the gradient of the pressure.

Other terms that regularly appear in the models are total, incident and scattered fields. The incident field is the acoustic field generated by the emitters into the free space; that is, no reflectors or obstacles that affect the emitted waves are in the domain. The total field is the pressure distribution that exists in the space when all the elements that affect the wave are considered; ideally, the total field is what gets measured in the experiments. The total, incident and scattered fields are linear for both pressure and velocity under the assumptions of most of the models. Consequently, total = incident + scattered; thus by having two of the fields, the other field can be obtained. Some models calculate just the incident field, whereas other models determine the scattered field or directly obtain the total field.

2.2.1 Generated Acoustic Field

2.2.1.1 Free-Field Piston Source

This is one of the simplest models to calculate an incident field generated by one or multiple emitters which are approximately shaped as circular radiating pistons. The model is only valid for the far-field of the emitters; this is usually not a problem since levitation occurs in the far-field. In general, this method is not suitable for calculating models with complex reflecting geometry or particles which are larger than half-wavelength since the scattered field would have a significant magnitude. Simple planar reflectors can be approximated by mirroring the emitters and adding an attenuation coefficient depending on the material. On the other hand, this method is fast and can run in real time for hundreds of emitters [51].

The complex acoustic pressure p at point \mathbf{r} due to a piston source emitting at a single frequency can be modeled as [52]:

$$p(\mathbf{r}) = P_0 V \frac{D_f(\theta)}{d} e^{i(\varphi+kd)}$$

where P_0 is a constant that defines the transducer output efficiency and V is the excitation signal peak-to-peak amplitude. D_f is a far-field directivity function that depends on the angle θ between the piston normal and the point \mathbf{r} . The directivity function of a piston source can be expressed as $D_f = 2J_1(ka \sin \theta)/ka \sin \theta$, where J_1 is a first-order Bessel function of the first kind and a is the radius of the piston [53]. This directivity function can be simplified as $D_f = \text{sinc}(ka \sin \theta)$. Other geometries such as square or line transducers can be approximated with other directivity functions. The term $1/d$ accounts for divergence, where d is the propagation distance in free space. $k = 2\pi/\lambda$ is the wavenumber and λ is the wavelength. φ is the emitting phase of the source.

The total acoustic field (P) generated by N transducers is the addition of the individual fields, i.e., $P = \sum_{j=1}^N p_j$. To characterize a transducer, the constant (P_0) and the piston radius (a) are needed; the constants for different transducers can

be found in the supplementary information of [54]. For instance, the commonly used MA40S4S (Murata Electronics, Japan) has these values: $a = 4.5\text{ mm}$ and $P_0 = 0.17 \frac{\text{Pascal} \times \text{Meter}}{\text{Volt}}$.

2.2.1.2 Scattered Field From a Particle Using Spherical Harmonics

If the particle is larger than half-wavelength, the generated scattered field would influence the simulations; thus, modeling only the incident field may not be sufficient. A way of obtaining the scattered field is using spherical harmonics. Here, we explain the overall method, but complete solutions are described in [42, 55, 56].

The linearity of the acoustic fields allows us to represent the incident p_{in} and scattered p_{sc} fields as series of spherical harmonics $Y_n^m(\Omega)$ (where $\Omega = (\theta, \varphi)$ is the solid angle in spherical coordinates), with modal amplitudes A_n^m and T_n^m . The incident field can be expressed as:

$$p_{in}(r) = p_0 \sum_{n=0}^{\infty} \sum_{m=-n}^n j_n(kr) A_n^m Y_n^m(\Omega).$$

And the scattered field as:

$$p_{sc}(r) = p_0 \sum_{n=0}^{\infty} \sum_{m=-n}^n h_n^{(1)}(kr) T_n^m A_n^m Y_n^m(\Omega).$$

where $(h_n^{(1)})$ is a Hankel function. The scattering coefficients T_n^m characterize the properties of the scattering particle: They depend on the particle shape, the boundary conditions and the internal properties of the particle as well as on the frequency. For a rigid sphere [57] of radius a , the scattering coefficient is given by $T_n^m = -j'_n(ka)/h_n^{(1)'}(ka)\delta_{nm}$, where $'$ denotes differentiation and δ_{nm} is the Kronecker's delta. Other coefficients can be obtained for non-solid particles of different shapes.

Using the orthogonality property of the spherical harmonics, the expansion coefficients A_n^m (often called beam-shape coefficients) can be obtained as:

$$p_0 A_n^m = \frac{1}{j_n(kR)} \iint_{\Omega} p_{in}(R, \Omega) Y_n^{m*}(\Omega) d\Omega,$$

where R is the radius of the spherical volume in which the incident field p_{in} propagates; this volume contains the trapped object.

The incident and scattered field in the far-field ($r \rightarrow \infty$) can be expressed as:

$$p_{in} \approx \frac{p_0}{kr} \sum_{n=0}^{\infty} \sum_{m=-n}^n \sin(kr - n\pi/2) A_n^m Y_n^m(\Omega);$$

$$p_{sc} \approx \frac{p_0}{ikr} e^{ikr} \sum_{n=0}^{\infty} \sum_{m=-n}^n i^{-n} A_n^m T_n^m Y_n^m(\Omega).$$

This method requires the calculation of the incident field, for instance, using the previously described free-field piston model. The analytical scattered field generated by the particle can be added to the incident field to get the total field. This model cannot capture the reflections caused by reflectors of complex shapes or other objects affecting the field apart from the levitated object.

2.2.1.3 Numerical Methods

Numerical methods are preferred to calculate the acoustic field when the domain to be simulated contains complex geometry, for instance hollow tubes of different lengths [46, 58], a levitated particle of complex shape [44] or a curved reflector [59]. In general, these methods take more time to execute than the analytic methods and are less precise but are the only feasible alternative when there are complex geometries in the domain.

One of the simplest numerical methods is the finite-difference time-domain (FDTD) simulation in which the spatial domain is divided into a staged grid for pressure and velocity [60]. More generally, finite element modeling is also possible [61]. If the propagation is on liquids, then it is sufficient to use a scalar pressure and velocity vector, but on solids a complete simulation requires the use of stress tensors [62].

The most employed numerical method in the literature is the boundary elements from the COMSOL package. It allows for irregular meshes of different densities, thus giving a good compromise between accuracy and execution time.

If the trapped particle is smaller than half-wavelength, it could be possible to simulate the field without the particle inside the levitator. The obtained field could be used to calculate forces, independently from the type and position of the particle. However, for large particles and resonant levitators, a simulation with the particle inside is recommended.

2.2.2 Acoustic Radiation Force

The acoustic field will exert a radiation force on the particles contained inside the field. There are other effects such as thermal or viscous contributions [63], but here we focus on the radiation force since it is the dominant force for particles that are large in comparison with the viscous layer [1].

Two methods are presented—one is the Gor'kov potential which is a simple method to calculate the force acting on a particle. The Gor'kov potential only requires the incident field to determine the forces acting on a particle, but it assumes that

the particle is much smaller than the wavelength, spherical and rigid. On the other hand, the flux integral is a more general method to calculate the force acting on an arbitrary-shaped object of any size; it is a more complex approach since it requires the calculation of the total field and an integration over the surface of a sphere that encloses the trapped object.

2.2.2.1 Gor'kov Potential

Gor'kov derived a simplification of the forces acting on a particle when it is inside an acoustic field [3]. A modern and more detailed derivation of the Gor'kov potential was described by Bruus [1]. To calculate the force exerted on a sphere significantly smaller than the wavelength due to a complex pressure field, the negative gradient of the Gor'kov potential can be used $\mathbf{F} = -\nabla U$ where the potential U can be defined in terms of the incident pressure:

$$U = 2K_1(|p|^2) - 2K_2(|p_x|^2 + |p_y|^2 + |p_z|^2)$$

$$K_1 = \frac{1}{4}V\left(\frac{1}{c_0^2\rho_0} - \frac{1}{c_s^2\rho_s}\right)$$

$$K_2 = \frac{3}{4}V\left(\frac{\rho_0 - \rho_s}{\omega^2\rho_0(\rho_0 + 2\rho_s)}\right)$$

where V is the volume of the spherical particle, ω is the frequency of the emitted waves, ρ is the density and c is the speed of sound (subscripts 0 and s refer to the propagation medium and the particle material, respectively). p is the complex pressure and p_x , p_y , p_z are its spatial derivatives over x , y and z . U can also be expressed as a function of the pressure (p) and the velocity (\mathbf{v}), but since the velocity can be obtained as the gradient of the pressure [1], we consider the provided expression more compact. In any case, the fields should be calculated without the particle in the model.

2.2.2.2 Radiation Flux Integral

The radiation force acting on an object can be obtained by the integration of the momentum fluxes over an enclosing sphere. If the total field is given in the frequency domain, the second-order approximation of the radiation force can be expressed as [64]:

$$\mathbf{F} = \iint_S \left\{ \left(\frac{1}{4}\rho|\mathbf{v}|^2 - \frac{1}{4\rho c^2}|p|^2 \right) \mathbf{n} - \frac{1}{2}\rho \operatorname{Re}[\mathbf{v}^*(\mathbf{v} \cdot \mathbf{n})] \right\} dS,$$

where p and \mathbf{v} are the complex pressure and particle velocity due to an acoustic field with time dependence $\exp(-i\omega t)$, S is a surface, \mathbf{n} is normal to the surface enclosing the system, and $*$ is the complex conjugation.

If the pressure and velocity fields are in the time domain, the expression is as follows [56, 61, 65]:

$$\mathbf{F} = \iint_S -\frac{1}{2\rho c^2} \langle p^2 \rangle + \frac{1}{2} \rho \langle \mathbf{v}^2 \rangle - \rho \langle (\mathbf{v}\mathbf{n}) \cdot \mathbf{v} \rangle d\mathbf{a},$$

where $\langle \rangle$ represents the time average.

2.3 Levitator Geometries

The most employed configuration for acoustic levitators is the single-axis levitator [38] which can be divided into two main categories. On the one hand, a standing wave can be generated between an emitter and an opposed reflector; the shape, distance and material of the reflector greatly affects the efficiency. On the other hand, two opposed emitters can be employed to add extra acoustic power and versatility [66].

Another classification attends to the resonant nature of the levitator; there are non-resonant [66] and resonant [67] levitators. This division is more like a continuous spectrum in which the levitators have a certain degree of resonance. Resonant devices are more efficient (i.e., larger trapping forces per input power), but are harder to tune due to changes in atmospheric temperature, humidity and barometric pressure. Non-resonant levitators are simpler to use since they do not need tuning, but are not that efficient. In general, a low ratio of distance between the opposed elements and their emission aperture leads to a highly resonant device, whereas levitators with small radiating surfaces and large separations will be less resonant.

Langevin horns are a common design for the emitters; they are devices made of piezoelectric disks clamped between a backing material and a resonating horn [68]. They can operate at high voltages (typically 100–1000 V) and generate high acoustic pressures with a single emitter; however, they have some disadvantages. It is difficult to tune Langevin horns to a specific resonant frequency; Weber et al. [66] built dozens of horns to obtain two horns with a sufficiently close resonant frequency. Also, the high voltage required to operate the horns can be dangerous. Furthermore, Langevin horns typically heat up over time and shift their resonant frequency. One alternative is to employ small ultrasonic transducers used predominantly in distance ranging applications. They are capable of outputting enough power to obtain levitation of samples of up to 7 g/cm³ [54]. To summarize, the emitters used for levitation are either Langevin horns or off-the-shelf range-finding transducers.

An example of different standing-wave levitator configurations is shown in Fig. 2.2; each of the arrangements is described with more detail in the following subsections.

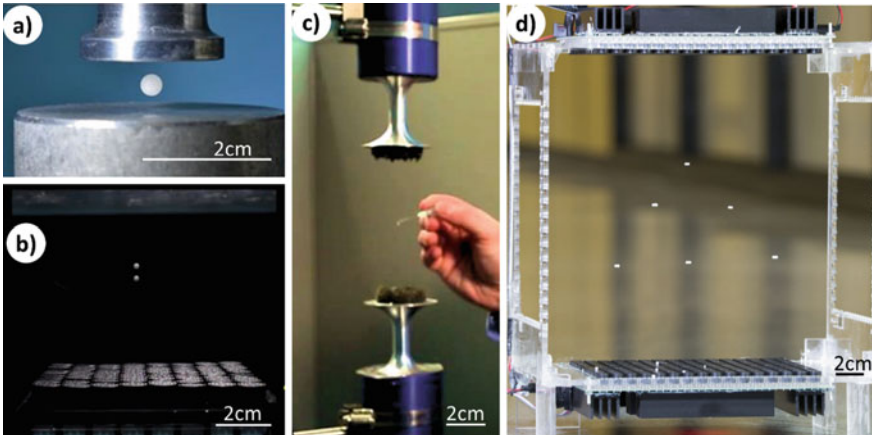


Fig. 2.2 **a** Emitter on top and reflector on the bottom, figure extracted from [48]. **b** Phased array on the bottom and reflector on top. **c** Two opposed emitters, figure extracted from [66]. **d** two opposed phased arrays

2.3.1 Single Emitter and a Reflector

In this configuration, an emitter generates an acoustic wave that reflects on an element placed in front of it at a certain distance. The reflected wave superposes with the emitted wave making a standing wave.

Most of the times, the emitter is a high-power Langevin transducer [68]. An emitter with large diameter of the radiator leads to more stable levitation [69–71]; therefore, Langevin horns for acoustic levitation usually have special designs with a large diameter of the radiation surface (i.e., horn shape).

Considerable research has been conducted on the shape and size of the reflector. A concave reflector leads to stronger acoustic traps than the common planar reflector [59, 70, 71]. Using a concave emitter increased significantly the efficiency of the levitators by locally concentrating the acoustic energy [67]. To improve the adaptability of emitter–reflector levitators, a morphing reflector made of water or elastic materials was employed [72, 73]. It is also possible to enclose the levitator with a tube to improve the performance [74].

When the levitator is resonant, a change in temperature can detune the levitator and reduce the trapping strength [75]. Similarly, introducing large samples in the levitator can shift the resonant frequency [76] and create instabilities [77]. Also, nonlinear behaviors such as second harmonic generation can reduce the trapping force [78].

2.3.2 Two Opposed Emitters

Instead of using a passive reflector to create the standing wave, another possibility is to use two opposed emitters. This allows to put more direct acoustic power and also to move the samples along the axis between the emitters by changing their relative phase [38]. Given the extra acoustic power and phase adjustment, these systems can be used to create non-resonant levitators which are more versatile [66]. Using this approach, a levitator is more robust to external conditions (e.g., temperature, humidity or barometric pressure) and can operate at temperatures ranging from -40 to $+40$ °C, requiring less calibration of the separation between the emitters.

2.3.3 Phased Array and a Reflector

Phased arrays are an assortment of transducers that transmit or receive using defined phases or time delays. They are commonly used in radar [79] or sonar [80] given their ability to dynamically steer and shape the beam. Phased arrays are employed also in standing-wave levitators [7, 51, 54] for their capability of refocusing and shifting the standing waves, thus moving the trapped particles dynamically. However, the trapped particles cannot be moved perpendicularly to the reflector; they can only be moved in a plane parallel to it.

The traps can be moved without displacing the levitator by adjusting the phase of the emitters. A common configuration is to use a phased array opposed to a parallel reflector. The principle of operation is the same as the emitter–reflector, but this time the emitted focal point can be moved dynamically; it is also possible to create multiple focal points. These focal points reflect on the opposed reflector and create standing waves. This has been shown for manipulating multiple samples and merging them in mid-air [13, 82, 83].

2.3.4 Two Opposed Phased Arrays

Using two opposed phased arrays is possible to create standing waves that also shift their nodes perpendicularly to the arrays. First, it was shown that with two opposed arrays, 3D positioning of one particle was possible [81], and then that the individual positioning of multiple particles can be achieved [50]. An iterative back-propagation (IB) algorithm is employed to generate multiple functional traps using arbitrary arrangements of transducers [50]. Two opposed 256-emitter phased arrays are manipulating individually 6 millimetric particles in Fig. 2.3.

When designing standing-wave levitators made of phased arrays, it must be taken into account that the strongest trapping forces are achieved with emitting arrays that satisfy Nyquist sampling [50] (i.e., the emitters are half-wavelength in size) and an

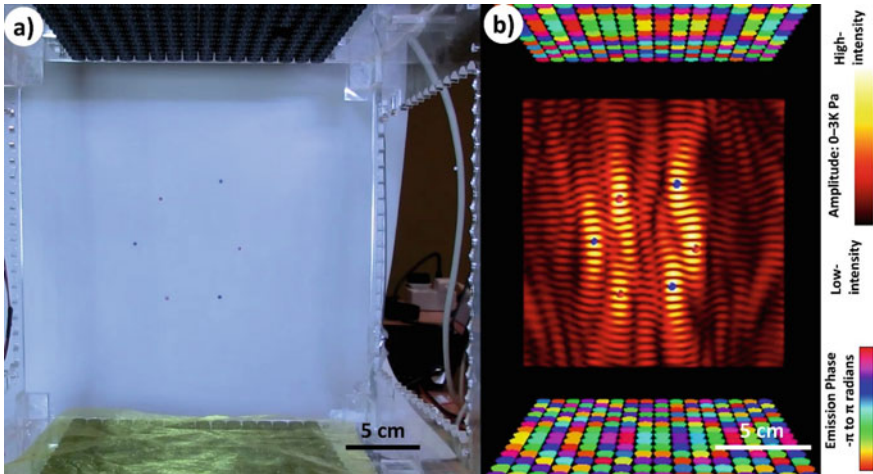


Fig. 2.3 **a** Two opposed arrays made of 16×16 ultrasonic transducers operating at 40 kHz are trapping six spherical particles made of Styrofoam. **b** The simulated amplitude pressure field as well as the emission phases of the transducers

emission phase discretization of $\pi/8$ radians [51]. That is, for standing-wave trapping applications, there is no increase in the trapping strength when having emitters smaller than half-wavelength or creating electronics that support phase resolutions of more than 16 divisions per period.

2.3.5 Other Geometries

There are other geometries apart from the ones presented here: four orthogonal emitters [84] or arrays [85], emitters arranged in a heptagon [86] or in a circle [87–89]. Also, instead of using phased arrays, the required phase modulations can be achieved using metamaterials [39, 46, 58] or a mix of metamaterials and phased arrays [90]. Although this method has less complexity (regarding hardware and cost), it only enables static levitation or restricted movement.

2.4 Conclusion

An acoustic standing wave with enough pressure amplitude will trap at its nodes particles smaller than half-wavelength and of positive acoustic contrast (the particle has

more acoustic impedance than the medium). This is the basic principle behind acoustic levitation and enables multiple applications in contactless manipulation of samples for spectroscopic analysis of materials, amorphous crystallization of solutions or characterization of liquid properties.

Multiple levitator configurations can be used to generate standing waves of high amplitude. Single-axis levitators made of an emitter and an opposed reflector are a simple way to hold samples in mid-air. More complex devices based on phased arrays allow the manipulation of multiple particles independently and thus enable more complex protocols such as mixing of samples. Despite the advances in acoustic trapping with vortices or tractor beams, standing waves remain as the main method to trap particles in mid-air.

References

1. H. Bruus, Acoustofluidics 7: The acoustic radiation force on small particles. *Lab Chip* **12**(6), 1014–1021 (2012). <https://doi.org/10.1039/c2lc21068a9>
2. A.A. Doinikov, On the radiation pressure on small spheres. *J. Acoust. Soc. Am.* **100**(2), 1231–1233 (1996). <https://doi.org/10.1121/1.41596915>
3. L.P. Gorkov, Forces acting on a small particle in an acoustic field within an ideal fluid. *Dokl. Akad. Nauk SSSR* **140**(1), 88 (1961)
4. L.V. King, On the acoustic radiation pressure on spheres. *Proc. R. Soc. A* **147**(861), 212–240 (1934). <https://doi.org/10.1098/rspa.1934.0215>
5. E.H. Brandt, Acoustic physics: Suspended by sound. *Nature* **413**(6855), 474–475 (2001). <https://doi.org/10.1038/35097192>
6. K.C. Neuman, S.M. Block, Optical trapping. *Rev. Sci. Instrum.* **75**(9), 2787–2809 (2004). <https://doi.org/10.1063/1.1785844>
7. A. Marzo, S.A. Seah, B.W. Drinkwater, D.R. Sahoo, B. Long, S. Subramanian, Holographic acoustic elements for manipulation of levitated objects. *Nat. Commun.* **6**, 8661 (2015). <https://doi.org/10.1038/ncomms9661>
8. N.A. Mauro, K.F. Kelton, A highly modular beamline electrostatic levitation facility, optimized for in situ high-energy x-ray scattering studies of equilibrium and supercooled liquids. *Rev. Sci. Instrum.* **82**(3), 035114 (2011)
9. A.L. Yarin, G. Brenn, J. Keller, M. Pfaffenlehner, E. Ryssel, C. Tropea, Flowfield characteristics of an aerodynamic acoustic levitator. *Phys. Fluids* **9**(11), 3300–3314 (1997). <https://doi.org/10.1063/1.869444>
10. A. El Hajjaji, M. Ouladsine, Modeling and nonlinear control of magnetic levitation systems. *IEEE Trans. Ind. Electron.* **48**(4), 831–838 (2001). <https://doi.org/10.1109/41.937416>
11. A.K. Geim, M.D. Simon, M.I. Boamfa, L.O. Heflinger, Magnet levitation at your fingertips. *Nature* **400**(6742), 323 (1999). <https://doi.org/10.1038/22444>
12. M.V. Berry, A.K. Geim, Of flying frogs and levitrons. *Eur. J. Phys.* **18**(4), 307 (1997). <https://doi.org/10.1088/0143-0807/18/4/012>
13. D. Foresti, M. Nabavi, M. Klingauf, A. Ferrari, D. Poulikakos, Acoustophoretic contactless transport and handling of matter in air. *Proc. Natl. Acad. Sci. U S A* **110**(31), 12549–12554 (2013). <https://doi.org/10.1073/pnas.130186011019>
14. T. Kozuka, K. Yasui, T. Tuziuti, A. Towata, Y. Iida, Y, Noncontact acoustic manipulation in air. *Jpn. J. Appl. Phys. Part 1* **46**(7S), 4948 (2007). <https://doi.org/10.1143/jjap.46.4948>
15. C.J. Benmore, J.K.R. Weber, Amorphization of molecular liquids of pharmaceutical drugs by acoustic levitation. *Phys. Rev. X* **1**(1), 011004 (2011). <https://doi.org/10.1103/physrevx.1.011004>

16. A.M. Seddon, S.J. Richardson, K. Rastogi, T.S. Plivelic, A.M. Squires, C. Pfrang, Control of nanomaterial self-assembly in ultrasonically levitated droplets. *J. Phys. Chem. Lett.* **7**(7), 1341–1345 (2016). <https://doi.org/10.1021/acs.jpclett.6b00449>
17. L. Puskar, R. Tuckermann, T. Frosch, J. Popp, V. Ly, D. McNaughton, B.R. Wood, Raman acoustic levitation spectroscopy of red blood cells and *Plasmodium falciparum* trophozoites. *Lab Chip* **7**(9), 1125–1131 (2007). <https://doi.org/10.1039/b706997a>
18. M. Sundvik, H.J. Nieminen, A. Salmi, P. Panula, E. Häggström, Effects of acoustic levitation on the development of zebrafish, *Danio rerio*, embryos. *Sci. Rep.* **5**, 13596 (2015). <https://doi.org/10.1038/srep1359652>
19. W.J. Xie, C.D. Cao, Y.J. Lü, Z.Y. Hong, B. Wei, Acoustic method for levitation of small living animals. *Appl. Phys. Lett.* **89**(21), 214102 (2006). <https://doi.org/10.1063/1.2396893>
20. C.T. Vi et al., Tastyfloats: A contactless food delivery system. in *Proceedings of the 2017 ACM International Conference on Interactive Surfaces and Space*. (ACM, 2017)
21. E. Trinh, T.G. Wang, Large-amplitude free and driven drop-shape oscillations: Experimental observations. *J. Fluid Mech.* **122**, 315–338 (1982). <https://doi.org/10.1017/s0022112082002237>
22. Y. Tian, R.G. Holt, R.E. Apfel, A new method for measuring liquid surface tension with acoustic levitation. *Rev. Sci. Instrum.* **66**(5), 3349–3354 (1995). <https://doi.org/10.1063/1.1145506>
23. E.H. Trinh, P.L. Marston, J.L. Robey, Acoustic measurement of the surface tension of levitated drops. *J. Colloid Interface Sci.* **124**(1), 95–103 (1988). [https://doi.org/10.1016/0021-9797\(88\)90329-3](https://doi.org/10.1016/0021-9797(88)90329-3)
24. Y. Tian, R.G. Holt, R.E. Apfel, Investigation of liquid surface rheology of surfactant solutions by droplet shape oscillations: Experiments. *J. Colloid Interface Sci.* **187**(1), 1–10 (1997). <https://doi.org/10.1006/jcis.1996.4698>
25. S. Bauerecker, B. Neidhart, Formation and growth of ice particles in stationary ultrasonic fields. *J. Chem. Phys.* **109**(10), 3709–3712 (1998). <https://doi.org/10.1063/1.476971>
26. W.J. Xie, C.D. Cao, Y.J. Lü, B. Wei, Eutectic growth under acoustic levitation conditions. *Phys. Rev. E* **66**(6), 061601 (2002). <https://doi.org/10.1103/physreve.66.061601>
27. A.L. Yarin, G. Brenn, D. Rensink, Evaporation of acoustically levitated droplets of binary liquid mixtures. *Int. J. Heat Fluid Flow* **23**(4), 471–486 (2002). [https://doi.org/10.1016/s0142-727x\(02\)00142-x](https://doi.org/10.1016/s0142-727x(02)00142-x)
28. A. Ermoline, M. Schoenitz, V.K. Hoffmann, E.L. Dreizin, Experimental technique for studying high-temperature phases in reactive molten metal based systems. *Rev. Sci. Instrum.* **75**(12), 5177–5185 (2004). <https://doi.org/10.1063/1.1819011>
29. H.L. Cao, D.C. Yin, Y.Z. Guo, X.L. Ma, J. He, W.H. Guo, X.-Z. Xie, B.R. Zhou, Rapid crystallization from acoustically levitated droplets. *J. Acoust. Soc. Am.* **131**(4), 3164–3172 (2012). <https://doi.org/10.1121/1.3688494>
30. A. Stindt, M. Albrecht, U. Panne, J. Riedel, CO₂ laser ionization of acoustically levitated droplets. *Anal. Bioanal. Chem.* **405**(22), 7005–7010 (2013). <https://doi.org/10.1007/s00216-012-6500-y>
31. D. Zang et al., Inducing drop to bubble transformation via resonance in ultrasound. *Nat. Commun.* **9**(1), 3546 (2018)
32. M.S. Westphall, K. Jorabchi, L.M. Smith, Mass spectrometry of acoustically levitated droplets. *Anal. Chem.* **80**(15), 5847–5853 (2008). <https://doi.org/10.1021/ac800317f>
33. S. Santesson, J. Johansson, L.S. Taylor, I. Levander, S. Fox, M. Sepaniak, S. Nilsson, Airborne chemistry coupled to Raman spectroscopy. *Anal. Chem.* **75**(9), 2177–2180 (2003). <https://doi.org/10.1021/ac026302w>
34. B.R. Wood, P. Heraud, S. Stojkovic, D. Morrison, J. Beardall, D. McNaughton, A portable Raman acoustic levitation spectroscopic system for the identification and environmental monitoring of algal cells. *Anal. Chem.* **77**(15), 4955–4961 (2005). <https://doi.org/10.1021/ac050281z>
35. R.J. Weber, C.J. Benmore, S.K. Tumber, A.N. Tailor, C.A. Rey, L.S. Taylor, S.R. Byrn, Acoustic levitation: Recent developments and emerging opportunities in biomaterials research. *Eur. Biophys. J.* **41**(4), 397–403 (2012). <https://doi.org/10.1007/s00249-011-0767-3>

36. S. Santesson, S. Nilsson, Airborne chemistry: Acoustic levitation in chemical analysis. *Anal. Bioanal. Chem.* **378**(7), 1704–1709 (2004). <https://doi.org/10.1007/s00216-003-2403-2>
37. F. Priego-Capote, L. de Castro, Ultrasound-assisted levitation: Lab-on-a-drop, TrAC. *Trends Anal. Chem.* **25**(9), 856–867 (2006). <https://doi.org/10.1016/j.trac.2006.05.014>
38. R.R. Whymark, Acoustic field positioning for containerless processing. *Ultrasonics* **13**(6), 251–261 (1975). [https://doi.org/10.1016/0041-624x\(75\)90072-4](https://doi.org/10.1016/0041-624x(75)90072-4)
39. K. Melde et al., Holograms for acoustics. *Nature*. **537.7621**, 518 (2016)
40. Sadayuki Ueha, Yoshiki Hashimoto, Yoshiakazu Koike, Non-contact transportation using near-field acoustic levitation. *Ultrasonics* **38**(1-8), 26–32 (2000)
41. M.A.B. Andrade, A.L. Bernassau, Julio C. Adamowski. Acoustic levitation of a large solid sphere. *Appl. Phys. Lett.* **109.4**, 044101 (2016)
42. Asier Marzo, Mihai Caleap, Bruce W. Drinkwater, Acoustic virtual vortices with tunable orbital angular momentum for trapping of mie particles. *Phy. Rev. Lett.* **120**(4), 044301 (2018)
43. S. Inoue et al., Acoustic macroscopic rigid body levitation by responsive boundary hologram. arXiv preprint [arXiv:1708.05988](https://arxiv.org/abs/1708.05988) (2017)
44. L. Cox et al., Acoustic lock: Position and orientation trapping of non-spherical sub-wavelength particles in mid-air using a single-axis acoustic levitator. *Appl. Phys. Lett.* **113**(5), 054101 (2018)
45. C.E.M. Démoré et al., Acoustic tractor beam. *Phys. Rev. Lett.* **112.17**, 174302 (2014)
46. A. Marzo et al., Realization of compact tractor beams using acoustic delay-lines. *Appl. Phys. Lett.* **110**(1), 014102 (2017)
47. Diego Baresch, Jean-Louis Thomas, Régis Marchiano, Observation of a single-beam gradient force acoustical trap for elastic particles: acoustical tweezers. *Phys. Rev. Lett.* **116**(2), 024301 (2016)
48. M.A.B. Andrade, N. Pérez, J.C. Adamowski. Review of progress in acoustic levitation. *Brazilian J. Phys.* **48.2**, 190–213 (2018)
49. Bruce W. Drinkwater, Dynamic-field devices for the ultrasonic manipulation of microparticles. *Lab a Chip* **16**(13), 2360–2375 (2016)
50. Asier Marzo, Bruce W. Drinkwater, Holographic acoustic tweezers. *Proc. Natl. Acad. Sci.* **116**(1), 84–89 (2019)
51. Asier Marzo, Tom Corkett, Bruce W. Drinkwater, Ultraino: An open phased-array system for narrowband airborne ultrasound transmission. *IEEE Trans. Ultrason. Ferroelectr. Freq. Control* **65**(1), 102–111 (2017)
52. H.T. O’Neil, Theory of focusing radiators. *J. Acoust. Soc. Amer.* **21**(5), 516–526 (1949)
53. R.M. Aarts, A.J.E.M. Augustus, On-axis and far-field sound radiation from resilient flat and dome-shaped radiators. *J. Acoust. Soc. Am.* **125.3**, 1444–1455 (2009)
54. Asier Marzo, Adrian Barnes, Bruce W. Drinkwater, TinyLev: A multi-emitter single-axis acoustic levitator. *Rev. Sci. Instrum.* **88**(8), 085105 (2017)
55. Oleg A. Sapozhnikov, Michael R. Bailey, Radiation force of an arbitrary acoustic beam on an elastic sphere in a fluid. *J. Acoust. Soc. Am.* **133**(2), 661–676 (2013)
56. Diego Baresch, Jean-Louis Thomas, Régis Marchiano, Three-dimensional acoustic radiation force on an arbitrarily located elastic sphere. *J. Acoust. Soc. Am.* **133**(1), 25–36 (2013)
57. J.J. Faran Jr, Sound scattering by solid cylinders and spheres. *J. Acoust. Soc. Am.* **23.4**, 405–418 (1951)
58. G. Memoli et al. Metamaterial bricks and quantization of meta-surfaces. *Nat. Commun.* **8**, 14608 (2017)
59. W.A. Oran, L.H. Berge, H.W. Parker, Parametric study of an acoustic levitation system. *Rev. Sci. Instrum.* **51**(5), 626–631 (1980). <https://doi.org/10.1063/1.1136268>
60. A. Allen, N. Raghuvarsh, Aerophones in flatland: Interactive wave simulation of wind instruments. *ACM Trans. Graphics (TOG)* **34**(4), 134 (2015). <https://doi.org/10.1145/2767001>
61. P. Glynn-Jones et al., Efficient finite element modeling of radiation forces on elastic particles of arbitrary size and geometry. *J. Acoust. Soc. Am.* **133.4**, 1885–1893 (2013)
62. Y. Tanikaga, T. Sakaguchi, Y. Watanabe, A study on analysis of intracranial acoustic wave propagation by the finite difference time domain method. in *Proceedings of Forum Acusticum*, vol. 4 no 4 (Sevilla, 2002)

63. Mikkel Settnes, Henrik Bruus, Forces acting on a small particle in an acoustical field in a viscous fluid. *Phys. Rev. E* **85**(1), 016327 (2012)
64. Peter J. Westervelt, Scattering of sound by sound. *J. Acoust. Soc. Am.* **29**(2), 199–203 (1957)
65. F.E. Borgnis, Acoustic radiation pressure of plane compressional waves. *R. Modern Phys.* **25**(3), 653 (1953)
66. J.K.R. Weber, C.A. Rey, J. Neufeld, C.J. Benmore, Acoustic levitator for structure measurements on low temperature liquid droplets. *Rev. Sci. Instrum.* **80**(8), 083904 (2009)
67. M.A. Andrade, F. Buiochi, J.C. Adamowski, Finite element analysis and optimization of a single-axis acoustic levitator. *IEEE Trans. Ultrason. Ferroelectr. Freq. Control* **57**(2), 469–479 (2010)
68. S. Lin, Study on the multifrequency Langevin ultrasonic transducer. *Ultrasonics* **33**(6), 445–448 (1995)
69. E.H. Trinh, Compact acoustic levitation device for studies in fluid dynamics and material science in the laboratory and microgravity. *Rev. Sci. Instrum.* **56**(11), 2059–2065 (1985)
70. W.J. Xie, B. Wei, Parametric study of single-axis acoustic levitation. *Appl. Phys. Lett.* **79**(6), 881–883 (2001). <https://doi.org/10.1063/1.139139850>
71. W.J. Xie, B. Wei, Dependence of acoustic levitation capabilities on geometric parameters. *Phys. Rev. E* **66**(2), 026605 (2002)
72. D. Foresti, G. Sambatakakis, S. Bottan, D. Poulikakos, Morphing surfaces enable acoustophoretic contactless transport of ultrahigh-density matter in air. *Sci. Rep.* **3**, 3176 (2013). <https://doi.org/10.1038/srep0317616>
73. Z.Y. Hong, W.J. Xie, B. Wei, Acoustic levitation with self-adaptive flexible reflectors. *Rev. Sci. Instrum.* **82**(7), 074904 (2011)
74. H. Jiang et al., Analysis and experimental study on the effect of a resonant tube on the performance of acoustic levitation devices. *AIP Adv.* **6**.9, 095302 (2016)
75. W.J. Xie, B. Wei, Temperature dependence of single-axis acoustic levitation. *J. Appl. Phys.* **93**(5), 3016–3021 (2003)
76. X. Wen-Jun, W. Bing-Bo, Resonance shift of single-axis acoustic levitation. *Chin. Phys. Lett.* **24**(1), 135 (2007)
77. M.A.B. Andrade et al., Experimental investigation of the particle oscillation instability in a single-axis acoustic levitator. *AIP Adv.* **9**.3, 035020 (2019)
78. M.A. Andrade, T.S. Ramos, F.T. Okina, J.C. Adamowski, Nonlinear characterization of a single-axis acoustic levitator. *Rev. Sci. Instrum.* **85**(4), 045125 (2014)
79. C. Pell, Phased-array radars. *IEE Rev.* **34**(9), 363–367 (1988)
80. J.H.G. Ender, A.R. Brenner, PAMIR—A wideband phased array SAR/MTI system. *IEEE Proc.-Radar Sonar Navigat.* **150**(3) 165–172 (2003)
81. T. Omirou et al., LeviPath: Modular acoustic levitation for 3D path visualisations. in *Proceedings of the 33rd Annual ACM Conference on Human Factors in Computing Systems*. (ACM, 2015)
82. Ayumu Watanabe, Koji Hasegawa, Yutaka Abe, Contactless fluid manipulation in air: Droplet coalescence and active mixing by acoustic levitation. *Sci. Reports* **8**(1), 10221 (2018)
83. M.A.B. Andrade, T.S.A. Camargo, A. Marzo, Automatic contactless injection, transportation, merging, and ejection of droplets with a multifocal point acoustic levitator. *Rev. Sci. Instr.* **89**.12, 125105 (2018)
84. M.K. Nichols et al., Fabrication of micropatterned dipeptide hydrogels by acoustic trapping of stimulus-responsive coacervate droplets. *Small* **14**.26, 1800739 (2018)
85. Y. Ochiai, T. Hoshi, J. Rekimoto, Pixie dust: graphics generated by levitated and animated objects in computational acoustic-potential field. *ACM Trans Graphics (TOG)* **33**(4), 85 (2014)
86. F. Gesellchen, et al., Cell patterning with a heptagon acoustic tweezer—application in neurite guidance. *Lab Chip* **14**.13, 2266–2275 (2014)
87. C.R.P. Courtney et al., Independent trapping and manipulation of microparticles using dexterous acoustic tweezers. *Appl. Phys. Lett.* **104**.15, 154103 (2014)
88. S.A. Seah, et al., Correspondence: Dexterous ultrasonic levitation of millimeter-sized objects in air. *IEEE Trans. Ultrason. Ferroelectr. Frequency Control* **61**.7, 1233–1236 (2014)

89. D. Foresti, D. Poulikakos, Acoustophoretic contactless elevation, orbital transport and spinning of matter in air. *Phys. Rev. Lett.* **112**(2), 024301 (2014)
90. M.A. Norasikin et al., SoundBender: dynamic acoustic control behind obstacles. in *The 31st Annual ACM Symposium on User Interface Software and Technology* (ACM, 2018)

Chapter 3

Design of Single-Axis Acoustic Levitators



Marco A. B. Andrade

Abstract In this chapter, a numerical procedure based on the finite element method (FEM) is presented for simulating and designing single-axis acoustic levitators. We first present an overview of the equations governing the propagation of mechanical waves in solids, piezoelectric materials and the air medium. We then show how axisymmetric models based on FEM can be utilized for simulating piezoelectric transducers and the acoustic cavity of the levitator. To illustrate the design procedure, the finite element method is applied to simulate and design a 25-kHz bolt-clamped Langevin-type transducer. The FEM is also used to design a resonant single-axis acoustic levitator and to investigate the behavior of a non-resonant acoustic levitator.

3.1 Introduction

Different acoustic levitation methods [1, 2] are available for suspending solids and liquids in mid-air, including the standing wave levitation method [3–5], the near-field levitation [6–8] and the single-beam trapping (also called tractor beam) [9, 10]. Among these methods, single-axis levitators based on standing waves are the most popular, with the standing wave being generated between an emitter and a reflector [4, 11, 12], two opposing emitters [13] or two opposing arrays of transducers [14, 15].

Single-axis acoustic levitators can be divided into resonant [4, 11] and non-resonant [14, 16, 17] devices. For resonant devices consisting of an emitter and an opposing reflector, the emitter–reflector distance should be adjusted to one of the resonant states of the acoustic cavity such that a standing wave of high acoustic pressure amplitude is established between them. Non-resonant levitators, in contrast, do not require a precise separation distance between the acoustic elements, and the

M. A. B. Andrade (✉)

Institute of Physics, University of São Paulo, 05508-090 São Paulo, Brazil
e-mail: marcobrizzotti@gmail.com

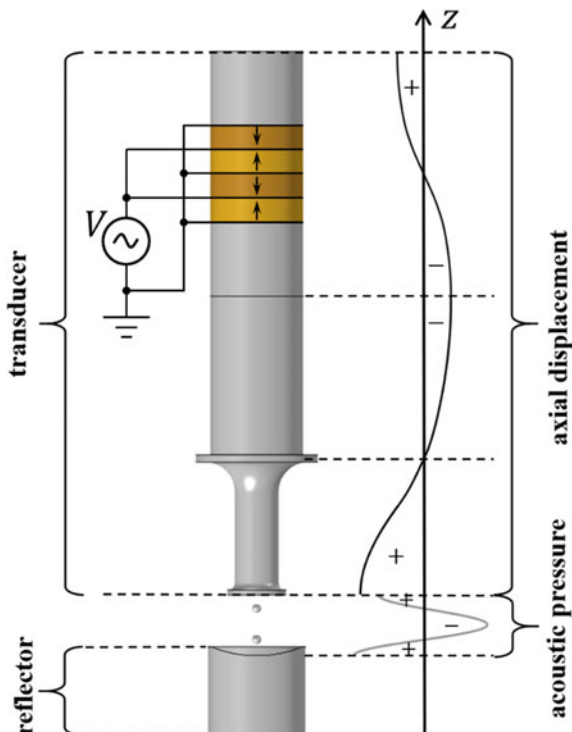
standing wave is generated by the superposition of two counter-propagating waves. Resonant levitators have the main advantage of being more efficient, allowing the levitation of high-density materials [18] with relatively low power.

A typical resonant single-axis acoustic levitator is illustrated in Fig. 3.1. In this figure, the acoustic wave is generated by a bolt-clamped Langevin-type transducer [19, 20], which is formed by two main parts: (1) a sandwich structure consisting of a back mass, a stack of piezoelectric ceramics and a front mass, and (2) a mechanical amplifier formed by two cylindrical blocks of different diameters. Each transducer part works as a half-wavelength resonator.

The conversion of electric energy into mechanical energy occurs in the sandwich structure. This transducer part is formed by pairs of piezoelectric rings, which are compressed between two masses by a central bolt (not shown in Fig. 3.1). The piezoelectric ceramics have alternate polarization (indicated by the arrows in Fig. 3.1). Thereby, when a sinusoidal electric signal is applied, all the piezoceramics contract or expand at the same time.

The mechanical amplifier is used to increase the displacement amplitude generated by the sandwich structure. The mechanical amplification is achieved by reducing the diameter of the bottom cylinder with respect to the upper cylinder. Similar to the sandwiched structure, the mechanical amplifier also works as a half-wavelength

Fig. 3.1 Resonant single-axis acoustic levitator consisting of an ultrasonic transducer and an opposed reflector



resonator. The sandwich structure and the mechanical amplifier should be carefully designed to ensure that each transducer part resonates at the same frequency. Due to the relative complex geometry, a bolt-clamped Langevin transducer is usually designed using numerical methods, such as the finite element method (FEM) instead of analytical approaches.

The levitation performance of a single-axis acoustic levitator also depends on the geometry of the acoustic cavity. Although a single-axis acoustic levitator can be built with both transducer and reflector having plane surfaces, the use of concave surfaces allows a significant increase in the acoustic radiation force acting on the levitated objects [4, 12, 21]. Therefore, the design of the reflector is of fundamental importance on the levitator behavior.

In this chapter, a numerical procedure to design single-axis acoustic levitators is presented. In Sect. 3.2, we present an overview of the theory used to describe the propagation of time-harmonic mechanical waves in solids, piezoelectric materials and fluid media. In Sect. 3.3, the numerical procedure to design a Langevin-type transducer is presented. In Sect. 3.4, a numerical model for simulating the acoustic cavity of a single-axis acoustic levitator is described. In Sect. 3.5, we apply the numerical models described in Sects. 3.3 and 3.4 to design a 25-kHz Langevin-type transducer. Finally, Sects. 3.6 and 3.7 describe the development of a resonant and a non-resonant acoustic levitator, respectively.

3.2 Governing Equations

The numerical modeling of a single-axis acoustic levitator requires a set of equations to describe the propagation of mechanical waves in three types of materials: solid, piezoelectric material and the air medium. Since the acoustic wavelength λ is much larger than the interatomic distances, these materials can be modeled as a continuous medium. In the next sections, we present an overview of the governing equations that describe the propagation of time-harmonic waves in solids, piezoelectric materials and fluid media. A complete discussion and detailed derivation of the equations are beyond the scope of this chapter. A more complete description of the theory can be found in numerous textbooks [22–25].

3.2.1 Solid

Let us consider an infinitesimal element of a solid, as shown in Fig. 3.2. This small element has a volume $dV = dx dy dz$ and it is located at a position $\mathbf{r} = x\hat{\mathbf{i}} + y\hat{\mathbf{j}} + z\hat{\mathbf{k}}$, in which $\hat{\mathbf{i}}, \hat{\mathbf{j}}$ and $\hat{\mathbf{k}}$ are the Cartesian unit vectors. The element can be subjected to two kinds of forces: body forces and surface forces. Body forces can be described by the vector \mathbf{F} , which represents the force per unit of volume acting on the element. Surface

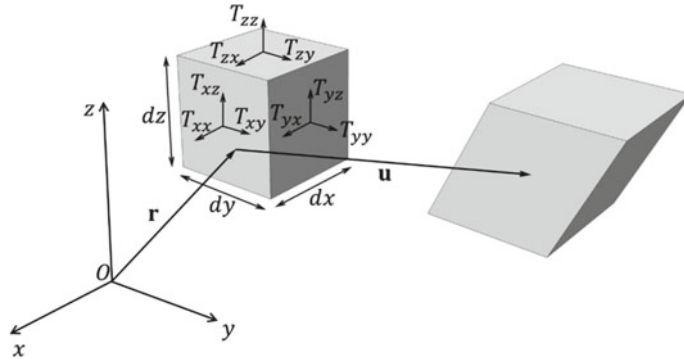


Fig. 3.2 Normal and shear stresses at the surfaces of an infinitesimal solid element. When external forces are applied on the solid material, the undeformed element (left-hand side) becomes deformed (right-hand side) and its displacement is represented by the vector \mathbf{u}

forces are described by the second-order stress tensor \mathbf{T} , which is represented by the matrix

$$\mathbf{T} = \begin{bmatrix} T_{xx} & T_{xy} & T_{xz} \\ T_{yx} & T_{yy} & T_{yz} \\ T_{zx} & T_{zy} & T_{zz} \end{bmatrix}. \quad (3.1)$$

The components T_{xx} , T_{yy} and T_{zz} are the normal forces per unit area (normal stresses) acting on the surfaces of the element, whereas the components T_{xy} , T_{xz} , T_{yx} , T_{yz} , T_{zx} and T_{zy} are the shear forces per unit area (shear stresses). The stress tensor \mathbf{T} is symmetric, resulting in $T_{xy} = T_{yx}$, $T_{xz} = T_{zx}$ and $T_{yz} = T_{zy}$.

When the infinitesimal element of Fig. 3.2 is subjected to external forces, it is displaced from its equilibrium position and the element of volumes becomes deformed. The displacement from its equilibrium position is represented by the vector $\mathbf{u} = u_x \hat{\mathbf{i}} + u_y \hat{\mathbf{j}} + u_z \hat{\mathbf{k}}$ and its deformation can be described by the strain tensor \mathbf{S} , given by

$$\mathbf{S} = \begin{bmatrix} S_{xx} & S_{xy} & S_{xz} \\ S_{yx} & S_{yy} & S_{yz} \\ S_{zx} & S_{zy} & S_{zz} \end{bmatrix}, \quad (3.2)$$

where the elements of the strain tensor are:

$$S_{xx} = \frac{\partial u_x}{\partial x}, \quad (3.3)$$

$$S_{yy} = \frac{\partial u_y}{\partial y}, \quad (3.4)$$

$$S_{zz} = \frac{\partial u_z}{\partial z}, \quad (3.5)$$

$$S_{xy} = \frac{1}{2} \left(\frac{\partial u_x}{\partial y} + \frac{\partial u_y}{\partial x} \right), \quad (3.6)$$

$$S_{yz} = \frac{1}{2} \left(\frac{\partial u_y}{\partial z} + \frac{\partial u_z}{\partial y} \right), \quad (3.7)$$

$$S_{xz} = \frac{1}{2} \left(\frac{\partial u_x}{\partial z} + \frac{\partial u_z}{\partial x} \right). \quad (3.8)$$

Similar to the stress tensor, the strain tensor is also symmetric, which means that $S_{xy} = S_{yx}$, $S_{yz} = S_{zy}$ and $S_{xz} = S_{zx}$.

When the infinitesimal element of Fig. 3.2 is subjected to a sufficiently small stress, we can assume that strain changes linearly with the applied stress. In this situation, the deformation of the body is governed by the Hooke's law, given by

$$\mathbf{T} = \mathbf{C} : \mathbf{S}, \quad (3.9)$$

where \mathbf{C} is the fourth-order stiffness tensor and the symbol “:” is the double dot product between the fourth-order tensor \mathbf{C} and the second-order tensor \mathbf{S} . This product results in the second-order tensor \mathbf{T} . In many textbooks, the Hooke's law is usually written using the indicial notation. In indicial notation, Eq. (3.9) is equivalent to $T_{ij} = C_{ijkl} S_{kl}$, with each index varying from 1 to 3 and repeated indices implying summation (Einstein summation convention).

The stress, the strain and the stiffness tensors are symmetric. Therefore, we can use the Voigt notation to reduce the order of these tensors. In Voigt notation, the second-order stress tensor can be written as

$$\mathbf{T} = \begin{bmatrix} T_1 \\ T_2 \\ T_3 \\ T_4 \\ T_5 \\ T_6 \end{bmatrix} = \begin{bmatrix} T_{xx} \\ T_{yy} \\ T_{zz} \\ T_{yz} \\ T_{xz} \\ T_{xy} \end{bmatrix}. \quad (3.10)$$

In Eq. (3.10), instead of representing the stress tensor as a 3×3 matrix, the stress tensor is represented by a column matrix of six elements. Similarly, the strain tensor can be described as

$$\mathbf{S} = \begin{bmatrix} S_1 \\ S_2 \\ S_3 \\ S_4 \\ S_5 \\ S_6 \end{bmatrix} = \begin{bmatrix} S_{xx} \\ S_{yy} \\ S_{zz} \\ 2S_{yz} \\ 2S_{xz} \\ 2S_{xy} \end{bmatrix}. \quad (3.11)$$

In the Voigt notation, the stiffness tensor is represented by a symmetric matrix of 6×6 elements:

$$\mathbf{C} = \begin{bmatrix} C_{11} & C_{12} & C_{13} & C_{14} & C_{15} & C_{16} \\ C_{12} & C_{22} & C_{23} & C_{24} & C_{25} & C_{26} \\ C_{13} & C_{23} & C_{33} & C_{34} & C_{35} & C_{36} \\ C_{14} & C_{24} & C_{34} & C_{44} & C_{45} & C_{46} \\ C_{15} & C_{25} & C_{35} & C_{45} & C_{55} & C_{56} \\ C_{16} & C_{26} & C_{36} & C_{46} & C_{56} & C_{66} \end{bmatrix}. \quad (3.12)$$

In general, the stiffness tensor has 21 independent constants, but depending on the structure of the solid, the number of independent constants can be reduced. For an isotropic solid, the stiffness tensor \mathbf{C} reduces to only 2 independent constants and it can be written as

$$\mathbf{C} = \frac{E}{(1+\nu)(1-2\nu)} \begin{bmatrix} 1-\nu & \nu & \nu & 0 & 0 & 0 \\ \nu & 1-\nu & \nu & 0 & 0 & 0 \\ \nu & \nu & 1-\nu & 0 & 0 & 0 \\ 0 & 0 & 0 & \frac{1-2\nu}{2} & 0 & 0 \\ 0 & 0 & 0 & 0 & \frac{1-2\nu}{2} & 0 \\ 0 & 0 & 0 & 0 & 0 & \frac{1-2\nu}{2} \end{bmatrix}, \quad (3.13)$$

where E is Young's modulus and ν is the Poisson's ratio. Consequently, the Hooke's law for an isotropic material is given by

$$\begin{bmatrix} T_1 \\ T_2 \\ T_3 \\ T_4 \\ T_5 \\ T_6 \end{bmatrix} = \frac{E}{(1+\nu)(1-2\nu)} \begin{bmatrix} 1-\nu & \nu & \nu & 0 & 0 & 0 \\ \nu & 1-\nu & \nu & 0 & 0 & 0 \\ \nu & \nu & 1-\nu & 0 & 0 & 0 \\ 0 & 0 & 0 & \frac{1-2\nu}{2} & 0 & 0 \\ 0 & 0 & 0 & 0 & \frac{1-2\nu}{2} & 0 \\ 0 & 0 & 0 & 0 & 0 & \frac{1-2\nu}{2} \end{bmatrix} \begin{bmatrix} S_1 \\ S_2 \\ S_3 \\ S_4 \\ S_5 \\ S_6 \end{bmatrix}. \quad (3.14)$$

Equation (3.14) can also be written as

$$\mathbf{T} = \mathbf{CS}, \quad (3.15)$$

where the stress \mathbf{T} , stiffness \mathbf{C} and strain \mathbf{S} tensors are given in Eqs. (3.10), (3.13) and (3.11), respectively.

In addition to the constitutive equation of the solid, given in Eq. (3.15), the dynamic modeling of a solid also requires the equation of motion, given by [24]

$$\rho \frac{\partial^2 \mathbf{u}}{\partial t^2} = \nabla \cdot \mathbf{T} + \mathbf{F}, \quad (3.16)$$

where ρ is the material density. Equation (3.16) is Newton's second law for the solid element of Fig. 3.2. The term on the left-hand side represents the product of the mass $dm = \rho dx dy dz$ and the element acceleration, and the right-hand side corresponds to the total force acting on the infinitesimal element of volume dV .

The acoustic levitator is usually driven by a sinusoidal electric signal of angular frequency ω . We assume that the amplitude of the electric signal is sufficiently small to model the motion of the transducer by linear equations. In this case, all the quantities can be described by time-harmonic functions of the form

$$f = A \cos(\omega t + \phi), \quad (3.17)$$

where A and ϕ represent, respectively, the amplitude and the phase of the quantity f . As it is usual in physics, time-harmonic quantities are represented by complex numbers. Equation (3.17) is then written as

$$f = \operatorname{Re}[A e^{j(\omega t + \phi)}] = \operatorname{Re}[A e^{j\phi} e^{j(\omega t)}] = \operatorname{Re}[A_c e^{j(\omega t)}], \quad (3.18)$$

where $j = \sqrt{-1}$ is the imaginary number and $\operatorname{Re}[f]$ denotes the real part of f . In Eq. (3.18), the amplitude A and phase ϕ can be grouped into the complex amplitude $A_c = A e^{j\phi}$. Using the complex number, the equation of motion given in Eq. (3.16) can be rewritten as

$$-\rho \omega^2 \mathbf{u} = \nabla \cdot \mathbf{T} + \mathbf{F}. \quad (3.19)$$

Given an elastic solid body subjected to time-harmonic forces, Eq. (3.19) can be solved in order to find the complex displacement \mathbf{u} in the body. Note that Eq. (3.19) is a linear equation, which means that if the external forces have an angular frequency ω , all the points of the body will also vibrate with the same frequency and with a displacement amplitude proportional to the applied forces.

3.2.2 Piezoelectric

As described by the Hooke's law, the strain of a solid body is proportional to the applied stress. Similarly, the linear electric behavior of a dielectric material can be described by

$$\mathbf{D} = \boldsymbol{\epsilon} \mathbf{E}, \quad (3.20)$$

where \mathbf{D} is the electrical displacement, \mathbf{E} is the electric field and $\boldsymbol{\epsilon}$ is the permittivity matrix. In a piezoelectric material, the mechanical behavior of the material is coupled with its electrical behavior. In a piezoelectric material, the stress \mathbf{T} depends not only on the strain \mathbf{S} , but it also depends on the applied electrical field \mathbf{E} . The same happens with the electrical displacement \mathbf{D} , which depends not only on the electric field \mathbf{E} but also varies with the strain \mathbf{S} . Therefore, assuming a linear behavior, the constitutive equations of a piezoelectric material can be described by the following equations:

$$\mathbf{T} = \mathbf{C}^E \mathbf{S} - \mathbf{e}^t \mathbf{E}, \quad (3.21)$$

$$\mathbf{D} = \mathbf{e} \mathbf{S} + \boldsymbol{\epsilon}^S \mathbf{E}, \quad (3.22)$$

where \mathbf{C}^E is the stiffness matrix at constant electric field, \mathbf{e} is matrix of piezoelectric constants and $\boldsymbol{\epsilon}^S$ is the permittivity matrix at constant strain. In Eq. (3.21), the superscript t represents the transpose of a matrix. For the general case, the stiffness matrix \mathbf{C}^E has 21 independent constants, the piezoelectric matrix \mathbf{e} has 18 independent constants and the permittivity matrix $\boldsymbol{\epsilon}^S$ has 6 independent constants.

The number of independent constants can be reduced by considering the symmetry of the piezoelectric material. Piezoelectric materials commonly used in ultrasonic transducers have $6mm$ symmetry class. Piezoelectric materials belonging to the $6mm$ symmetry class with a polarization in the z direction have the following material properties [26]:

$$\mathbf{C}^E = \begin{bmatrix} C_{11}^E & C_{12}^E & C_{13}^E & 0 & 0 & 0 \\ C_{12}^E & C_{11}^E & C_{13}^E & 0 & 0 & 0 \\ C_{13}^E & C_{13}^E & C_{33}^E & 0 & 0 & 0 \\ 0 & 0 & 0 & C_{44}^E & 0 & 0 \\ 0 & 0 & 0 & 0 & C_{44}^E & 0 \\ 0 & 0 & 0 & 0 & 0 & \frac{1}{2}(C_{11}^E - C_{12}^E) \end{bmatrix}, \quad (3.23)$$

$$\boldsymbol{\epsilon}^S = \begin{bmatrix} \epsilon_{11}^S & 0 & 0 \\ 0 & \epsilon_{11}^S & 0 \\ 0 & 0 & \epsilon_{33}^S \end{bmatrix}, \quad (3.24)$$

$$\mathbf{e} = \begin{bmatrix} 0 & 0 & 0 & 0 & e_{15} & 0 \\ 0 & 0 & 0 & e_{15} & 0 & 0 \\ e_{31} & e_{31} & e_{33} & 0 & 0 & 0 \end{bmatrix}, \quad (3.25)$$

In addition to the constitutive equations given in Eqs. (3.21) and (3.22), the modeling of piezoelectric materials also requires the equation of motion [Eq. (3.19)] and the equations that describe the electric behavior of the material. The electrical behavior of a piezoelectric material can be described by the following equations:

$$\mathbf{E} = -\nabla V, \quad (3.26)$$

$$\nabla \cdot \mathbf{D} = \rho_c. \quad (3.27)$$

In Eq. (3.26), V is the electrical potential and, in Eq. (3.27), ρ_c is the charge density.

3.2.3 Air

The propagation of mechanical waves of small amplitude in the air medium can be described by the linear wave equation [25]:

$$\nabla^2 p = \frac{1}{c_0^2} \frac{\partial^2 p}{\partial t^2}, \quad (3.28)$$

where p is the acoustic pressure and c_0 is the speed of sound in the air medium. The relationship between the acoustic pressure and the particle velocity vector \mathbf{v} is given by the linear Euler's equation:

$$\rho_0 \frac{\partial \mathbf{v}}{\partial t} = -\nabla p, \quad (3.29)$$

where ρ_0 is the unperturbed density of the air medium. Assuming time-harmonic waves, the acoustic pressure can be described by $p(\mathbf{r}, t) = p(\mathbf{r})e^{j(\omega t)}$, where $p(\mathbf{r})$ is the complex amplitude. Replacing this equation into Eq. (3.28) yields

$$\nabla^2 p(\mathbf{r}) + k^2 p(\mathbf{r}) = 0, \quad (3.30)$$

which is the Helmholtz equation. In this equation, $k = \omega/c_0$ is the wavenumber.

3.3 Transducer Simulation

The Langevin-type transducer to be designed consists of a sandwich structure and a mechanical amplifier. Because of the complex geometry of the transducer, numerical models such as the finite element method are widely used to design the transducer. However, instead of using only one numerical simulation to design the whole transducer, it is simpler to divide the transducer design into two parts. Using this strategy, one numerical model is implemented to design the sandwich structure and another model is implemented to design the mechanical amplifier. As illustrated in Fig. 3.1,

each transducer part vibrates as a half-wavelength resonator, and therefore, the sandwich structure and the mechanical amplifier must have the same resonance frequency. After designing each part separately, the individual parts are coupled together and a new simulation is performed to evaluate the dynamic behavior of the entire transducer. In most cases, when the individual parts are merged, the whole transducer will have the same resonance frequency. In case the resonance frequency of the transducer does not match the resonance frequency of each individual part, the dimensions of the whole assembly can be adjusted to make the transducer resonate at the desired frequency.

The vibration behavior of this type of transducer can be described by the set of equations presented in Sect. 3.2. For simple transducer geometries, approximate analytical solutions can be found, but in most cases, numerical models based on the finite element method are used for transducer design. Moreover, as Langevin-type transducers have circular symmetry, the computational time can be reduced by using axisymmetric simulations.

A typical axisymmetric numerical model of a transducer is shown in Fig. 3.3. The model of Fig. 3.3a is used to simulate the sandwich structure, whereas the model of Fig. 3.3b is used in the mechanical amplifier design. It is worth mentioning that due to the large acoustic impedance mismatch between the transducer and the air medium, the transducer can be simulated separately from the air medium.

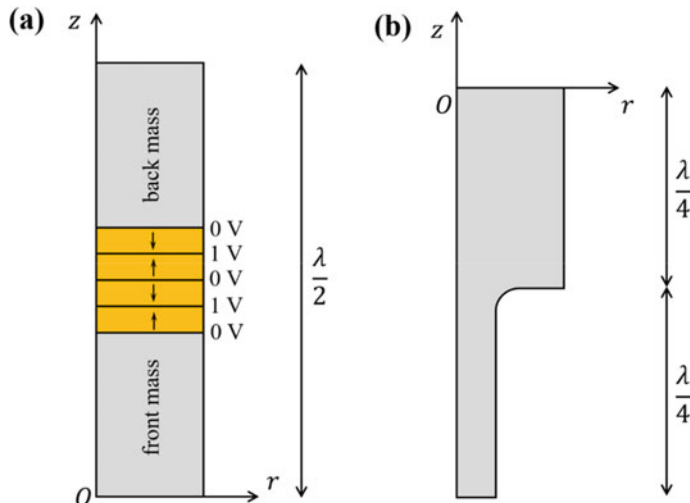


Fig. 3.3 Axisymmetric numerical models used in the design of a Langevin-type transducer. **a** Model of the sandwich structure. **b** Model of the mechanical amplifier

3.4 Levitation Simulation

Given the levitator geometry and the normal velocity distribution v_0 over the transducer radiating surface, we are interested in calculating the acoustic radiation force that acts on a rigid sphere of radius R located at a position \mathbf{r} (see Fig. 3.4a). One possibility is to employ three-dimensional simulations to find the acoustic pressure p and the particle velocity distribution \mathbf{v} around the sphere, and then use the following expression for calculating the time-averaged acoustic radiation pressure p_{rad} on the sphere surface [1]:

$$p_{\text{rad}} = \frac{1}{2\rho_0 c_0^2} \langle p^2 \rangle - \frac{\rho_0}{2} \langle \mathbf{v} \cdot \mathbf{v} \rangle, \quad (3.31)$$

where the angle brackets $\langle \rangle$ represent the time average over one period. After calculating the radiation pressure on the sphere surface, the total acoustic radiation force \mathbf{F}_{rad} is determined by integrating the radiation pressure over the sphere surface:

$$\mathbf{F}_{\text{rad}} = - \int_{S_0} p_{\text{rad}} \mathbf{n} \, dS, \quad (3.32)$$

where \mathbf{n} is the surface normal vector pointing outward the sphere and the integral is evaluated over the sphere surface S_0 . It is worth mentioning that Eqs. (3.31) and (3.32) can also be used for calculating the acoustic radiation force on the reflector [27], which is useful for finding the resonant states of a resonant acoustic levitator.

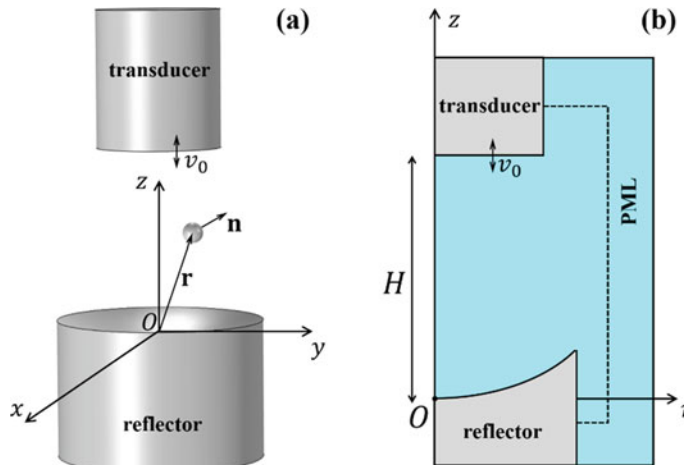


Fig. 3.4 Numerical model used to obtain the acoustic radiation force on a small rigid sphere. **a** Geometry of a typical single-axis acoustic levitator. **b** Axisymmetric acoustic model

The problem of determining the acoustic radiation force can be enormously simplified if we assume that the sphere is much smaller than the acoustic wavelength and that the levitator has a circular symmetry. If these two conditions are met, then the acoustic radiation force on a rigid sphere can be calculated by combining the axisymmetric acoustic model of Fig. 3.4b with the Gor'kov equation [28]:

$$U = 2\pi R^3 \left[\frac{1}{3\rho_0 c_0^2} \langle p_{in}^2 \rangle - \frac{\rho_0}{2} \langle \mathbf{v}_{in} \cdot \mathbf{v}_{in} \rangle \right]. \quad (3.33)$$

The Gor'kov equation says that the potential U of the acoustic radiation force \mathbf{F}_{rad} acting on a small sphere of radius R can be calculated by considering only the incident acoustic pressure p_{in} and the incident particle velocity \mathbf{v}_{in} on the sphere. The main advantage of using the Gor'kov equation is that it only requires the incident fields on the sphere and no scattering calculations are required. This means that numerical simulations can be carried out without the sphere.

After determining the potential U (also called Gor'kov potential), the acoustic radiation force \mathbf{F}_{rad} on a small sphere is calculated:

$$\mathbf{F}_{rad} = -\nabla U. \quad (3.34)$$

In order to find the Gor'kov potential, we first use the acoustic model of Fig. 3.4 to find the pressure and velocity fields in the air medium. In this model, the Helmholtz equation is solved numerically to find the acoustic pressure distribution in the air medium. In this model, the reflector is considered as a rigid wall and the following boundary condition is considered in the transducer radiating surface:

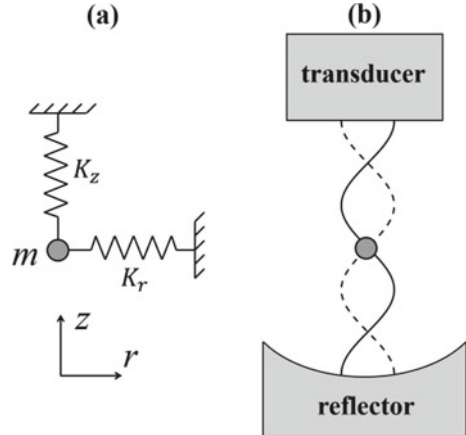
$$\frac{\mathbf{n}}{\rho_0} \cdot \nabla p = j\omega v_0, \quad (3.35)$$

where \mathbf{n} is the surface normal vector. In addition to the boundary condition given in Eq. (3.35), perfectly matched layers (PML) are also employed for absorbing the acoustic waves reaching the edges of the air domain. From the acoustic pressure field p_{in} calculated with the Helmholtz equation [Eq. (3.30)], the incident particle velocity \mathbf{v}_{in} can be found using the linear Euler's equation [Eq. (3.29)].

For a small displacement of the levitating object with respect to its equilibrium position, the levitation behavior can be analyzed by making an analogy with a two-dimensional spring-mass system [29], as illustrated in Fig. 3.5. If the sphere of mass m is displaced from its equilibrium position, the restoring forces push the particle back to the rest position. To simplify the levitator analysis, gravity forces are not considered, although the equations can be easily modified to include the effects of a gravitational force [30]. For the case of a spring-mass system, the restoring forces in the axial and radial directions can be described in terms of the energy potential:

$$U = \frac{1}{2} (K_z z^2 + K_r r^2). \quad (3.36)$$

Fig. 3.5 Analogy between the acoustic levitation of a small sphere and a two-dimensional spring-mass system:
a spring-mass system;
b single-axis acoustic levitator



where K_z and K_r are the elastic constants in the axial and radial directions, respectively. From the energy potential, the vertical and radial forces F_z and F_r on the object can be calculated:

$$F_z = -\frac{\partial U}{\partial z} = -K_z z, \quad (3.37)$$

$$F_r = -\frac{\partial U}{\partial r} = -K_r r, \quad (3.38)$$

with the elastic constants given by

$$K_z = \frac{\partial^2 U}{\partial z^2}, \quad (3.39)$$

$$K_r = \frac{\partial^2 U}{\partial r^2}. \quad (3.40)$$

3.5 Transducer Design

This section illustrates the design and fabrication of a 25-kHz Langevin-type transducer. The frequency of 25 kHz was chosen because it is higher than the frequency of the human hearing and the generated wavelength is large enough to allow the levitation of millimetric objects. The Langevin-type transducer will be formed by a sandwich structure containing two piezoelectric rings and a mechanical amplifier with a plane radiating surface of 20 mm diameter. Numerical simulations are carried out to analyze the dynamic behavior of the transducer and to obtain a geometry that

leads to a resonance frequency of 25 kHz. As we shall see in Sect. 3.6, the designed transducer will be used to build a resonant acoustic levitator consisting of a transducer and a concave reflector. In this section, the transducer design is illustrated using the FEM software COMSOL Multiphysics, but the simulations can also be carried out in other software, such as ANSYS or OnScale.

3.5.1 Sandwich Structure

Bolt-clamped Langevin-type transducers are normally built with low loss piezoelectric ceramics, such as lead zirconate titanate (PZT) of types 4 or 8. In general, the maximum diameter of the piezoelectric ceramics should be less than one-quarter of the wavelength in order to avoid mode coupling between radial and axial vibration modes [19]. In our design, the sandwich structure is formed by an aluminum front mass, an aluminum back mass and a stack of two PZT-4 piezoelectric ceramics with alternate polarization. The piezoelectric ceramics are a ring of 6.35 mm thickness, 12.7 mm internal diameter and 38.1 mm external diameter. The piezoceramics are compressed by a M10 Allen steel bolt of 60 mm length. A steel washer of 3 mm thickness, 23 mm external diameter and 10 mm diameter is placed between the bolt and the back mass. Although the washer is not strictly necessary, it is used for distributing the pressure of the bolt head on the upper surface of the back mass. The numerical model of the sandwich structure is shown in Fig. 3.6a.

In the numerical model, the piezoelectric ceramics have alternate polarization and the polarization of the upper piezoceramic ring is inverted by multiplying the matrix

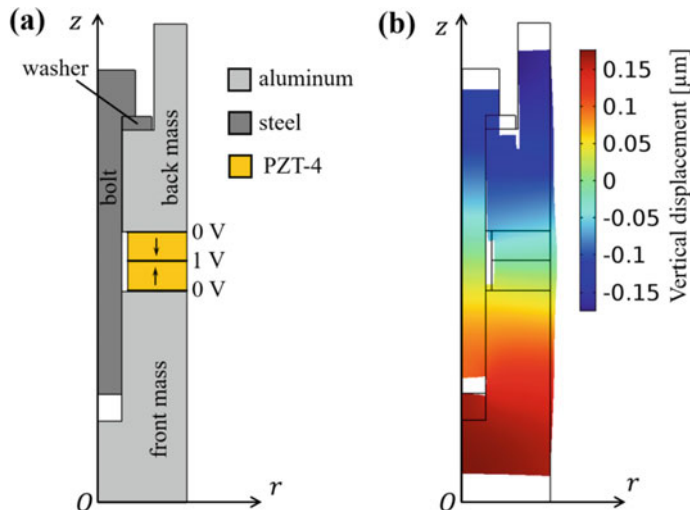


Fig. 3.6 Numerical model of the sandwich structure. **a** Axisymmetric model. **b** Simulated deformation of the structure at 25 kHz

of piezoelectric constants by minus one. The electrical excitation of the transducer is made by applying a voltage of 1 V on the surface between the top and bottom piezoelectric ceramics and 0 V on the other horizontal surfaces of the piezoelectric rings. Although a typical transducer operates with voltage amplitudes ranging from tens to hundreds of volts, our numerical model is linear, meaning that the transducer behavior at higher voltages can be determined by simply multiplying the result obtained with 1 V by a certain constant.

An initial guess for the total length L of the sandwich structure can be obtained by approximating it by a cylindrical bar of radius much smaller than the bar length. Assuming that the bar vibrates in the fundamental mode, the total length can be estimated by

$$L = \frac{1}{2f} \sqrt{\frac{E}{\rho}}, \quad (3.41)$$

where f is the desired resonance frequency, E is Young's modulus of the aluminum and ρ is the aluminum density. Using Eq. (3.41) with the material properties of Table 3.1, the estimated length for a resonance frequency of 25 kHz corresponds to $L = 102.25$ mm. With this estimated value, the lengths of the front and back masses

Table 3.1 Material properties

<i>PZT-4</i>	
C_{11}^E (10^{10} N/m 2)	13.90
C_{12}^E (10^{10} N/m 2)	7.78
C_{13}^E (10^{10} N/m 2)	7.43
C_{33}^E (10^{10} N/m 2)	11.54
C_{44}^E (10^{10} N/m 2)	2.56
e_{31} (C/m 2)	-5.20
e_{33} (C/m 2)	15.08
e_{15} (C/m 2)	12.72
$\varepsilon_{11}^S/\varepsilon_0$	762.5
$\varepsilon_{33}^S/\varepsilon_0$	663.2
ρ (kg/m 3)	7500
<i>Aluminum</i>	
E (10^{10} N/m 2)	7.11
ν	0.33
ρ (kg/m 3)	2720
<i>Steel</i>	
E (10^{10} N/m 2)	20.5
ν	0.28
ρ (kg/m 3)	7850

are adjusted such that the sandwich structure has a total length of 102.25 mm. Then, the numerical model of Fig. 3.6a is executed to find the resonance frequency of the structure. If the difference between simulated resonance frequency and the desired frequency is higher than a certain limit, then the lengths of the front mass and back mass are adjusted and the simulation is executed again. In our case, the total length of 102.25 mm results in a resonance frequency of 25.24 kHz, which is slightly higher than the desired frequency. We then adjust the transducer's total length until the sandwich structure vibrates at the desired resonance frequency. Figure 3.6b shows the simulated deformation of the structure at 25 kHz after this adjustment process.

3.5.2 Mechanical Amplifier

The axisymmetric model of the mechanical amplifier is shown in Fig. 3.7a. The mechanical amplifier geometry is slightly different than the mechanical amplifier of Fig. 3.3b. In its central region, the model of Fig. 3.7a includes a fixing point of 50 mm diameter and 3 mm thickness to attach the transducer to a supporting frame. When designing the mechanical amplifier, the fixing point should be located at a displacement node. This is necessary in order to avoid transmitting vibration to the structure where the transducer is attached.

Using a procedure similar to that used in the sandwich structure design, the initial guess for the mechanical amplifier length is also estimated using Eq. (3.41). Then, a modal analysis is carried out and the length of the top and bottom masses is adjusted

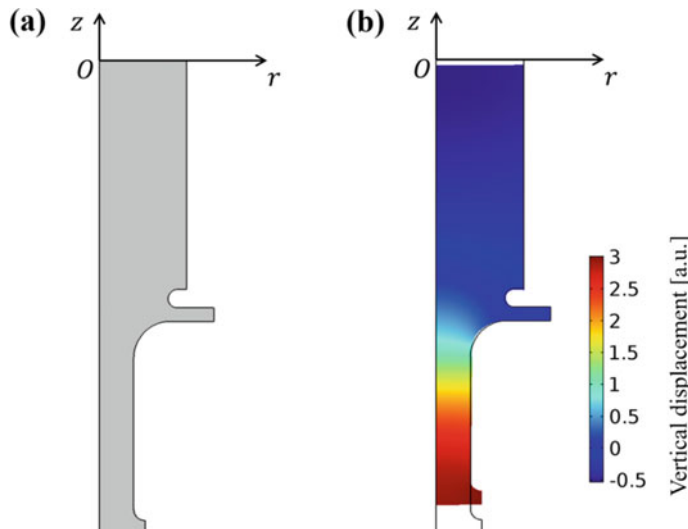


Fig. 3.7 Numerical model of the mechanical amplifier. **a** Axisymmetric model. **b** Simulated deformation at 25 kHz

until the mechanical amplifier resonates at the desired frequency. The simulated deformation of the mechanical amplifier at 25 kHz is shown in Fig. 3.7b. In this figure, the sandwich structure has a total length of 103.4 mm, which is slightly higher than the length estimated using Eq. (3.41).

3.5.3 Transducer

After simulating and determining the geometry of the sandwich structure and mechanical amplifier separately, the two parts are coupled and a new simulation is carried out to evaluate the dynamic behavior of the whole transducer. The dimensions of the transducer are presented in Fig. 3.8a and the simulated deformation at 25 kHz is shown in Fig. 3.8b. As shown in Fig. 3.8b, the maximum displacement occurs at the transducer radiating surface. We can also observe a small displacement amplitude at the transducer fixing point.

The simulated axial displacement along the z axis is shown in Fig. 3.9a. The region from $z = 0$ to $z = 93.4$ mm corresponds to the sandwich structure, whereas the region from $z = -103.5$ mm to $z = 0$ corresponds to the mechanical amplifier. We can clearly see in Fig. 3.9a that both parts vibrate as a half-wavelength resonator. We can also observe the increase in the displacement amplitude along the mechanical amplifier. The displacement amplitude changes from $0.084 \mu\text{m}$ at the junction between the sandwich structure and the mechanical amplifier to $0.466 \mu\text{m}$ at the

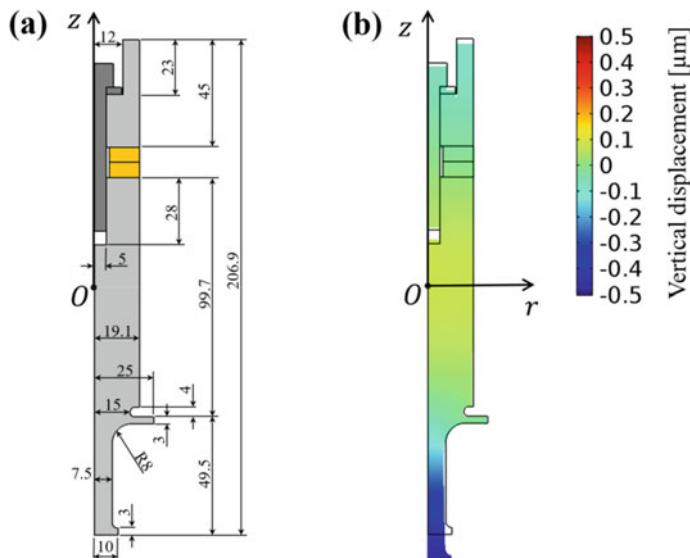


Fig. 3.8 Numerical model of the complete transducer (sandwich structure and mechanical amplifier). **a** Axisymmetric model. **b** Simulated deformation at 25 kHz

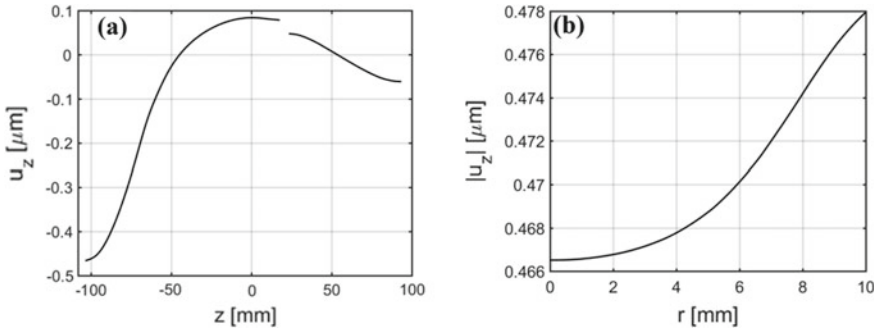


Fig. 3.9 Simulated displacement of the transducer at 25 kHz. **a** Vertical displacement along the z -axis. **b** Displacement amplitude along the transducer radiating surface

transducer radiating surface, which gives us an amplification of 5.48. The displacement amplitudes of Figs. 3.8b and 3.9 were simulated for the transducer voltage amplitude of 1 V. In practice, the transducer can be excited with an electrical signal of few hundred volts, generating displacement amplitudes as high as 100 μm .

The displacement amplitude distribution along the transducer radiating surface is almost constant (Fig. 3.9b). It changes from 0.466 μm at the center of the transducer to 0.478 μm at the edge of the radiating surface. The difference between the maximum and minimum displacement amplitude is less than 3%. It was also observed in the simulation that all the points of the radiating surface vibrate in phase, indicating that the designed transducer can be considered as a plane piston in which the radiating surface vibrates with constant displacement amplitude.

After simulating and determining the geometry of the transducer, the transducer parts were machined and a transducer prototype was assembled. The exploded view of the transducer assembly is shown in Fig. 3.10. The electrodes were made with

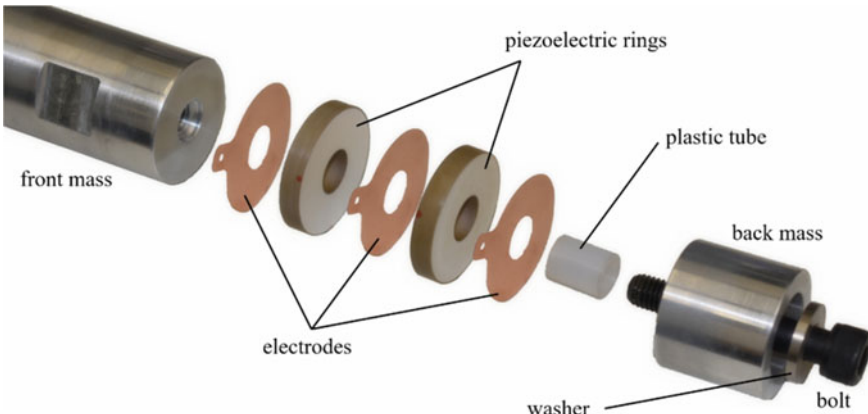


Fig. 3.10 Exploded view of the transducer assembly

a copper sheet of 0.15 mm thickness, which was fabricated using laser cutting. In the transducer assembly, we also used a plastic tube of 10 mm internal diameter, 12.7 mm external diameter and 16.5 mm length. The plastic tube has two purposes: It is used to align the aluminum parts with the piezoelectric rings, and it serves as an electrical insulator. Using a torque wrench, the transducer was assembled with a torque of 50 Nm.

A picture of the assembled transducer is shown in Fig. 3.11a and its simulated vibration behavior is shown in Fig. 3.11b. In Fig. 3.11a, the transducer is attached to the support by two aluminum flanges. Two plastic rings are also inserted between the transducer fixing point and each flange.

An important step when designing an ultrasonic transducer is to verify its dynamic behavior experimentally. One of the simplest approaches to evaluate the transducer behavior is to measure its electrical impedance curve. The modulus of the electrical impedance of the transducer is shown in Fig. 3.12. The experimental impedance curve was measured using an HP4194A impedance analyzer, and the simulated electrical impedance curve was obtained with the numerical model of Fig. 3.8. The frequency at which the electrical impedance is minimum is called resonance frequency, whereas the frequency of largest impedance is called anti-resonance frequency. As shown in

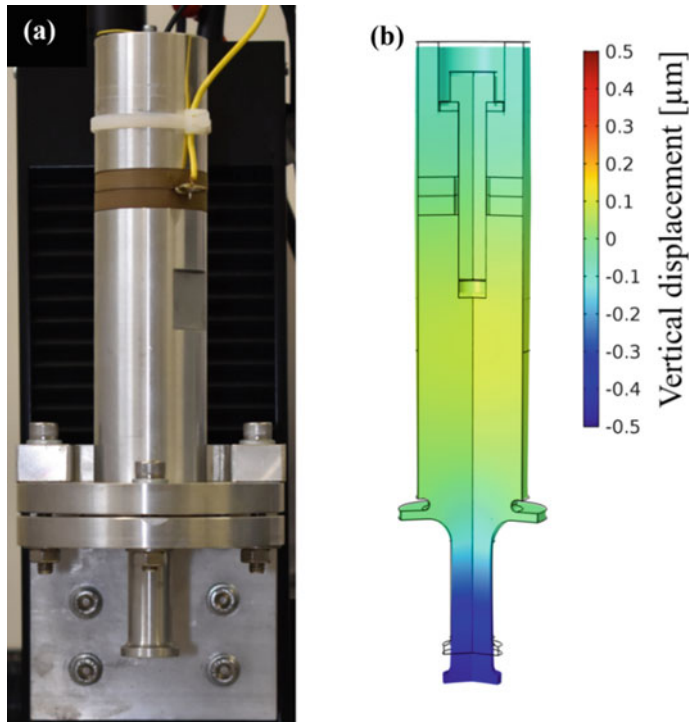


Fig. 3.11 **a** Picture of the assembled transducer. **b** Simulated displacement at 25 kHz for a voltage amplitude of 1 V

Fig. 3.12 Modulus of the electrical impedance of the transducer

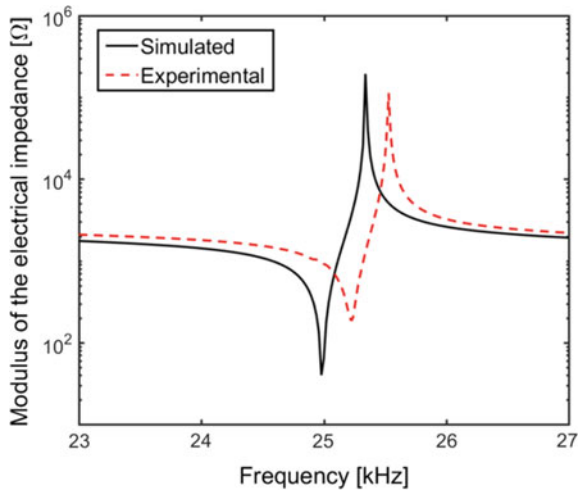


Fig. 3.12, the experimental resonance frequency is 25.25 kHz, whereas the simulated resonance frequency is 25 kHz. The difference between simulated and experimental resonance frequency is 1%, suggesting that the transducer works as expected.

3.6 Resonant Acoustic Levitator

This section describes the design of a resonant single-axis acoustic levitator, which will be formed by the Langevin-type transducer described in Sect. 3.5 and a concave reflector of 40 mm diameter. We are interested in designing a levitator to operate with four pressure nodes between the transducer and the reflector and we want to maximize the acoustic radiation force on the object located at the third pressure node (from bottom to top). Assuming a plane wave, the resonances occur when H is set to a distance corresponding to an integer multiple of half the wavelength. Consequently, the resonance for the fourth mode would occur when the transducer–reflector distance is $H = 2\lambda$. However, as pointed out by Xie and Wei [21], the resonance of a real levitator occurs when the transducer–reflector distance is slightly larger than the distances assumed by the plane wave hypothesis.

To simulate the acoustic levitator, the acoustic model of Fig. 3.4b is used to calculate the acoustic pressure and velocity fields in the air gap between the transducer and the reflector. These fields are then replaced in the Gor’kov expression [Eq. (3.33)] to find the potential of the acoustic radiation in a small rigid sphere. Simulations were carried out with $c_0 = 343$ m/s and air density of $\rho_0 = 1.2$ kg/m³. To simplify the analysis, it was assumed that the transducer surface vibrates with uniform velocity distribution of $v_0 = 1$ m/s. In the calculation of the Gor’kov potential, it was assumed a rigid sphere of 1 mm radius.

The model of Fig. 3.4 can also be used to find the optimal curvature radius R_c of the reflector and the optimal separation distance H between the transducer and the reflector. In this analysis, the elastic constant K_z of the third pressure node (from bottom to top) was determined for different values of H and R_c . As shown in Fig. 3.13, the maximum value for K_z is obtained when $H = 29.78 = 2.19\lambda$ mm and $R_c = 33$ mm = 2.43λ . In agreement with the results of Xie and Wei [21], the resonance occurs when the transducer–reflector distance is slightly higher than that predicted by the plane wave hypothesis.

Although the levitator is optimized to operate over the fourth mode of the acoustic cavity, the levitator has many other resonance states that can also be used for levitation. A useful approach for finding the resonance states of the acoustic cavity consists in determining the acoustic radiation force on the reflector as a function of the transducer–reflector distance H [27, 31]. To obtain this curve, the numerical model of Fig. 3.4b is used for calculating the acoustic pressure p and particle velocity \mathbf{v} distributions over the reflector surface. Then, these distributions are replaced in Eq. (3.31) to find the radiation pressure over the reflector, and finally, the radiation pressure is integrated over the reflector surface [Eq. (3.32)] to find the total force on the reflector as a function of H . The simulated radiation force on the reflector versus H is shown in Fig. 3.14. As we can see in Fig. 3.14, there are numerous resonance peaks that can be used for levitation. It is also interesting to note that although the levitator was optimized to operate under the fourth mode (third peak of Fig. 3.14), the force on the reflector produced by the second peak is higher than that provided in the third peak.

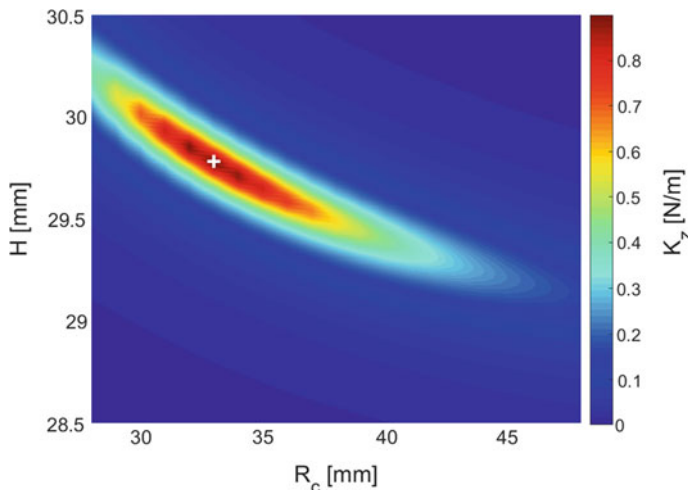
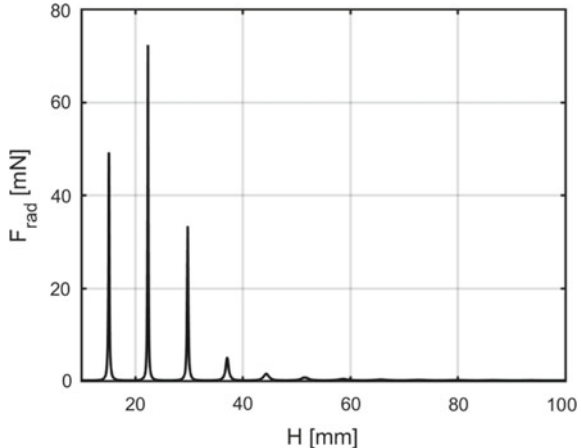


Fig. 3.13 Simulated elastic constant K_z as a function of the transducer–reflector distance H and the radius of curvature of the reflector R_c for the levitator operating at 25.25 kHz. The maximum elastic constant (cross mark) is obtained for $H = 29.78$ mm and $R_c = 33$ mm

Fig. 3.14 Acoustic radiation force on the reflector as a function of the transducer–reflector distance H . The resonant levitator consists of a 25.25 kHz transducer with a plane radiating surface of 20 mm diameter and a concave reflector of 40 mm diameter and curvature radius of 33 mm



From the optimized values of Fig. 3.13, an aluminum reflector of 40 mm diameter and curvature radius of 33 mm was machined. The reflector was then positioned at a distance of approximately 29.78 mm from the transducer, and a polypropylene sphere was positioned at the third pressure node of the standing wave field established between the transducer and the reflector. The comparison between simulated and experimental results is shown in Fig. 3.15. As we can see, there is a good agreement between the levitating position of the sphere and the position of minimum Gor'kov potential (cross mark in Fig. 3.15). The designed levitator can also be used for levitating liquid drops in mid-air, which has a wide range of applications in the areas of analytical chemistry [32, 33], biology [34, 35] and drop dynamics [36, 37].

The Gor'kov potential of Fig. 3.15c can also be used for calculating trapping stiffness in the axial and radial directions. This is done by fitting a parabola in the neighborhood of a given trapping point. As an example, Fig. 3.16a, b shows the Gor'kov potential along the axial and radial directions, respectively. By fitting a parabola and then using Eqs. (3.39) and (3.40), we obtain $K_z = 0.88 \text{ N/m}$ and $K_r = 0.065 \text{ N/m}$. It is worth mentioning that these elastic constants were determined for the transducer radiating surface vibrating with velocity amplitude of 1 m/s at 25.25 kHz. As the acoustic pressure amplitude is proportional to the transducer velocity amplitude and the Gor'kov potential U scales with the acoustic pressure squared, the elastic constant is proportional to the square of the transducer velocity amplitude. This means that the elastic constant in the axial and radial directions can be altered by varying the voltage amplitude applied to the transducer.

The elastic constants K_z and K_r can also be used for calculating the frequency on which the levitated object oscillates when it is displaced from its equilibrium position. By making a simple analogy a spring-mass system, the frequency of the vertical and horizontal oscillations of an object of mass m can be calculated:

$$\omega_z = \sqrt{\frac{K_z}{m}}, \quad (3.42)$$

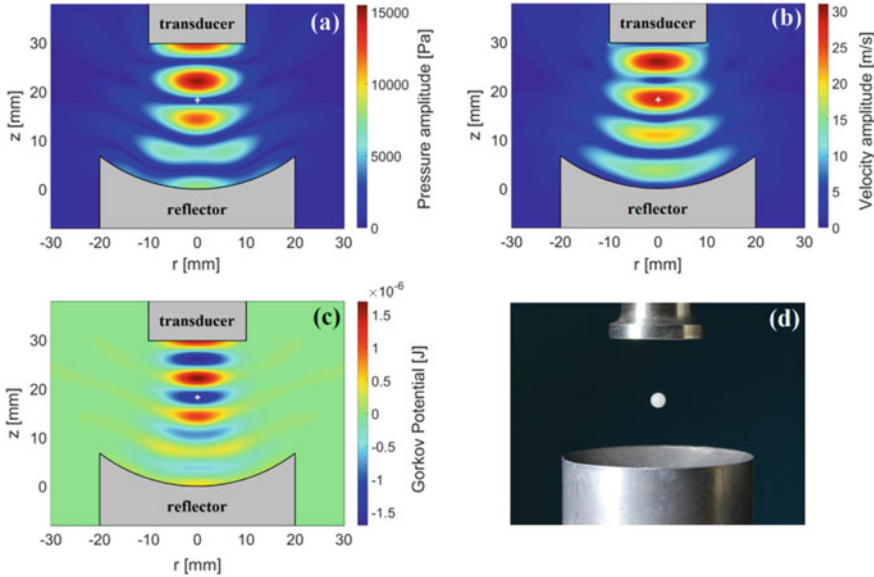


Fig. 3.15 Single-axis acoustic levitator operating at 25.25 kHz with a transducer–reflector distance of 29.78 mm. **a** Acoustic pressure amplitude. **b** Velocity amplitude. **c** Potential of the acoustic radiation force. **d** Acoustic levitation of a sphere at the third pressure node

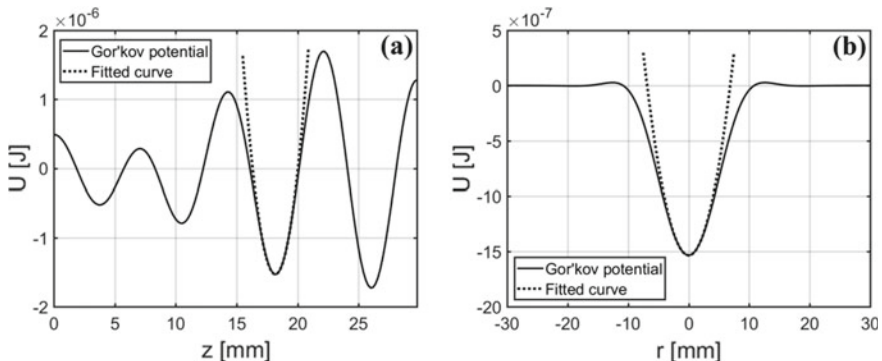


Fig. 3.16 Potential of the acoustic radiation force for the levitator operating with a velocity amplitude of 1 m/s. **a** Potential along the z -axis. **b** Potential along the radial direction for $z = 18.19$ mm

$$\omega_r = \sqrt{\frac{K_r}{m}}. \quad (3.43)$$

For small displacements with respect to the equilibrium position, Eqs. (3.42) and (3.43) provide a good estimate for the oscillation angular frequencies of the levitated

object [38, 39]. However, for larger displacements, the oscillation behavior becomes nonlinear [40], requiring a nonlinear stiffness model for the acoustic restoring force.

3.7 Non-resonant Acoustic Levitator

In a resonant acoustic levitator, such as that exemplified in Sect. 3.6, the ultrasonic wave emitted by the transducer is reflected multiple times between the transducer and the reflector. When the transducer–reflector distance is set to one of the resonant states of the acoustic cavity, the multiple reflected waves interfere in such a way that the amplitude of the resulting wave is much larger than the amplitude of the wave emitted by the transducer. In contrast, when the levitator operates outside the resonance, the multiple reflected waves are summed incoherently, resulting in a standing wave of very low amplitude. In general, the acoustic radiation force on the object is weak when the levitator operates outside the resonance and levitation is only possible when the emitter–reflector distance is carefully adjusted to one of the resonant states of the acoustic cavity.

Acoustic levitators based on standing waves can also be non-resonant. In contrast to a resonant device, non-resonant levitators do not require the emitter–reflector distance to be set to a resonant state. The general idea for designing a non-resonant acoustic levitator is to minimize high-order reflections such that the standing wave is essentially formed by the superposition of two counter-propagating waves. This can be done through the superposition of the waves emitted by two opposing emitters [13] or two opposing arrays of transducers [14]. Another possibility is to reduce high-order reflections by reducing the transducer [17] or reflector [16] size.

In the non-resonant acoustic levitator presented in this section, the levitator consists of a 23.7 kHz transducer with a circular radiating surface of 10 mm diameter and a concave reflector of 40 mm diameter and curvature radius of 33 mm, as illustrated in Fig. 3.17. As described previously [17], the transducer emits a nearly spherical wave that travels in the air medium until it reaches the concave surface of the reflector. Then, the wave is reflected and the superposition between the incident and reflected waves generates a standing wave in the neighborhood of the reflector, as shown in Fig. 3.17. Because of the small transducer diameter, only a small fraction of the wave is reflected by the transducer surface and thus we can neglect high-order reflections when analyzing this levitator. In the non-resonant levitator of Fig. 3.17, small light objects can be levitated at the pressure nodes of the standing wave and the objects can be manipulated by moving the reflector with respect to the transducer. The reflector can also be tilted and moved horizontally without significantly affecting the levitation performance.

The non-resonant behavior of the levitator can be analyzed by simulating the acoustic radiation force on the reflector as a function of the separation distance between the transducer and the reflector. Using the same procedure adopted in Sect. 3.6, the acoustic radiation force on the reflector versus H is simulated with the numerical model of Fig. 3.4b. The simulated curve is shown in Fig. 3.18. Although

Fig. 3.17 A non-resonant acoustic levitator consisting of a 23.7 kHz ultrasonic transducer with a radiating surface of 10 mm diameter and a concave reflector of 40 mm diameter and curvature radius of 33 mm

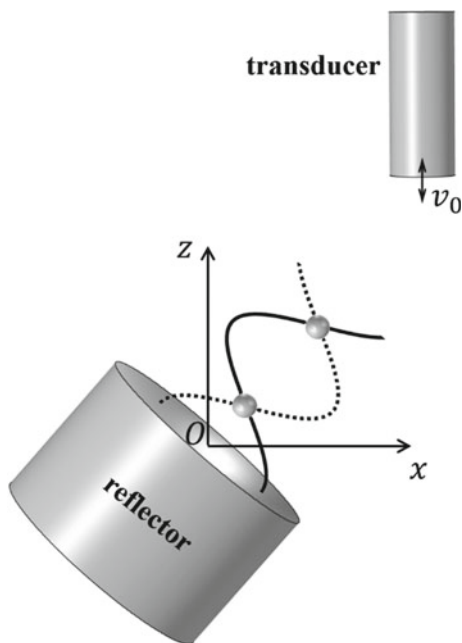
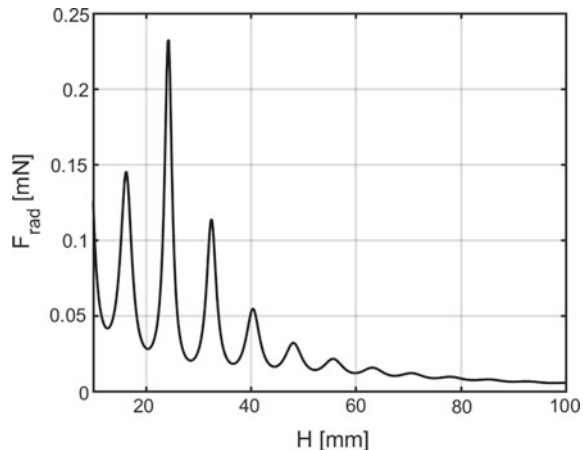


Fig. 3.18 Acoustic radiation force on the reflector as a function of the transducer–reflector distance H . The non-resonant levitator consists of a 23.7 kHz transducer with a plane radiating surface of 10 mm diameter and a concave reflector of 40 mm diameter and curvature radius of 33 mm



the levitator is considered non-resonant, we can observe resonance peaks for transducer–reflector distances less than 50 mm. The heights of the peaks decrease with H and a non-resonant behavior can be obtained for H varying between 50 and 100 mm.

Although the radiation force generated by a non-resonant levitator is much weaker than that of a resonant levitator, it is strong enough to levitate and manipulate expanded polystyrene particles, as shown in Fig. 3.19. This figure also shows that

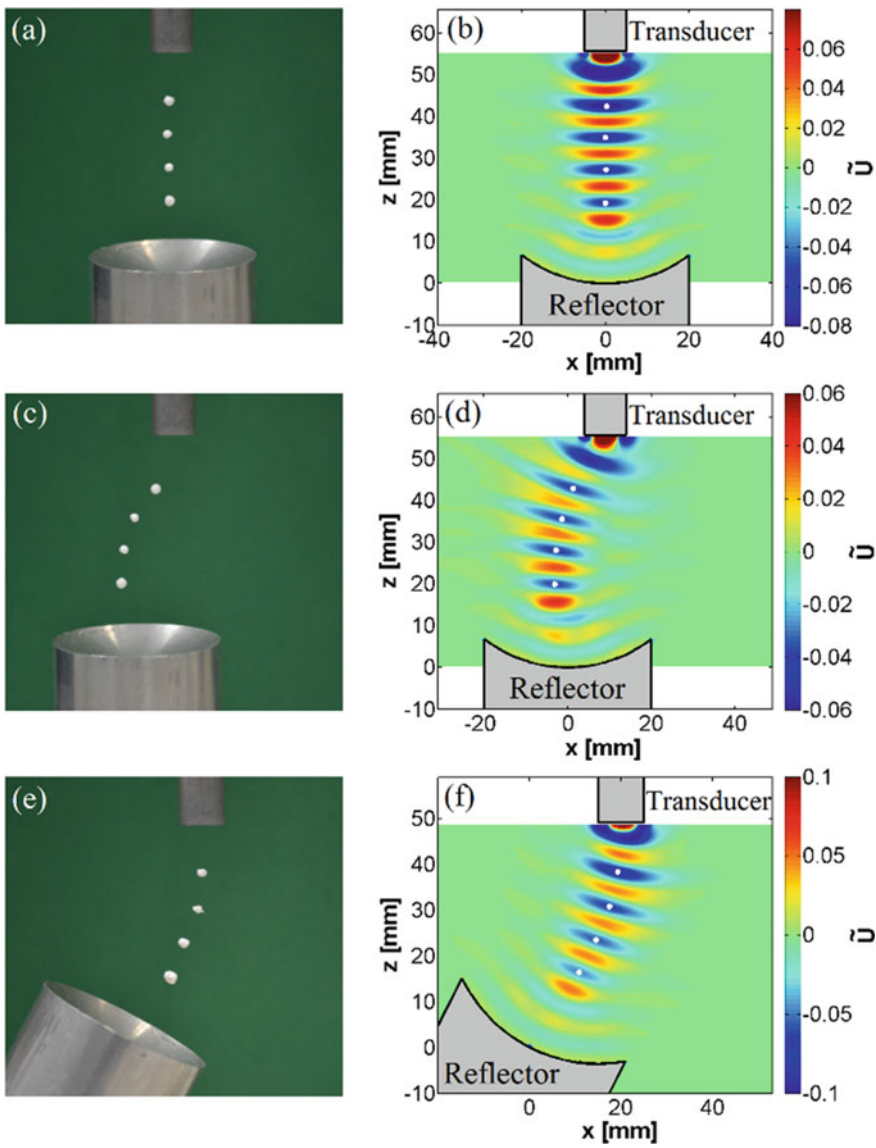


Fig. 3.19 Acoustic levitation (**a**, **c** and **e**) of small particles and the simulated dimensionless Gor'kov potential (**b**, **d** and **f**) in a 23.7-kHz non-resonant acoustic levitator. Reprinted from [17], with the permission of AIP Publishing

the levitating particles can be manipulated by tilting and translating the transducer vertically or horizontally.

The non-resonant levitator presented here can only be used for suspending light particles, but there are also non-resonant levitators that can be used for levitating liquid drops such as the TinyLev [14] or the single-axis levitator developed by Weber et al. [13].

In summary, this chapter presented a numerical approach for designing single-axis acoustic levitators. This procedure was exemplified by designing a simple levitator consisting of a piezoelectric transducer and a reflector. For further information and other types of single-axis levitators, the reader is strongly encouraged to read additional material [4, 11, 13–15, 21, 41, 42].

The procedure adopted in the design of a single-axis acoustic levitator can also be extended to simulate and design piezoelectric devices for manipulating and separating small particles and cells in a fluid medium [43–45]. In addition, although the levitator was used for levitating small particles much smaller than the acoustic wavelength, the designed transducer can also be combined with other transducers in order to levitate objects larger than the wavelength [46].

References

1. M.A.B. Andrade, N. Pérez, J.C. Adamowski, Review of progress in acoustic levitation. *Braz. J. Phys.* **48**(2), 190–213 (2018)
2. L. Meng, F. Cai, F. Li, W. Zhou, L. Niu, H. Zheng, Acoustic tweezers. *J. Phys. D Appl. Phys.* **52**(27), 273001 (2019)
3. E.H. Brandt, Acoustic physics. Suspended by sound. *Nature* **413**(6855), 474–475 (2001)
4. W.J. Xie, B. Wei, Parametric study of single-axis acoustic levitation. *Appl. Phys. Lett.* **79**(6), 881–883 (2001)
5. R.R. Whymark, Acoustic field positioning for containerless processing. *Ultrasonics* **13**(6), 251–261 (1975)
6. Y. Hashimoto, Y. Koike, S. Ueha, Acoustic levitation of planar objects using a longitudinal vibration mode. *J. Acoust. Soc. Japan* **16**(3), 189–192 (1995)
7. Y. Hashimoto, Y. Koike, S. Ueha, Near-field acoustic levitation of planar specimens using flexural vibration. *J. Acoust. Soc. Am.* **100**(4), 2057–2061 (1996)
8. S. Ueha, Y. Hashimoto, Y. Koike, Non-contact transportation using near-field acoustic levitation. *Ultrasonics* **38**(1), 26–32 (2000)
9. A. Marzo, B.W. Drinkwater, Holographic acoustic tweezers. *Proc. Natl. Acad. Sci.* **116**(1), 84–89 (2019)
10. A. Marzo, A. Ghobrial, L. Cox, M. Caleap, A. Croxford, B.W. Drinkwater, Realization of compact tractor beams using acoustic delay-lines. *Appl. Phys. Lett.* **110**(1), 014102 (2017)
11. E.H. Trinh, Compact acoustic levitation device for studies in fluid dynamics and material science in the laboratory and microgravity. *Rev. Sci. Instrum.* **56**(11), 2059–2065 (1985)
12. M.A.B. Andrade, F.C. Buiochi, J. Adamowski, Finite element analysis and optimization of a single-axis acoustic levitator. *IEEE Trans. Ultrason. Ferroelectr. Freq. Control* **57**(2), 469–479 (2010)
13. J.K.R. Weber, C.A. Rey, J. Neufeind, C.J. Benmore, Acoustic levitator for structure measurements on low temperature liquid droplets. *Rev. Sci. Instrum.* **80**(8), 083904 (2009)
14. A. Marzo, A. Barnes, B.W. Drinkwater, TinyLev: a multi-emitter single-axis acoustic levitator. *Rev. Sci. Instrum.* **88**(8), 085105 (2017)

15. A. Marzo, T. Corkett, B.W. Drinkwater, Ultraino: an open phased-array system for narrowband airborne ultrasound transmission. *IEEE Trans. Ultrason. Ferroelectr. Freq. Control* **65**(1), 102–111 (2018)
16. C.A. Rey, D.R. Merkley, G.R. Hammarlund, T.J. Danley, Acoustic levitation technique for containerless processing at high temperatures in space. *Metall. Trans. A* **19**(11), 2619–2623 (1988)
17. M.A.B. Andrade, N. Pérez, J.C. Adamowski, Particle manipulation by a non-resonant acoustic levitator. *Appl. Phys. Lett.* **106**(1), 014101 (2015)
18. W.J. Xie, C.D. Cao, Y.J. Lü, B. Wei, Levitation of iridium and liquid mercury by ultrasound. *Phys. Rev. Lett.* **89**(10), 104304 (2002)
19. J.A. Gallego-Juarez, Piezoelectric ceramics and ultrasonic transducers. *J. Phys. E: Sci. Instrum.* **22**(10), 804–816 (1989)
20. A. Abdulla, M. Shahini, A. Pak, An approach to design a high power piezoelectric ultrasonic transducer. *J. Electroceramics* **22**(4), 369–382 (2009)
21. W.J. Xie, B. Wei, Dependence of acoustic levitation capabilities on geometric parameters. *Phys. Rev. E—Stat. Nonlinear, Soft Matter Phys.* **66**(2), 026605 (2002)
22. T.J. Chung, *Applied Continuum Mechanics* (Cambridge University Press, New York, 1996)
23. A.B. Auld, *Acoustics Fields and Waves in Solids*, vol. 1 (Wiley, New York, 1973)
24. D. Royer, E. Dieulesaint, *Elastic Waves in Solids I: Free and Guided Propagation* (Springer, Berlin, 2000)
25. L.E. Kinsler, A.R. Frey, A.B. Coppens, J.V. Sanders, *Fundamentals of Acoustics* (Wiley, New York, 1999)
26. IEEE Standard on piezoelectricity, ANSI/IEEE Std. 176-1987 (The Institute of Electrical and Electronics Engineers, New York, 1987)
27. Z.Y. Hong, W. Zhai, N. Yan, B. Wei, Measurement and simulation of acoustic radiation force on a planar reflector. *J. Acoust. Soc. Am.* **135**(5), 2553–2558 (2014)
28. L.P. Gor'kov, On the forces acting on a small particle in an acoustical field in an ideal fluid. *Sov. Phys. Dokl.* **6**, 773–775 (1962)
29. M. Barmatz, P. Collas, Acoustic radiation potential on a sphere in plane, cylindrical, and spherical standing wave fields. *Acoust. Soc. Am.* **77**(March), 928–945 (1985)
30. P. Collas, M. Barmatz, C. Shipley, Acoustic levitation in the presence of gravity. *J. Acoust. Soc. Am.* **86**(2), 777–787 (1989)
31. M.A.B. Andrade, T.S. Ramos, F.T.A. Okina, J.C. Adamowski, Nonlinear characterization of a single-axis acoustic levitator. *Rev. Sci. Instrum.* **85**(4), 045125 (2014)
32. R. Tuckermann, L. Puskar, M. Zavabeti, R. Sekine, D. McNaughton, Chemical analysis of acoustically levitated drops by Raman spectroscopy. *Anal. Bioanal. Chem.* **394**(5), 1433–1441 (2009)
33. S. Santesson, S. Nilsson, Airborne chemistry: acoustic levitation in chemical analysis. *Anal. Bioanal. Chem.* **378**(7), 1704–1709 (2004)
34. T. Vasileiou, D. Foresti, A. Bayram, D. Poulikakos, A. Ferrari, Toward contactless biology: acoustophoretic DNA transfection. *Sci. Rep.* **6**, 20023 (2016)
35. A. Scheeline, R.L. Behrens, Potential of levitated drops to serve as microreactors for biophysical measurements. *Biophys. Chem.* **165–166**, 1–12 (2012)
36. D. Zang, Y. Yu, Z. Chen, X. Li, H. Wu, X. Geng, Acoustic levitation of liquid drops: dynamics, manipulation and phase transitions. *Adv. Colloid Interface Sci.* **243**, 77–85 (2017)
37. W. Di et al., Shape evolution and bubble formation of acoustically levitated drops. *Phys. Rev. Fluids* **3**(10), 103606 (2018)
38. M.A.B. Andrade, N. Pérez, J.C. Adamowski, Experimental study of the oscillation of spheres in an acoustic levitator. *J. Acoust. Soc. Am.* **136**(4), 1518–1529 (2014)
39. K. Hasegawa, K. Kono, Oscillation characteristics of levitated sample in resonant acoustic field. *AIP Adv.* **9**(3), 035313 (2019)
40. T. Fushimi, T.L. Hill, A. Marzo, B.W. Drinkwater, Nonlinear trapping stiffness of mid-air single-axis acoustic levitators. *Appl. Phys. Lett.* **113**(3), 034102 (2018)

41. C.R. Field, A. Scheeline, Design and implementation of an efficient acoustically levitated drop reactor for in situ measurements. *Rev. Sci. Instrum.* **78**(12), 125102 (2007)
42. E.G. Lierke, Deformation and displacement of liquid drops in an optimized acoustic standing wave levitator. *Acta Acust. United Acust.* **88**, 206–217 (2002)
43. A. Lenshof, M. Evander, T. Laurell, J. Nilsson, Acoustofluidics 5: building microfluidic acoustic resonators. *Lab Chip* **12**(4), 684–695 (2012)
44. B.W. Drinkwater, Dynamic-field devices for the ultrasonic manipulation of microparticles. *Lab Chip* **16**(13), 2360–2375 (2016)
45. X. Ding et al., Surface acoustic wave microfluidics. *Lab Chip* **13**(18), 3626 (2013)
46. M.A.B. Andrade, A.L. Bernassau, J.C. Adamowski, Acoustic levitation of a large solid sphere. *Appl. Phys. Lett.* **109**(4), 044101 (2016)

Chapter 4

Lattice Boltzmann Method for Acoustics Levitation



Xiao-Peng Chen

Abstract In this chapter, a novel computational method for flow, lattice Boltzmann method, is introduced. We first present the fundamentals and general implements of the method, followed by non-reflective boundary condition techniques, which is important for acoustic simulations. The von Neumann analysis shows lattice Boltzmann method is promising for acoustic simulations. In the latter part of this chapter, we present the applications of lattice Boltzmann method on sound phenomena, such as aeroacoustics, non-linear sound effect and acoustic levitation.

4.1 Introduction

Sound generation and propagation have inherent fundamentals of fluid dynamics, where the media carrying sound waves is considered as a compressible fluid. It is shown that the simplest wave equation can be derived from the governing equations of fluid dynamics (Navier–Stokes/N–S equations) with the assumption of extremely small density and velocity fluctuation [1]:

$$\frac{\partial^2 \phi}{\partial t^2} - c^2 \nabla \phi = 0. \quad (4.1)$$

In the equation, ϕ denotes velocity potential: $\mathbf{u}' = -\nabla \phi$, and $c = \sqrt{(\partial p / \partial \rho)_s}$ is speed of sound. The disturbed pressure is $p' = -\rho_0 \partial \phi / \partial t$. It is also revealed that acoustic energy is propagated with sound wave: $E = \frac{1}{2} \rho_0 u'^2 + \frac{1}{2} \frac{c^2 \rho'^2}{\rho_0}$. In this chapter, we denote the deviations of the respective quantities from their equilibrium values, which are denoted with the subscript “0”, by using primed letters. Non-linear effects can be further explored by taking account of the second-order terms ($O(M^2)$, $M = |\mathbf{u}'|/c$) in the N–S equations [2]. Burger’s equation is applicable (in one-dimensional space):

X.-P. Chen (✉)

School of Marine Science and Technology, Northwestern Polytechnical University, 710072 Xi'an, Shaanxi, China

e-mail: xchen76@nwpu.edu.cn

$$\frac{\partial u'}{\partial t} + u' \frac{\partial u'}{\partial x} = \nu \frac{\partial^2 u'}{\partial x^2}, \quad (4.2a)$$

which successfully predicts the occurrence of shockwave from a sinusoidal wave, and ν is viscosity. The last term on the right-hand side represents a dissipation effect. Combined with mass conservation equation, it can be recast as

$$\frac{\partial^2 u'}{\partial t^2} - \left(c^2 + \nu \frac{\partial}{\partial t} \right) \frac{\partial^2 u'}{\partial x^2} = 0. \quad (4.2b)$$

Although the linear sound theory achieves great successes in sound prediction, the mechanical fundamentals of sound are still worthy of studying in many complicated situations. One of the notable subjects is aeroacoustics, which normally refers to the study on noise generation via either turbulent flow or aerodynamic forces interacting with surfaces. The topics include the aeolian tones produced by wind blowing over fixed objects. Starting from N-S equations, the celebrated Lighthill equation of aeroacoustics is derived without any additional assumptions:

$$\frac{\partial^2 \rho}{\partial t^2} - c_0^2 \nabla^2 \rho = \nabla \nabla : \mathbf{T}, \quad (4.3)$$

where \mathbf{T} is the Lighthill stress tensor (second-order tensor). The last term in the equation is the source term, which can also include monopole, dipole and quadrupole motions of the fluid depending on flow conditions [3–5]. On the other hand, almost all the studies on non-linearity of sound phenomena root in N-S equations, while different mathematical approaches are applied [6, 7].

Therefore, well-developed numerical methods on fluid dynamics, known as Computational Fluid Mechanics (CFD), are supposed to be valuable in acoustic studies. In this chapter, lattice Boltzmann method, a promising numerical method, is to be introduced, and its applications on acoustics and acoustic levitations will be included as well.

4.2 Fundamentals on Lattice Boltzmann Method (LBM)

4.2.1 Governing Equations and Mathematics

It has been realized that the particle dynamics in a massive system can be applied to recover fluid flow. For these particle systems, various numerical approaches are developed, such as smooth particle hydrodynamics (SPH), molecular dynamics (MD) and moving particle semi-implicit method (MPS). A slightly different method is lattice Boltzmann method (LBM), which could be obtained from the classical Boltzmann equation (Fig. 4.1):

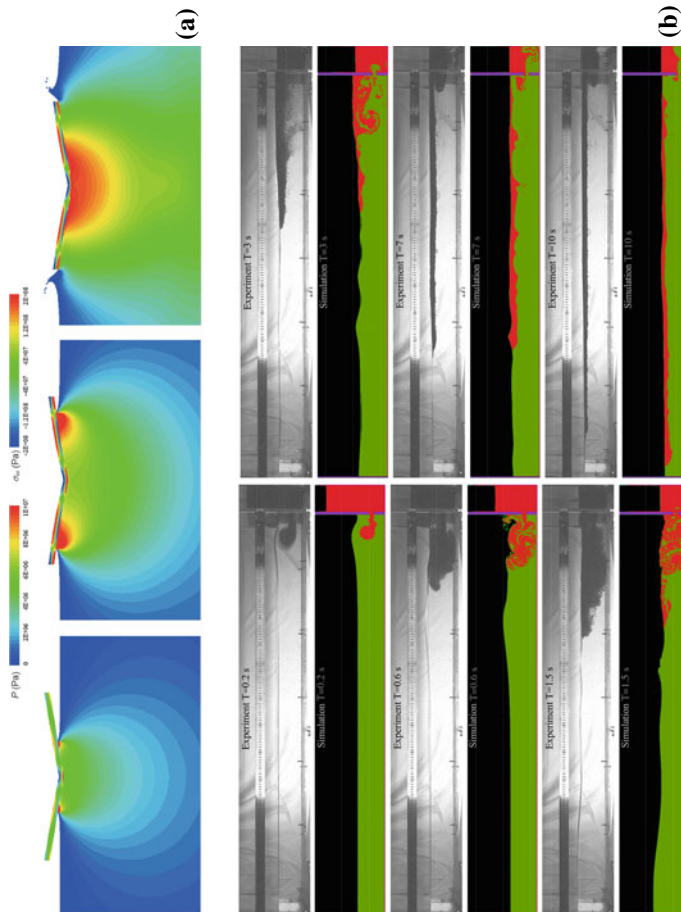


Fig. 4.1 Computational results from particle-based methods. **a** SPH modelling of water entry of an elastic wedge while the inherent features of free surface evolution, fluid-structure interaction, wave propagation and water jet are well captured (see: Liu and Zhang, Sci. China-Phys., Mech. Astron. 2019, 62:984701). **b** Simulated oil spill in water by using MPS method. Experimental results are compared. (see: Duan, Chen, Zhang and Wang, Comput. Meth. Appl. Mech. Engg., 2017, 320:133–161)

$$\frac{\partial f}{\partial t} + \mathbf{e} \cdot \frac{\partial f}{\partial \mathbf{x}} + \mathbf{a} \cdot \frac{\partial f}{\partial \mathbf{e}} = -\frac{1}{\tau}(f - f^{\text{eq}}), \quad (4.4)$$

where $f(\mathbf{x}, \mathbf{e}, t)$ denotes the particle population (or velocity distribution function) with microscopic velocity \mathbf{e} at position \mathbf{x} and time t (see Fig. 4.2a, b), and \mathbf{a} is the acceleration due to forces exerted on the particles. The first two terms on the left-hand side show a propagation process. On the right-hand side, we use BGK assumption, named after Bhatnagar, Gross and Krook. The BGK assumption implies f approaches the Maxwell-Boltzmann distribution, f^{eq} , after a large number of collisions preserving mass, momentum and kinetic energy conservation [8, 9]. τ is a relaxation time, which reflects the strength and frequency of the collisions and determines the viscosity of the fluid (to be shown in the rear part of this subsection). Therefore, this method is essentially a partial differential equation-based method, although it has strong particle kinetics background.

For computer-aided calculations, a discretization process is implemented as in Fig. 4.2c. The lattice shown has three major contents: the geometry of the control volume, the discrete microscopic velocity set (see \mathbf{e}_i in the panel) and time step (δt). In standard LBM, it is supposed that the particle will jump to the neighbouring point at $\mathbf{x} + \mathbf{e}_i \delta t$ in each time step. For convenience, $\delta t = 1$ and the size of the lattice are chosen as the units of time and length, respectively. Equation (4.4) is then discretized (ignoring the volumetric force term) as

$$f_i(\mathbf{x} + \mathbf{e}_i \delta t, t + \delta t) - f_i(\mathbf{x}, t) = -\frac{1}{\tau}(f_i(\mathbf{x}, t) - f_i^{\text{eq}}), \quad (4.5)$$

and the corresponding Maxwell distribution is

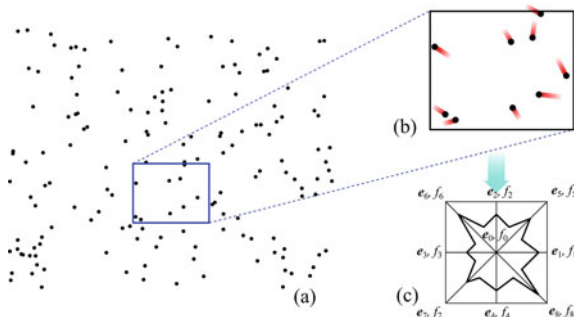


Fig. 4.2 Discretization of a particle system. **a** A particle system. The particles walk randomly, freely without interactions except when they collide with each other. **b** A volume element in the particle system. The space is discretized accordingly. **c** The microscopic velocity in panel (b) is discretized into nine velocities (\mathbf{e}_i , $i = 0, 1, 2 \dots 8$) according to the lattice model chosen. Since two-dimensional space and nine discretized microscopic velocities are chosen, it is named as D2Q9 lattice. f_i denotes the particle population with microscopic velocity \mathbf{e}_i

$$f_i^{\text{eq}}(\rho, \mathbf{u}) = \omega_i \rho(\mathbf{x}) \left[1 + 3 \frac{\mathbf{e}_i \cdot \mathbf{u}}{c^2} + \frac{9(\mathbf{e}_i \cdot \mathbf{u})^2}{c^4} - \frac{3\mathbf{u}^2}{2c^2} \right]. \quad (4.6a)$$

The local macroscopic quantities can be easily assembled from the moments of f_i : density $\rho = \sum_i f_i$ and momentum $\rho\mathbf{u} = \sum_i f_i \mathbf{e}_i$. $c = 1/\sqrt{3}$ is the speed of sound on D2Q9 lattice, and

$$\omega_i = \begin{cases} 4/9, & i = 0 \\ 1/9, & i = 1, 2, 3, 4 \\ 1/36, & i = 5, 6, 7, 8. \end{cases} \quad (4.6b)$$

Equation (4.5) is a typical LB equation. On numerical side, the calculations can be implemented quite easily, and that is one of the important reasons that LBM is applied in many fields explosively [10, 11].

The Chapman-Enskog expansion can be applied to recover N-S equations from Eqs. (4.5) and (4.6). To do so, we first introduce a multi-scale expansion:

$$f_i = f_i^{(0)} + \epsilon f_i^{(1)} + \epsilon^2 f_i^{(2)} + \dots, \quad (4.7)$$

$$\partial_t = \partial_{t0} + \epsilon^2 \partial_{t1}, \quad \partial_\alpha = \epsilon \partial_{\alpha 0}. \quad (4.8)$$

The subscripts t and α denote the derivatives with respect to time and position, respectively, and ϵ is a small number proportional to Knudsen number (the ratio between the mean free path of the particles and the characteristic length of the problem). Conduct Taylor expansion on Eq. (4.5) and use (4.8).

$$\begin{aligned} & f_i(x + e_i \delta t, t + \delta t) - f_i(x, t) \\ &= \left[\partial_t f_i + e_{i\alpha} \partial_\alpha f_i + \frac{1}{2} (\partial_t^2 f_i + 2e_{i\alpha} \partial_t \partial_\alpha f_i + e_{i\alpha} e_{i\beta} \partial_\beta \partial_\alpha f_i) \right] \delta t \\ &= \left[\underbrace{\epsilon (\partial_{t0} + e_{i\alpha} \partial_{\alpha 0})}_{D_i^{(0)}} f_i + \epsilon^2 \partial_{t1} f_i + \right. \\ &\quad \left. \frac{1}{2} \epsilon^2 \delta t (\partial_{t0}^2 + 2e_{i\alpha} \partial_{t0} \partial_{\alpha 0} + e_{i\alpha} e_{i\beta} \partial_{\beta 0} \partial_{\alpha 0}) f_i + \dots \right] \delta t \\ &= \left[\epsilon D_i^{(0)} f_i + \epsilon^2 \partial_{t1} f_i + \epsilon^2 \frac{\delta t}{2} D_i^{(0)2} f_i + \dots \right] \delta t. \end{aligned} \quad (4.9)$$

In the equation, Einstein's notation is used. Substituting (4.9), (4.7) to (4.5), we can get the following cascaded equations with the consideration of the coefficients of each order of ϵ :

$$\epsilon^{0:0} = f_i^{(0)} - f_i^{\text{eq}}, \quad (4.10)$$

$$\epsilon^1 : D_i^{(0)} f_i^{(0)} = -\frac{1}{\tau \delta t} f_i^{(1)}, \quad (4.11)$$

$$\epsilon^2 : \partial_{t1} f_i^{(0)} + D_i^{(0)} f_i^{(1)} + \frac{\delta t}{2} \left[D_i^{(0)} \right]^2 f_i^{(0)} = -\frac{1}{\tau \delta t} f_i^{(2)}. \quad (4.12)$$

On the other hand, it is easy to know

$$\begin{aligned} \sum_i f_i^{(0)} &= \sum_i f_i^{\text{eq}} = \rho \\ \sum_i f_i^{(0)} \mathbf{e}_i &= \sum_i f_i^{\text{eq}} \mathbf{e}_i = \rho \mathbf{u}, \end{aligned} \quad (4.13a)$$

and

$$\sum_i f_i^{(k)} = 0, \quad \sum_i f_i^{(k)} \mathbf{e}_i = 0, \quad k > 0. \quad (4.13b)$$

Multiplying Eq. (4.11) by 1 and \mathbf{e}_i , respectively, and taking summation over i , we can obtain the mass and momentum equation at the order of ϵ^1 :

$$\partial_{t0} \rho + \partial_{\alpha 0} (\rho u_{\alpha}) = 0, \quad (4.14)$$

$$\partial_{t0} (\rho u_{\alpha}) + \partial_{\alpha 0} \pi_{\alpha \beta}^{(0)} = 0, \quad (4.15)$$

where $\pi_{\alpha \beta}^{(0)} = \sum_i e_{i\alpha} e_{i\beta} f_i^{(0)} = \rho u_{\alpha} u_{\beta} + p \delta_{\alpha \beta}$ is the zeroth-order momentum flux tensor, and $\delta_{\alpha \beta}$ is Kronecker delta, $p = c^2 \rho$, respectively (please refer to Refs. [9, 10] for details). Equations (4.14) and (4.15) are Euler equations.

On ϵ^2 level, it can be easily derived following the above process:

$$\partial_{t1} \rho = 0, \quad (4.16)$$

$$\partial_{t1} (\rho u_{\alpha}) + \left(1 - \frac{1}{2\tau} \right) \partial_{\alpha 0} \pi_{\alpha \beta}^{(1)} = 0, \quad (4.17)$$

where $\pi_{\alpha \beta}^{(1)} = \sum_i e_{i\alpha} e_{i\beta} f_i^{(1)}$. To obtain the macroscopic meaning of $\pi_{\alpha \beta}^{(1)}$, (4.11) is treated

$$\begin{aligned} -\frac{1}{\tau \delta} \sum_i e_{i\alpha} e_{i\beta} f_i^{(1)} &= \partial_{t0} \sum_i e_{i\alpha} e_{i\beta} f_i^{(0)} + \partial_{\gamma 0} \sum_i e_{i\alpha} e_{i\beta} e_{i\gamma} f_i^{(0)} \\ &= \partial_{t0} (\rho u_{\alpha} u_{\beta} + c^2 \rho \delta_{\alpha \beta}) + \partial_{\gamma 0} [c^2 \rho (u_{\alpha} \delta_{\beta \gamma} + u_{\beta} \delta_{\gamma \alpha} + u_{\gamma} \delta_{\alpha \beta})] \\ &= c^2 [\partial_{t0} \rho + \partial_{\gamma 0} (\rho u_{\gamma})] \delta_{\alpha \beta} + u_{\beta} [\partial_{t0} (\rho u_{\alpha}) + \partial_{\alpha 0} p] \\ &\quad + u_{\alpha} [\partial_{t0} (\rho u_{\beta}) + \partial_{\beta 0} p] + c^2 \rho [\partial_{\alpha 0} u_{\beta} + \partial_{\beta 0} u_{\alpha}] \end{aligned}$$

$$\begin{aligned}
&= c^2 \rho [\partial_{\alpha 0} u_\beta + \partial_{\beta 0} u_\alpha] - \partial_{\gamma 0} (\rho u_\alpha u_\beta u_\gamma) \\
&= c^2 \rho [\partial_{\alpha 0} u_\beta + \partial_{\beta 0} u_\alpha] + O(M^3),
\end{aligned} \tag{4.18}$$

where M is Mach number. Further using the results in (4.14) and (4.15), (4.18) leads to

$$\pi_{\alpha\beta}^{(1)} = -\tau p \delta t (\partial_{\alpha 0} u_\beta + \partial_{\beta 0} u_\alpha), \tag{4.19}$$

after neglecting the $O(M^3)$ term.

Finally, we combine the equations on ϵ^1 and ϵ^2 scales and get the hydrodynamic equations

$$\frac{\partial \rho}{\partial t} + \nabla \cdot (\rho \mathbf{u}) = 0, \tag{4.20}$$

$$\frac{\partial(\rho u_\alpha)}{\partial t} + \nabla(\rho \mathbf{u} \mathbf{u}) = -\nabla p + \nabla \cdot [\rho \nu (\nabla \mathbf{u} + \nabla \mathbf{u}^T)]. \tag{4.21}$$

They also show the kinematic viscosity

$$\nu = c^2 \left(\tau - \frac{1}{2} \right) \delta t. \tag{4.22}$$

As a matter of fact, in both (4.6) and (4.19), we use low Mach number assumption, which is fortunately the usual situation for acoustic phenomenon. On the other hand, with low Mach number condition, LBM is considered as a semi-incompressible flow solver.

4.2.2 Implement of LBM Simulation

In Eq. (4.5), only one relaxation time (τ) is presented for all f_i 's relaxation and the approach is named as single relaxation time (SRT) LBM. The calculation generally goes in two steps:

$$f_i^+(\mathbf{x}, t) = f_i(\mathbf{x}, t) - \frac{1}{\tau} (f_i(\mathbf{x}, t) - f_i^{\text{eq}}(\rho, \mathbf{u})), \tag{4.23a}$$

$$f_i(\mathbf{x} + \mathbf{e}_i \Delta t, t + \delta t) = f_i^+(\mathbf{x}, t), \tag{4.23b}$$

where the first one is collision step and the second one streaming step. The code is then organized as follows:

- STEP 1: Initiate f_i on each grid node.
- STEP 2: Calculate ρ, \mathbf{u} (the moments of f_i) according to f_i .
- STEP 3: Calculate equilibrium states, $f_i^{\text{eq}}(\rho, \mathbf{u})$, according to (4.6a).
- STEP 4: Implement collision step according to (4.23a).
- STEP 5: Swap f_i between neighbouring grids following (4.23b).
- STEP 6: Return STEP 2, if the stop criterion is not reached. Otherwise terminate the calculation.

The superior features of LBM will be introduced in the next section. Besides that, a well-proposed boundary condition should be applied in capturing acoustic phenomenon in numerical simulations. That is because the computational domain is usually truncated. In many acoustic simulations, the disturbance/sound propagated from the domain inside should penetrate the boundary without reflection, because the reflections could be of the same order as the real sound waves and contaminate the results [12]. The well-developed non-reflecting boundary conditions (NRBC) in traditional CFD can be applied in LBM. Although they must not be applicable, some of them do show great successes. Following the traditional classification, there are three categories of NRBC: open boundary (extrapolation method, EMBC), characteristics-based boundary condition (NSCBC) and absorbing layer boundary condition (ABC).

EMBC possibly was first proposed to remove the apparent influences of boundaries on flow field when the computational domain is truncated. In these domains, the influences of the model on the flow are hardly dissipated at the far end of the domain. For instance, the shedding vortex can reach the outlet boundary periodically in flow around a cylinder (see Fig. 4.3). Therefore, the quantities on the boundary are actually unknown for the calculations, leading to inapplicability of fixed velocity/pressure boundary condition. On inlet side, a poor-posed condition could lead to wrong results.

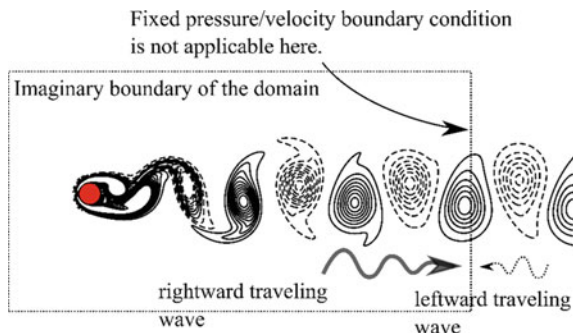


Fig. 4.3 An imaginary computational domain, where fixed pressure/velocity boundary condition cannot be applied on the outlet. The wavy arrows indicate the direction of flow information propagating. They could be from inside the domain (thick) or outside (thin) in real flow. The later one should be designed/modelled because it is unknown in calculations

Table 4.1 EMBC used by Chen [13]. The subscripts “*I*”, “*O*” denote inlet and outlet of the domain, respectively

Boundary	Prescribed quantity on the boundary	Extrapolated quantity on the boundary
Inlet	$\mathbf{u}_I = \mathbf{U}$	$\rho_I = \rho_I^n = \frac{\bar{\rho}^n + \alpha_I \rho_I^{n-1}}{1 + \alpha_I}$
Outlet	$p_O^n = \frac{p_O^{n-1} + \rho c (\bar{u}_O^n - \bar{u}_O^{n-1}) + \alpha_O \Delta t P}{1 + \alpha_O \Delta t}$	$\mathbf{u}_O^n = \bar{\mathbf{u}}^n$

The overbars represent extrapolated variables, and the capitals are prescribed ones. The superscripts represent time step. α 's are adjustable parameters. A damping effect is applied in p_O^n

A simple remedy is to extrapolate the variables, either macroscopic ones or mesoscopic ones (f_i 's), near the boundary from in the domain. Table 4.1 shows an example applied by Chen [13], where the author extrapolates macroscopic variables. The mesoscopic quantities are then constructed according to non-equilibrium extrapolating method proposed by Guo et al. [14]. The unknown mesoscopic values are also constructed directly by using the extrapolation technique. Yu et al. [15] noticed the reflected wave can largely contaminate the meaningful pressure signal, and both equilibrium and deviated components of the distribution function are extrapolated. Smooth density distributions are obtained in the flows around cylinder and airfoil with different Reynolds numbers, respectively.

Another important NRBC roots in the disturbance/information propagation fundamentals in fluid. It is known that two symmetric or asymmetric waves meeting with each other on the boundary results in a Dirichlet boundary (either for pressure or velocity) [16]. It shares the common concept of characteristic line in fluid mechanics, so it is called NSCBC. The mathematical basis can be illustrated through one-dimensional derivation, also named as local one-dimensional inviscid (LODI) equation. The basic idea of NSCBC is presented as follows.

Supposing we have an unknown vector: $\mathbf{U} = [\rho, u_x]^T$, the one-dimensional flow governing equations read

$$\frac{\partial}{\partial t} \mathbf{U} + \boldsymbol{\Gamma}_x \frac{\partial}{\partial x} \mathbf{U} = 0$$

$$\boldsymbol{\Gamma}_x = \begin{bmatrix} u_x & \rho \\ c^2/\rho & u_x \end{bmatrix} = \mathbf{S}^{-1} \boldsymbol{\Lambda} \mathbf{S}, \quad (4.24a)$$

$$\boldsymbol{\Lambda} = \begin{bmatrix} c + u_x & 0 \\ 0 & c - u_x \end{bmatrix}, \quad \mathbf{S} = \begin{bmatrix} \frac{c}{2\rho} & \frac{1}{2} \\ -\frac{c}{2\rho} & \frac{1}{2} \end{bmatrix}, \quad (4.24b)$$

Equation (4.24a) is recast as

$$\frac{\partial \rho}{\partial t} + \frac{\rho}{c} (L_1 + L_2) = 0, \quad (4.25a)$$

$$\frac{\partial u_x}{\partial t} + L_1 - L_2 = 0, \quad (4.25b)$$

$$L_1 = \frac{(u_x + c)}{2} \left(\frac{c}{\rho} \frac{\partial \rho}{\partial x} + \frac{\partial u_x}{\partial x} \right), \quad (4.25c)$$

$$L_2 = \frac{(u_x - c)}{2} \left(\frac{c}{\rho} \frac{\partial \rho}{\partial x} - \frac{\partial u_x}{\partial x} \right), \quad (4.25d)$$

where L_1 represents rightward travelling wave and L_2 leftward wave. We hope the flow state on the boundaries is influenced more from one side. For instance, in Fig. 4.3, the outlet is dominated by the flow upwind and an unknown incoming wave. Therefore, the leftward travelling wave should be suppressed artificially or modelled.

An example was presented by Izquierdo [17]. To obtain LODI equations, the authors used four inviscid flow equations (one mass, two momentum and one energy equations) and got four L_i 's (refer to Eq. 4.25). For an outlet with a prescribed pressure (p_O), the incoming wave is modelled according to a relaxation process:

$$L_1(\mathbf{x}_b, t - 1) = d[p(\mathbf{x}_b, t - 1) - p_O], \quad (4.26a)$$

rather than the original one:

$$L_1^*(\mathbf{x}_b, t - 1) = (u_x - c) \left(\frac{\partial p}{\partial x} - \rho c \frac{\partial u_x}{\partial x} \right). \quad (4.26b)$$

In the equation, the subscripts b , O denote the variables on the boundary and the prescribed quantity, respectively, and d is a parameter. As $d = 0$ no information comes into the domain and the pressure is entirely floating. Nonzero d implies a partial reflective boundary condition and makes p varies around p_O . Subsequently, the macroscopic variables are calculated numerically:

$$\rho_b^t = \rho_b^{t-1} + L_1^{t-1} - \frac{1}{c^2} L_3^{t-1}, \quad (4.27a)$$

$$u_{bx}^t = u_{bx}^{t-1} - \frac{1}{2\rho c} [L_4^{t-1} - L_1^{t-1}], \quad (4.27b)$$

$$u_{by}^t = u_{by}^{t-1} - L_2^{t-1}. \quad (4.27c)$$

By using the quantities, the equilibrium function on the boundary is obtained as $f_i^{eq+}(\rho_b, \mathbf{u}_b, t)$, which is further used to estimate the incoming distributions (through a virtual streaming step):

$$\begin{aligned} f_i(\mathbf{x}_{b-1}, t + 1) \\ = -f_i(\mathbf{x}_{b-1}, t) + 2f_i^{eq+}(\mathbf{x}_b, t) + (2 - s_v) \left[f_i(\mathbf{x}_{b-1}, t) - f_i^{eq+}(\mathbf{x}_b, t) \right], \end{aligned} \quad (4.28)$$

where the first term is antibounce back, the second term is for the Dirichlet pressure setting, and the last one is a correction to eliminate second-order error term (s_v is a dissipation parameter). $\mathbf{e}_{\bar{i}} = -\mathbf{e}_i$.

A third group of NRBC is ABC (or sponge layer condition), the key idea of which is to introduce extra damping effect in a zone around the boundary. Any waves will be dissipated gradually in this zone without reflection. Its ancestor can be also found in traditional CFD model [12] and the governing equation generally reads

$$\frac{\partial \mathbf{U}}{\partial t} + N(\mathbf{U}) = -\sigma(x)(\mathbf{U} - \mathbf{U}_O), \quad (4.29)$$

where N represent a non-linear operator and $\sigma(x)$ a spatially varying friction coefficient. Provided $\sigma(x)$ is large enough, the source term will drive \mathbf{U} to \mathbf{U}_O quickly. Therefore, to the absorbing zone, both incoming and reflected waves will be dissipated, no matter what kind of numerical boundary is imposed.

Xu and Sagaut gave a detailed analysis on the implement of ABC in LBM [18]. The LB equation in ABC zone is presented as

$$\begin{aligned} f_i(\mathbf{x} + \mathbf{e}_i \delta t, t + \delta t) - f_i(\mathbf{x}, t) \\ = -\frac{1}{\tau} (f_i(\mathbf{x}, t) - f_i^{\text{eq}}(\rho^*, \mathbf{u}^*)) + \chi (f_i^{\text{ref}}(\mathbf{x}, t) - f_i^*(\mathbf{x}, t)), \end{aligned} \quad (4.30)$$

where χ characterizes the absorbing strength in the zone. $f_i^{\text{ref}}(\mathbf{x}, t)$ denotes the reference state of $f_i(\mathbf{x}, t)$, and $f_i^*(\mathbf{x}, t)$ the possible representations of distribution functions. Xu and Sagaut [18] analysed and compared several choices of $f_i^{\text{ref}}(\mathbf{x}, t)$ and $f_i^*(\mathbf{x}, t)$. They suggest:

$$f_i^{\text{ref}}(\mathbf{x}, t) = f_i^{\text{eq}}(\rho_O, \mathbf{u}_O, t), \quad (4.31a)$$

$$f_i^*(\mathbf{x}, t) = f_i^{\text{eq}}(\rho, \mathbf{u}, t). \quad (4.31b)$$

In the equations, modified macroscopic density and velocity (ρ^* and \mathbf{u}^*) are applied considering the source term in Eq. (4.30) (the last one). They followed Guo et al. [19] to get the macroscopic quantities:

$$\rho^* = \sum_i f_i + \frac{1}{2} \sum_i \chi (f_i^{\text{eq}}(\rho_O, \mathbf{u}_O, t) - f_i^{\text{eq}}(\rho, \mathbf{u}, t)), \quad (4.32a)$$

$$\rho^* \mathbf{u}_\alpha^* = \sum_i \mathbf{e}_{i\alpha} f_i + \frac{1}{2} \sum_i \chi \mathbf{e}_{i\alpha} (f_i^{\text{eq}}(\rho_O, \mathbf{u}_O, t) - f_i^{\text{eq}}(\rho, \mathbf{u}, t)). \quad (4.32b)$$

The equations recover (4.29) and have a known mapping relation $\sigma_{\text{LBM}} \equiv g(\tau, \chi)$. It is found the sound speed is also tuned due to the source term; however, we do not really care about the physics in the absorbing layer and the flow in it can be ignored.

At last, given $\sigma_{\text{LBM}}(x)$, such as $\sigma_{\text{LBM}}(x) = \frac{3125(L-x)(x-x_0)^4}{256(L-x_0)}$ (where L is the width of the absorbing layer and x_0 is the inner most position of the layer), local damping parameter can be achieved: $\chi(x) = g^{-1}(\sigma_{\text{LBM}}(x), \tau)$.

The above methods are chosen in various studies according to the specific purposes, respectively. On the other hand, some of them can be combined with each other. In Fig. 4.4, a comparison of the boundary condition is presented, where panel (a) shows the density distribution slightly before the wave reaches the boundary layer. The (fully reflective) wall boundary (Fig. 4.4b) and Xu's (Fig. 4.4d) boundary [18] are the worst and best, respectively, for absorbing. A virtual layer of fluid with tuned viscosity is imposed around the computational domain in Fig. 4.4c. The viscosity profile in the boundary zone is of cosine: $\nu_{ABC} = \left[\frac{\nu - \nu_O}{2} (1 + \cos \frac{\pi x}{L}) + \nu_O \right]$, where $\nu_O > \nu$ is an increased virtual viscosity in absorbing layer. The sound wave is reflected partially on this boundary.

In this section, some basic ingredient of LBM is introduced, which might help the readers for their first LBM codes. LBM is actually considered as a general CFD solver in wide range of academic and applied fields, where free surface, turbulent and

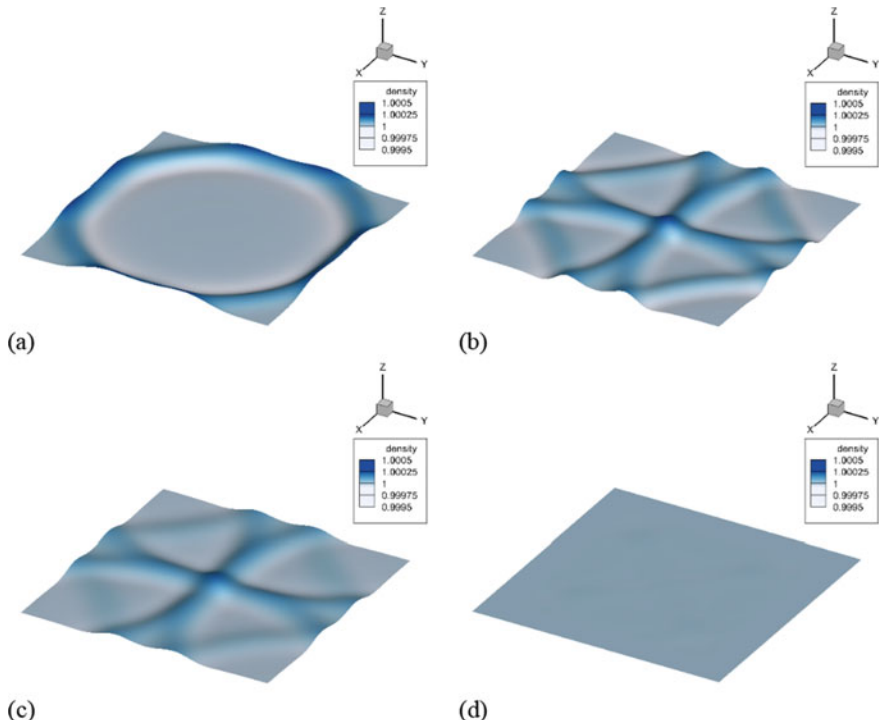


Fig. 4.4 Absorption of Gaussian density wave on the computational domain boundary. **a** Density distribution slightly before the density/pressure wave reaches the boundary (the “initial state”). Density distribution after the wave is “reflected” by **b** solid wall, **c** absorbing layer with tuned viscosity, **d** Xu & Sagaut’s ABC

thermal effects might be concerned. There are also fast improvement and extension on the subjects in the very recent years. The readers are strongly suggested referring to relative publications for details, some of which are presented in the context.

4.3 Acoustic Studies by Using LBM

In the presenting section, we mentioned the flow fundamentals for aeolian tones, which theoretically can be explored by using proper flow model. With consideration of environment protection, aero/hydro-acoustics emerges as one of the most important subjects in modern aircraft, automobile and high-speed train industry. Noise control of marine vehicles is also required urgently for animal health. On the other hand, acoustic techniques are also widely used in the frontier of precise machinery, such as acoustic levitation, acoustic tweezer and cavitation bubble manipulation.

Computational aeroacoustics (CAA) has been developed as an efficient tool for the studies [5]. Deviating from normal CFD, there are special requirements for CAA. For instance, the unsteadiness and scale separation require high temporal and special resolution of the numerical model; the magnitude of acoustic wave is far smaller than the flow itself, which places stringent requirement on numerical accuracy. Therefore, two types of approaches are developed: direct numerical simulation (DNS) and indirect (hybrid) one. Sound and flow are computed together in the former one; only flow scale is resolved in numerical in the later one, while the propagation of sound is computed by using simplified model (like linearized Euler equation). In this section, the numerical feature of LBM is introduced, followed by the applications on both direct and indirect simulation levels.

4.3.1 *The Dispersion Relation in LBGK Model*

Interestingly, LBM is quite suitable for the sound capture in low speed (semi-incompressible) flow. In fact, one who conducts LBM simulation can always observe acoustic/pressure waves shortly after the calculation is started. The relative studies in fact have been carried out in the last decade, where the stability of the method is focused in. The propagation and development of disturbance are considered in both quiescent and flowing fluid. The validation of LBM on acoustic simulation is directly demonstrated in the framework of mathematics, or specifically, by using von Neumann analysis.

As described by Sagaut and Cambon [20], the N–S equations imply that the fluctuation can be divided into acoustic (longitudinal) and vorticity (shear) mode, which correspond to compressible and incompressible motion, respectively. There is another energy (entropic) mode, and it is neglected in LBM analysis because we normal focus on isothermal processes and the variation of entropy is neglected. Simplified N–S equations lead to a dissipation parameter and dispersion relation:

$$\alpha = \frac{k^2 v'}{2}, \quad \frac{\omega}{k} = c \sqrt{1 + \frac{k^2 v'^2}{4c^2}}. \quad (4.33)$$

The details can be found in the relative textbooks and references [2, 16, 21]. The results will be compared simply with the LBM results obtained in the rear part of this section.

The key idea of the von Neumann analysis is described as: tracking the evolution of fluctuations with various frequency in a numerical approach. Fortunately, in many circumstances, the speed of sound is much higher than mean flow (low Mach number assumption: $M \ll 1$) and the sound propagation and flow are decoupled with each other [see also Eq. (4.3)]. Then we focus on sound capture in media at rest. Meanwhile, with infinitesimally weak fluctuation, the governing equation can be linearized, which makes feasibility for the analysis. Both the macroscopic and mesoscopic quantities can be decomposed as a mean and fluctuating part, respectively:

$$\rho(\mathbf{x}, t) = \rho_0 + \rho'(\mathbf{x}, t), \quad (4.34a)$$

$$p(\mathbf{x}, t) = p_0 + p'(\mathbf{x}, t), \quad (4.34b)$$

$$\mathbf{u}(\mathbf{x}, t) = \mathbf{0} + \mathbf{u}'(\mathbf{x}, t), \quad (4.34c)$$

$$f_i(\mathbf{x}, t) = F_i^{\text{eq}} + f'_i(\mathbf{x}, t), \quad (4.34d)$$

$$\rho_0 \gg \rho'(\mathbf{x}, t), \quad p_0 \gg p'(\mathbf{x}, t), \quad \mathbf{u}' \ll 1,$$

noting ideal gas equation of state is applicable in isothermal LBM (see Sect. 4.1): $p = c^2 \rho$ and $p = \rho/3$ in D2Q9 lattice model. F_i^{std} denotes the distribution function for resting state. According to Eq. (5.6),

$$F_i^{\text{std}} = F_i^{\text{eq}}(\rho_0, \mathbf{0}) = \omega_i \rho_0, \quad (4.35)$$

where the non-linear parts are dropped off. It is worthy knowing that f'_i corresponds to unsteady flow. Without losing generality, $f'_i = f_i^\circ e^{i(\omega^* t - \mathbf{k} \cdot \mathbf{x})}$, where ω^* is angular speed and $\mathbf{k} = 2\pi/\lambda \hat{\mathbf{k}}$ the wavenumber vector, λ is the wave-length. Calculate the moments:

$$\begin{aligned} \begin{bmatrix} \rho \\ \rho \mathbf{u}' \end{bmatrix} &= \begin{bmatrix} \rho_0 \\ 0 \end{bmatrix} + \begin{bmatrix} \rho^\circ \\ \rho_0 \mathbf{u}^\circ \end{bmatrix} e^{i(\omega^* t - \mathbf{k} \cdot \mathbf{x})} \\ &= \begin{bmatrix} \sum_i F_i^{\text{std}} \\ \sum_i F_i^{\text{std}} \mathbf{e}_i \end{bmatrix} + \begin{bmatrix} \sum_i f_i^\circ \\ \sum_i f_i^\circ \mathbf{e} \end{bmatrix} e^{i(\omega^* t - \mathbf{k} \cdot \mathbf{x})}, \end{aligned} \quad (4.36)$$

and the equilibrium state is expended as

$$\begin{aligned} f_i^{\text{eq}}(F_j^{\text{std}} + f'_j) &= F_i^{\text{eq}}(\rho_0, \mathbf{0}) + \frac{\partial f_i^{\text{eq}}}{\partial f_j} \Big|_{f_j=F_j^{\text{std}}} f'_j + O(f_j^{\circ 2}) \\ &= \omega_i \rho_0 + \underbrace{\omega_i \left(\rho' + 3 \frac{\rho_0 \mathbf{u}' \cdot \mathbf{e}_i}{c^2} \right)}_{f_i^{\text{eq}}} + \dots \end{aligned} \quad (4.37)$$

Substitute Eq. (4.37) into (4.5), we obtain

$$f'_i(\mathbf{x} + \mathbf{e}_i, t + 1) = \left(1 - \frac{1}{\tau}\right) f'_i(\mathbf{x}, t) + \frac{1}{\tau} f_i'^{\text{eq}}(\mathbf{x}, t), \quad (4.38a)$$

and by using sinusoidal wave denotation,

$$f_i^{\circ} e^{i(\omega^* - \mathbf{k} \cdot \mathbf{e}_i)} = \left(1 - \frac{1}{\tau}\right) f_i^{\circ} + \frac{\omega_i}{\tau} \left(\sum_j f_j^{\circ} + \frac{3\mathbf{e}_i}{c^2} \cdot \sum_j \mathbf{e}_j f_j^{\circ} \right), \quad (4.38b)$$

Set $\mathbf{f}^{\circ} = [f_0^{\circ}, f_1^{\circ}, \dots, f_8^{\circ}]^T$, the equations can be re-organized as

$$\begin{aligned} e^{i\omega^*} \mathbf{f}^{\circ} &= \mathbf{A}^{-1} \left(\mathbf{I} - \frac{1}{\tau} \mathbf{B} \right) \mathbf{f}^{\circ} = \mathbf{M} \mathbf{f}^{\circ}, \\ \mathbf{A} &= \text{diag}[1, e^{-ik \cdot \mathbf{e}_1}, e^{-ik \cdot \mathbf{e}_2}, \dots, e^{-ik \cdot \mathbf{e}_8}], \end{aligned} \quad (4.38c)$$

which leads to an eigenvalue problem. The dispersion relation can be obtained through the characteristic equation:

$$\det(\mathbf{M} - \mathbf{I} e^{i\omega^*}) = g(\omega^*, \mathbf{k}, \tau) = 0. \quad (4.39)$$

Generally speaking, an analytical solution cannot be obtained easily. In fact, the above introduction only gives a very simple route for the dispersion relation. A more complicated version is given by Marie [22] and Lallemand [23], respectively, who considered the non-linear terms in f_i^{eq} 's. Figure 4.5 shows the relations indicating ideal speed of sound and dissipation can be preserved in small wavenumber. It is suggested roughly 12 points should be applied to capture sound propagation properly.

4.3.2 Applications of LBM in CAA

In the recent decades, LBM has already been demonstrated as a great candidate for acoustic simulations. The studies range on three levels: fundamentals and techniques, modelled flow simulations and industrial applications.

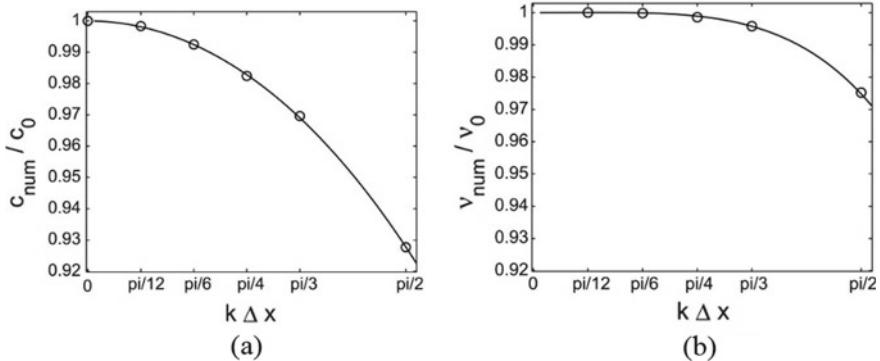


Fig. 4.5 The speed of sound (dispersion relation) (a) and dissipation (b) variations against wave number. The curves indicate the theoretical results and the symbols are numerical ones [22]

On technical levels, there are some valuable developments on the elementary issues about LBM simulation besides the aforementioned dispersion analyses and NRBC's. These work supplies more feasibility and accuracy for the simulations.

- Sound source in LBM. They could be modelled as solid boundary motion or point pressure oscillation. Many sounds are emitted from wall oscillation. Especially when the wall geometry should be concerned, it is naturally that we simply impose oscillating motion on a wall. Barrios and Rechtman [24] added additional source term, $Q_i = \omega_i P e_{iy}$, in the collision step [see Eq. (4.23a)] on the lattice coinciding with the acoustic source. The subscript y denotes the vibrating direction, and $P = P_0 \cos \omega t$. The modification leads to instantaneous input of momentum from the wall. Chen and Ren [25] directly imposed oscillating pressure on the boundary, and standing acoustic wave could be achieved. On the other hand, point sources are interested in many circumstances. They are valuable for both numerical models and many industrial designs. One can of course set some points in a simple manner like $f_i(\mathbf{x}, t) = f_i^{\text{ed}}(\rho_0 \cos \omega t, \mathbf{0})$. However, the flow/wave information is entirely isolated from the points. Viggen [26] extended the idea of Barrios and Rechtman's [24] to multipole acoustic sources, by which the simulated noise is greatly decreased.
- In Sect. 5.2.1, we derive the dispersion relation of BGK-LBM. It is shown that BGK-LBM still suffers from some drawbacks, such as anisotropic and conditional stability [22, 23]. One of the successful improvements is multiple-relaxation time LBM (MRT-LBM), where the relaxation of moments/macrosopic quantities is applied rather than the density populations in collision step [23]. A relaxation time matrix is proposed,

$$\mathbf{T} = \mathbf{M}^{-1} \boldsymbol{\Lambda} \mathbf{M}, \boldsymbol{\Lambda} = \text{diag}(s_0, s_1, \dots, s_8), \quad (4.40a)$$

and the collision process is undergone on the corresponding moment space:

$$\mathbf{m} = \mathbf{M}\mathbf{f}, \quad \mathbf{f} = [f_0, f_1, \dots, f_8]^T. \quad (4.40b)$$

In MRT-LBM, the relaxation of the density distributions is coupled; however, the speed of it can be adjusted independently. In Eq. (4.40a), $s_0 = s_1 = \dots = s_8 = 1/\tau$ recovers the SRT-LBM. By tuning the bulk damping property of the fluid (in numerical calculations), the stability of the calculation is strengthened. Filter techniques are further proposed [27, 28] to remedy the overdamping on acoustic waves in MRT-LBM.

In aeroacoustics, there are bunch of standard flows which result in sound emission. They basically relate to aeroacoustic theories and also have realistic meanings. For instance, the Lighthill equation describes a flow without solid boundary, which can occur in free jet flow. To simulate high Reynolds number (characterizing the ratio between kinetic energy and viscous dissipation of the flow) jet flow can not only be used to explore fluid mechanics but also assess numerical method. Coupled with certain turbulence model, such as VLES, RNG- $k - \varepsilon$ model, SRT-LBM can well predict the turbulent flow ejected from a nozzle [29, 30]. The results show the prior feature of LBM on capturing both flow details and sound signals.

Guo and Chen [31] conducted LBM simulation on two-dimensional vortex motion and investigated the sound emission. In their studies, a vortex pair (VP), either co-rotating or counter-rotating, is set in a space with or without wall boundary. Two approaches were applied to obtain the far field sound: direct measurement from numerical results and calculations according to Lighthill theory. Although large Reynolds number was applied, which traditionally is treated with simple inviscid flow model, the results showed a subtle viscous influence on the vortices motion, and therefore influence the sound emission. Recalling the mathematical analysis in Sect. 4.2.1, it is not surprising that directly simulated results agree with the theoretical results on both mean flow and disturbance propagation (see Figs. 4.5 and 4.6).

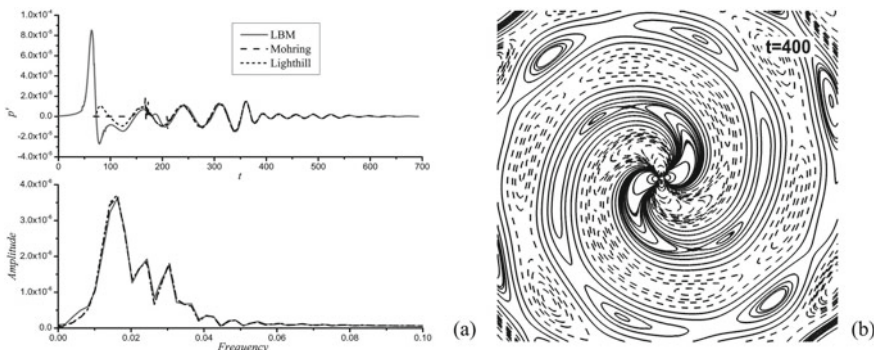


Fig. 4.6 LBM simulation of vortex pair dynamics in a free space and the sound emission. **a** Far field sound pressure oscillation obtained by direct measurement in numerical results and theoretical predictions (upper part). The spectra of the signals are compared in the lower part. **b** The sound pressure distribution of a co-rotating vortex pair in free space [31]

LBM simulation has been applied in industry. As proposed in the previous part, turbulent jet flow is well studied in CAA, which has important practical purposes, such as assessment of noise level in jet propelling of airplane. The similar numerical approaches are used in many other problems. Khorrami et al. [32] conducted large-scale numerical simulations on the flow and noise performance of Gulfstream aircraft model. Compared to experiments and third party numerical results, the LBM simulation is demonstrated very accurate and effective. In the simulations, flowing $M = 0.2$ and the flap deflected 39° are applied. The former condition almost touches the LBM's low Mach number limit, and the later one is obviously very tough for CFD technique due to severe flow separation. Besides that, the flows at the flap inboard and outboard tips and main landing gear are captured correctly, which is considered as main noise sources on landing phase of aircraft. The authors also applied Ffowcs-Williams and Hawkins acoustic analogy approach to the numerical results and obtained good agreement on far-field noise prediction.

Coupled with various turbulence model, LBM is validated as a powerful tools addressing industrial flows and noise predictions.

4.4 LB Simulation in Acoustic Levitation and Second-Order Acoustic Flow

Buick et al. showed LBM can well reproduce non-linear acoustic effects, which is not surprise concerning its dispersion and dissipation features [2]. For large-scale flows, to capture their acoustic footprint depends also on turbulence model as aforementioned: in fact that is a key issue for the accuracy. On the other hand, more precise control of sound phenomena, such as propagation, reflection and deflection, also has plenty of potentials for application. The flows in these circumstances are normally laminar and many theoretical models were actually proposed. On the numerical side, the requirement for dissipation and dispersion feature makes LBM very applicable.

Haydock and Yeomas [33, 34] firstly used LBM to reproduce acoustic streaming correctly. In their study, a simple version of BGK-LBM is applied for classical Rayleigh streaming and Eckart streaming. Both of the streaming originates from attenuation, and they can be illustrated through a simple model as follows.

Suppose the oscillation of the fluid element is damped along the wave line and has a general form of $u_x = U e^{-\alpha x} \cos(\omega t - kx)$. It leads to Reynolds stress and a pressure gradient:

$$\partial_x P_2 = F_x = -\rho_0 \langle 2u_x u_x \rangle = \rho_0 \alpha U^2 e^{-2\alpha x}, \quad (4.41)$$

where the point bracket denotes time average value. It implies a steady flow. Obviously, the flow is of second order. If the dissipation is mainly in the boundary layer near a wall, the streaming driven by the Reynolds stress is call Rayleigh streaming; if the dissipation occurs in the bulk, Eckart streaming is resulted in. It is shown that both

time dependent first order flow and the streaming are predicted well by using LBM correctly. Furthermore, Haydock and Yeomas [34] and Rafat et al. [35] extended the method to more complicated geometries, which is not well described by theories.

Following their prediction of LBM targeting detailed acoustic simulation, Haydock [36] further investigated acoustic radiating forces on a (two-dimensional) cylinder. Full N–S equations were simulated through LBM in low viscosity regime. A viscous penetrating depth was introduced: $\beta^{-1} = \sqrt{2v/\omega}$. The results show that the deviation of acted force on the cylinder against inviscid prediction vanishes linearly as $(a\beta)^{-1}$ approaches zero, where a is radius of the cylinder. By setting the cylinder in a standing acoustic wave, its trajectory was presented, which approaches a pressure node. The model was further set in a channel, where Rayleigh streaming was induced by longitudinal standing wave. The viscous force is dominant and also leads to transversal motion of the cylinder to the centre of the channel. Barrios and Rechtmann [24] simulated acoustic levitation in details by using LBM. The density ratio, levitator geometry and acoustic strength are investigated. It is interesting that two pressure nodes are found as a rounded cavity is used, which destabilizes the cylinder oscillation. Barrios and Rechtmann also propose that, although larger oscillation and non-periodic motion of the “levitated” particle are obtained for rounded cavity, it is easily to be levitated in weak sound waves. Chen and Ren [25] compared the details of simulated acoustic flow and theoretical predictions around a cylinder. Their results show that the viscous flow in boundary layer is discerned clearly from the periodic far-field flow. The later can be described well by using potential flow theory. The measured boundary thickness fulfils the theoretical prediction very well. In the time averaged flow field, one or two layers of steady recirculation are found depending on $(a\beta)^{-1}$.

4.5 Summary

In this chapter, we introduce the fundamentals, implement issues and applications of lattice Boltzmann method in acoustics. It should be said that lattice Boltzmann method is comparatively easy for coding and of high efficiency for parallel computing. It could be considered as a substitutional approach for N–S equation-based computational methods and beyond. By using von Neumann analysis, we show that correct dispersion relation can be obtained when the wavenumber is small. Of course, recently improvement on lattice Boltzmann method allows further lower grid resolution for acoustic simulations. The prior features of the method lay solid basis for acoustic simulation, which includes both aeolian tones and precise sound wave reproducing. For the later one, non-linear motions may play important roles. On acoustic levitations, lattice Boltzmann simulations show the viscous forces become more salient as the viscous penetrating depth grows. As well, interesting results are revealed for cavity geometry, etc. Besides the theoretical study, lattice Boltzmann simulation makes more precise design for levitation equipment and deeper understanding of physics is presented available.

References

1. D.L. Landau, E.M. Lifshitz, *Fluid Mechanics* (Butterworth-Heinemann, Oxford, 1999)
2. J.M. Buick, C.L. Buckley, C.A. Created, J. Gilbert, Lattice Boltzmann BGK simulation of nonlinear sound waves: the development of a shock front. *J. Phys. A: Math. Gen.* **33**, 3917–3928 (2000)
3. M. Goldstein, *Aeroacoustics* (McGraw-Hill Inc., New York, 1976)
4. J.E. Ffowcs-Williams, Aeroacoustics. *Annu. Rev. Fluid Mech.* **9**, 447–468 (1977)
5. M. Wang, J.B. Freund, S.L. Lele, Computational prediction of flow-generated sound. *Annu. Rev. Fluid Mech.* **38**, 483–512 (2006)
6. S.S. Sadhal, Acoustofluidics 15: streaming with sound waves interacting with solid particles. *Lab Chip* **12**, 2600–2611 (2012)
7. M. Settnes, H. Bruus, Forces acting on a small particle in an acoustical field in a viscous fluid. *Phys. Rev. E* **85**, 016327 (2012)
8. C.K. Aidun, J.R. Clausen, Lattice-Boltzmann method for complex flows. *Annu. Rev. Fluid Mech.* **42**, 437–472 (2010)
9. S. Chen, G.D. Doolen, Lattice Boltzmann method for fluid flows. *Annu. Rev. Fluid Mech.* **30**, 329–364 (1998)
10. Z. Guo, C. Shu, *Lattice Boltzmann method and its applications in engineering* (World Scientific Publishing, Singapore, 2013)
11. H. Huang, M.C. Sukop, X.-Y. Lu, *Multiphase lattice Boltzmann methods* (Wiley, Singapore, 2015)
12. T. Colonius, Modeling artificial boundary conditions for compressible flow. *Annu. Rev. Fluid Mech.* **36**, 315–345 (2004)
13. X.-P. Chen, Applications of lattice Boltzmann method to turbulent flow around two-dimensional airfoil. *Engg. Appl. Compt. Fluid Mech.* **6**, 572–580 (2012)
14. Z. Guo, C. Zheng, B. Shi, Non-equilibrium extrapolation method for velocity and pressure boundary conditions in the lattice Boltzmann method. *Chin. Phys.* **11**, 366–374 (2002)
15. D. Yu, R. Mei, W. Shyy, Improved treatment of the open boundary in the method of lattice Boltzmann equation. *Prog. Comput. Fluid Des.* **5**, 3–12 (2003)
16. E.M. Viggen, Sound waves, in *The Lattice Boltzmann* (Springer Nature, Switzerland, 2017), pp. 493–529
17. S. Izquierdo, N. Fueyo, Characteristic nonreflecting boundary conditions for open boundaries. *Phys. Rev. E* **78**, 046707 (2008)
18. H. Xu, P. Sagaut, Analysis of the absorbing layers for the weakly-compressible lattice Boltzmann method. *J. Comput. Phys.* **245**, 14–42 (2013)
19. Z. Guo, C. Zheng, B. Shi, Discrete lattice effects on the forcing term in the lattice Boltzmann method. *Phys. Rev. E* **65**, 046308 (2002)
20. P. Sagaut, C. Cambon, *Homogeneous Turbulence Dynamics* (Cambridge University Press, Cambridge, 2008)
21. A. Wilde, Calculation of sound generation and radiation from instationary flows. *Comput. Fluids* **35**, 986–993 (2006)
22. S. Marie, D. Ricot, P. Sagaut, Comparison between lattice Boltzmann method and Navier-Stokes high order schemes for computational aeroacoustics. *J. Comput. Phys.* **228**, 1056–1070 (2009)
23. P. Lallemand, L.-S. Luo, Theory of the lattice Boltzmann method: dispersion, dissipation, isotropy, Galilean invariance, and stability. *Phys. Rev. E* **61**, 6546–6562 (2003)
24. G. Barrios, R. Rechtman, Dynamics of an acoustically levitated particle. *J. Fluid Mech.* **596**, 191–200 (2008)
25. X.-P. Chen, H. Ren, Acoustic flows in viscous fluid: a lattice Boltzmann study. *Int. J. Numer. Methods Fluids* **79**, 183–198 (2015)
26. E.M. Viggen, Acoustic multipole sources for the lattice Boltzmann method. *Phys. Rev. E* **87**, 023306 (2013)

27. D. Ricot, S. Marie, P. Sagaut, C. Bailly, Lattice Boltzmann method with selective viscosity filters. *J. Comput. Phys.* **228**, 4478–4490 (2009)
28. S. Marie, X. Gloerfelt, Adaptive filtering for the lattice Boltzmann method. *J. Comput. Phys.* **333**, 212–226 (2017)
29. F.D. da Silva, C. J. Deschamps, Assessment of jet-plate interaction noise using the lattice boltzmann method, in *21st AIAA/CEAS Aeroacoustics Conference* (AIAA 2015-2207), Dallas, TX (2015)
30. D. Casalino, S.K. Lele, *Lattice-Boltzmann simulation of coaxial jet noise generation* (Center for Turbulence Research, Stanford, 2014)
31. R.-Q. Guo, X.-P. Chen, Sound generation by two dimensional vortex pair motion and the influence of viscosity. *Comput. Math Appl.* **78**, 2761–2771 (2019)
32. M.R. Khorrami, E. Fares, D. Casalino, Towards full aircraft airframe noise prediction, in *20th AIAA/CEAS Aeroacoustic Conference* (AIAA 2014-2480), Atlanta, GA (2014)
33. D. Haydock, J.M. Yeomas, Lattice Boltzmann simulations of acoustic streaming. *J. Phys. A: Math. Gen.* **34**, 5201–5213 (2001)
34. D. Haydock, J.M. Yeomas, Lattice Boltzmann simulations of attenuation-driven acoustic streaming. *J. Phys. A: Math. Gen.* **36**, 5683–5694 (2003)
35. Y. Rafat, K. Habibi, L. Mongeau, Direct numerical simulations of acoustic streaming in standing wave tubes using the lattice Boltzmann method. *Proc. Mtgs. Acoust.* **19**, 045006 (2013)
36. D. Haydock, Lattice Boltzmann simulations of the time-averaged forces on a cylinder in a sound field. *J. Phys. A: Math. Gen.* **38**, 3265–3277 (2005)

Chapter 5

Dynamics of Acoustically Levitated Drops



Zehui Zhang, Kangqi Liu, and Duyang Zang

Abstract Levitation of liquid droplet is one of the most important applications of acoustic levitation, not only for the study of fluid physics, but also for bio/chemical analysis. In this chapter, we review various behaviors of acoustically levitated drops, ranging from evolution of static equilibrium shape, oscillation, to different drop instabilities. We also discuss drop manipulation by using acoustic levitation. At last, we propose several possible future directions to stimulate multi-discipline researches based on the technique.

5.1 Introduction

Drop dynamics is of great importance for both industrial applications and fundamental researches. For instance, in spray coating and cooling, inkjet printing, drop dynamics plays crucial role. Therefore, it is highly desired to sufficiently understand its dynamics and control it. Researchers have performed extensive studies of drop impinging dynamics onto solid surface, either superhydrophobic or with designed patterns [1]. Alternatively, polymer additives could also be introduced to change the rheological properties [2] or enhance the contact line friction [3] thus leading to adhesion of the impacting drops, which would be greatly expected for pesticide spread.

It is well known the drop dynamics is significantly affected by the contact lines where the energy dissipation is strong. Owing to this reason, drop dynamics has also been studied under levitation condition, for instance in space station [4].

On the ground, however, drop levitation dynamics could be studied via acoustics levitation techniques [5]. One of the main advantages of acoustics levitation over other levitation techniques, such as electrostatic [6], electromagnetic [7] and optical tweezers [8], is that the electromagnetic properties of the levitation sample are not required, thus making it suitable for a broader range of materials. In particular, it

Z. Zhang · K. Liu · D. Zang (✉)

Soft Matter & Complex Fluids Group, School of Physical Science and Technology, Northwestern Polytechnical University, 710129 Xi'an, China

e-mail: dyzang@nwpu.edu.cn

is ideal for the study of complex drops via their dynamic behaviors ranging from oscillation [9, 10], shape evolution, to evaporation [11–13].

In this chapter, we review the equilibrium shape of acoustically levitated drops with the effect of acoustics radiation force. Various behaviors of the levitated drops, including oscillation (translation and sectorial), instability behaviors, will be discussed. The manipulation of droplet via acoustics levitation is one of its promising application since it provides a contact-free manipulation approach, which will also be reviewed.

5.2 Equilibrium Shape of Acoustically Levitated Droplets

For a small free droplet exposed to gravitational field (diameter less than capillary length), its shape tends to remain spherical dominated by surface tension. However, when the droplets are levitated in the sound field, their equilibrium shape is jointly determined by sound radiation pressure P_A , surface tension σ and internal pressure P_i of the droplets [14] (Eq. 5.1).

$$P_i - P_A = \sigma \nabla \cdot \mathbf{n} \quad (5.1)$$

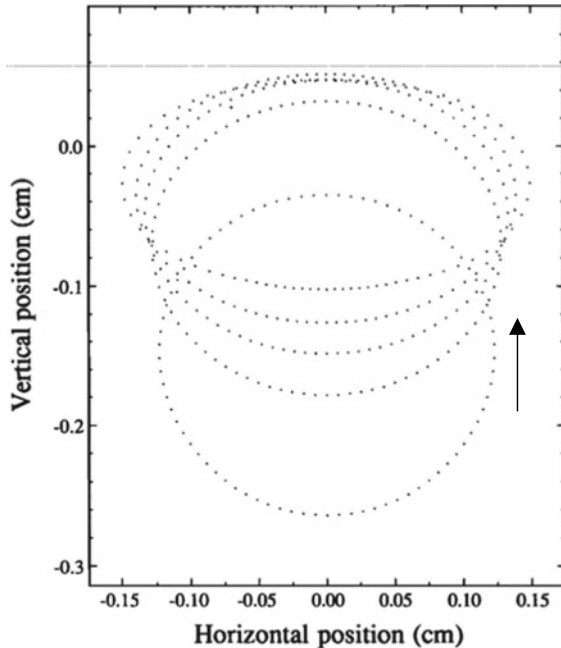
where P_A is a time-averaged pressure caused by ultrasound, \mathbf{n} is the unit vector on the drop surface pointing outward, and $\nabla \cdot \mathbf{n}$ denotes the total local curvature. In order to describe the droplet equilibrium shape in a simpler manner, the droplet equilibrium shape function can be written based on polar coordinate [15–17]:

$$R_s(\theta) = R_L \left[1 - \frac{3R_L P_A^2}{64\sigma\rho c_0^2} \left(1 + \frac{7}{5}(k_0 R_L)^2 \right) (3 \cos^2 \theta - 1) \right] \quad (5.2)$$

where $R_s(\theta)$ is the polar coordinate of the drop contour, R_L is the equatorial radius of the drop, ρ is the density of the drop.

The uneven distribution of acoustic radiation pressure on the surface of droplets results in the non-spherical shape of the acoustically levitated droplets. To understand the equilibrium shape of liquid droplets in sound field, researchers have developed different theoretical methods to calculate the shape of liquid droplets. Trinh and Hsu [18] have performed levitation experiments with water, glycerol, silicon oil and other liquids and obtained the relationship between droplet aspect ratio and sound intensity. The authors have compared their experimental results with Marston's [19] theoretical prediction. It was found that Marston's theoretical results were in good agreement with the experimental results when the shape of the levitated droplets was slightly deviated from spherical shapes. However, when the droplet is far from spherical (the ratio of long axis to short axis is $a/b > 1.2$), the theory was failed to predict the equilibrium shape of the droplet.

Fig. 5.1 Shape profile of acoustically levitation droplet with increasing sound intensity [15]



Tian et al. [15] have considered the scattering effect of non-spherical liquid droplet and the influence of gravitational field on the levitation position, and calculated the balanced force exerted on drop surface. Therefore, the equilibrium shape and levitation position of liquid droplets have been obtained (Fig. 5.1). The theory can be reduced to Marston's theory when the droplets are small and nearly spherical. Tian et al's theory can also calculate the equilibrium shape of flat droplets with high deformation, which is in agreement with the experimental results. Based on this, Shi [20] has carried out Fourier transformation to the Helmholtz equation which controls the scattering wave and developed a new method for calculating the droplet equilibrium shape in sound field. The method is applicable to the situation under which the droplet is deformed into a flattened film.

Sound intensity (sound pressure) is the main factor that dominates the shape of acoustically levitated droplets. The gravitational force only changes the levitation position of the droplets, however, has little effect on the equilibrium shape of the droplets (Fig. 5.2). In order to obtain the equilibrium shape of droplets at different sound pressure levels, a numerical damping approach was introduced into the simulation of droplet shape. With the increase of sound pressure, the aspect ratio (equatorial radius a' over polar radius b' , a'/b') increases, resulting in a disk shape of the drop. At higher sound pressures, the center of the top and bottom surfaces even changes from convex to concave (Fig. 5.2c, g). Compared with the levitation under micro-gravity, the shape variation (caused by increasing sound pressure) of drops under normal gravity condition is similar, although the levitation position of the droplets is

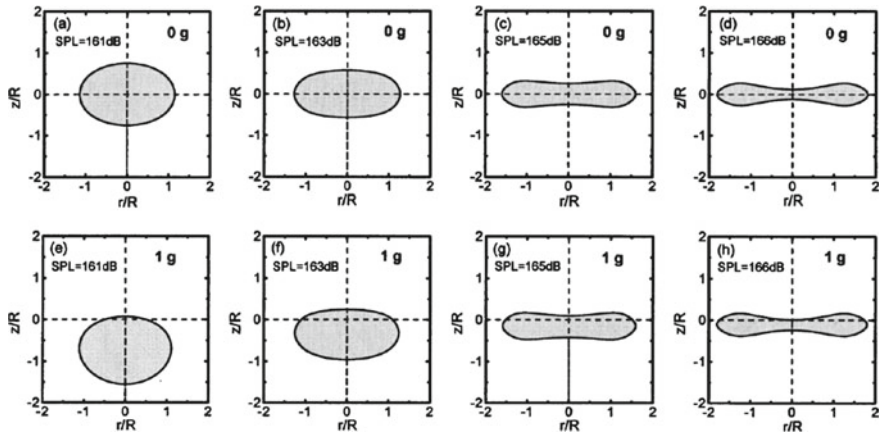


Fig. 5.2 Equilibrium shapes of acoustically levitation with increasing sound pressure level [21]. **a-d** correspond to zero gravity condition whereas **e-h** refers to gravity condition. The sound pressure level from left to right is 161, 163, 165 and 166 dB respectively

lifted up with the increase of the sound pressure (Fig. 5.2d, h). Under microgravity condition [21], however, the mass center of the droplet is always located in the plane of the acoustic pressure node.

In general, the size of the acoustically levitated sample is limited by the half wavelength of the sound wave [14]. However, this limit can be exceeded when two bubbles are vertically stacked together (Fig. 5.3). The vertical length can reach $5\lambda/6$, significantly beyond $\lambda/2$ [22]. This is because a toroidal-shaped high-pressure region is formed around the waist of the two bubbles, which greatly enhances the trapping effect of the sound potential well. Furthermore, the acoustically bubbles show

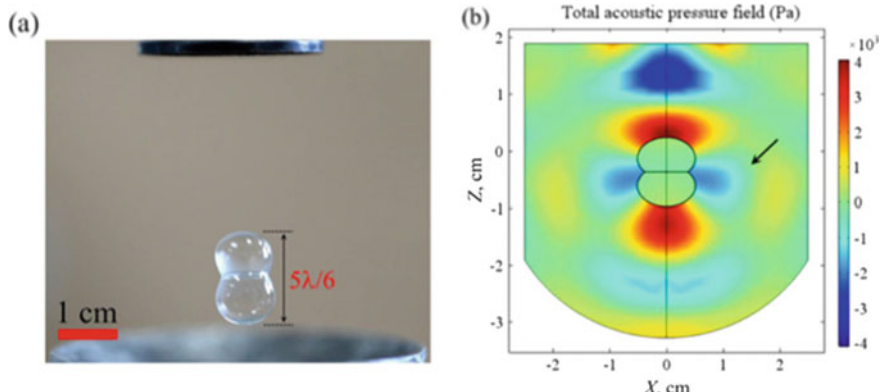


Fig. 5.3 Acoustic levitation of two vertically-stacked bubbles [22]. **a** Image showing the vertical length of the bubbles is $5\lambda/6$. **b** Sound filed with the levitated bubbles. The arrow indicates the toroidal high-pressure region

extraordinary stability, i.e., the bubbles can be levitated for tens of minutes without bursting.

5.3 Oscillation of Drops

The acoustically levitated droplets usually exhibit two different types of oscillation: (1) the translational oscillation in which the levitation position vibrates; (2) sectorial oscillation.

The levitated drop oscillates around its equilibrium position once it is deviated slightly from the original levitation position. This kind of oscillation is in a harmonic mode where its restoring force is provided by acoustic radiation force and gravity [22]. It should be noted associating with the translational oscillation the drop also exhibits shape oscillation because the acoustic radiation force is varied as its levitation position is changed. The shape oscillation frequency of the droplet is twice that of the vertical one. It has been found that the oscillation dynamics is dependent on the equilibrium shape of the drops. As illustrated in Fig. 5.4a, the larger the surface area is, the faster the oscillation damping is [23]. The damping is also enhanced by liquid viscosity (Fig. 5.4b).

Becker et al. [24] have found that when the oscillation amplitude is large, i.e., exceeds 10% of the radius of the droplet, the frequency of vertical oscillation of the droplet would be related to the amplitude. Namely, the oscillation frequency of droplets tends to be smaller for larger oscillation amplitude.

For small-amplitude oscillation of free droplets, the oscillation frequency f of the drop is determined by the surface tension σ and droplet size R_S . The relation can be described by Rayleigh equation [25]:

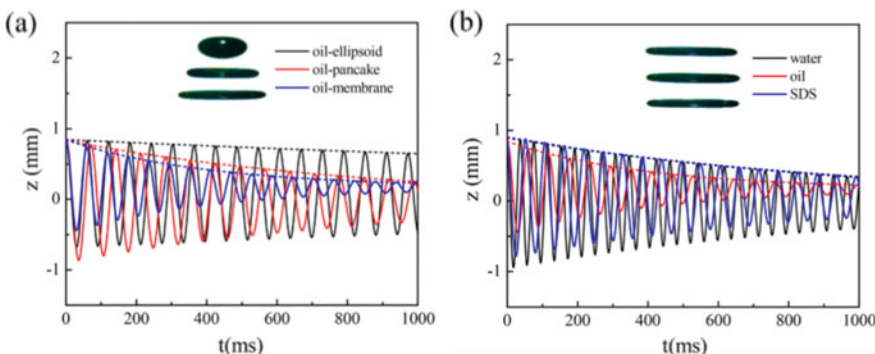


Fig. 5.4 Vertical oscillation damping of acoustically levitated drops of different liquids: water, SDS solution, and castor oil. The fitted dashed lines show the decay of oscillation amplitude [23]. **a** The oscillation damping behavior for castor oil drops ($20 \mu\text{L}$) of varied surface areas. **b** The oscillation damping behavior for drops ($20 \mu\text{L}$) with the same surface area of different liquids: water, SDS solution and castor oil

$$f = \frac{1}{2\pi} \sqrt{\frac{\sigma}{\rho_L R_s^3}} l(l-1)(l+2) \quad (5.3)$$

where ρ_L is the density of liquid and l is the mode of oscillation. Rayleigh equation indicates that the oscillation frequency of a droplet is constant for a given size and surface tension.

By contrast, acoustically levitated drops often exhibit sectorial oscillation during which the shape of the droplet is always kept rotational symmetry about the vertical axis. When a certain modulation voltage is applied to the working voltage of the levitator, the emitter could generate sound waves with a modulated amplitude. These sound waves do not affect the levitation stability of the liquid droplets, however, excite the sectorial oscillation of a certain mode. The mode of the sectorial oscillation is usually influenced by the radius, and viscosity of the drop, as well as the sound frequency.

Yan et al. have accomplished a high mode sectorial oscillation (up to 9th) of water droplets by using a single-axis acoustic levitator [26–30]. It is found that the frequency of sectorial oscillation decreases with the increase of the equatorial radius of the flattened droplets. Shen et al. [30] have proposed a modified Rayleigh formula through replacing the spherical drop radius R_s by the equatorial radius a' :

$$f = \frac{\psi}{2\pi} \sqrt{\frac{\sigma}{\rho a'^3}} l(l-1)(l+2) \quad (5.4)$$

where ψ is a coefficient related to the droplet deformation. The sectorial oscillation frequency calculated by the modified Rayleigh formula is in good agreement with the experimental results.

The sectorial oscillation dynamics strongly depends on the drop viscosity. Shao et al. [31] have studied the sectorial oscillation by using glycerol-aqueous solutions of different concentrations, which exhibits varied viscosity but almost constant surface tension. It is found that the viscosity of the drop should be smaller than a critical value to enable the excitation of the oscillation. The critical viscosity decreases exponentially with the increase of the oscillation order. Therefore, it is difficult to stimulate high-mode sectorial oscillation for high-viscosity droplets.

The sectorial oscillation is also influenced by the surface rheological/mechanical properties of the drops. For instance, the coating of a particle shell on drop surface (leading to the formation of a liquid marble) could significantly enhance the compression/dilatational moduli of the drop surface, and in turn changes the oscillation amplitude and frequency (Fig. 5.5). Zang et al. [32] have proposed a new model to understand the sectorial oscillation of these complex drops by introducing the compression modulus of the nanoparticles layers into the modified Rayleigh equation, which build the theoretical relationship between the interfacial compression modulus and the oscillation frequency. The calculated results using this model are in agreement with those obtained by the Wilhelmy plate method, thus opening up a new way to study the interfacial mechanical/rheological properties by using acoustic levitation technique.

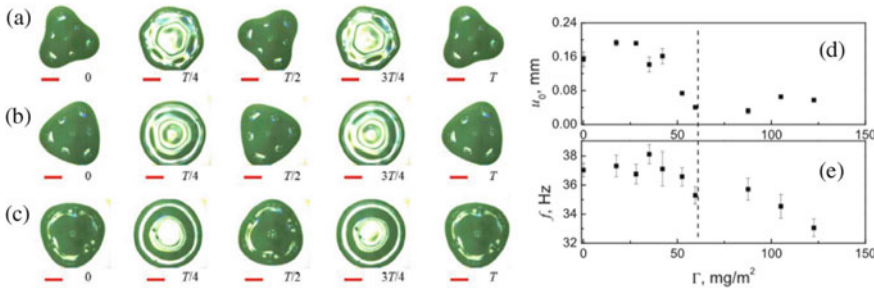


Fig. 5.5 Third-mode sectorial oscillation of droplets coated with different amount of nanoparticles [32]. **a** $T = 28.0 \text{ mg/m}^2$ **b** $T = 70.0 \text{ mg/m}^2$ **c** $T = 122.6 \text{ mg/m}^2$. **d** and **e** showing the sectorial oscillation amplitude μ_0 and frequency f for droplets with different surface particle concentrations. The vertical dashed line indicates the occurrence of buckling

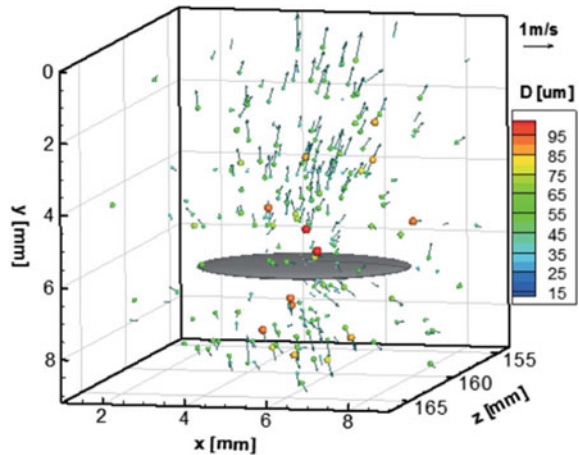
5.4 Instability of Droplets

5.4.1 Plateau–Rayleigh Instability

Capillary wave is the key factor that induces the Plateau–Rayleigh (P–R) instability of acoustically levitated droplets. When the sound field is strong enough, the levitated droplets usually be flattened into thin film, which becomes unstable and atomizes into a large number of small droplets due to the disturbance of sound waves. Lee et al. [33] have found that the capillary wave, which was generated by acoustic disturbance [27], first appeared near the center of the levitated film. As the sound intensity increases, the capillary wave amplitude on the surface of the liquid film increases. Once the amplitude of the capillary wave becomes comparable to the thickness of the liquid film, the liquid film begins to destabilize and atomize. Before atomization, the frequency of capillary wave on its surface is consistent with that of acoustic wave, indicating it is the resonance mechanism that makes the liquid film atomized. Yao et al. [34] have studied the instability of acoustic levitated droplets by using digital holographic particle tracking velocimetry system and obtained the spatial and velocity distribution of the atomized droplets (Fig. 5.6). The size of the atomized daughter droplets ranges in 10–140 μm . However, droplets with radius of $\sim 50 \mu\text{m}$ have the largest numbers. The critical conditions for atomization of acoustically levitated droplets are related to the sound Bond number and the critical radius of droplets [16]. Moreover, the atomization can be suppressed by enhancing liquid viscosity [33].

The change in surface tension, which depends on temperature, could also lead to the P–R instability. The surface temperature of an acoustically levitated droplet increases sharply when it was exposed to laser, which lead to the decrease of surface tension and the oscillation of the droplets [35]. If this process is performed to droplets of diesel oil and kerosene, the droplets will atomize (with sub-droplet around) before they are flattened. However, atomization does not occur to ethanol droplets [36, 37].

Fig. 5.6 Size and spatial distribution of atomized droplets under acoustic levitation [34]



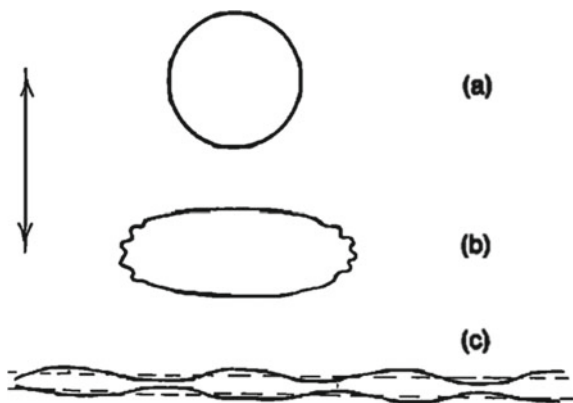
5.4.2 Kelvin–Helmholtz Instability (K–H Instability)

The Kelvin–Helmholtz instability is the interfacial instability caused by the shearing of two relatively moving fluids. When the acoustical droplets contact with the surrounding air, a shear layer will be formed due to the different velocity. The high-velocity fluid will increase the velocity of some low-velocity fluid through the viscous effect, so the disturbance will occur at the contact surface. In the disturbance, the interface of the two kinds of fluids is distorted, and some heavy fluids are bumped into the upper light fluids. In the same way, because of the continuity assumption, some heavy fluids are bumped back into the lower light fluids, which is actually equal to the exchange of position and velocity between the two fluids. Therefore, the fluids are mixed, which makes the stable laminar flow. The Kelvin–Helmholtz instability occurs mainly in the contact area between the levitated droplet and the surrounding media. The shear layer will be formed at the interface due to the velocity gradient, which is disturbed by sound waves and become unstable once the fluid velocity reaches a critical value v_{crit} . v_{crit} can be written as [37]:

$$v_{crit} = \sqrt{\frac{2(\rho_1 + \rho_0)}{\rho_1 \rho_0} \sqrt{\sigma(\rho_1 - \rho_0)g}} \quad (5.5)$$

where ρ_1 represents the density of the fluid, ρ_0 is the density of air, σ is the surface tension, g is the gravitational acceleration. Danilov et al. [38]. have systematically studied the K–H instability of acoustically levitated liquid droplets cause by heating. It has been found that the K–H instability largely occurs at the equator area of the droplet mainly caused by acoustic streaming [39], as illustrated in Fig. 5.7.

Fig. 5.7 Evolution of a droplet in high-intensity sound field. **a** initially spherical shape, **b** Kelvin–Helmholtz instability, **c** growing capillary waves on a flattened droplet [38]



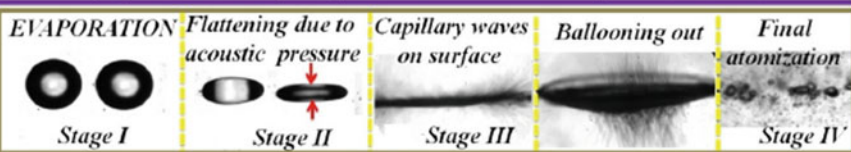
5.4.3 Buckling Instability and Helmholtz Resonance

Pathak et al. [40] have studied the instability behaviors of binary-component droplets heated by laser under acoustic levitation. Due to the coupling effect of sound field and heating, two different instability behaviors have been observed (Fig. 5.8), which are called atomization type (Fig. 5.8a) and buckling instability type (Fig. 5.8b), respectively. Atomization type refers to the direct atomization of droplets without forming a curved liquid film. Buckling instability, however, experiences several different stages: caving stage, ligament initiation and growth, ligament break up. The atomization type mainly occurs in droplets with low benzene concentration (<70% volume). Buckling instability has been observed in droplets with high benzene concentration (>70% by volume), which characterized by the formation of a buckled film. The reduced surface tension caused by heating is responsible for the expansion of liquid film and its buckling.

Similar phenomenon has been evidenced by Lee et al. [33] where the buckling of an acoustically levitated film was caused by increasing sound intensity. As found by Zang et al. [32] the buckling instability can occur in different liquids: silicone oil, surfactant solution, even pure water. However, only those have sufficient bulk viscosity or with stabilization of surfactant can accomplish drop-to-bubble transition where the inhibition of atomization is necessary. The phenomenon can generally be divided into five stages: slight deformation, rapid flattening, deceleration flattening, buckling and rapid expansion closure [41] (Fig. 5.9).

Zang et al. [41] have proposed an acoustics resonance mechanism to account for this buckling instability and drop-to-bubble transition. When the cavity reaches the critical volume, the bubble volume increases sharply. It is found that the critical volume is independent of the type of liquid and the initial size of droplets, but significantly depends on the frequency of sound field. This is because the cavity formed by the buckled liquid film actually acts as a Helmholtz resonator. When the volume of the buckled cavity reaches a suitable value, it resonates with the ultrasonic field and absorbs sound energy rapidly, which leads to dramatic expansion and rapid

(a) In low vapor pressure fluid droplet (type A)



(type B)

(b) In Lower concentration of volatile component in bi-component droplet [Stage I and Stage II are similar to (a)]

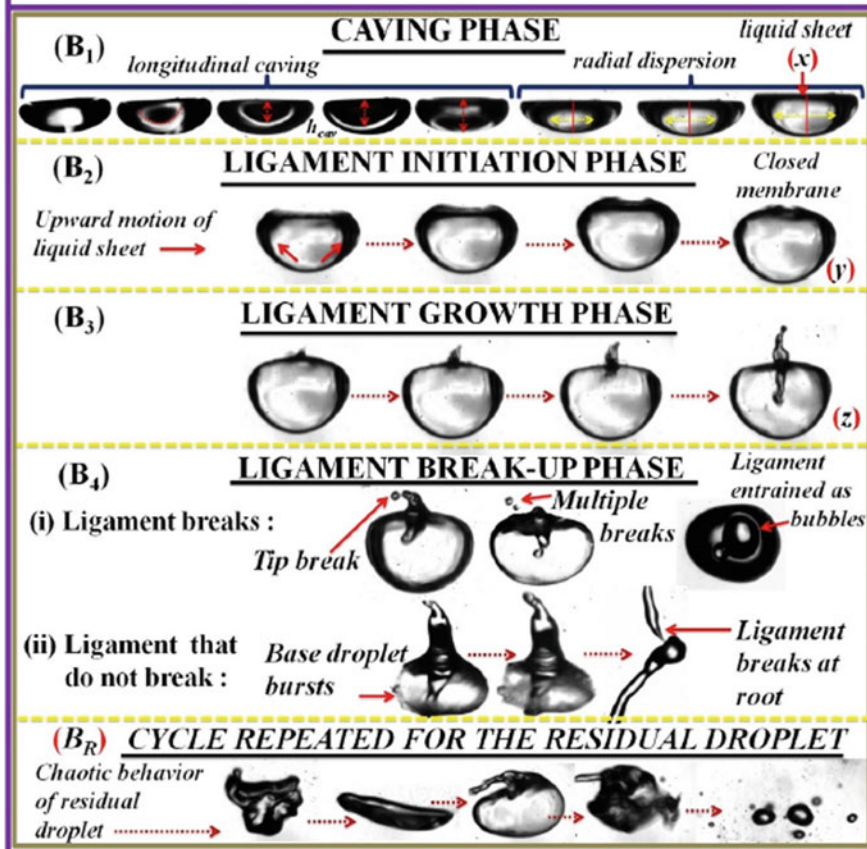


Fig. 5.8 Different instability behaviors of acoustically levitated droplets [40]. **a** In low vapor pressure fluid droplet (type A). **b** In lower concentration of volatile component in bicomponent droplet (Stage I and Stage II are similar to (a)) (type B)

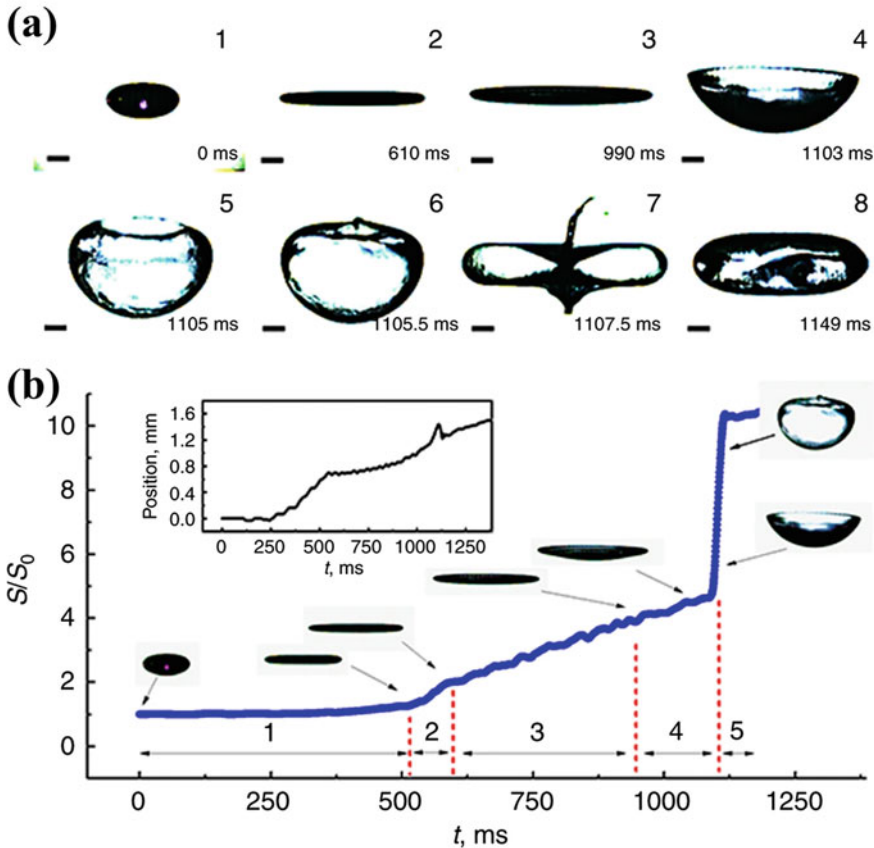


Fig. 5.9 Drop-to-bubble transition of an acoustically levitated droplet upon increasing sound intensity [41]. **a** Snapshot showing the transition. **b** The variation of area during the transition

closure of the cavity. In this case, the sound field not only provides levitation force, but also provides energy to generate new surfaces.

This buckling instability may establish a unique bubble formation method for the use of ultrasound contrast agents or for separation of water and oil. The technique may also be used for fabricating of core-shell like materials via the acoustic resonance mechanism.

5.4.4 Rayleigh–Taylor Instability

Plesset [42] has analyzed the interface evolution of a bubble under different pressure distribution conditions during oscillation, expansion and bursting. The interface

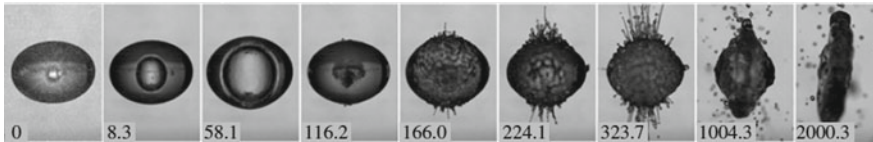


Fig. 5.10 Rayleigh–Taylor instability of bubble rupture under acoustic levitation [43]

becomes unstable upon perturbations if the growth function increases sharply, which established the Rayleigh–Taylor instability theory for a spherical surface. Gonzalez et al. [43] have studied the Rayleigh–Taylor instability dynamics of acoustic levitated droplets during laser-induced cavitation. It has been observed that jets appeared at the north and south poles of the bubble driven by transient pressure release during bubble bursting. Rayleigh–Taylor instability can be evidenced as the jet grows sufficiently long (Fig. 5.10, $t = 166.0$ ms). Zeng et al. [44] have further studied the Rayleigh–Taylor instability mechanism of the cavitation of acoustically levitated droplet. By means of both experiments and numerical calculations (OpenFoam), different instability modes of droplet cavitation have been revealed. The theoretically calculated results are in good agreement with the experimental observations.

5.5 The Manipulation of Droplet

5.5.1 Spatial Movement of Droplets

Acoustically, levitated droplet is usually trapped in one of the potential wells of the levitator. The potential wells can be adjusted by changing the emitter-reflector distance, the energy input (voltage), the phase and amplitude of the emitter. Consequently, the spatial movement of the acoustically levitated droplets can be accomplished. Bjelobrk et al. [45] realized the combination and splitting of potential wells by changing the height of the acoustic field. The levitated droplets move from the edge of the emitter to the center by the combination of potential wells and then transfer to the other side of the emitter through the splitting of potential wells. In this way, the manipulation of levitated droplets can be realized by moving potential wells. Min et al. [46] used three transmitters to form acoustic standing wave field and change the length of the chamber to realize the switching of acoustic field mode. During the process, the levitated droplets levitated in it could be manipulated due to the movement of the potential well. In the process of switching the sound field mode of the chamber, the droplet may first fall for some distance, until reach to a new equilibrium position when the acoustic field becomes stable. The rising height of the droplet can reach to 40 mm. Foresti et al. [47] have successfully transported droplet during levitation via gradually increasing the voltage of two adjacent transducers. Feng et al. [48] had proven that the levitation force can be increased to 3 mN by

adjusting the input voltage. Thomas et al. [49] had moved the levitated sphere by changing the vibration amplitude of the transmitter. In addition, Marzo et al. [50] have successfully driven an object to move or rotate by using 60 arrays of 40 kHz ultrasonic transducers. According to the same principle, the method developed by Thomas or Marzo can be used to manipulate liquid droplets as well.

5.5.2 Opening and Closing of the Particle Layer of Liquid Marbles

Liquid marble is a type of composite droplet which is coated with hydrophobic micro-/nanoparticles at its interface. Because of the non-wetting particle layer, liquid marbles provide a unique physical/chemical micro-environment, which is very suitable for applications as micro-bio/chemical reactors. The opening and closing of the particle layer of liquid marbles, therefore, is of great importance to enable introducing of chemical agents. Zang et al. [51] have realized the opening and closing operation of particle layers by using acoustic levitation. By enhancing the sound intensity in the levitation, the shape of the levitation droplet can be transformed from quasi-spherical to oblate ellipsoid. In this process, the particles are rearranged on the droplet surface. The particles migrate from the pole region to equator region, which leads to the formation of opened windows at the pole regions (Fig. 5.11a). When the sound intensity is decreased, the particles move back to the “bare” area, resulting to the close of the particle shell (Fig. 5.11b).

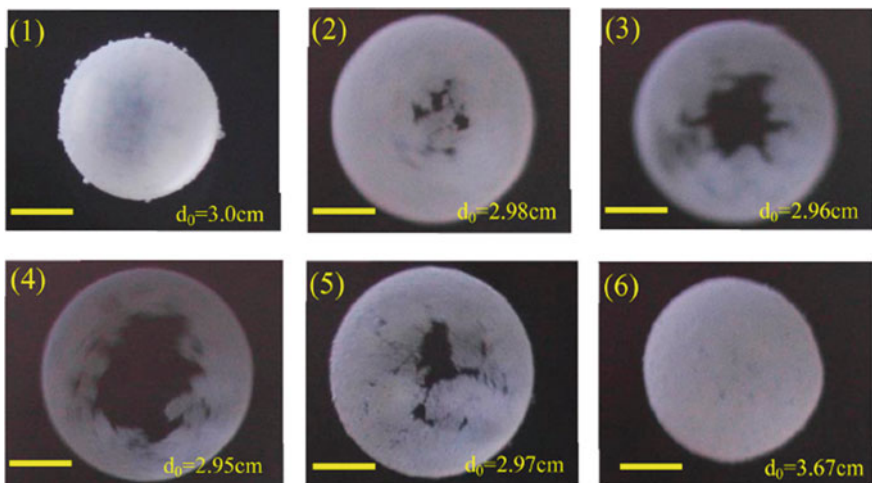


Fig. 5.11 Opening and closing switch of the particle shell of a liquid marble coated with PTFE microparticles [51]. Snapshots (1)–(3) showing the opening of the particle shell caused by increasing sound intensity while (4)–(5) showing its closing driven by reduced sound intensity

One of the advantages of acoustic levitation in controlling the particle layer on droplet surface is that it has no requirement of the electron/magnetic properties of the particles. Therefore, this method provides a reference for the operation of liquid marbles coated with non-ferromagnetic particles.

5.5.3 *Fusion and Coalescence of Droplets*

The coalescence and separation of droplets can be achieved by ejecting a secondary droplet from a micro-channel with a mechanical device to a already levitated drop. The volume of the droplet depends on the size of the nozzle, the shape of the voltage pulse and the physical parameters of the liquid, such as surface tension, viscosity and density. By adjusting the distance between the transducer and the reflector and changing the position of the pressure node in the acoustic field, the droplet levitation can be manipulated. The mixing of two-phase droplet can be achieved through vibration, whereas separation of the droplet can be realized by adjusting the incorporated magnetic field. This coalescence and separation technique can be used to develop biochemical analyzer with higher sensitivity, to enable dynamic measurement by using fluorescent particle labeling.

Micron-sized droplets would be trapped by the sound potential wells when they are injected into the sound field of a single-axis levitator, thus forming a regular droplet array close to the pressure nodes [52]. Nakamura et al. [53] have realized the relative motion of two droplets along a circumferential trajectory by adjusting the intensity of acoustic field, which results in the coalescence of the two droplets into a larger one. Eventually, a larger droplet could be obtained by repeating this operation [54]. If the introduced droplets containing different reactants, the operation could achieve specific chemical reactions. In addition, the chemical reaction [55] can also be achieved by injecting reactants directly into the pressure nodes and fusing them in turn.

Acoustic levitation can also fuse two or more liquid marbles. When two liquid marbles are located into the sound field of the levitator, they move toward each other driven by the acoustic radiation force. A liquid bridge is formed in between the liquid marble. The liquid bridge expands rapidly in a few milliseconds, resulting in the final coalescence [55] (Fig. 5.12). The acoustic radiation force not only provides the levitation force which balances gravity, but also gives the attraction force between liquid marbles which pull the liquid marbles together and make them coalesce. This approach suggests that expected chemical reactions can be triggered with multiple reagents contained in isolated liquid marbles via acoustic levitation, which may represent a novel technique for biological or chemical analysis.

Watanabe et al. [56] have designed a non-contact droplet coalescence and mixing technique via acoustic levitation based on ultrasonic phased array. This technique changes the phase of the transducer to control the position of the sound potential well, consequently, the levitated droplets move gradually toward the center of the potential well and eventually coalesce.

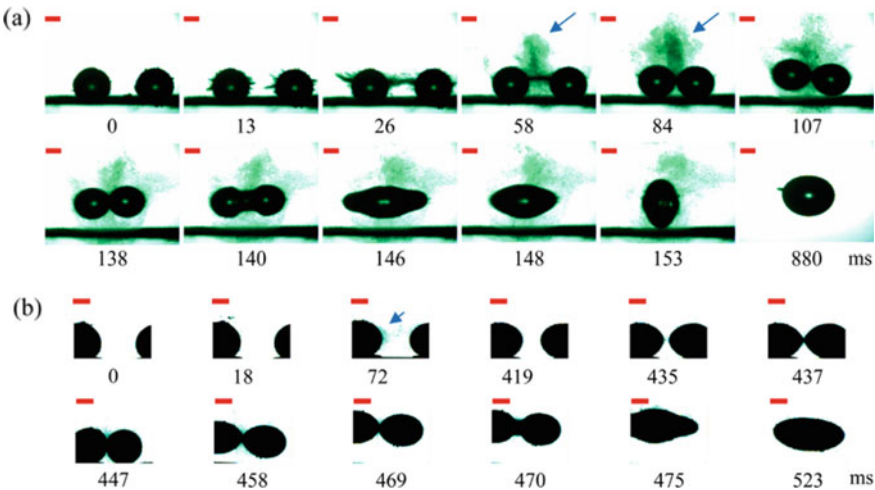


Fig. 5.12 Coalescence process of two liquid marbles ($10 \mu\text{L}$) coated with different particles under acoustic levitation [55], **a** silica nanoparticles, **b** PTFE particles ($5 \mu\text{m}$)

5.6 Concluding Remarks

This chapter has reviewed the dynamics of acoustically levitated drops and discussed the possibility of droplet manipulation by using acoustic levitation technique. The gravity is balanced by the acoustic radiation force exerted on the drop surface, which also stimulus various dynamic behaviors of the drops. This is the underlying reason that acoustic levitation can be utilized to study the liquid rheology based on drop oscillation, capillary waves, atomization, etc. Moreover, the acoustic radiation force not only provides force against gravity, but also competes with surface tension which causes the shape deformation as well as enables the control of opening/closing switch of liquid marbles.

It could be expected that acoustic levitation would have more important applications in the field of drop dynamics study, particular for that of complex liquids. The non-contact character is one of the most advantages of acoustic levitation. The active stimulus of drops via sound field is promising for the study of drop physics and liquid rheology, which could also be utilized for the manipulation of drops.

Acknowledgements We thank the National Natural Science Foundation of China (Nos. U1732129 and 11972303) for financial support. The chapter has been partially published in *Scientia Sinica Physica, Mechanica & Astronomica* (in Chinese).

References

1. L.M. Yahua Liu, X. Xu, Pancake bouncing on superhydrophobic surfaces. *Nat Phys.* **10**(7), 515–519 (2014)
2. D.B.V. Bergeron, J.Y Martin, L Vovelle, Controlling droplet deposition with polymer additives. *Nature.* **405**(772), 6788(2000)
3. D. Zang, X. Geng, Y. Zhang, Y. Chen, Impact dynamics of droplets with silica nanoparticles and polymer additives. *Soft Matter* **9**, 394 (2013)
4. M. Mohr, R.K. Wunderlich, S. Koch et al., *Surface Tension and Viscosity of Cu50Zr50 Measured by the Oscillating Drop Technique on Board the International Space Station*. Microgravity Science and Technology (2019)
5. D. Zang, Y. Yu, Z. Chen, X. Li, H. Wu, X. Geng, Acoustic levitation of liquid drops: Dynamics, manipulation and phase transitions. *Adv. Colloid Interface Sci.* **243**, 77–85 (2017)
6. L. Hu, H.P. Wang, L.H. Li et al., Electrostatic levitation of plant seeds and flower buds. *Chin. Phys. Lett.* **29**(6), 064101 (2012)
7. R. Liu, T. Volkmann, D. Herlach, Undercooling and solidification of Si by electromagnetic levitation. *Acta Mater.* **49**, 439–444 (2001)
8. A. Ashkin, J. Dziedzic, Optical levitation of liquid drops by radiation pressure. *Science* **187**(4181), 1073–1075 (1975)
9. D.L. Geng, W.J. Xie, N. Yan, B. Wei, Vertical vibration and shape oscillation of acoustically levitated water drops. *Appl. Phys. Lett.* **105**(10), 104101–104104 (2014)
10. C. Shen, W. Xie, B. Wei, Digital image processing of sectorial oscillations for acoustically levitated drops and surface tension measurement. *Sci. China Phys. Mech. Astron.* **12**, 131–136 (2010)
11. A.L. Yarin, G. Brenn, O. Kastner, D. Rensink, C. Tropea, Evaporation of acoustically levitated droplets. *J. Fluid Mech.* **23**(4), 471–486 (2002)
12. A. L. Yarin, G. Brenn, D. Rensink, Evaporation of acoustically levitated droplets of binary liquid mixtures. *Int. J. Heat Fluid Flow.* **23**(4), 471–486 (2002)
13. G. Brenn, L.J. Deviprasath, F. Durst, C. Fink, Evaporation of acoustically levitated multi-component liquid droplets. *Int. J. Heat Mass Trans.* **50**(25–26), 5073–5086 (2007)
14. C.P. Lee, A.V. Anilkumar et al., Static shape and instability of an acoustically levitated liquid drop. *Phys. Fluids A Fluid Dyn.* **3**(11), 2497 (1991)
15. Y.R. Tian, R.G. Holt et al., Deformation and location of an acoustically levitated liquid-drop. *J. Acoust. Soc. Am.* **93**(6), 3096–3104 (1993)
16. A.V. Anilkumar, C.P. Lee et al., Stability of an acoustically levitated and flattened drop—an experimental-study. *Phys. Fluids a-Fluid Dyn.* **5**(11), 2763–2774 (1993)
17. M. Barmatz, N. Jacobi, Equilibrium shapes of acoustically levitated liquid-drops. *IEEE Trans. Sonics Ultrason.* **27**(3), 175 (1980)
18. E.H. Trinh, C.J. Hsu, Equilibrium shapes of acoustically levitated drops. *J. Acoust. Soc. Am.* **79**(5), 1335–1338 (1986)
19. P.L. Marston, Shape oscillation and static deformation of drops and bubbles driven by modulated radiation stresses-theory. *J. Acoust. Soc. Am.* **67**(1), 15–26 (1980)
20. W.T. Shi, R.E. Apfel, Deformation and position of acoustically levitated liquid drops. *J. Acoust. Soc. Am.* **99**(4), 1977–1984 (1996)
21. W.J. Xie, B. Wei, Dynamics of acoustically levitated disk sample. *Phys. Rev. E: Stat., Nonlin., Soft Matter Phys.* **70**(4), 046611 (2004)
22. D. Zang, K. Lin et al., Acoustic levitation of soap bubbles in air: Beyond the half-wavelength limit of sound. *Appl. Phys. Lett.* **110**(12), 121602 (2017)
23. D.Y. Zang, Z.C. Zhai, L. Li, K.J. Lin, X.G. Li, X.G. Geng, Vertical vibration dynamics of acoustically levitated drop containing two immiscible liquids. *Appl. Phys. Lett.* **109**, 101602 (2016)
24. E. Becker, W.J. Hiller et al., Experimental and theoretical investigation of large-amplitude oscillations of liquid droplets. *J. Fluid Mech.* **231**, 189–210 (1991)

25. L. Rayleigh, On the capillary phenomena of jet. *Proc. Royal Soc. London* **29**, 71–97 (1879)
26. C.L. Shen, W.J. Xie et al., Parametrically excited sectorial oscillation of liquid drops floating in ultrasound. *Phys. Rev. E* **81**(4), 046305 (2010)
27. Z. Yan, W. Xie et al., Surface capillary wave and the eighth mode sectorial oscillation of acoustically levitated drop. *Acta Phys. Sin.* **60**(6), 64302–064302 (2011)
28. Z.L. Yan, W.J. Xie et al., The ninth-mode sectorial oscillation of acoustically levitated drops. *Chin. Sci. Bull.* **56**(31), 3284–3288 (2011)
29. C.L. Shen, W.J. Xie et al., Non-axisymmetric oscillation of acoustically levitated water drops at specific frequencies. *Chin. Phys. Lett.* **27**(7), 076801 (2010)
30. C. Shen, W.J. Xie, B. Wei, Parametrically excited sectorial oscillation of liquid drops floating in ultrasound. *Phys. Rev. E* **81**(4), 046305 (2010)
31. X.P. Shao, W.J. Xie, Sectorial oscillation of acoustically levitated viscous drops. *Acta Physica Sinica* **61**(13), 134302 (2012)
32. D. Zang, Z. Chen et al., Sectorial oscillation of acoustically levitated nanoparticle-coated droplet. *Appl. Phys. Lett.* **108**(3), 031603 (2016)
33. C.P. Lee, A.V. Anilkumar et al., Static shape and instability of an acoustically levitated liquid-drop. *Phys. Fluids a-Fluid Dyn.* **3**(11), 2497–2515 (1991)
34. L.C. Yao, X.C. Wu et al., Characterization of atomization and breakup of acoustically levitated drops with digital holography. *Appl. Opt.* **54**(1), A23–A31 (2015)
35. M. Kawakami, Y. Abe et al., Effect of laser heating on nonlinear surface deformation of acoustically levitated droplet. *Microgravity Sci. Technol.* **22**(3), 353–359 (2010)
36. B. Pathak, S. Basu, Phenomenology of break-up modes in contact free externally heated nanoparticle laden fuel droplets. *Phys. Fluids* **28**(12), 123302 (2016)
37. S. Basu, A. Saha et al., Thermally induced secondary atomization of droplet in an acoustic field. *Appl. Phys. Lett.* **100**(5), 054101 (2012)
38. S.D. Danilov, Breakup of a droplet in a high-intensity sound field. *J. Acoust. Soc. Am.* **92**(5), 2747 (1992)
39. A. Yarin, G. Brenn et al., Evaporation of acoustically levitated droplets. *J. Fluid Mech.* **399**, 151–204 (1999)
40. B. Pathak, S. Basu, Deformation pathways and breakup modes in acoustically levitated bicomponent droplets under external heating. *Phys. Rev. E* **93**(3), 033103 (2016)
41. D. Zang, L. Li, W. Di et al., Inducing drop to bubble transformation via resonance in ultrasound. *Nat. Commun.* **9**, 3546 (2018)
42. S.M. Plesset, On the stability of fluid flows with spherical symmetry. *J. Appl. Phys.* **25**(1), 96 (1954)
43. G.A.S. Roberto, C.-D. Ohl, Fragmentation of acoustically levitating droplets by laser-induced cavitation bubbles. *J. Fluid Mech.* **805**, 551–576 (2016)
44. Q. Zeng, S.R. Gonzalez-Avila, S. Ten Voorde, et al., Jetting of viscous droplets from cavitation-induced Rayleigh–Taylor instability. *J. Fluid Mech.* (2018)
45. N. Bjelobrk, M. Nabavi, D. Poulikakos, Acoustic levitator for contactless motion and merging of large droplets in air. *J. Appl. Phys.* **112**(5), 053510 (2012)
46. S.L. Min, R.G. Holt et al., Simulation of drop dynamics in an acoustic positioning chamber. *J. Acoust. Soc. Am.* **91**(6), 3157–3165 (1992)
47. D. Foresti, N. Majid et al., Acoustophoretic contactless transport and handling of matter in air. *Proc Natl Acad Sci U S A* **110**(31), 12549–12554 (2013)
48. K. Feng, Y. Liu, M. Cheng, Numerical analysis of the transportation characteristics of a self-running sliding stage based on near-field acoustic levitation. *J. Acoust. Soc. Am.* **138**(6), 3723–3732 (2015)
49. P.L. Thomas Gilles, A.B.M. Andrade, et al., Acoustic levitation transportation of small objects using a ring-type vibrator, in *Proceedings of the 2015 ICU International Congress on Ultrasonics*, 2015, pp. 59–62, ed. by N.F. Declercq
50. M. Asier, S.A. Seah, et al., Holographic acoustic elements for manipulation of levitated objects *Nature Communications*, **6** (2015)

51. D. Zang, J. Li et al., Switchable opening and closing of a liquid marble via ultrasonic levitation. *Langmuir* **31**(42), 11502–11507 (2015)
52. E.T. Chainani, W.H. Choi et al., Mixing in colliding, ultrasonically levitated drops. *Anal. Chem.* **86**(4), 2229–2237 (2014)
53. R. Nakamura, Y. Mizuno, et al., Demonstration of noncontact ultrasonic mixing of droplet. *Japanese J. Appl. Phys.* **52**(7), 07HE02 (2013)
54. Z.N. Pierre, C.R. Field et al., Sample handling and chemical kinetics in an acoustically levitated drop microreactor. *Anal. Chem.* **81**(20), 8496–8502 (2009)
55. Z. Chen, D. Zang et al., Liquid marble coalescence and triggered microreaction driven by acoustic levitation. *Langmuir* **33**(25), 6232–6239 (2017)
56. A. Watanabe, K. Hasegawa, et al., Contactless fluid manipulation in air: Sroplet coalescence and active mixing by acoustic levitation. *8*(1), 10221 (2018)

Chapter 6

Flow Fields and Heat Transfer Associated with an Acoustically Levitated Droplet



Koji Hasegawa

Considering the potential applications, a better understanding of the flow fields in an acoustically levitated droplet is of great significance in scientific fields. The flow generated by a nonlinear acoustic field is known as acoustic streaming. Using acoustic levitation, multi-scale acoustic streaming can be induced both inside and outside the droplet. In the internal flow field, the streaming configuration is affected by the physical properties of the droplet, i.e., the droplet diameter and rotation. The external flow field can be characterized by the applied sound pressure, physical properties of the droplet, and surrounding gas. These flow fields play an important role in the heat and mass transfer of the levitated droplet. This chapter provides a comprehensive review of the flow fields, the general theory of acoustic streaming, and an understanding of the heat transfer/mixing enhancement.

6.1 Literature Review

Acoustic streaming is typically caused by acoustic waves [1] and can be classified into two types. The first is caused by spatial attenuation, which arises due to compressibility. The second is caused due to the strong nonlinear behavior at interfaces and can occur even if the fluid is considered to be incompressible. For example, a vibrating sphere in an otherwise quiescent liquid [2]. Using the undercooling process in the analysis of the effect of acoustic streaming on molten liquid materials, Chung and Trinh [3] reported that acoustic streaming possibly affects an obstacle in space by changing the internal motion of a droplet. In an experimental investigation of the external streaming flow around an acoustically levitated droplet, Trinh and Robey [4] analyzed the external flow and demonstrated that toroidal vortices existed around the droplet. Using a numerical simulation, Rednikov et al. [5–7] provided

K. Hasegawa (✉)

Department of Mechanical Engineering, Kogakuin University, Tokyo, Japan

e-mail: kojihasegawa1118@gmail.com

an explanation of the flow phenomena observed by Trinh and Robey [4]. Rednikov and Riley [5] revealed the existence of multi-scale acoustic streaming, using mathematical and numerical models. To understand the mechanism of the external flow and its influence on the internal circulation of an acoustically levitated droplet, a three-dimensional observation of the internal flow is required. Zhao et al. [8, 9] numerically investigated the relation between the internal and external flows driven by the recirculation in the Stokes layer, which is required to explain the flow fields inside and outside the droplet. Yarin et al. [10] theoretically studied the formulation of the streaming flow around an acoustically levitated droplet and suggested that the internal circulation may be generated by the gas flow near the droplet surface. The characteristics of the flow fields, in the absence and presence of the sample in a levitator, were described. Based on their previous work [10], Yarin et al. [11] further developed the theoretical model of the evaporation of an acoustically levitated binary droplet. Recently, Hasegawa et al. experimentally visualized the flow fields around an acoustically levitated droplet by using particle image velocimetry (PIV) and revealed that the configurations of the internal and external flows are influenced by the properties and phase-change of the levitated droplet [12–15]. As mentioned above, many investigations have been conducted over the past thirty years to exploit the potential of acoustic levitation [16–25]. Even though many analytical techniques for investigating the flow fields around a droplet have been developed, multi-scale acoustic flow fields have not been completely understood experimentally. To achieve perfect sample manipulation, using acoustic levitation, a better understanding of the underlying physical mechanism of acoustic streaming on a levitated droplet is of great significance. This chapter aims to provide a fundamental understanding and practical knowledge of the flow fields associated with an acoustically levitated droplet.

6.2 Principles of Acoustic Streaming

Generally, acoustic streaming is regarded as the flow generated by the force arising from the time-averaged acoustic momentum flux in a fluid. The first theoretical model to thoroughly describe acoustic streaming flows was derived by Rayleigh in the nineteenth century [26]. Since Rayleigh's pioneering work, there have been a large number of published studies on acoustic streaming, with analytical, numerical, and experimental investigations. More recently, acoustic streaming has presented a wide range of biotechnological and microfluidic applications.

6.2.1 General Theory

Attenuation of sound wave causes the pressure and velocity amplitudes, in the propagation direction of the sound wave, to decrease. On time average, this causes a net force with nonlinear effects in space and induces the net flow. Another mechanism

arises from the friction between the fluid medium and a solid wall when the former is vibrating in contact with the latter, for example, a wave traveling down a waveguide, a standing wave in a resonant chamber, or a wave scattering on an object interface. Unlike the spatial attenuation mentioned earlier, this effect is largely confined to a thin viscous boundary layer (known as the shear-wave layer or the Stokes layer) of thickness $\delta \sim (\nu/\omega)^{1/2}$. Here, ν is the kinematic viscosity, and ω is the angular frequency. This layer also represents a significant dissipation mechanism and provides a strong force to drive acoustic streaming. While the medium outside the layer vibrates irrotationally similar to that in a sound field, the medium within the layer is forced to vibrate rotationally (i.e., with vorticity) because its motion has to conform to the no-slip condition on the wall. Most of the discussion in this chapter relates to this secondary streaming.

Figure 6.1 presents an unsteady oscillatory flow and steady streaming [27]. In the experiment, these multi-scale flows overlap and interact with each other. The flow around an oscillating cylinder is clearly illustrated in Ref. [28]. Here, one can see recirculating zones near the cylinder walls, as well as the outer streaming (corresponding “outer steady streaming” in Fig. 6.1).

Mathematically, acoustic streaming can be explained by the existence of the non-linear terms of the steady, non-zero component. For example, the displacement x and velocity u of the sound wave can be obtained from

$$x = x_0 - \frac{u_0}{\omega} \cos \left[\omega \left(t - \frac{x_0}{c_0} \right) \right], \quad (6.1)$$

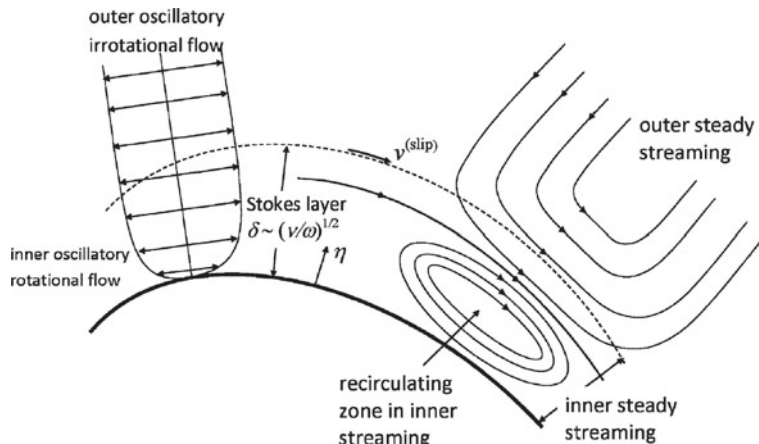


Fig. 6.1 A schematic of the various flow characterizations. The region between the solid line (solid boundary) and dotted line is the Stokes layer, which is the inner region with nonzero vorticity for the leading-order unsteady flow. The inner region contains a steady recirculating zone [27]. This figure reproduced with permission of the right holder, Royal Society of Chemistry

$$u = u_0 \sin \left[\omega \left(t - \frac{x}{c_0} \right) \right], \quad (6.2)$$

where, x_0 is the initial displacement, u_0 is the velocity amplitude, t is the time, and c_0 is the speed of sound. By applying the second-order Taylor series expansion around x_0 of Eq. (6.2) with Eq. (6.1), we obtain

$$\begin{aligned} u &= u_0 \sin \left[\omega \left(t - \frac{x_0}{c_0} \right) \right] - (x - x_0) u_0 \frac{\omega}{c_0} \cos \left[\omega \left(t - \frac{x_0}{c_0} \right) \right] \\ &= u_0 \sin \left[\omega \left(t - \frac{x_0}{c_0} \right) \right] + \frac{u_0^2}{c_0} \cos^2 \left[\omega \left(t - \frac{x_0}{c_0} \right) \right]. \end{aligned} \quad (6.3)$$

Based on this result, the velocity takes on non-zero values on time-average from the second term on the right-hand side. Although the leading-order solution is oscillatory, higher order terms include not only higher harmonics but also steady contributions to the velocity. The existence of this steady streaming was first pointed out by Rayleigh in his work on Kundt's tube [26], and this phenomenon in a boundary layer was further studied by Schlichting [29]. A more detailed mathematical framework can be found in [27, 30, 31].

6.2.2 Multi-scale Acoustic Streaming

It is known widely that an acoustic streaming is generated by a nonlinear acoustic wave. Acoustic streaming via acoustic levitation can be classified into three types based on different length scales: (1) Eckart streaming, (2) Schlichting streaming, and (3) Rayleigh streaming [27].

6.2.2.1 Eckart Streaming

Eckart streaming, formerly known as “quartz wind,” is the flow formed by the dissipation of acoustic energy into the bulk of a fluid. As an acoustic wave propagates through a fluid, a proportion of the acoustic energy is absorbed by the fluid at a rate that is typically proportional to the square of its frequency. The amplitude of the acoustic wave is attenuated, which causes the acoustic pressure amplitude to decrease with an increase of the distance from the acoustic source. This loss of acoustic energy results in a steady momentum flux, forming a fluid jet inside the acoustic beam in the direction of acoustic propagation.

Eckart streaming can be generated in both standing and traveling waves; however, it will occur at significantly lower velocities in the former because the steady Reynolds stress generated in opposing directions partially cancels itself out.

6.2.2.2 Schlichting Streaming and Rayleigh Streaming

Boundary layer-driven acoustic streaming is formed by the viscous dissipation of acoustic energy into the boundary layer of a fluid, along any solid boundary that is comparable or greater in length (in the direction of acoustic propagation) than a quarter of the acoustic wavelength. Furthermore, the streaming flow is typically observed in fluid cavities where at least a single dimension, perpendicular to the direction of acoustic propagation, is comparable in size to the acoustic wavelength. The dissipation into the boundary layer is significant in comparison with the bulk dissipation because of the steep velocity gradient that is formed perpendicular to the solid boundary, as the acoustic wave propagates parallel to it.

In the case of a standing wave that is parallel to the surface, viscous dissipation results in a steady momentum flux that is typically oriented from the pressure antinodes to the pressure nodes and close to the solid boundary. Due to the spatially fixed pressure nodes and antinodes, this results in a steady boundary layer vorticity termed as inner boundary layer streaming or “Schlichting streaming.”

Once established, the powerful inner boundary layer streaming flow then generates counter-rotating streaming vortices within the bulk of the fluid. These counter-rotating streaming vortices are termed as outer boundary layer streaming or “Rayleigh streaming.” As well known as Kundt’s tube, clear flow field can be seen that there is typically a vortex–antivortex pair per half wavelength along the direction of acoustic propagation. It should also be noted that when the dimension perpendicular to the boundary becomes larger in comparison with the acoustic wavelength, the Rayleigh streaming vortices become turbulent.

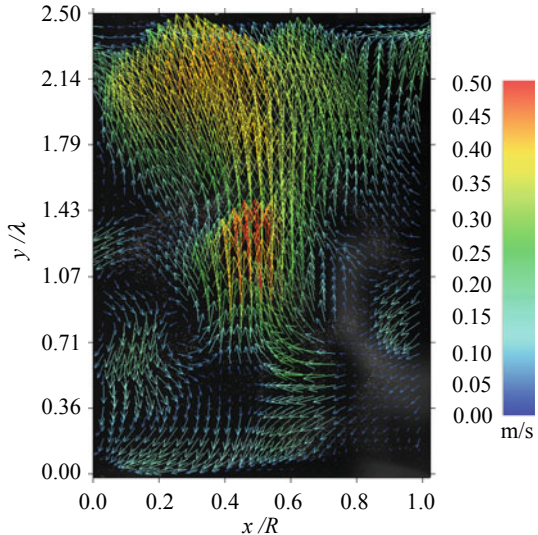
6.3 Flow Field of an Acoustically Levitated Droplet

The internal and external flow fields of an acoustically levitated droplet can be identified by using visualization measurement. The acoustic streaming observed in this study is induced by the theoretically predicted Stokes-layer recirculation. This recirculation drives the internal and external flow fields through the droplet interface. The significance of these results is that this experimental data can contribute to the further development of experimental investigations, numerical models, and theories pertaining to this field.

6.3.1 Flow Field by Acoustic Field

In the absence of a sample fluid, the flow field is strongly influenced by the Sound Pressure Level (SPL) [32]. Nevertheless, an acoustic standing wave is generated between the horns, causing the appearance of a vertically upward flow. It is considered that the nonlinearity of the sound field produces this flow field because of

Fig. 6.2 Average velocity vector fields without a drop at different SPL: **a** SPL = 160 dB, **b** SPL = 161 dB, **c** SPL = 162 dB, **d** SPL = 163 dB, **e** SPL = 164 dB [32]. This figure reproduced with permission of the right holder, Old City Publishing



the spatial attenuation of a wave in the transducer-reflector gap. This nonlinearity of high intensity sound generates harmonics of the inputted sound wave. Thus, time average of this flow field does not cancel out, but instead generates a streaming flow. These sensitive flow fields are important because they are superimposed on the flow structure induced when a drop is levitated.

Figure 6.2 depicts the average velocity vector field, obtained by using PIV, at 162 dB [32]. The record speed and exposure time were 2000 fps and 500 μ s, respectively. The average velocity vector field consists of 3000 instantaneous data. In Fig. 6.2, the x and y axes are normalized by the diameter of the horn R , and wavelength of sound λ , respectively. Here, $R = 36$ mm and $\lambda = 19$ mm. Vertical velocity distributions at different SPL along the central axis of the horn ($x/R = 0.5$) are shown in Fig. 6.3. A vertically upward flow is generated along the central axis at 162 dB. However, this flow field changes at a different SPL. At 160 dB, the vertical velocity rapidly decreases whereas the streaming flow is significantly distorted at 164 dB.

6.3.2 Internal Flow

Figure 6.4 shows the result of 2-dimensional-3-component (2D-3C) PIV measurements estimated by the stereo images of the equatorial plane of the levitated water and glycerol droplets [32]. The record speed and the exposure time were 500 fps and 200 ms, respectively. The average velocity vector field consists of 1500 instantaneous data. The color contour shows the velocity along the z -axis. The axial velocity observed in the levitated water droplet is shown in Fig. 6.4a. However, the same axial velocity v is hardly observed in the levitated glycerol droplet, as shown in Fig. 6.4b.

Fig. 6.3 Vertical velocity distributions at SPL of 160, 162, and 164 dB, along the central axis of the horn [32]. This figure reproduced with permission of the right holder, Old City Publishing

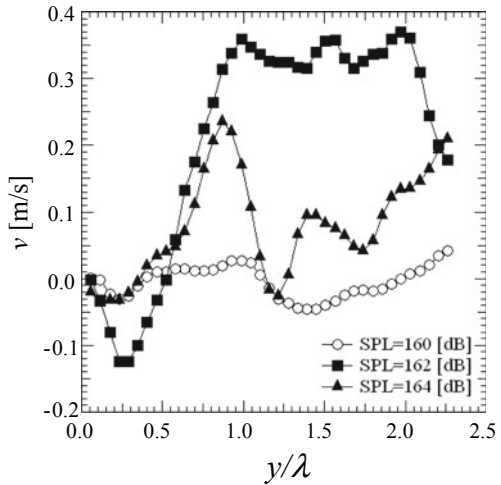
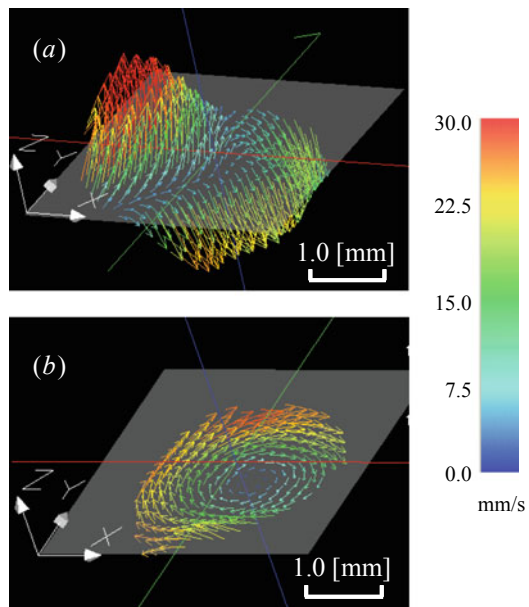


Fig. 6.4 Average velocity vector fields in a droplet. **a** Water droplet ($d = 4.10$ mm, $b/a = 1.50$). **b** Glycerol droplet ($d = 3.80$ mm, $b/a = 1.55$) [32]. This figure reproduced with permission of the right holder, Old City Publishing



As there is insignificant difference in the surface tension and density of the water and glycerol droplets, the difference in the internal flow is due to the difference in the viscosity of the two droplets. These results suggest that the shear stress on the droplet surface, due to the viscosity of the fluid, causes the difference in the internal flows of the water and glycerol droplets.

6.3.3 External Flow

Figure 6.5 shows the average velocity vector fields around a water and glycerol droplet, at 162 dB [32]. Figure 6.5a depicts the water droplet having toroidal vortices below it. In the glycerol droplet, toroidal vortices are visible below and above, as shown in Fig. 6.5b. The record speed and the exposure time were 8000 fps and 125 μ s, respectively. The average velocity vector field consists of 3000 instantaneous data. In Fig. 6.5, the x and y axes are normalized by the major axis of the droplet. The droplets are displaced by approximately 1.0–1.5 mm from the nearest pressure node because of the gravitational force. Counter-rotating vortexes appear around both the droplets. The length scale of each vortex is approximately in the same order as that of the major axis of each droplet.

Figure 6.6 shows the velocity distributions around the water droplet [32]. In Fig. 6.6, the x - and y -axes are normalized by the major axis of the droplet as well. The black oblate represents the droplet. It is confirmed that a jet like flow appears above and below each droplet. The velocity fluctuation exists at $y/b = 1.59$. This fluctuation may lead to an acceleration in the rotation of the droplet. The significance of these

Fig. 6.5 Average velocity vector fields around a water droplet. **a** Water droplet ($d = 4.30$ mm, $b/a = 2.33$) and **b** glycerol droplet ($d = 4.41$ mm, $b/a = 2.32$) [32]. This figure reproduced with permission of the right holder, Old City Publishing

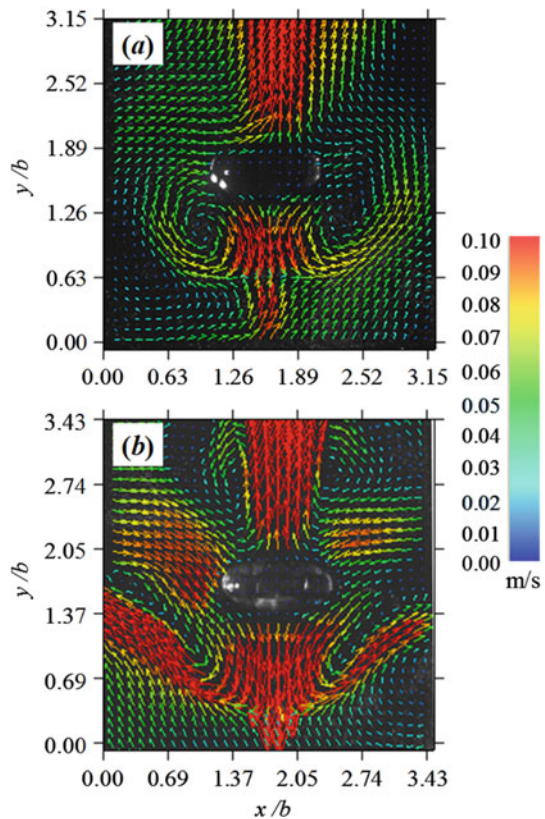
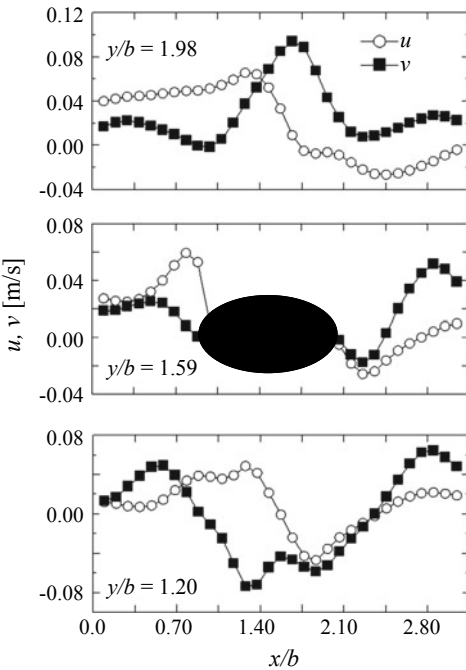


Fig. 6.6 Velocity distributions around a water droplet [32]. This figure reproduced with permission of the right holder, Old City Publishing



results is that the external flow was affected not by the viscosity of the gas, but by the viscosity of the levitated fluid. Besides, despite the vertically upward flow that was observed without a levitated droplet, the circulation direction of the toroidal vortices was away from the droplet. It is interesting to note that the toroidal vortices are located on the upstream side.

6.3.4 Internal and External Flow Fields with Evaporation

Figure 6.7 represents the temporal evolution of the internal and external flow fields of water/ethanol mixtures with an initial ethanol fraction of 50 wt% [15]. Average velocity vector fields of the internal flow are visualized by PIV. The external flow field is obtained by the multiply-exposed trajectory. At $t = 0$ s, internal and external flow fields are the same as those of the ethanol droplet, which exhibits toroidal vortexes in and near the droplet surface. The configuration of the flow fields changes as time progresses, and at the final stage of evaporation ($t = 600$ s), internal and external flow fields are the same as those of the water droplet, which exhibits one circulation in the droplet, and no toroidal vortexes are present in the vicinity of the droplet surface. This result shows that the toroidal vortexes (forced convection) that affect the mass transfer of the levitated droplet appeared near the droplet surface because of the higher concentration of ethanol. The Marangoni effect, which is the mass transfer

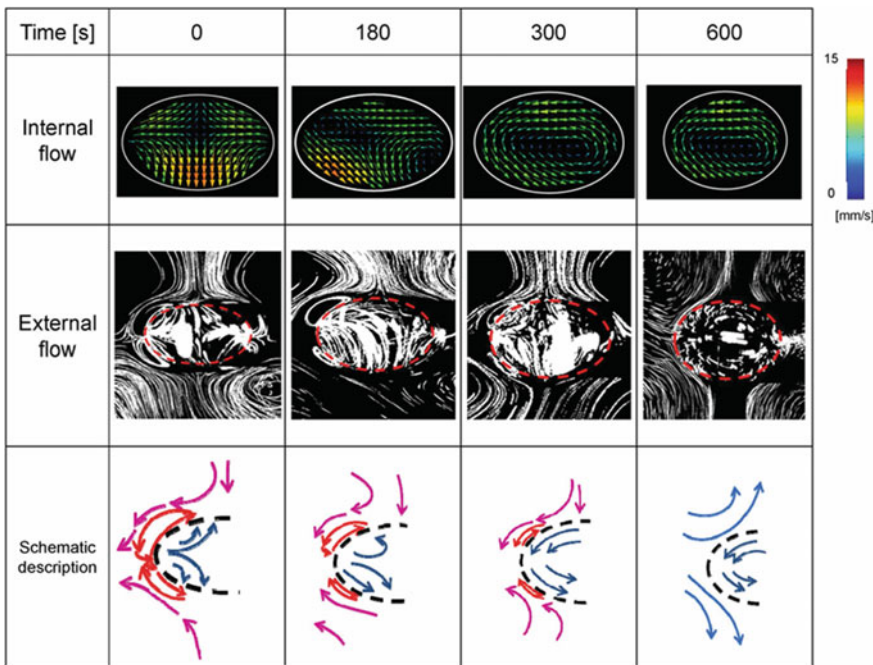


Fig. 6.7 Temporal evolution of the internal and external flow fields of water/ethanol mixtures with an initial ethanol fraction of 50 wt% [15]. This figure reproduced with permission from Koji Hasegawa, Yutaka Abe, and Atsushi Goda, “Microlayered flow structure around an acoustically levitated droplet under a phase-change process,” *npj Microgravity* 2, 16004, 2016. Copyright 2016 Author(s), licensed under CC BY-NC-SA 4.0 (<http://creativecommons.org/licenses/by-nc-sa/4.0/>)

along an interface between two fluids due to surface tension gradient, may be one of the causes of these phenomena.

The acoustic streaming observed in this study is induced by the theoretically predicted Stokes-layer recirculation by Zhao et al. [9]. This recirculation drives internal and external flow fields through the droplet interface. Figure 6.7 indicates that the concentration of ethanol solution also affects the temporal evolution of flow configurations. It is clearly identified the internal and external flow fields of the acoustically levitated droplet of the binary mixture by visualization measurement. These experimental data can contribute to the further development of existing theoretical prediction. The significance of these results is that the acoustic streaming affects the tangential fluid motion on the levitated droplet surface for a higher concentration of volatile droplet, as well as the acoustic streaming was affected by the changes in the concentration of the surrounding fluid due to droplet evaporation.

Although the visualization of a smaller scale boundary layer flow has not been obtained experimentally, future studies will aim for a better understanding of the induced pressure and flow field in the vicinity of the droplet interface and in the Stokes layer via a direct visualization with the help of interferometers and numerical simulations.

6.4 Enhancement of the Heat Transfer in a Levitated Droplet

The nonlinear and dynamic behavior of an acoustically levitated droplet also affects its physical processes such as the heat and mass transfer due to the existence of acoustic streaming around the droplet [33–35]. The toroidal vortices (forced convection) that appear near the droplet interface affect the heat transfer of the levitated droplet. To provide a deeper insight into the flow fields associated with acoustic levitation, further examples are presented from the viewpoint of heat transfer enhancement.

In acoustic levitation, the temperature on the droplet surface and the droplet volume change because the heat of the droplet dissipates mid-air due to droplet evaporation. Figure 6.8 shows a time series change in the surface temperature of the levitated droplet, measured using an IR camera [33]. The horizontal axis represents the time and the vertical axis represents the minimum surface temperature of the levitated droplet. In this experiment, the room temperature and humidity were approximately 28 °C and 53%, respectively. The SPL of water, 50 wt% ethanol solution and ethanol were 162, 161, and 160 dB, respectively. After levitation, the surface temperature decreases in all the fluids. In the case of water, the surface temperature decreased by approximately 7 °C from the room temperature and then it remained constant 50 s after the levitation. In the case of 50 wt% ethanol solution, the surface temperature decreased rapidly by approximately 10 °C. After that, it gradually reached the same temperature as that of the water droplet. In the case of ethanol, the surface temperature decreased rapidly by approximately 12 °C. Then, it gradually increased 150 s from the levitation. The surface temperature of the ethanol droplet was higher than that of the water droplet.

Figure 6.9 presents the time series change in the droplet volume. The levitated droplet is assumed to be a spheroid, and its diameter is defined as the volume equivalent diameter of a sphere [33]. Time is represented on the horizontal axis and the vertical axis represents the volumetric change of the levitated droplet (the cube of the diameter divided by the cube of the initial diameter). The initial diameter of the water,

Fig. 6.8 Time series change of the surface temperature [33]. This figure reproduced with permission of the right holder, Springer Nature

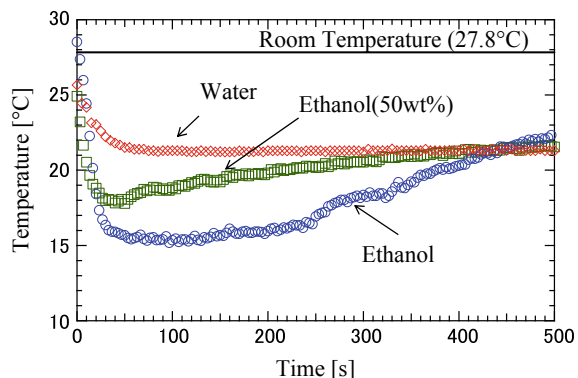
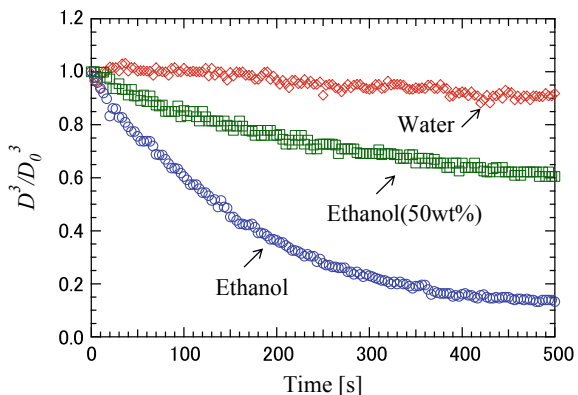


Fig. 6.9 Time series change of the droplet diameter [33]. This figure reproduced with permission of the right holder, Springer Nature



50 wt% ethanol, and ethanol droplet were 3.5, 2.5, and 2.6 mm, respectively. The volume of the water droplet decreased linearly by approximately 10% in 500 s. The volume of the 50 wt% ethanol droplet decreased by approximately 40% in 500 s, and the volume of the ethanol droplet decreased by approximately 90% in 500 s. Here, in the case of the fluids including ethanol droplets, the droplet volume decreased linearly for 100 s after the levitation. Then, the gradient of the volume became smaller and decreased linearly in the same manner as that of the water droplet. The latent and specific heats of the ethanol droplets are lower than those of the water droplet. Additionally, the surface temperature of the 50 wt% ethanol solution increased to the same surface temperature as that of the water. The gradient of the droplet volume reached the same value as that of the water droplet as well. It appears that the 50 wt% ethanol droplet and pure ethanol droplet have similar characteristics as that of the water droplet for the following reasons: (1) the water concentration of the ethanol droplet increased because the water vapor contained in the ambient air condensed on the surface of the ethanol droplet or (2) the water concentration of the ethanol droplet has increased due to the preferential evaporation of the ethanol.

Although the IR camera can measure the surface temperature of the levitated droplet, it is difficult to measure the temperature near the droplet surface. In order to understand the heat transfer of the droplet in more detail, the temperature distribution near the surface of the droplet was measured by using a very thin thermocouple with a tip diameter of 25 μm . Figure 6.10 shows the visualized image of the temperature measurement near the droplet surface and the time series change of the measured temperature [33]. In this experiment, the room temperature and humidity were approximately 27 °C and 50%, respectively. The SPL was set at 161 dB for all droplets. The initial diameter of the water, 50 wt% ethanol and ethanol droplets were 4.0 mm, 2.3 mm, and 1.8 mm, respectively. Visualized images were taken 10 s after the levitation. The distance between the droplet surface and the thermocouple was approximately 0.3 mm. Although the temperature near the surface of the water droplet oscillates soon after starting the measurement, it stabilizes at approximately

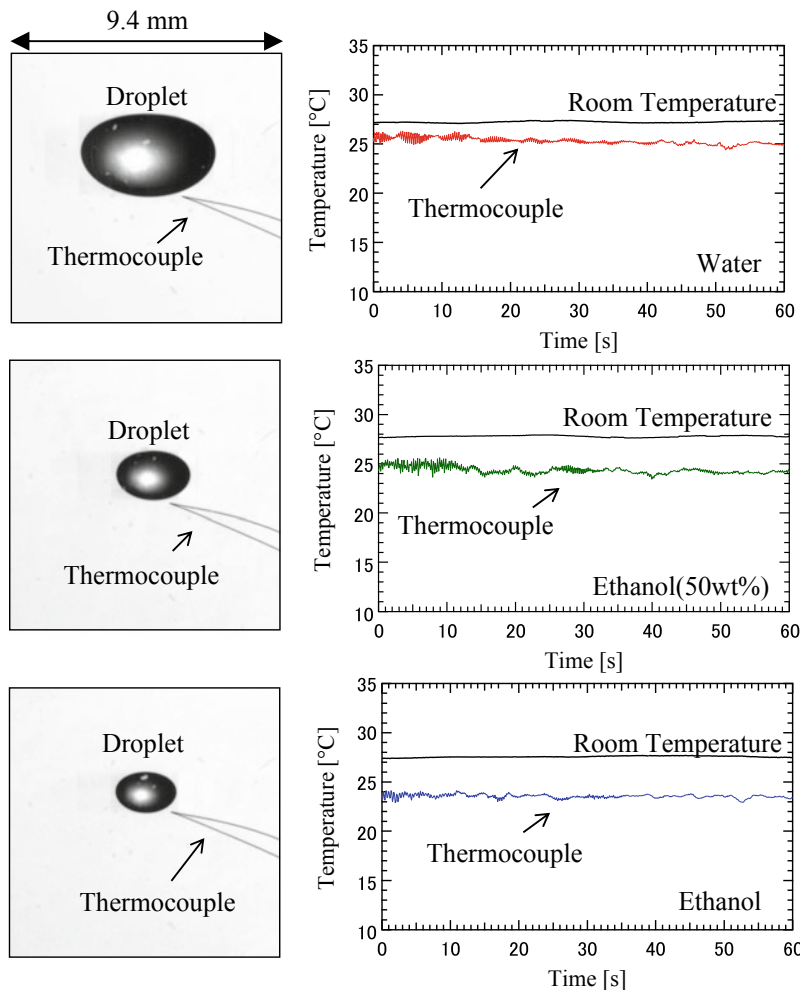
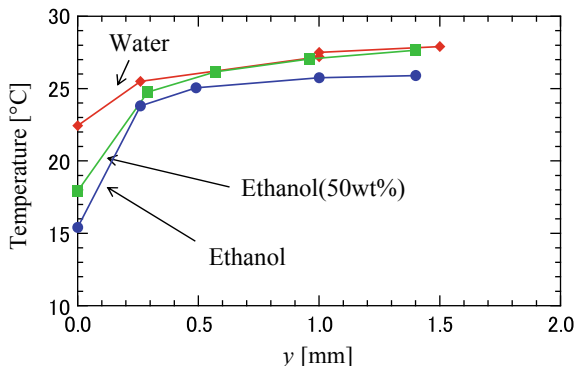


Fig. 6.10 Temperature measurement near the droplet surface [33]. This figure reproduced with permission of the right holder, Springer Nature

3 °C lower than the room temperature, after 60 s. Here, it is considered that the fluctuation of the temperature is because of the oscillation of the levitated droplet that occurred soon after the levitation. Also, in the case of the 50 wt% ethanol droplet, the measured temperature oscillated at the beginning of the temperature measurement. However, it gradually stabilizes at approximately 3.5 °C lower than the room temperature, in the end. In the case of the ethanol droplet, the measured temperature was initially approximately 3 °C lower than the room temperature. Then, after 60 s, it stabilizes at approximately 4 °C lower than the room temperature. Subsequently, in order to investigate the temperature distribution near the droplet surface in more

Fig. 6.11 Temperature distribution near the droplet surface [33]. This figure reproduced with permission of the right holder, Springer Nature



detail, the distance between the thermocouple and the droplet surface was increased, and the temperature distribution around the levitated droplets was measured.

Figure 6.11 shows the relationship between the distance of the thermocouple from the droplet surface and the temperature around the droplet [33]. The horizontal axis represents the distance from the droplet surface. The vertical axis represents the temperature measured by the IR camera and thin thermocouple. In this experiment, the thermocouple was moved 45° obliquely downward from the droplet. The surface temperature of the droplets was measured using the IR camera. Here, all temperatures were measured 10 s after the start of the temperature measurement. In all the liquids, a large temperature gradient was obtained between the droplet surface ($y = 0.0 \text{ mm}$ and $y = 0.3 \text{ mm}$), and the temperature gradually increased as the distance from the droplet surface increased. Based on these results, it can be inferred that the heat transfer was enhanced in an extremely small area near the droplet surface. In the case of the water and 50 wt% ethanol droplet, the temperature of the water droplet was higher at the droplet surface and at $y = 0.3 \text{ mm}$. But the temperatures of both the water droplet and the 50 wt% droplet coincide when $y > 0.6 \text{ mm}$. The measured temperature of the ethanol droplet was lower than the other liquids, across all measurement points. Thus, it is clear that the temperature distribution differed based on the type of the fluid. This is due to the difference in vaporization behaviors, concentration distributions, and flow behaviors of each liquid.

Subsequently, the heat transfer coefficient of the acoustically levitated droplet can be estimated by using the volume decrease and the temperature gradient near the droplet surface. By assuming that the entire heat of the droplet was lost only by evaporation, the amount of heat loss due to evaporation can be expressed by the following equation:

$$Q = L\rho_l \frac{dV}{dt}, \quad (6.4)$$

Here, Q is the heat quantity which lost from the droplet, L is the latent heat of vaporization, ρ_l is the density of the liquid, and dV/dt is the evaporation rate of the droplet volume. In the case of the water droplet, the volume decreased linearly

as shown in Fig. 6.9. In both the 50 wt% ethanol and pure ethanol, the gradient of the volume change decreased during the evaporation, as shown in Fig. 6.9. Thus, the amount of heat was estimated from the gradient that is calculated from the time series change of the droplet volume for 120 s, by linear approximation. Then, the heat transfer coefficient was calculated from the estimated heat quantity by using the equation below:

$$h = \frac{Q}{S(T_\infty - T_l)} = \frac{L\rho_l \frac{dV}{dt}}{S(T_\infty - T_l)}, \quad (6.5)$$

where, h is the heat transfer coefficient, S is the surface area of the droplet, T_∞ is the room temperature, and T_l is the surface temperature of the droplet. In addition, the standard deviation for the linear approximation of the time series change of the droplet volume was considered. Additionally, the heat transfer coefficient was estimated from the temperature gradient near the droplet surface. The temperature gradient was estimated by using the first and second closest temperature data from the droplet surface, as shown in Fig. 6.11. The heat flux was calculated by substituting the estimated temperature gradient into the following equation:

$$q = -k_a \frac{dT}{dy}, \quad (6.6)$$

where, q is the heat flux, k_a is the thermal conductivity of air, and dT/dy is the temperature gradient. Then, the heat transfer coefficient was estimated by using the equation below:

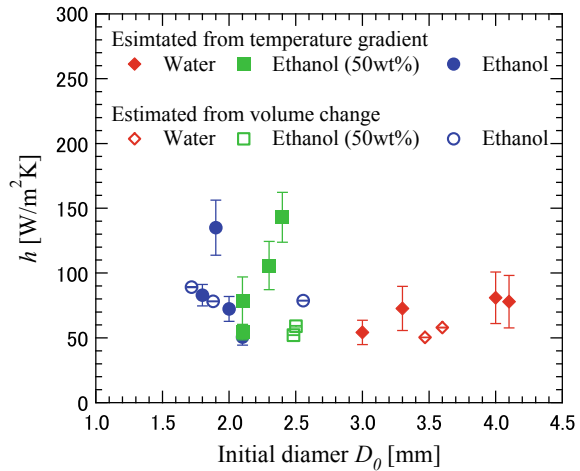
$$h = \frac{q}{(T_\infty - T_l)} = \frac{-k_a \frac{dT}{dy}}{(T_\infty - T_l)} \quad (6.7)$$

Additionally, the average value and standard deviation were calculated by estimating the value of the temperature gradient at 0, 10, 20, 30, and 40 s from the start of the temperature measurement.

Figure 6.12 shows the estimated heat transfer coefficient [33]. The horizontal axis represents the initial diameter, and the vertical axis represents the heat transfer coefficient. Based on this experimental result, the heat transfer coefficient of the levitated droplet was distributed in the range of 40–160 W/m² K. Some of the experimental data estimated from the temperature gradient is larger than other plots. This is considered to be a measurement error arising from the fact that the distance between the droplet surface and the thermocouple was very less. Thus, the estimated heat transfer coefficient seems to be stable in the range between 50 and 100 W/m² K. The estimated heat transfer coefficient can be expressed as the following equation:

$$h \equiv \frac{q}{(T_\infty - T_l)} = \frac{-k_a \frac{\partial T}{\partial y}}{(T_\infty - T_l)} \approx \frac{k_a}{\delta_T}, \quad (6.8)$$

Fig. 6.12 Heat transfer coefficient of the levitated droplet [33]. This figure reproduced with permission of the right holder, Springer Nature

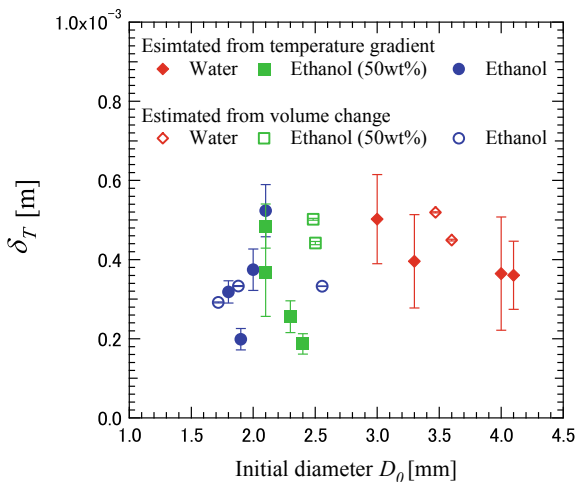


where, δ_T is the thickness of the thermal boundary layer. Thus, the thickness of the thermal boundary layer was estimated by the following equation:

$$\delta_T \approx \frac{k_a}{h}, \quad (6.9)$$

Figure 6.13 shows the estimated thickness of the thermal boundary layer [33]. Based on this result, the estimated thicknesses of the thermal boundary layer were in the range of approximately 200–600 μm . The thicknesses of the thermal boundary layer, estimated from both the temperature gradient and the volume change, were in

Fig. 6.13 Thickness of the thermal boundary layer [33]. This figure reproduced with permission of the right holder, Springer Nature



the same order. Thus, it suggests that the thickness of the thermal boundary layer estimated in this method is appropriate within a certain range.

Finally, the relationship between the external flow and the heat transfer is discussed. Nu number is defined as follows:

$$Nu = \frac{hD_0}{k_a}, \quad (6.10)$$

where, D_0 is the initial diameter and h is the estimated heat transfer coefficient. Figure 6.14 shows the relationship between the Re and Nu numbers. The horizontal axis represents the Re number, and the vertical axis represents the Nu number. The dashed lines represent the existing experimental correlations that are expressed below:

$$Nu = 2 + 0.6Re^{1/2}Pr^{1/3}, \quad (6.12)$$

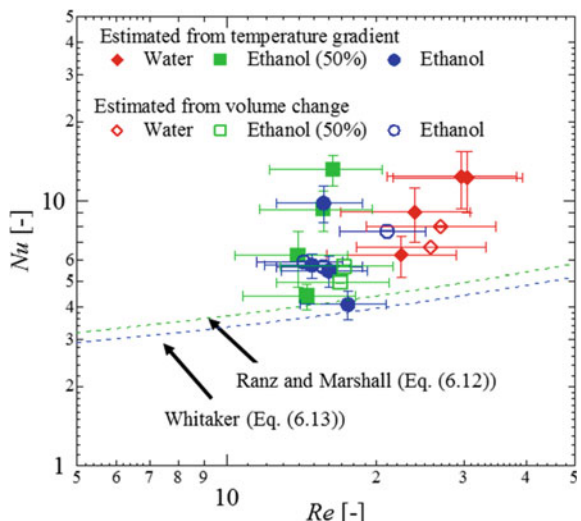
$(0.6 < Pr < 380, 1 < Re < 10^5)$

$$Nu = 2 + (0.4Re^{1/2} + 0.06Re^{2/3})Pr^{0.4}\left(\frac{\mu_a}{\mu_{a,w}}\right)^{1/4} \quad (6.13)$$

$(0.71 < Pr < 380, 3.5 < Re < 7.6 \times 10^4)$

Equation (6.12) is the experimental correlation of the heat transfer of a spherical droplet in a uniform flow field, proposed by Ranz and Marshall [36], and Eq. (6.13) is the experimental correlation of the heat transfer of a single sphere, proposed by Whitaker [37]. From the result, it is confirmed that the heat transfer coefficient of

Fig. 6.14 Heat transfer coefficient considering convection [33]. This figure reproduced with permission of the right holder, Springer Nature



the levitated droplet was greater than the value estimated by existing experimental correlations. One of the possible reasons is that the heat transfer of the acoustically levitated droplet has been enhanced by the complex flow structure around the droplet. Multi-scale acoustic streaming is generated near the droplet surface. These flow configurations were quite different as compared to the heat transfer around the sphere, in the homogeneous flow assumed in the existing theories or empirical correlations. Additionally, dynamic behaviors, such as the oscillation, rotation, and deformation, can promote further heat transfer in the levitated droplet.

$$Re = \frac{\rho_a D_0 U}{\mu_a}, \quad (6.11)$$

where, ρ_a is the density of air, U is the velocity of the external flow, and μ_a is the viscosity of air. The flow velocity was calculated by dividing the time by the moving distance of the tracer particles that pass through the area dozens of micrometers near the droplet surface. The average velocity and standard deviation of the velocity of the external flow were calculated by estimating 10 different particles.

6.5 Application of Flow Field: A Novel Mixing Device

Many lab-on-a-drop applications based on acoustic levitation have been proposed by researchers [16–24]. Herein, a recent application of mid-air, contactless mixing is introduced. Active mid-air mixing techniques can be effective for biomedical applications. Acoustic levitation also provides a contactless mixing technique with interfacial oscillations [38]. Shen et al. [39] reported that the oscillation mode of acoustically levitated droplets was induced by amplitude modulation of ultrasonic waves. The same method is described below. To apply oscillation to the droplets, without contact, the voltage applied to the transducers was modulated by a 0–1 square wave. The modulation frequency can be tuned in increments of 1 Hz. The test fluid was 2 cSt silicone oil. The modes were determined by the number of protrusions and classified into the 4th–7th mode. The oscillation frequency of the droplets coincided within $\pm 1\%$ of half of the modulation frequency. Therefore, it is considered that the oscillation mechanism was a parametric resonance, as described by Shen et al. [39]. To control the oscillation mode, the conditions under which the mode appears were described by the following the Rayleigh equation [38]:

$$f_n = \frac{1}{2\pi} \sqrt{\frac{8\sigma_L}{\rho_L b^2} n(n-1)(n+2)}, \quad (6.14)$$

where σ_L is the surface tension, ρ_L is the density of a droplet, b is the major diameter, and n is the oscillation mode. The Rayleigh equation, assuming a spherical droplet, can be extended to an acoustically levitated droplet by adopting the major diameter

as the diameter. This indicates that an oscillation mode is governed by the Rayleigh equation.

Differences in the mixing behaviors for two cases—the case with a mode and the case without a mode—were investigated with the help of laser-induced fluorescence (LIF). A 50 wt% glycerol aqueous solution was used for the observation of the mixing behavior. As the fluctuations in a viscous droplet after collision can be suppressed as much as possible, it is expected that the observation of the mixing behavior is accurate. The measurement procedure is illustrated in Fig. 6.15a. A droplet containing a fluorescent dye and a droplet without the dye coalesced and were levitated for 5 s to remove the disturbance caused by coalescence. The droplets were irradiated from one side with a Nd:YAG sheet laser, and the fluorescence emission was observed via a high-speed video camera from the bottom. The major diameter after coalescence was adjusted to approximately 3.9 mm. According to the Rayleigh equation, modes are not induced at an oscillation frequency of 500 Hz at this diameter, but the 6th mode is induced at an oscillation frequency of 450 Hz. Therefore, for 10 s after coalescence, the cases with oscillation frequencies of 450 and 500 Hz are compared.

Figure 6.15b shows the observation results pertaining to the mixing behavior. In the case without a mode, the luminance distribution became uniform 60 s after coalescence. In the case of the 6th mode, the luminance becomes uniform within 10 s after the mode appears. The mixed state was evaluated using the mixing parameter η [40]. Based on the LIF results, the average μ and standard deviation σ of the luminance in the N pixels mixed region were calculated. A standard deviation indicates the difference from the fully mixed state. The mixing parameter η is defined by using the normalized standard deviation stated below:

$$\eta = \frac{\left(\frac{\sigma}{\mu}\right)_t - \left(\frac{\sigma}{\mu}\right)_{t=\infty}}{\left(\frac{\sigma}{\mu}\right)_{t=0} - \left(\frac{\sigma}{\mu}\right)_{t=\infty}}. \quad (6.15)$$

The mixing parameter begins from $\eta = 1$ and approaches $\eta = 0$ as the mixing progresses. The measurement result of the time trace of η is shown in Fig. 6.15c. The image obtained when the droplet collided was used for $t = 0$, and the image obtained after 10 min—which confirmed that mixing was completed—was used for $t = \infty$. In the case without an oscillation mode, η converged to zero after approximately 60 s. In the case with the 6th mode, η converged to zero after 15 s, i.e., within 10 s after the mode appeared. These results show that the mixing of the droplets can be promoted without contact, by using an oscillation mode.

A characteristic mixing pattern is shown in Fig. 6.15d. In the case without a mode (shown in Fig. 6.15d-1), the mixing pattern shows a swirling characteristic at the center of the droplet. In the case with an oscillation mode (as shown in Fig. 6.15d-2), a vortex-like pattern is formed at the antinode of the oscillation. For a potential flow [41], the sectorial oscillation generates a flow fields in a droplet, however, enable the liquid to mix in the fluid dynamical system. From our experimental observations, it can be assumed that the effect of the nonlinear flow field contributed to the mixing

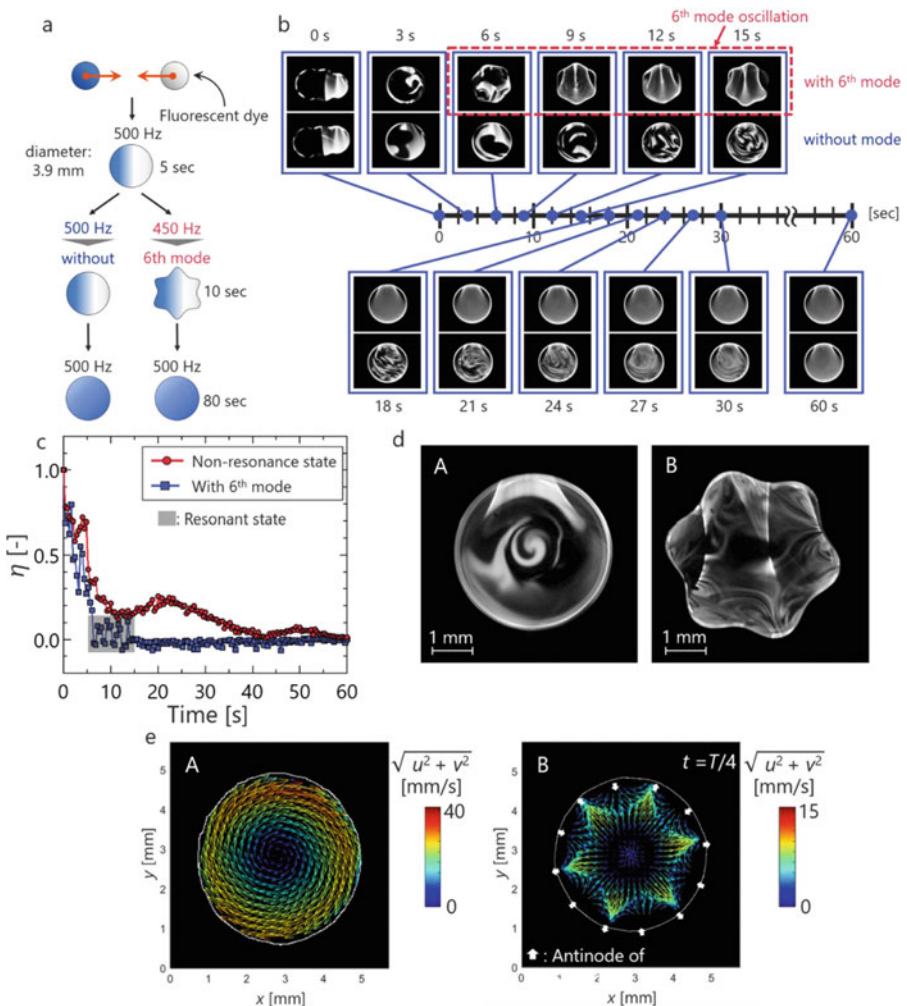


Fig. 6.15 Active mixing by an oscillation mode in an acoustically levitated droplet: **a** experimental procedure for observing mixing behavior. **b** Comparison of the mixing performance between the case without a mode and the case with a mode. **c** Comparison of transition of mixing parameter. **d** Comparison of mixing pattern between (*d*-1) the case without an oscillation mode and (*d*-2) the case with an oscillation mode. **e** Comparison of flow structure between (*e*-1) the case without an oscillation mode and (*e*-2) the case with a 6th-mode oscillation [38]. This figure reproduced with permission from Ayumu Watanabe, Koji Hasegawa, and Yutaka Abe, “Contactless Fluid Manipulation in Air: Droplet Coalescence and Active Mixing by Acoustic Levitation,” Sci. Rep. 8(1), 10221, 2018. Copyright 2018 Author(s), licensed under CC BY 4.0 (<https://creativecommons.org/licenses/by/4.0/>)

behavior in the droplet. To investigate the reason behind the variation in the mixing behavior, the internal flow structures of the droplets were compared using PIV. A 50 wt% glycerol aqueous solution was used as the test fluid. The droplets were irradiated from one side by a Nd:YAG sheet laser, and the fluorescence emission of the particles was observed via a high-speed video camera, from the bottom. Figure 6.15e-1 shows the PIV results for the case without oscillation. A rotational flow occurred around one axis inside the droplet. This is the same flow structure found in acoustically levitated glycerol droplets. Figure 6.15e-2 shows the PIV results for the case with the 6th mode. To clearly observe the flow induced by interface oscillation, the rotational component of the droplet was removed based on the rotational speed measured, by tracking the antinode of the oscillation. The white arrow in Fig. 6.15e-2 indicates the position of the oscillation antinode and movement direction of the interface. Near the oscillation antinode, flow occurs in the direction of the interface displacement. It is clarified that the flow difference, as compared to that in the non-oscillation state, is induced by interface oscillation.

After coalescence, the droplets can be mixed by the oscillation mode. Based on the visualization results pertaining to the mixing behavior, the fluorescent dye inside the droplet was homogenized within 10 s after the oscillation mode appeared and in approximately 60 s in the absence of an oscillation mode. Here, the order of diffusion and convection mixing is compared. The diffusion coefficient is approximately $D \sim 10^{-4} \text{ mm}^2/\text{s}$ [42], and the characteristic distance between the droplets was $l \sim 10^0 \text{ mm}$. Thus, the characteristic time of diffusion was $\sim l^2/D \sim 10^4 \text{ s}$. Consequently, regardless of the oscillation mode, convection is more dominant than diffusion. For the case without an oscillation mode, it is considered that the inertia of coalescence and acoustic streaming inside the droplets promoted the mixing process. In the case with an oscillation mode, the mixing behavior changed drastically due to the oscillation mode. Observational results showed that, when an oscillation mode appeared near the antinode of an oscillating droplet, the interface stretches and folds under the action of a flow [43], and this interfacial oscillation progressed toward the inside of the droplet. It is considered that the formation of vortices via stretching and folding, induced by oscillations, promotes mixing.

References

1. J. Lighthill, Acoustic streaming. *J. Sound Vib.* **61**(3), 391–418 (1978)
2. R. Green, M. Ohlin, M. Wiklund, T. Laurell, A. Lenshof, *Applications of Acoustic Streaming* (Royal Society of Chemistry, London, 2014), pp. 312–336
3. S.K. Chung, E.H. Trinh, Containerless protein crystal growth in rotating levitated drops. *J. Cryst. Growth* **194**(3–4), 384–397 (1998)
4. E.H. Trinh, J.L. Robey, Experimental study of streaming flows associated with ultrasonic levitators. *Phys. Fluids* **6**(11), 3567–3579 (1994)
5. A. Rednikov, N. Riley, A simulation of streaming flows associated with acoustic levitators. *Phys. Fluids* **14**(4), 1502–1510 (2002)

6. A.Y. Rednikov, H. Zhao, S.S. Sadhal, E.H. Trinh, Steady streaming around a spherical drop displaced from the velocity antinode in an acoustic levitation field. *Q. J. Mech. Appl. Math.* **59**(3), 377–397 (2006)
7. A.Y. Rednikov, S.S. Sadhal, Steady streaming from an oblate spheroid due to vibrations along its axis. *J. Fluid Mech.* **499**, 345–380 (2004)
8. H. Zhao, S.S. Sadhal, E.H. Trinh, Singular perturbation analysis of an acoustically levitated sphere: flow about the velocity node. *J. Acoust. Soc. Am.* **106**(2), 589–595 (1999)
9. H. Zhao, S.S. Sadhal, E.H. Trinh, Internal circulation in a drop in an acoustic field. *J. Acoust. Soc. Am.* **106**(6), 3289–3295 (1999)
10. A.L. Yarin, G. Brenn, O. Kastner, D. Rensink, C. Tropea, Evaporation of acoustically levitated droplets. *J. Fluid Mech.* **399**, 151–204 (1999)
11. A.L. Yarin, G. Brenn, D. Rensink, Evaporation of acoustically levitated droplets of binary liquid mixtures. *Int. J. Heat Fluid Flow* **23**(4), 471–486 (2002)
12. K. Hasegawa, Y. Abe, A. Fujiwara, Y. Yamamoto, K. Aoki, External flow of an acoustically levitated droplet. *Microgravity Sci. Technol.* **20**(3–4), 261 (2008)
13. Y. Yamamoto, Y. Abe, A. Fujiwara, K. Hasegawa, K. Aoki, Internal flow of acoustically levitated droplet. *Microgravity Sci. Technol.* **20**(3–4), 277 (2008)
14. K. Hasegawa, Y. Abe, A. Kaneko, Y. Yamamoto, K. Aoki, Visualization measurement of streaming flows associated with a single-acoustic levitator. *Microgravity Sci. Technol.* **21**(1), 9 (2009)
15. K. Hasegawa, Y. Abe, A. Goda, Microlayered flow structure around an acoustically levitated droplet under a phase-change process. *npj Microgravity* **2**, 16004 (2016)
16. S. Santesson, S. Nilsson, Airborne chemistry: acoustic levitation in chemical analysis. *Anal. Bioanal. Chem.* **378**(7), 1704–1709 (2004)
17. V. Vandaele, P. Lambert, A. Delchambre, Non-contact handling in microassembly: acoustical levitation. *Precis. Eng.* **29**(4), 491–505 (2005)
18. F. Priego-Capote, L. de Castro, Ultrasound-assisted levitation: lab-on-a-drop. *TrAC Trends Anal. Chem.* **25**(9), 856–867 (2006)
19. L. Puskar, R. Tuckermann, T. Frosch, J. Popp, V. Ly, D. McNaughton, B.R. Wood, Raman acoustic levitation spectroscopy of red blood cells and Plasmodium falciparum trophozoites. *Lab Chip* **7**(9), 1125–1131 (2007)
20. A. Scheeline, R.L. Behrens, Potential of levitated drops to serve as microreactors for biophysical measurements. *Biophys. Chem.* **165**, 1–2 (2012)
21. D. Foresti, M. Nabavi, M. Klingauf, A. Ferrari, D. Poulikakos, Acoustophoretic contactless transport and handling of matter in air. *Proc. Nat. Acad. Sci.* **110**(31), 12549–12554 (2013)
22. E.T. Chainani, W.H. Choi, K.T. Ngo, A. Scheeline, Mixing in colliding, ultrasonically levitated drops. *Anal. Chem.* **86**(4), 2229–2237 (2014)
23. C. Bouyer, P. Chen, S. Güven, T.T. Demirtas, T.J. Nieland, F. Padilla, U. Demirci, A bio-acoustic levitational (BAL) assembly method for engineering of multilayered, 3D brain-like constructs, using human embryonic stem cell derived neuro-progenitors. *Adv. Mater.* **1**, 161–167 (2016)
24. T. Vasileiou, D. Foresti, A. Bayram, D. Poulikakos, A. Ferrari, Toward contactless biology: Acoustophoretic DNA transfection. *Sci. Rep.* **6**, 20023 (2016)
25. A. Marzo, B.W. Drinkwater, Holographic acoustic tweezers. *Proc. Nat. Acad. Sci.* **116**(1), 84–89 (2019)
26. L. Rayleigh, On the circulation of air observed in Kundt's tubes, and on some allied acoustical problems. *Philos. Trans. R. Soc. Lond.* **175**, 1–21 (1884)
27. S.S. Sadhal, Acoustofluidics 13: analysis of acoustic streaming by perturbation methods. *Lab Chip* **12**(13), 2292–2300 (2012)
28. Tatsumi M (1982) Secondary streaming induced by an oscillating cylinder, in *An Album of Fluid Motion*, vol. 31
29. H. Schlichting, Berechnung ebener periodischer Grenzschichtstromungen. *Phys. z.* **33**, 327–335 (1932)
30. S.S. Sadhal, Acoustofluidics 15: streaming with sound waves interacting with solid particles. *Lab Chip* **12**(15), 2600–2611 (2012)

31. S.S. Sadhal, Acoustofluidics 16: acoustics streaming near liquid–gas interfaces: drops and bubbles. *Lab Chip* **12**(16), 2771–2781 (2012)
32. K. Hasegawa, Y. Abe, A. Kaneko, K. Aoki, PIV measurement of internal and external flow of an acoustically levitated droplet. *Int. J. Transp. Phenom.* **12**(3–4), 151–160 (2011)
33. K. Shitanishi, K. Hasegawa, A. Kaneko, Y. Abe, Study on heat transfer and flow characteristic under phase-change process of an acoustically levitated droplet. *Microgravity Sci. Technol.* **26**(5), 305–312 (2014)
34. A. Gopinath, A.F. Mills, Convective heat transfer from a sphere due to acoustic streaming. *J. Heat Transf.* **115**, 332–341 (1993)
35. Y. Niimura, K. Hasegawa, Evaporation of droplet in mid-air: pure and binary droplets in single-axis acoustic levitator. *PLoS ONE* **14**(2), e0212074 (2019)
36. W.E. Ranz, W.R. Marshall, Evaporation from drops. *Chem. Eng. Prog.* **48**(3), 141–146 (1952)
37. S. Whitaker, Forced convection heat transfer correlations for flow in pipes, past flat plates, single cylinders, single spheres, and for flow in packed beds and tube bundles. *AIChE J.* **18**(2), 361–371 (1972)
38. A. Watanabe, K. Hasegawa, Y. Abe, Contactless fluid manipulation in air: droplet coalescence and active mixing by acoustic levitation. *Sci. Rep.* **8**(1), 10221 (2018)
39. C.L. Shen, W.J. Xie, B. Wei, Parametrically excited sectorial oscillation of liquid drops floating in ultrasound. *Phys. Rev. E* **81**(4), 046305 (2010)
40. B. Carroll, C. Hidrovo, Droplet collision mixing diagnostics using single fluorophore LIF. *Exp. Fluids* **53**(5), 1301–1316 (2012)
41. C.L. Shen, W.J. Xie, Z.L. Yan, B. Wei, Internal flow of acoustically levitated drops undergoing sectorial oscillations. *Phys. Lett. A* **374**(39), 4045–4048 (2010)
42. C.T. Culbertson, S.C. Jacobson, J.M. Ramsey, Diffusion coefficient measurements in microfluidic devices. *Talanta* **56**(2), 365–373 (2002)
43. J.M. Ottino, *The kinematics of mixing: stretching, chaos, and transport* (Cambridge University Press, 1989)

Chapter 7

Droplet Evaporation Under Acoustic Levitation



Yanju Wei

Droplet evaporation is a ubiquitous phenomenon widely existing in nature and spray-based industrial applications, such as liquid fuel power engines, pharmaceutical manufacturing, powder and food processing, and chemical industry. Diffusion and convection-driven evaporation of single- and multi-component droplets of miscible liquids were investigated theoretically and experimentally in a number of previous studies [1–4]. These show that the lifetime of the evaporating droplets basically obeys the well-known d^2 -law [5]. However, some intrinsic errors were also introduced from the previously used experimental methods, such as free flight [6], free fall [7], or pendant suspension on a capillary or filament [8, 9]. Acoustic levitation provides an ideal contactless tool to study the drying process of droplets and particles. A single droplet is held in a node of a standing acoustic wave, avoiding hereby all contact to a thermally conducting holding device. The surrounding drying gas can be conditioned such that its temperature, relative humidity, and flow rate past the droplet could be precisely controlled. This chapter provides an overview of general theory, simulation, and experiments on the evaporation of the acoustically levitated droplets.

7.1 Literature Review

In spite of the fact that heat and mass transfer at the droplet surface in a stagnant gas or a gas flow without an acoustic field has received significant attention for a long time, the acoustic-driven counterparts of these processes are much less understood. Only a few works could be found to study the evaporation of a levitated droplet [10–12].

Y. Wei (✉)

School of Energy and Power Engineering, Xi'an Jiaotong University, 710049 Xi'an, China
e-mail: weiyanju@xjtu.edu.cn

A key element of the heat and mass transfer processes at the surface of levitated droplets is the acoustic streaming, first recognized by Rayleigh [13] in regard to Kundt's dust patterns in a channel. Schlichting [14, 15] considered the problem of an oscillating cylinder in a fluid or gas at rest. He extended the method of successive approximations and successfully explained the experimental findings of Andrade [16]. Another modification of the method of successive approximations was reviewed by Riley [17] who denoted the acoustic streaming of this type as Type (a), to distinguish it from the acoustic streaming due to sound attenuation in the bulk, which he denoted as Type (b) or "quartz wind".

Burdakov and Nakoryakov [18] and Lee and Wang [19, 20] calculated the acoustic streaming near an extremely small rigid sphere positioned in a standing plane sound wave. Burdakov and Nakoryakov [18] also calculated the mass transfer rate at the sphere surface and conducted an experiment to verify their theory. However, they got inconclusive results due to the usage of an erroneous multiplier.

Yarin et al. [21] derived a universal theory on the mass transfer rate at the levitated droplet surface, where the Prandtl and Schmidt numbers, and streaming Reynolds number as well, were of the order one. In their theory, they removed the restrictive assumptions, which were the foundation of Burdakov and Nakoryakov's [18] work and predicted the heat and mass transfer rates at the surface of oblate pure liquid droplets levitated acoustically and displaced below the pressure node. Besides explained the evaporation mechanism of the acoustically levitated droplets, they also validated the theory with experiments. They [22] then expanded their theory to binary liquid mixtures. Their heavyweight work established a big platform for studies on the heat and mass transfer problems of acoustically levitated droplets, where all the followers danced since then till today.

Zaitone [23] further compared the evaporation of pure liquid droplets in an acoustic field versus a glass-filament. They illustrated through numerical simulation the two steady toroidal vortices close to the droplet surface, known as outer acoustic streaming and explained how this "outer acoustic streaming" affects the heat and mass transfer. They found the evaporation of the levitated droplets could compose of four stages with the increase of the ventilation airflow rate divided by the elimination of the outer and inner vortices, and when the airflow was increased to a limit where the inner acoustic streaming is eliminated, the results to those obtained with the glass-filament method agreed well.

Although the inner and outer vortices played an important role in the evaporation of levitated droplets, Brenn [24] precisely predicted the evaporation of levitated drops of water, alcohols, and alkane, and their mixtures, in the condition considering the acoustic streaming field, however, without the inner and outer vortices as Yarin did.

Schiffer [25] found the acoustic field enhanced the evaporation and which gave no clue showing the inhibition of the vortices. Combe [26] also showed, irrespective the vortices, that the evaporation of levitated droplets of water, deuterioxide, and the salts solutions were well predicted by the modified Maxwell equation. And Zaitone [27] even revealed that evaporation of spheroidal droplets followed the well-known d^2 -law without seeing any influence of the aforementioned vortices.

Tuckermann [28] studied the effects of relative humidity on the evaporation rates and surface temperature of acoustically levitated alkane, alkanols drops. They found the water from a humid environment condensed on the drops' surface, and in the case of *n*-pentane, the condensed water froze as a result of the evaporative cooling. Niimura [29] reproduced this phenomenon that the droplets of highly soluble liquids such as ethanol, methanol, and acetone absorb water vapor from the ambient air as they evaporate, and thus leads to a two-stage evaporation.

7.2 Primary Theory

It is well known that for the pure and multi-component droplets in static state, the evaporation follows the d^2 -law, which expresses

$$\left(\frac{d}{d_0}\right)^2 = 1 - K \cdot t \quad (7.1)$$

where $K = \frac{8\rho_g D}{\rho_l} \ln(1 + B) \cdot \rho_g, \rho_l, D$ and B denotes the density of gas and liquid phase, mass, and heat diffusion coefficient, respectively.

When the droplet is acoustically levitated, the velocity field of the acoustic field produces two different types of toroidal vortices, i.e., the outer acoustic streaming and inner acoustic streaming, as clearly illustrated in Fig. 7.1a. However, the situation is a little bit different due to the different medium of the acoustic field; Fig. 7.1b, c show the experimental image [21] and the simulation [30] of the acoustic field in air; the vortices are distorted, and the inner ones are invisible due to the small thickness of boundary layer in air relative to that in water.

The vortices change the flow field surrounding the droplet from two aspects. One is that the convection mode at the surface is switched from natural convection to forced convection, which enhances the evaporation, however, and the vortices may trap the vapor and reduce the concentration gradient around the drop surface and thus inhibit evaporation.

For the former situation, a universal theory [21] to estimate the physics in the evaporation neglects the influence of the vapor accumulation toward the acoustic field, the penetration of sound into droplet, the inside flow, the component differences, and the Stefan flow at the droplet surface. The sound frequency-based Reynolds number

$$\text{Re} = \frac{\omega R_0^2}{\mu_0} \quad (7.2)$$

is assumed to be much larger than unity ($\text{Re} \gg 1$). Here, ω is the angular frequency of the incident sound wave, R_0 is an unperturbed volume-equivalent droplet radius, and μ_0 is the unperturbed kinematic viscosity of the gas surrounding the droplet.

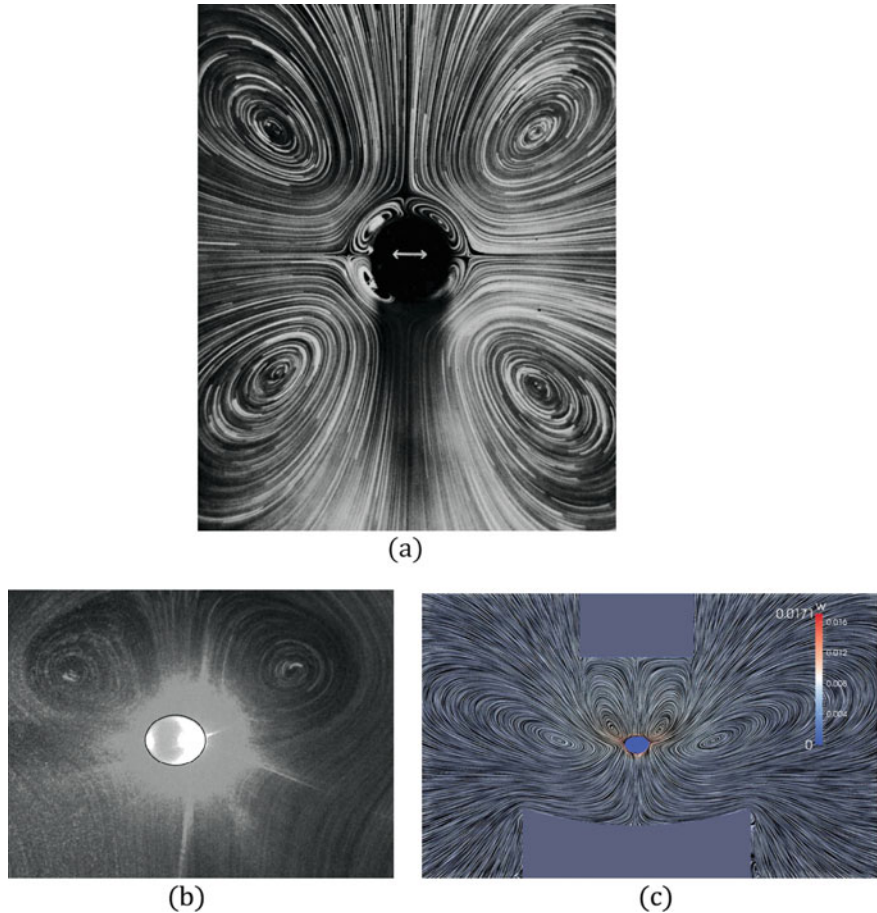


Fig. 7.1 **a** Secondary streaming induced by an oscillating cylinder in a water–glycerol mixture. The streamlines are directed toward the cylinder, along the axis of oscillation indicated by the arrows [27]; **b** visualization of the acoustic streaming induced by water droplet at ambient temperature of 24 °C; an air mixed with seeding particles is illuminated by laser sheet, droplet volume 2 μl. Transducer is located above the droplet [21, Fig. 3a]; and **c** mass fraction w superimposed by a visualization of the streaming around the droplet [30, Fig. 10b]

The gas particle velocity amplitude is introduced as

$$B = \frac{A_{0e}}{\rho_0 c_0} \quad (7.3)$$

where A_{0e} is the effective pressure amplitude of the incident acoustic field, ρ_0 is the unperturbed gas density, and c_0 is the sound velocity. The value of the pressure amplitude corresponding to the sound pressure level (SPL) of 160 dB is about A_{0e}

$= 2 \times 10^4$ dyne cm $^{-2}$. With $R_0 \sim 10^{-1}$ cm and sound frequency $f = 56$ kHz, B is estimated to be approximately 352 cm/s.

For the acoustic streaming flow, the characteristic scale of acoustic streaming velocity B_s is

$$B_s = \frac{B^2}{\omega R_0} \sim 10^{-2} \quad (7.4)$$

And the streaming Reynolds number Re_s is defined as

$$\text{Re}_s = \frac{B_s R_0}{\mu_0} = \frac{B^2}{\omega \mu_0} \quad (7.5)$$

For $R_0 \sim 10^{-1}$ cm and $\mu_0 \sim 0.15$ cm 2 /s, $\text{Re}_s \approx 2.35$.

Since the acoustic streaming velocity varies along the droplet surface, the average Sherwood number over the spherical surface, which indicates the ratio of the convective to diffusive mass transport, is expressed as

$$\overline{\text{Sh}} = \frac{B}{\sqrt{\omega D_0}} \quad (7.6)$$

where D_0 is the unperturbed value of mass diffusion coefficient.

Based on the calculations of the compressible acoustic boundary layer, acoustic streaming, and mass transfer in the gas near the droplet surface, the evaporation d^2 -law could be upgraded as

$$\left(\frac{d}{d_0} \right)^2 = 1 - K_* \cdot t \quad (7.7)$$

where

$$K_* = \left(\frac{45}{4\pi} \right)^{1/2} B \left(\frac{D_0}{\omega} \right)^{1/2} \frac{(c_{sb} - c_{s\infty})}{\rho_l} \quad (7.8)$$

And c_{sb} and $c_{s\infty}$ denote the vapor concentration at the surface and ambient air, and ρ_l is the liquid density.

The lifetime of a droplet is given by

$$t_l = \frac{\rho_l (4\pi\omega)^{1/2}}{B (45D_0)^{1/2} (c_{sb} - c_{s\infty})} \quad (7.9)$$

Figure 7.2 shows the measured evaporation behavior of droplets of the seven liquids investigated with an initial volume of 3 μl . The normalized drop surface of measured data coincides well with the two curves computed using the present theory with the constant and variable SPL value, respectively. The good agreement between

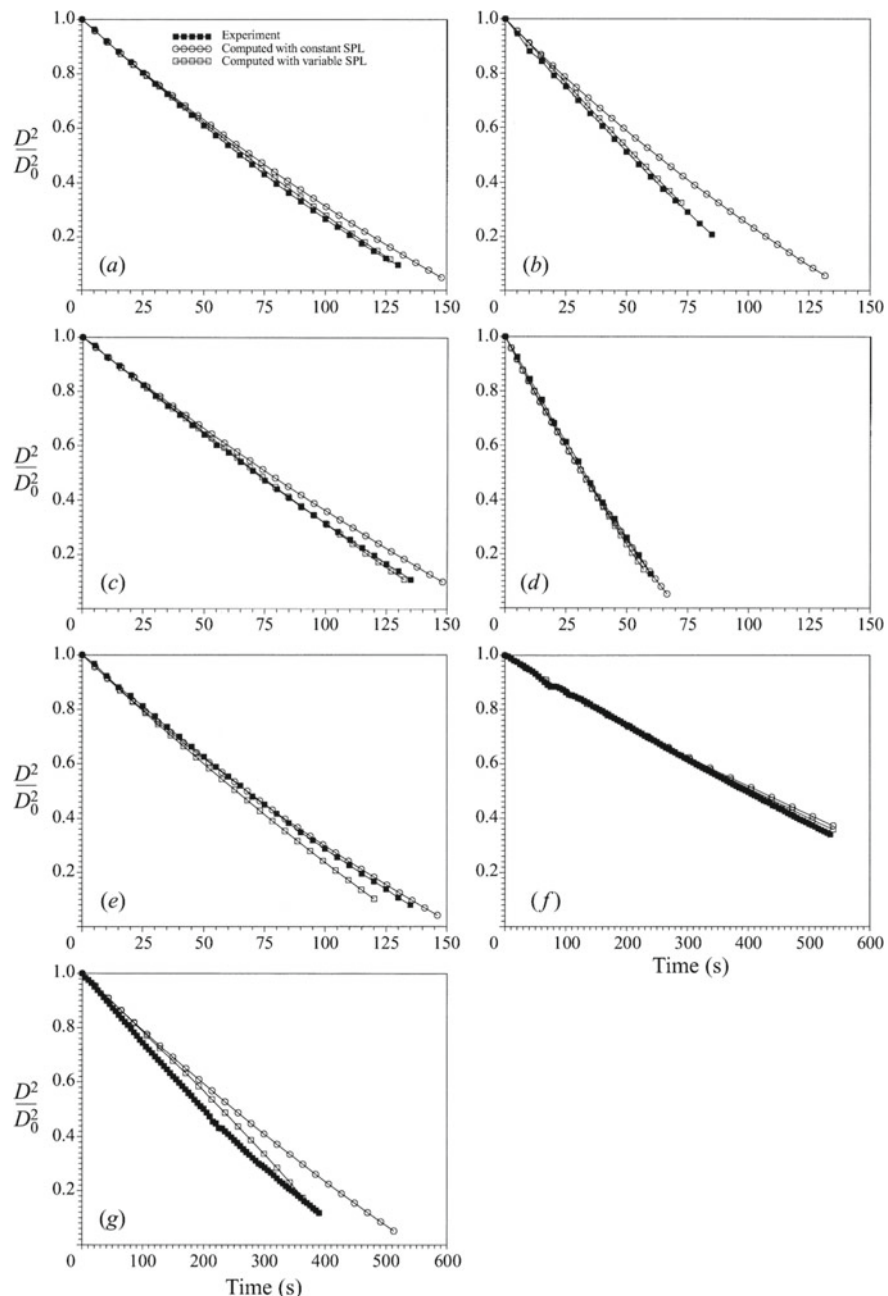


Fig. 7.2 Temporal evolution of the normalized drop surface for **a** methanol, **b** ethanol, **c** propanol-2, **d** n-heptane, **e** n-octane, **f** n-decane and **g** water droplets with an initial volume of 3 μl and initial SPL of 162.591, 162.531, 161.747, 161.872, 161.872, 162.184 and 165.875 dBe, respectively. The vapor concentration in the toroidal vortices is kept constant (close to zero for water, and zero for the other liquids) by ventilation. Blowing rate 1.4 ln/min. [21, Fig. 8] <https://doi.org/10.1017/S0022112099006266>

these latter curves and the measured data is clearly visible, indicating the correct representation of the evaporation process by the present theory.

Yarin et al. [21] also studied and discussed the effect of an additional blowing (a gas jet impinging on a droplet) on the evaporation rate, as well as the enrichment of gas at the outer boundary of the acoustic boundary layer by liquid vapor. Results showed that, even at relatively high rates of blowing, the droplet evaporation was still governed by the acoustic streaming in the relatively strong acoustic fields. This makes it impossible to study forced convective heat and mass transfer under the present conditions using droplets levitated in strong acoustic fields.

7.3 Influence of Acoustic Streaming

Zaitone et al. [23] further validated Yarin's theory by measuring the effects of ventilation airflow on the evaporation of an acoustically levitated water droplet. As the flow rate of ventilation air increases, different evaporation rates result. In order to set an appropriate airflow rate to remove the vortices of the outer acoustic streaming, airflow rates were set from 0 to 2.8 l/min; for larger airflow rates, the radial position of the droplet is no longer stable and the droplet may jump out of the node. For all of these measurements, the evaporation rate is determined and the dependence of this rate on the ventilation flow rate is assessed, as shown in Fig. 7.3. Different ranges can be distinguished in the curve:

- I. less than 0.4 l/min: almost no variation of the evaporation rate can be seen.
- II. 0.4–1.0 l/min: the evaporation rate increased significantly.
- III. 1.0–2.0 l/min: nearly no effect of blowing can be observed.
- IV. Greater than 2.0 l/min: the evaporation rate starts to increase again with the airflow rate.

In range I, the vapor coming from the droplet surface is trapped by the vortices of the outer acoustic streaming; the surface is thus isolated from the ventilating airflow till the outer vortices are removed by the increasing ventilation airflow in range II. In range III and IV, the evaporation repeats that of the range I and II; however, it is the

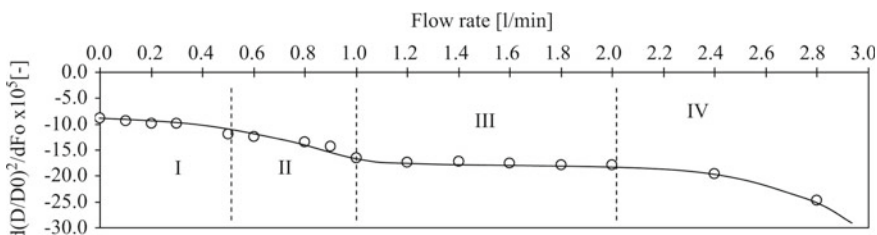


Fig. 7.3 Dimensionless evaporation rate versus airflow rate (water droplet of 1 μl initial volume), $\text{Fo}(\text{Fourier No.}) = D_0 \cdot t / D_0^2$. [23] <https://doi.org/10.1016/j.ces.2011.05.011>

inner acoustic vortices those play the leading role. The ventilation-driven convection begins to play the dominant role in mass transfer after the inner acoustic vortices are removed. The in situ airflow velocity, being an important parameter dividing the four stages, is unfortunately not given here.

Since the acoustic streaming converts the natural convective evaporation to forced one, the standing acoustic waves thus promote the evaporation, as shown in Fig. 7.4a–d. As the air blowing rate is increased up to 2.4 l/min (which corresponds

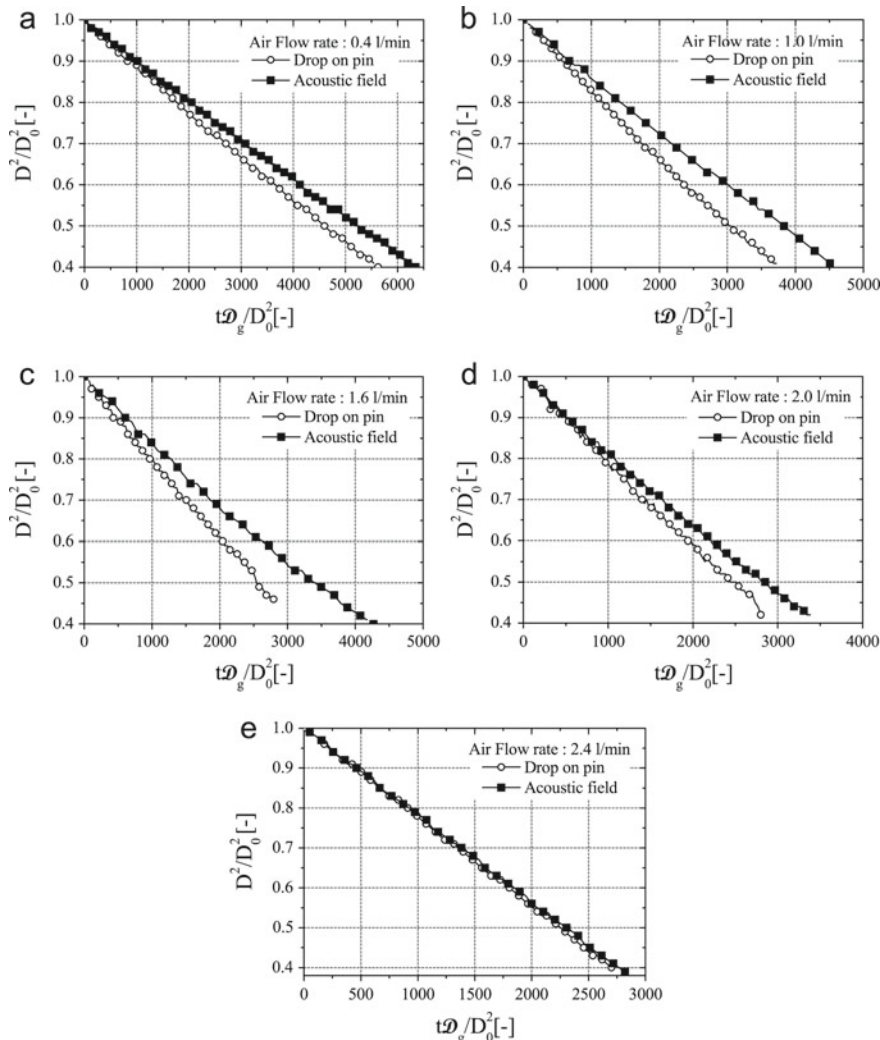


Fig. 7.4 Comparison of droplet evaporation of water in standing acoustic wave versus droplet suspended by glass-filament. Droplets are ventilated with an airflow. Air ambient temperature is 23 °C and relative humidity of 10%. Air blowing rates **a** 0.4, **b** 1.0, **c** 1.6, **d** 2.0, and **e** 2.4 l/min. [23] <https://doi.org/10.1016/j.ces.2011.05.011>

to the fourth range in Fig. 7.3), the airflow is strong enough to not only blow out the vapor from the outer acoustic streaming, but also to remove the inner acoustic boundary layer. Then, the effects of acoustic field are eliminated, and the evaporation driven by forced convection is the same for either acoustically levitated or filament suspended droplets, as depicted in Fig. 7.4e.

Brenn et al. [24] and Bänsch et al. [25] confirmed the acceleration of acoustic field on the evaporation process through numerical simulation; however, Bänsch found no accumulation of water vapor in the emerging toroidal vortices. And they further proved that the local evaporation rate was not uniform along the surface, it showed highest value at the equator and lowest at the poles of the sphere.

Other parameters such as the component and humidity [26–30] also play important roles in droplet evaporation process; however, they perform no difference with the ones positioned in air without acoustic field. Since in this book we only consider the effects of the acoustic field, we herein do not discuss those contents.

References

1. C.K. Law, M. Binark, Fuel spray vaporization in humid environment. *Int. J. Heat Mass Transf.* **22**, 1009–1020 (1979)
2. C.K. Law, T.Y. Xiong, C.H. Wang, Alcohol droplet vaporization in humid air. *Int. J. Heat Mass Transf.* **30**, 1435–1443 (1987)
3. K. Annamalai, W. Ryan, S. Chandra, Evaporation of multicomponent drop arrays. *Trans. ASME. J. Heat Transf.* **115**, 707–716 (1993)
4. G. Chen, S.K. Aggarwal, T.A. Jackson, G.L. Switzer, Experimental study of pure and multicomponent fuel droplet evaporation in a heated air flow. *Atomiz. Sprays* **7**, 317–337 (1997)
5. C.K. Law, H.K. Law, A d^2 -Law for multicomponent droplet vaporization and combustion. *AIAA J.* **20**(4), 522–527 (1982)
6. P. Nordine, R. Atkins, Aerodynamic levitation of laser-heated solids in gas jets. *Rev. Sci. Instrum.* **53**, 1456–1464 (1982)
7. G. Kinzer, R. Gunn, The evaporation, temperature and thermal relaxation time of freely-falling water drops. *J. Meteorol.* **8**, 71–83 (1951)
8. W. Ranz, W. Marshall, Evaporation from drops. Parts I and II. *Chem. Eng. Prog.* **48**, 141–156 and 173–180 (1952)
9. D. Charlesworth, W. Marshall, Evaporation from drops containing dissolved solids. *AIChE J.* **6**, 9–23 (1960)
10. P.S. Larsen, J.W. Jensen, Evaporation rates of drops in forced convection with superposed transverse sound field. *Int. J. Heat Mass Transf.* **21**, 511 (1978)
11. M. Seaver, J.R. Peele, Noncontact fluorescence thermometry of acoustically levitated water drops. *Appl. Opt.* **1990**, 29 (1956)
12. A. Gopinath, A.F. Mills, Convective heat transfer from a sphere due to acoustic streaming. *Trans. ASME: J. Heat Transf.* **115**, 333 (1993)
13. L. Rayleigh, On the circulation of air observed in Kundt's tubes and on some allied acoustical problems. *Phil. Trans. R. Soc. Lond.* **175**, 1 (1883)
14. H. Schlichting, Berechnung ebener periodischer Grenzschichtströmungen. *Phys. Z.* **33**, 327 (1932)
15. H. Schlichting, *Boundary Layer Theory* (McGraw-Hill, New York, 1979)
16. E.N. Andrade, On the circulation caused by the vibration of air in a tube. *Proc. R. Soc. Lond. A* **134**, 447 (1931)

17. N. Riley, Acoustic streaming, in *Encyclopedia of Acoustics*, vol. 1, ed. by M.J. Crocker (Wiley, Hoboken, 1997), p. 321
18. A.P. Burdakov, V.E. Nakoryakov, On mass transfer in an acoustic field. *J. Appl. Mech. Tech. Phys.* **6**(2), 51 (1965)
19. C.P. Lee, T.G. Wang, Near-boundary streaming around a small sphere due to orthogonal standing waves. *J. Acoust. Soc. Am.* **85**, 1081 (1989)
20. C.P. Lee, T.G. Wang, Outer acoustic streaming. *J. Acoust. Soc. Am.* **88**, 2367 (1990)
21. A.L. Yarin, G. Brenn, O. Kastner, D. Rensink, C. Tropea, Evaporation of acoustically levitated droplets. *J. Fluid Mech.* **399**, 151–204 (1999)
22. A.L. Yarin, G. Brenn, D. Rensink, Evaporation of acoustically levitated droplets of binary liquid mixtures. *Int. J. Heat Fluid Flow* **23**(4), 471–486 (2002)
23. B.A.A. Zaitone, C. Tropea, Evaporation of pure liquid droplets: comparison of droplet evaporation in an acoustic field versus glass-filament. *Chem. Eng. Sci.* **66**(17), 3914–3921 (2011)
24. G. Brenn, L.J. Deviprasath, F. Durst et al., Evaporation of acoustically levitated multi-component liquid droplets. *Int. J. Heat Mass Transf.* **50**(25–26), 5073–5086 (2007)
25. E. Bänsch, M. Götz, Numerical study of droplet evaporation in an acoustic levitator. *Phys. Fluids* **30**, 037103 (2018). <https://doi.org/10.1063/1.50179361>
26. H. Schiffter, G. Lee, Single-droplet evaporation kinetics and particle formation in an acoustic levitator. Part 1: evaporation of water microdroplets assessed using boundary-layer and acoustic levitation theories. *J. Pharma. Sci.* **96**(9), 2274–2283 (2007)
27. N.A. Combe, D.J. Donaldson, Water evaporation from acoustically levitated aqueous solution droplets. *J. Phys. Chem. A.* <https://doi.org/10.1021/acs.jpca.7b08050> (2017)
28. B.A. Zaitone, Oblate spheroidal droplet evaporation in an acoustic levitator. *Int. J. Heat Mass Transf.* **126**, 164–172 (2018)
29. R. Tuckermann, S. Bauerecker, B. Neidhart, Evaporation rates of alkanes and alkanols from acoustically levitated drops. *Anal. Bioanal. Chem.* **372**(1), 122–127 (2002)
30. N. Yuki, H. Koji, Evaporation of droplet in mid-air: pure and binary droplets in single-axis acoustic levitator. *PLoS ONE* **14**(2), e0212074 (2019)

Chapter 8

Crystallization in Acoustically Levitated Drops



Da-Chuan Yin and Duyang Zang

8.1 Introduction

Crystallization is a process of forming a phase with a highly ordered structure, in which the basic building units (atoms, molecules, or ions) are arranged in such a way that all units are positioned at 3D translationally periodic lattice. It is a very important process, and in that it produces crucial materials (crystals) that are indispensable for many industrial applications and scientific researches.

The influence of the physical environment on crystallization is a very important research direction in crystallization research. The most often used physical environments include a variety of physical fields, such as acoustic, light, electric, magnetic, and temperature fields. Among them, acoustic field (such as acoustic levitation, ultrasound irradiation) is a special physical environment, which can realize very unique crystallization processes, providing conditions for the preparation of crystals of desired properties and offering a very unique viewpoint for the theoretical studies of the crystallization processes.

Crystallization can be categorized into three groups: crystallization from melts, from solution, and from vapor. In the research field of crystallization in acoustic levitation condition, only crystallizations from solution and melts have been studied. In this chapter, we will focus on the studies of crystallization from liquids (solution comprises solute and solvent, and liquid materials) at around room temperature,

D.-C. Yin (✉)

Key Laboratory for Space Bioscience and Biotechnology, School of Life Sciences, Northwestern Polytechnical University, 710072 Xi'an, Shaanxi, People's Republic of China

e-mail: yindc@nwpu.edu.cn

Shenzhen Research Institute of Northwestern Polytechnical University, 518057 Shenzhen, People's Republic of China

D. Zang

Soft Matter & Complex Fluids Group, School of Physical Science and Technology, Northwestern Polytechnical University, 710129 Xi'an, People's Republic of China

although crystallization from melts (solidification from a liquid alloy) will be briefly introduced in Sect. 8.5.

Studies related to crystallization from liquids usually include instrumentation of acoustic levitation for crystallization from liquids, crystallization processes of different materials (small molecules like salt, organics and pharmaceuticals, and macromolecules like proteins), in situ monitoring techniques, and theoretical studies taking advantages of the acoustic levitation. Here, in this chapter, we will not discuss the instrumentation of the acoustic levitation technique as similar contents (mostly general to all research topics) are introduced in other chapters.

8.2 Crystallization of Different Materials in Acoustically Levitated Droplets

Utilization of acoustic levitation for crystallization in droplets provides a unique environment (e.g., high degree of supersaturation or supercooling) for preparing crystal or non-crystal materials that are not easy to obtain via normal procedures [1].

In this section, we will introduce the crystallization of small and large molecules. According to the researches reported, the studied small molecules usually include inorganic materials, pharmaceuticals, and others (like organics), and the large molecules generally refer to proteins.

8.2.1 *Crystallization of Small Molecules*

8.2.1.1 Crystallization of Inorganic Materials

Typical inorganic materials studied include NaCl [2], NH₄Cl [2], molybdate catalyst precursors [3], CaCO₃ [4], (NH₄)₂SO₄ [5, 6], and Na₂SO₄ [5].

Cao et al. [2] reported the comparison of crystallization of NaCl and NH₄Cl with and without acoustic levitation. It was found that, by using the crystallization chamber equipped with the acoustic levitator they developed, crystals generally grew to a bigger size or showed more optically perfect facet morphology (Fig. 8.1). Interestingly, NaCl crystals grown in levitated droplets showed an ordered array (Fig. 8.2).

Knutsson [6] developed an acoustic levitation instrument (called LevMac) with which she tested the crystallization of ammonium sulfate ((NH₄)₂SO₄) in an aqueous droplet. Figure 8.3 shows the time sequence of the droplet images during the crystallization. With the help of in situ light scattering measurements, obvious crystallization can be observed between 170 and 180s after starting from the experiment.

Crystallization of CaCO₃ is also a focused interest among the studies. Sacher and Krammer [7] studied the crystallization of CaCO₃ in the acoustically levitated

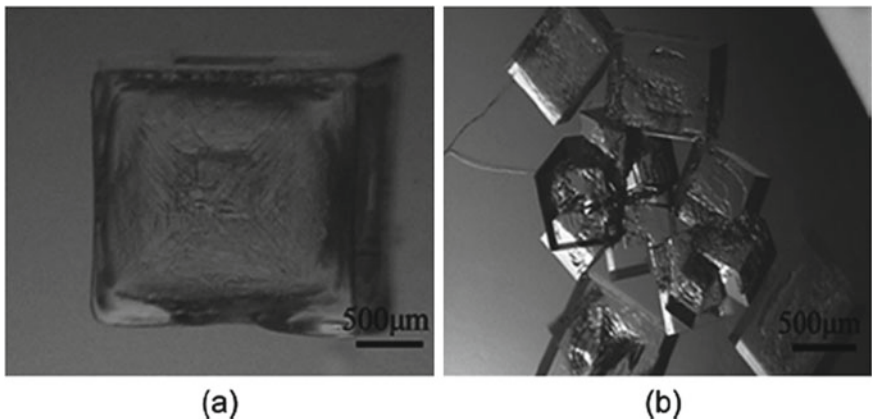
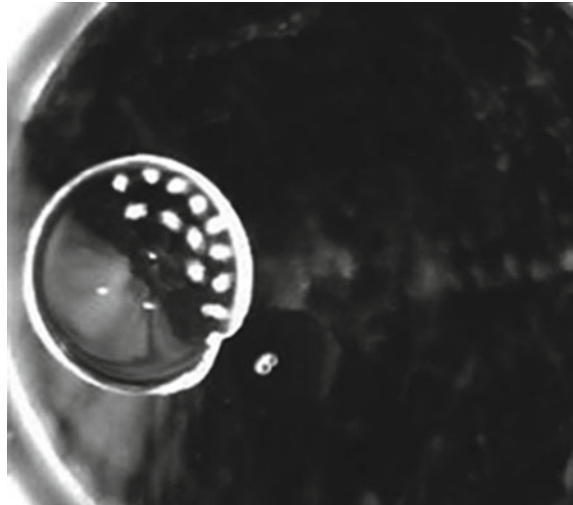


Fig. 8.1 NaCl crystals grown with (a) and without (b) acoustic levitation [2]

Fig. 8.2 NaCl crystals grown in the levitated droplets showed an ordered array [2]



droplet. They found that crystal habits can be influenced by controlling the temperature and applied shear stress. The morphologies can be prismatic, shell-like or spherical like, as illustrated in Fig. 8.4. These results showed that the morphology, habits, and size of the crystals can be controllable by selecting appropriate temperature and shear stress.

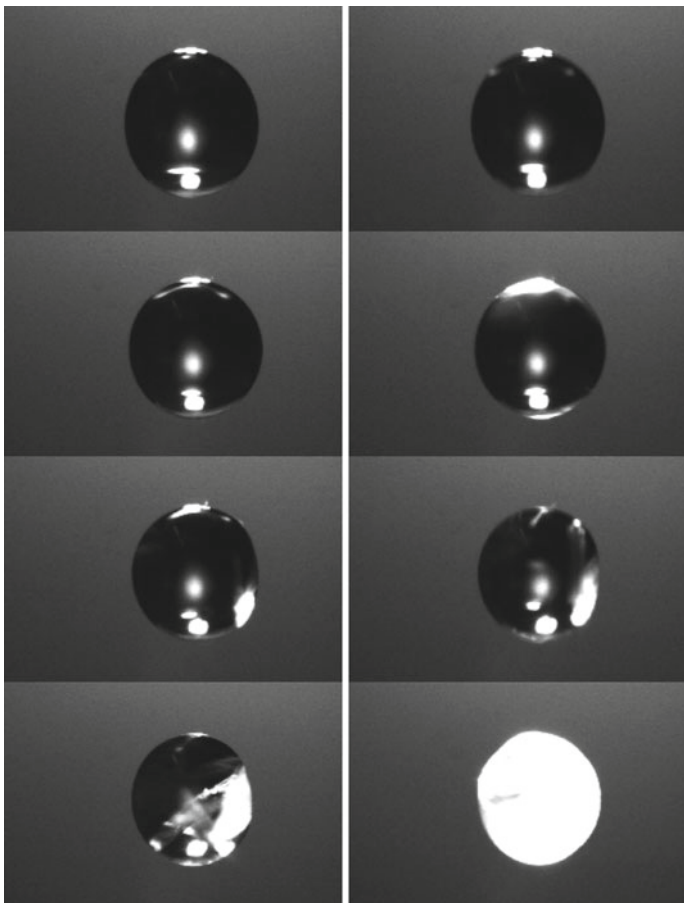


Fig. 8.3 Crystallization process of $(\text{NH}_4)_2\text{SO}_4$. Pictures were taken at 0, 40, 80, 120, 140, 160, 170, and 180s [6]

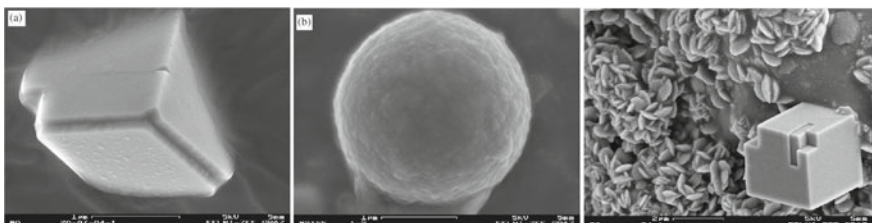


Fig. 8.4 Different morphologies of CaCO_3 crystals prepared under different parameters. **a** Prismatic; **b** Spherical; **c** Shell-like (mixed with a prismatic crystal). Modified from Figs. 8.2 and 8.3

8.2.1.2 Crystallization of Pharmaceuticals

For pharmaceuticals, polymorphism and solubility are both important in clinical applications. Different crystalline forms may show dramatically different efficacies in treating diseases. While suitable solubility is required to achieve for different situations, higher solubility for better bioavailability, lower solubility may be helpful for the sustainable release of the drug. Hence, a good control to obtain an exact crystalline form, or non-crystalline form, is a big issue for researchers in the field of pharmaceutical development.

In this research topic, several different pharmaceuticals, such as benzamide [8], indomethacin [8], vitamin C [9], acetylsalicylic acid (aspirin) [9], and caffeine [10], were crystallized using acoustic levitation technique. It was found that, in the acoustically levitated droplets, only one type of caffeine crystalline form (pure α -caffeine crystal) can be obtained, while in the droplets dispensed on a glass slide, two crystalline forms (α - and β -) were obtained [10]. In the studies of crystallization of benzamide and indomethacin [8], it was found that two types of crystal modifications were obtained for both compounds. All these studies showed that polymorphism may be controlled using the acoustic levitation technique.

Some other pharmaceuticals, like cinnarizine, carbamazepine, miconazole nitrate, probucol, and clotrimazole [11], are necessary to be in the form of non-crystalline state, so that the solubility can be high enough for increasing bioavailability for oral administration [12]. Utilization of acoustic levitation provides an environment of fast evaporation, so that it is good for preparing materials at amorphous states. Furthermore, the containerless condition is not favorable for inhomogeneous nucleation because there is no solid surface acting as the nucleation site, so that crystallization can be more difficult in such a containerless state. Therefore, acoustic levitation is a valuable choice to prepare amorphous pharmaceuticals [12]. In the literatures, it is often used to simulate the spraying drying in the pharmaceutical industry because both the spray drying and acoustic levitation techniques exhibit a high evaporation rate [1, 11–13].

8.2.1.3 Crystallization of Other Materials

Formation of mesocrystal was also studied using the acoustically levitated droplets. Mesocrystal formation is often related to biominerization in which anisotropic nanocrystals are assembled into a structured framework. It is a very important process for living things, and thus, related studies attached immense interest. Agthe et al. [14] carried out an investigation of mesocrystal (array of maghemite nanocubes) formation in such a special environment coupled with in situ small angle X-ray scattering (SAXS) measurements. What unique in this study is that the formation of mesocrystals is in the levitated droplet, without contact with any solid surface (substrate-free), and furthermore, it provided a time-resolved SAXS analysis. More importantly, they showed that the formation of mesocrystals follows a two-step mechanism (first step, formation of a liquid like disordered phase; second step, transition of disordered to

ordered structure) which is similar to that well-established in the theoretical description of nucleation of crystals. These results may give some indication to explore more general processes of phase transition.

8.2.2 *Crystallization of Proteins*

Protein crystallization is another focus of the research in this field. Presently, protein crystallization is a very essential process to obtain crystals of proteins so as to provide diffraction samples for their structural determination. This approach contributed more than 90% of the structures deposited in the protein databank (PDB). Apart from the structural determination using crystallography, protein crystallization also provides a chance to produce high-quality purified proteins, which can be used as biopharmaceuticals, or biochemical reagents. Furthermore, protein crystallization is also an excellent crystallization model for studying general processes of crystallization for its advantageously slow kinetics.

In this research direction, major works are related to the purpose of growing high-quality protein crystals, or finding an optimized crystallization conditions.

8.2.2.1 **Obtaining High-Quality Protein Crystals**

Early in the beginning of 1990s, acoustic levitation was proposed to grow protein crystals [15]. One of the purposes is to obtain high-quality protein crystals [1, 16], because it is essential for high-resolution structural determination. The acoustic levitated droplet may provide a good environment for obtaining high-quality protein crystals, because the droplet is containerless, which means that there will be no contamination coming from the container and no inhomogeneous nucleation site on the container. Further, the convection may be controllable in a specially levitated condition (electrostatic-acoustic hybrid levitation, which is said to simulate space condition, which is a well-known approach for obtaining high-quality protein crystals) [17] so that high-quality protein crystals may be obtained. Figure 8.5 shows lysozyme and proteinase K crystals grown in such an environment.

Cao et al. [2] developed an acoustic levitator, equipped with a levitation chamber having the ability to control temperature and humidity. They used the instrument to grow protein crystals and found that the nucleation and growth of proteins in such conditions are speeded up (protein crystals can be visible within minutes), indicating that the processes have the potential to realize high efficient protein crystallization. Figure 8.6 shows the comparison of protein crystals (lysozyme and proteinase K) grown with and without acoustic levitation [2], and it can be seen that the acoustic levitation showed a better effect on obtaining larger and well-faceted protein crystals.

Protein crystals may form ordered array under the acoustically levitated condition. Figure 8.7 shows the series of images of a droplet of lysozyme crystallization solution. It can be seen that the lysozyme crystals finally grow to a ring-like array.

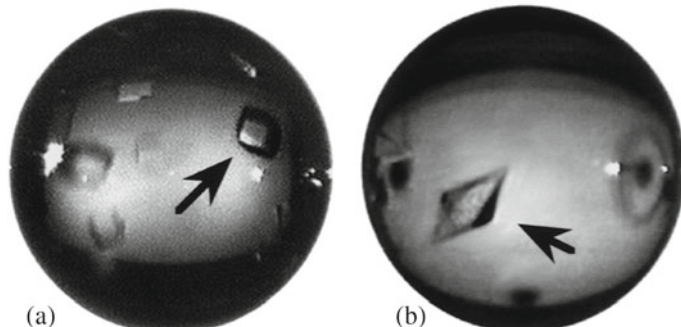


Fig. 8.5 Protein crystals grown in electric–acoustic hybrid levitated droplets. **a** Lysozyme crystals; **b** proteinase K crystals [17]

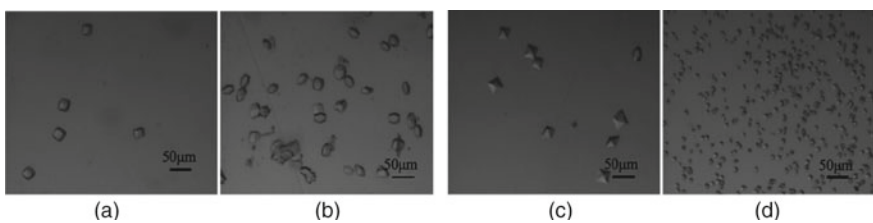


Fig. 8.6 Protein crystals grown with and without acoustic levitation. **a** Lysozyme crystals grown with acoustic levitation; **b** lysozyme crystals grown without acoustic levitation; **c** proteinase K crystals grown with acoustic levitation; **d** proteinase K crystals grown without acoustic levitation. This figure is modified from [2]

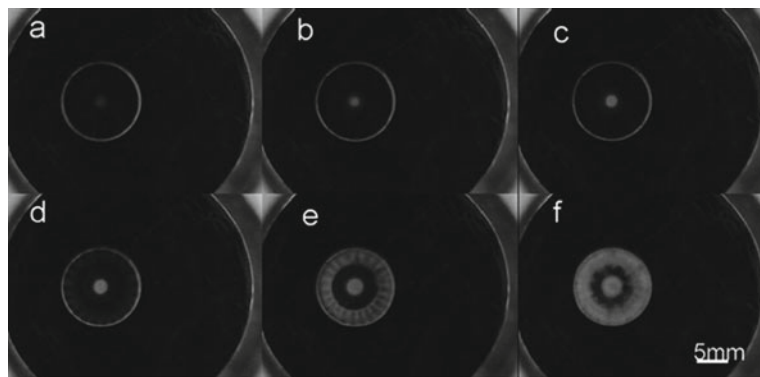


Fig. 8.7 Time sequence of levitated droplet images of lysozyme crystallization solution. **a–f** The levitated droplet images taken against the time [2]

8.2.2.2 Crystallization Screening

One of the major works in protein crystallization is to find suitable crystallization condition. It is well-known that protein crystallization is often challenging because it is hard to find a crystallization condition, and it is also hard to find an optimized condition to produce high-quality protein crystals. Many efforts have been taken to solve the problems. Utilization of acoustic levitation is one of the many ways.

Santesson et al. [16] made the effort to realize the rapid screening of crystallization conditions for proteins. They used a piezoelectric flow through dispensers to eject droplets (50–100 pL droplets at 1–9000 droplets/s) and used an acoustic levitator to capture the ejected droplets. With the help of acoustic levitation conditions, the solubility information of the proteins can be rapidly screened, and crystallization conditions can be easily obtained. They tested this idea by using two model proteins (alcohol dehydrogenase and D-serine dehydratase, the former is easy to crystallize, but the latter is not easy to crystallize. These two proteins are chosen for probing the effect of acoustic levitation environment to see if it promotes or inhibits the crystallization of proteins). Their results confirmed that the acoustic levitation technique is a powerful tool for searching for crystallization conditions. It is easy to modify the crystallization conditions (type of protein, additives, precipitants, and their concentration), and due to the fast evaporation the levitated droplet can cover a large concentration range so that large crystallization space can be screened. The overall consumption of sample can be minimized (consumable-saving), together with the benefit that the screening process is fast (time-saving), the authors suggest that this technique be used for practical protein crystallization.

8.3 In Situ Analytical Techniques Combined with Other Noninvasive Techniques

Acoustic levitation condition is unique in that it keeps the sample in a containerless and levitated condition, so that the sample can be studied free of any direct contact. Such a feature provides a perfect chance for researchers to carry out analytical studies of the sample fully isolated and free of any disturbances from the container or any sample holder. It has been already studied in analytical techniques involving analytical chemistry and analytical biochemistry. One or more remote detection techniques (such as fluorescence imaging detection [18], right-angle light scattering, Raman spectroscopy, X-ray diffraction, X-ray tomography [19], SAXS, WAXS) [20] are used combined with the acoustic levitation instrument, so that the sample can be studied in real-time and in situ. In this section, we will introduce some typical studies using Raman spectroscopy and X-ray-based techniques (scattering, diffraction, etc.).

8.3.1 Raman Spectroscopy

Raman spectroscopy has been used as a powerful tool combined with acoustic levitation to study the processes that occur in the levitated droplets. Early in the beginning of this century, Santesson et al. [8] combined Raman spectroscopy with the acoustic levitation technique for the first time, and they used such combination to study the crystallization of benzamide and indomethacin. Taking advantage of Raman spectroscopy, the crystalline forms can be distinguished according to the measurements. From the *in situ* studies, they concluded that both benzamide and indomethacin yields two types of crystal modifications, showing that the materials exhibit polymorphism. According to the Raman spectra, it is possible to judge what happens in the droplets. Figure 8.8 shows an example of the time sequence of the Raman spectra, and it can be seen that a metastable phase appeared before the materials finally transformed into the stable phase.

In 2009, Tuckermann et al. [5] reported another *in situ* chemical analysis of acoustically levitated droplets undergoing crystallization using Raman spectroscopy. The studied model materials are $(\text{NH}_4)_2\text{SO}_4$ and Na_2SO_4 . They have found that the crystallization occurs from inside of the droplet, which is a strong indication that the crystallization occurred starting from a homogeneous nucleation process. This is theoretically important because purely homogeneous nucleation is hard to achieve. In their studies, they found the coexistence of two phases in the process of crystallization. Further, in the case of the crystallization of Na_2SO_4 , they have found an intermediate state of $\text{Na}_2\text{SO}_4 \cdot 10\text{H}_2\text{O}$ in the transformation process to anhydrous Na_2SO_4 crystals. These results clearly show that Raman spectroscopy can provide detailed information during the phase transition, hence it is a powerful technique in analyzing the crystallization process.

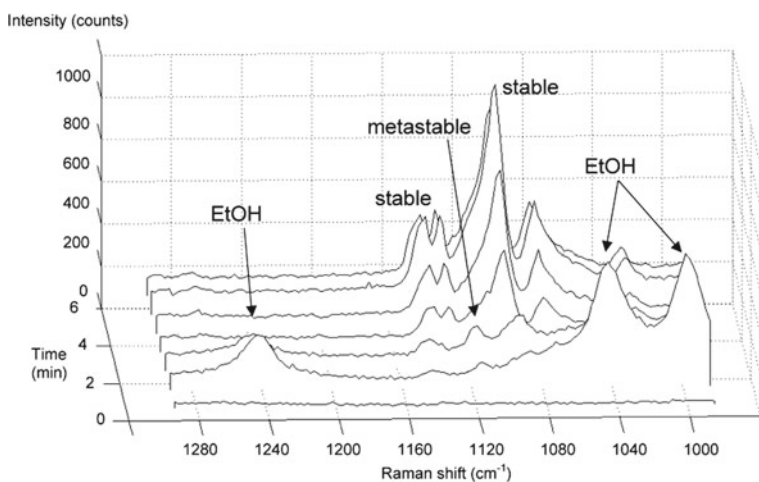


Fig. 8.8 Raman spectra of benzamide in ethanol in a levitated droplet [8]

8.3.2 X-Ray-Based Techniques

8.3.2.1 X-Ray Diffraction

X-ray diffraction is another powerful tool often used in studying acoustically levitated droplets. In the beginning of this century, Cerenius et al. [21] did a preliminary test on the synchrotron facility in Sweden [MAX II (at that time), Lund University], showing that XRD would be potentially useful in studying the crystallization process, however they did not do real-time crystallization experiments.

In 2006, Leiterer et al. [22] reported the first time dependence of X-ray diffraction study of NaCl crystallization from solution. Figure 8.9 shows the diffraction results against time, and from the diffraction pattern, the crystallization processes were clearly seen judging from the evolution of the Bragg peaks.

Later, Leiterer et al. [10] used the micro-focus X-ray beam at synchrotron facility BESSY, to study the crystallization process of caffeine in aqueous solution. Figure 8.10 shows a comparison of diffraction pattern of the sample in levitated and non-levitated states. It can be seen that in the levitated state, the diffraction rings are complete and nearly homogeneous (probably due to that the crystals in the droplet are turning and rotating all the time because of irradiation of the acoustic sound wave), while in the case without levitation, the incomplete rings (arcs) showed preferred orientation of the crystal in the droplet. Furthermore, they have found that, in the levitated droplet, only one type of caffeine crystal (pure α -caffeine crystal) was obtained, while in the case without levitation, two types (α - and β -) of crystals were obtained.

In 2010, the same group [3] reported the X-ray diffraction study of complex molybdate catalyst precursors, and they compared the results with the spray drying process. They showed that both processes yielded similar crystal forms (the diffraction peaks matched well with each other), but the peak width is apparently larger in the case of spray drying, indicating that spray drying produced smaller crystals.

Fig. 8.9 Diffraction pattern of levitated NaCl crystallization solution against time [22]

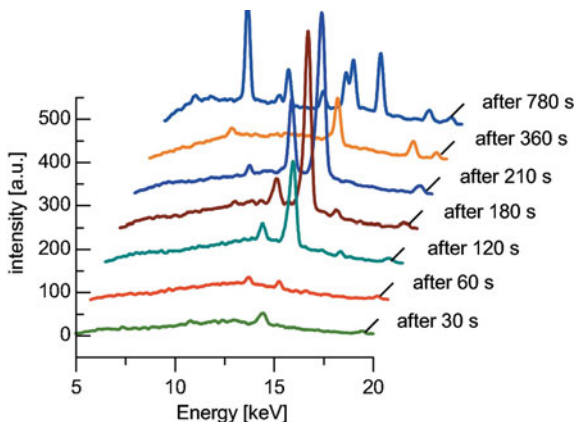
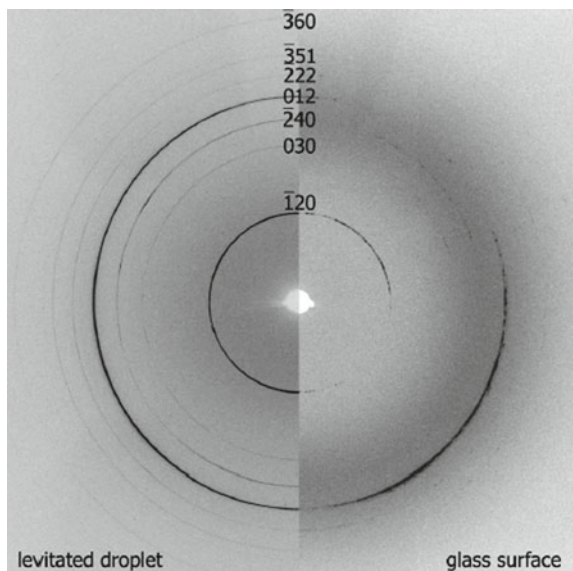


Fig. 8.10 Comparison of diffraction pattern of levitated (left) and non-levitated caffeine solution



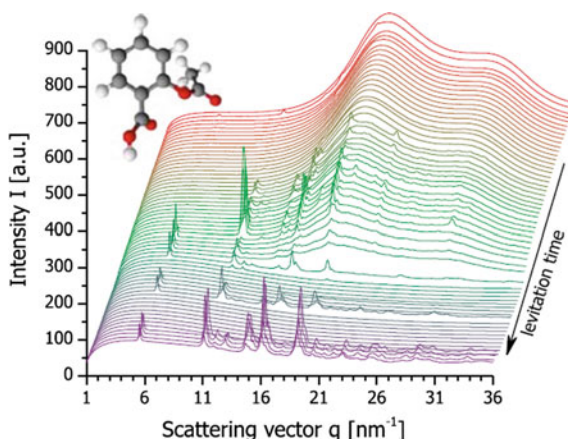
According to the results, they suggested that the acoustic levitation can be a good method for simulation of the spraying drying process.

More recently, the time-resolved structural study of many materials system (esp. proteins and complexes) becomes a very hot topic. It is not uncommon for time-resolved studies to be done on synchrotron radiation. However, these studies require large quantities of crystals, and the time scale of process studies is often controlled in nanoseconds and milliseconds, which is difficult. Tomizaki et al. [1] developed an acoustic levitation diffractometer combining Swiss Light Source (Paul Scherrer Institute, PSI), which, to some extent, provided a new methodological option for the time-resolved study of structural dynamics. The acoustic levitator can levitate a droplet containing crystal, and the droplet was diffracted using a synchrotron radiation source equipped with a fast frame rate X-ray image detector. Since the crystal rotates spontaneously in the droplet, no special rotating device is needed. In this way, the kinetic change of the ligand-binding process at room temperature can be easily studied.

Using the above technologies, the author has collected data at a frequency of 0.1 kHz and completed data collection in a few seconds using an EIGER*16M detector [23]. When the faster detector EIGER*1M is used, the process can be completed in hundreds of milliseconds.

The above technology has some obvious advantages: (1) room temperature process: the structure can be obtained at room temperature; (2) dynamic process: time-resolved structural dynamics can be studied; (3) controllable conditions: the conditions of the solution can be easily controlled, for example, pH value (by using volatile chemicals like ammonia [1]), concentration, temperature, humidity, etc.; (4)

Fig. 8.11 Typical scattering curves of aspirin solution measured against time. The curves were measured every 30 s for a total process of 31 min [9]



slow processes, such as soaking structure changes, can be studied; (5) the number of crystals required in the research is small (a single crystal is enough).

8.3.2.2 X-Ray Scattering (SAXS, WAXS)

Scattering techniques (small angle X-ray scattering and wide angle X-ray scattering) are also often used for *in situ* study of the acoustic levitated droplet. From the point view of instrumentation, these techniques are similar to diffraction. Hence, these techniques are often carried out by similar groups.

Leiterer et al. [9] studied the crystallization of acetylsalicylic acid (Aspirin) and vitamin C using SAXS and WAXS. Figure 8.11 shows a typical example of the scattering study of crystallization of acetylsalicylic acid against time. The evolution of the curves clearly indicated the crystallization process.

It is also possible to do combined measurements using different noninvasive techniques. For example, it was reported that SAXS and circular dichroism (CD) can be combined to study pharmaceutical and protein solution [24].

8.4 Miscellaneous

8.4.1 Theoretical Studies of Nucleation Process

As a unique condition for crystallization, acoustic levitation provides a perfect chance for the theoretical study of crystallization. Especially, it provides a condition without any direct contact with solid surfaces or interfaces, so that the crystallization can occur without heterogeneous nucleants. Purely homogeneous nucleation or nearly pure homogeneous nucleation can be studied. Taking advantages of such special

condition, Wolf et al. [4] studied the crystallization process of calcium carbonate and found the evidence of early homogeneous amorphous precursors before final crystallization occurs. This discovery matched perfectly with the currently accepted two-step nucleation theory.

Studying of mesocrystal formation under acoustic levitation condition showed similar phenomenon [14] but in a larger size scale. Such discoveries indicated the possibility of broader and more general rules in nature.

8.4.2 Sample Handling or Delivery Systems for X-Ray Crystallography

In the experimental study of protein crystallography, crystal harvesting and crystal mounting are necessary procedures. These procedures often require manual operation, slowing down the efficiency. Tsujino et al. [25] developed a technique which is fully automated to realize high-throughput (an order of magnitude higher than normal methods) sample delivery for serial crystallography using acoustic levitation (see the illustration in Fig. 8.12). By using crystal containing droplet ejection methods, (such as piezoelectric technology (piezoelectric injection), or acoustic droplet ejection (ADE) [26, 27]) the droplet can be ejected to the levitation position and diffracted using the synchrotron beam. Because the crystal rotates automatically in the liquid, the mechanical rotation process is not necessary. With faster detectors and

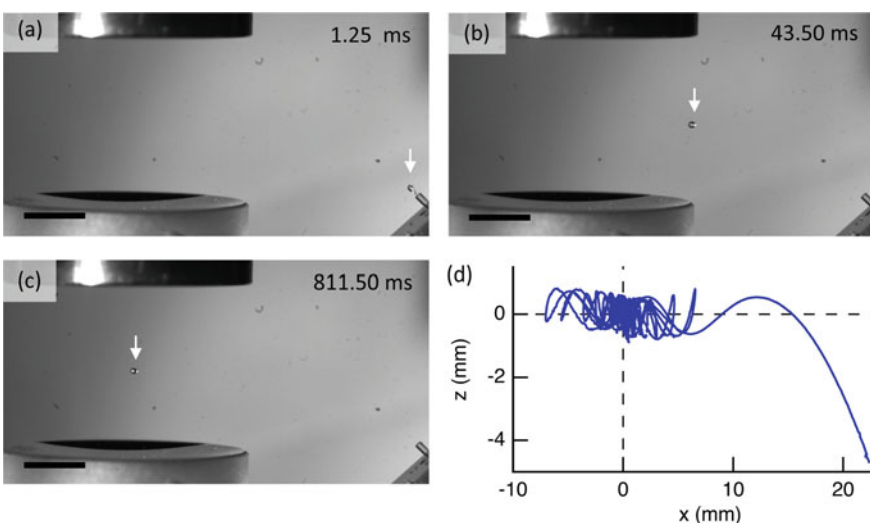


Fig. 8.12 Loading of droplet to levitation position. **a–c** Series of images after ejection of the droplet. The droplet will be captured by the acoustic levitator. **d** The trajectory of the droplet after the ejection [25]

stronger light sources, the technology is expected to play a more important role. In particular, in recent years, the development of new technology of X-ray free electron laser (XFEL) enabled diffraction—before—destruction so that structure determination using micro- or even nanocrystals is possible, and time-resolved structure determination at room temperature is one of the advantages of this technology. One of the key steps of this technology is the sample delivery system. At present, many experimental techniques have been developed, which can be divided into two categories: fixed target and moving target sample delivery systems. Increasing the hitting rate and efficiency is still an important research direction. Tsujino et al. work may provide a new option of sample delivery system for serial crystallography.

8.5 Crystallization from Melts

Acoustic levitation is no doubt able to provide container-free condition to alloys since the materials of the highest density (Iridium) had already been levitated by this technique [28]. However, there are still existing challenges for the processing of alloy melts where high temperature is often necessary. This is mainly because the sound field in the levitator will be changed owing to heating or cooling of the alloy samples, which seriously influence the levitation stability. Consequently, in the last decades, the solidification study by using acoustic levitation is mainly focused on low melting point systems [29, 30]. Only recently, this technique was extended to high-temperature alloys, such as Ag–Cu [31], Al–Cu–Si [32] by Bingbo Wei's group thanks to the enhanced levitation stability provided by the flexible and adaptive reflector of the levitator [33, 34].

8.5.1 Effect on Temperature Field

It is well known that solidification of the liquid alloy is closely related to the heat and mass transfer in the system. For an acoustically levitated liquid alloy drop, the temperature field in the melt is influenced by the sound field [35]. This is mainly caused by (1) acoustic radiation-controlled drop shape which determines the boundary condition for thermal transfer; (2) the acoustic streaming surrounding the levitated drop and the flows inside the drops. Geng et al. [31] have studied the temperature distribution in an Ag–Cu eutectic alloy utilizing CMOS image analysis and numerical simulation. They found a temperature gradient along the drop surface where the temperature is the highest at the Pole region, whereas lowest at the equator region. This unique temperature field also resulted in the solidification of cyclohexane solely through acoustic levitation processing [36], as illustrated in Fig. 8.13. It should also be noted that a stronger sound intensity leads to a more flattened shape of the drop, and in turn, a higher cooling rate to the liquid alloy.

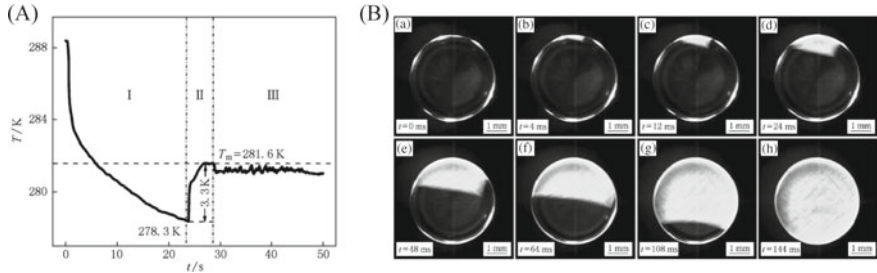


Fig. 8.13 Evaporation-induced solidification of an acoustically levitated cyclohexane drop [36]. **A** The temperature curve during solidification; **B** snapshots showing the drop solidified from the equator region

8.5.2 Capillary Wave and Surface Nucleation

Capillary waves often be observed on an acoustically levitated drops, which is arising from the parametric instability stimulated by low-amplitude surface vibration [37, 38]. This phenomenon could be found at room temperature for water, aqueous solutions, and other low melting point liquids [39] and at high temperature for liquid alloys [40], as illustrated in Fig. 8.14. However, for liquid alloys, the capillary wave can interact with solidification: (1) influence nucleation, which is supported by the fact that capillary wave center often to be a potent nucleation site [41]; (2) compete with solidification [31], which results in different solidified surface patterns [34].

8.5.3 Effect on Solidification Microstructure

To obtain an optimized microstructure of alloys is one of the most important aims of solidification processing, which can usually be achieved through improving the undercooling and cooling rate of the alloy melt. Acoustic levitation, however, does not show much advantage to obtain high undercooling and cooling rate. It could also influence significantly the solidification microstructure, for instance leading to broken lamellae in eutectic alloys [28, 41] and suppressed macro-segregation in monotectic alloys [42], as shown in Fig. 8.15a. The underlying mechanism is largely attributed to the complicated internal flows in the acoustically levitated drops [41], which are jointly caused by the surface capillary wave, shape oscillation, bulk vibration, and rotation of the drops. It should be noted that acoustic levitation can greatly reduce the gravity-induced segregation, however, may produce additional effect of segregation owing to centrifugal effect [43] (Fig. 8.15b).

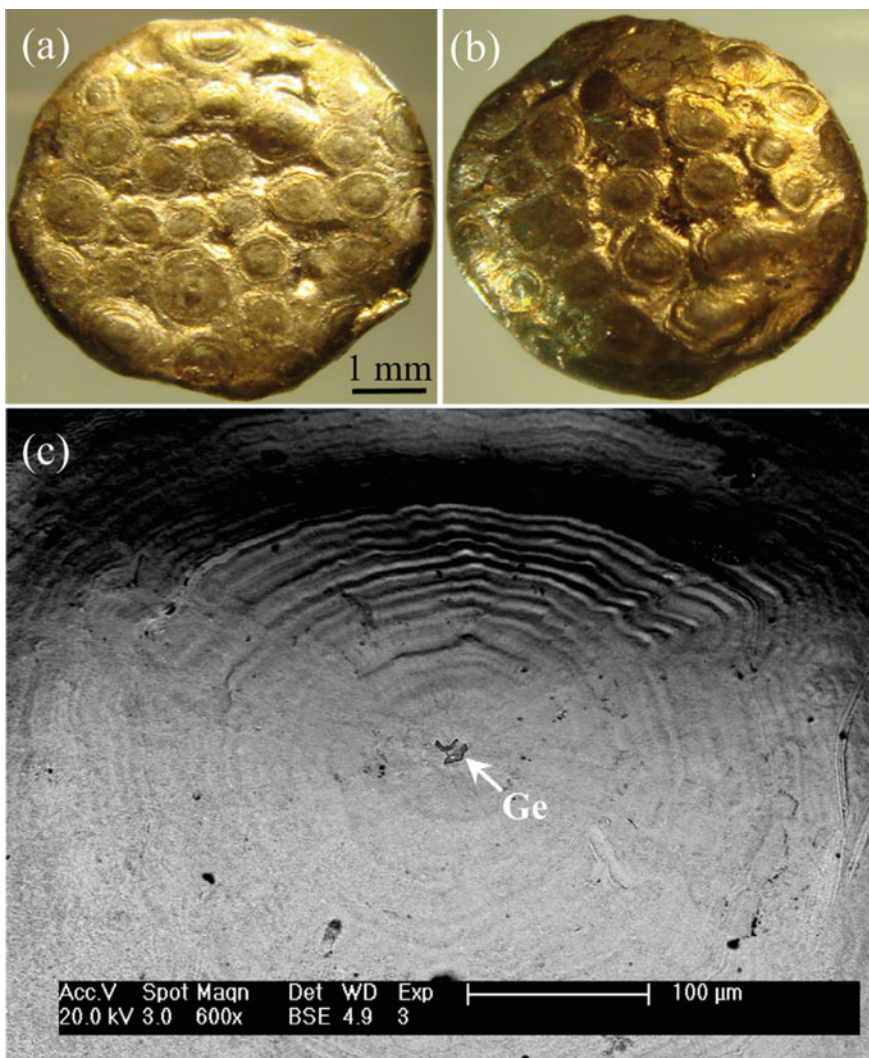


Fig. 8.14 Surface wave patterns on the solidified sample from an acoustically levitated Ag–Cu–Ge alloy drop [40]. **a** Top surface; **b** bottom surface; **c** the local enlargement of a single wave cell. The average wavelength of the capillary ripples in each cell is $\sim 8 \mu\text{m}$

8.6 Concluding Remarks

In the research field of crystallization, the investigation of the effects of physical environments on the crystallization processes is an important research direction. Among the many physical environments, acoustic levitation has received extensive attention

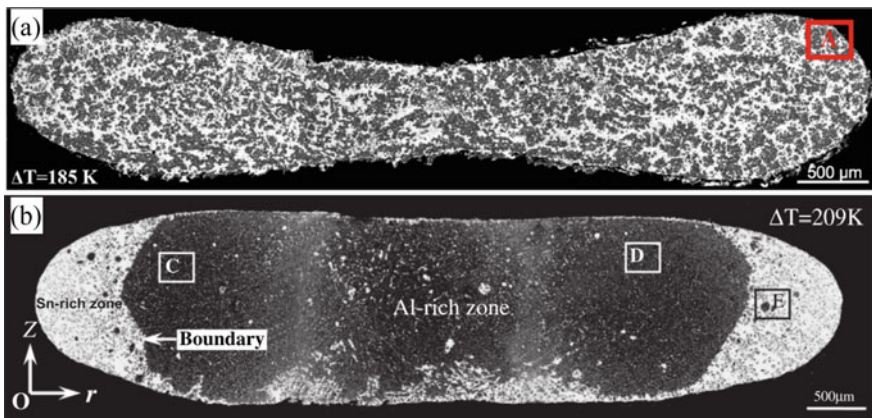


Fig. 8.15 Effect of acoustic levitation on the solidification microstructures. **a** Al–5%Cu–65%Sn alloy where the macro-segregation is suppressed [42], **b** “Poached-egg” microstructure of a Al–15%Cu–55%Sn alloy drop [43]

in the field of crystallization, and extensive and in-depth researches have been conducted in the past two decades. In general, acoustic levitation, as a technology that provides a special physical environment for the crystallization process, allows the levitated liquid droplets to be in a state of containerless condition, so that the crystallization process will not be affected by the container wall, hence no contamination will occur. Moreover, there will be no contact with any solid surfaces for the newly grown crystal so that there will be no lattice distortion. Furthermore, the levitated containerless condition provides a unique and nearly perfect condition for realizing homogeneous nucleation. All these advantages are helpful for growing better quality crystals and helpful for studying the mechanism of crystallization. In addition, the physical properties of the acoustic wave may also affect the internal flows and the heat and mass transfer of the levitated drop, hence providing a new way to influence the crystallization process.

This chapter overviewed the existing researches that are already extensive. In the future, there will be still much work to do for further development using the acoustic levitation technique in crystallization. In particular, achieving challenging tasks (such as preparation of high-quality crystals) or contributing to frontier researches (such as sample delivery systems for serial crystallography) will be important research directions worthy of attention. In addition, acoustic levitation conditions can provide unique real-time dynamic conditions for the research of the crystallization process, so that the important fundamental research theme (like nucleation mechanism) can be studied in depth. Apparently, it can be expected that the acoustic levitation technique will play an essential role in the field of crystallization research.

References

1. R.J.K. Weber et al., Acoustic levitation: recent developments and emerging opportunities in biomaterials research. *Eur. Biophys. J. Biophys. Lett.* **41**(4), 397–403 (2012)
2. H.-L. Cao et al., Rapid crystallization from acoustically levitated droplets. *J. Acoust. Soc. Am.* **131**(4), 3164–3172 (2012)
3. J. Leiterer et al., Flying droplets as model system for spray drying—an *in situ* synchrotron X-ray scattering study on complex oxides catalyst precursors. *Catal. Today* **155**(3–4), 326–330 (2010)
4. S.E. Wolf et al., Early homogenous amorphous precursor stages of calcium carbonate and subsequent crystal growth in levitated droplets. *J. Am. Chem. Soc.* **130**(37), 12342–12347 (2008)
5. R. Tuckermann et al., Chemical analysis of acoustically levitated drops by Raman spectroscopy. *Anal. Bioanal. Chem.* **394**(5), 1433–1441 (2009)
6. M. Knutsson, Acoustic levitation—optimization of instrumental parameters of the LevMac instrument for protein crystallization applications. (Lund University, 2006), p. 91
7. S. Sacher, G. Krammer, Investigation of different crystal habits without chemical additives in a three-phase reactor. *Chem. Eng. Sci.* **60**(22), 6307–6312 (2005)
8. S. Santesson et al., Airborne chemistry coupled to Raman spectroscopy. *Anal. Chem.* **75**(9), 2177–2180 (2003)
9. J. Leiterer et al., Structure analysis using acoustically levitated droplets. *Anal. Bioanal. Chem.* **391**(4), 1221–1228 (2008)
10. J. Leiterer et al., Tracing coffee tabletop traces. *Langmuir* **24**(15), 7970–7978 (2008)
11. C.J. Benmore et al., Structural characterization and aging of glassy pharmaceuticals made using acoustic levitation. *J. Pharm. Sci.* **102**(4), 1290–1300 (2013)
12. J.K.R. Weber et al., Using containerless methods to develop amorphous pharmaceuticals. *Biochim. Biophys. Acta. Gen. Subj.* **1861**(1), 3686–3692 (2017)
13. C.J. Benmore, J.K.R. Weber, Amorphization of molecular liquids of pharmaceutical drugs by acoustic levitation. *Phys. Rev. X* **1**(1) (2011)
14. M. Agthe et al., Following in real time the two-step assembly of nanoparticles into mesocrystals in levitating drops. *Nano Lett.* **16**(11), 6838–6843 (2016)
15. Y. Ishikawa, S. Komada, Development of acoustic and electrostatic levitators for containerless protein crystallization. *Fujitsu Sci. Tech. J.* **29**(4), 330–338 (1993)
16. S. Santesson et al., Screening of nucleation conditions using levitated drops for protein crystallization. *Anal. Chem.* **75**(7), 1733–1740 (2003)
17. S.K. Chung, E.H. Trinh, Containerless protein crystal growth in rotating levitated drops. *J. Cryst. Growth* **194**(3–4), 384–397 (1998)
18. J. Leiterer et al., Acoustically levitated droplets—a contactless sampling method for fluorescence studies, in *Fluorescence Methods and Applications: Spectroscopy, Imaging, and Probes*, ed. by O.S. Wolfbeis (2008), pp. 78–84
19. F.J.S. Doerr, I.D.H. Oswald, A.J. Florence, Quantitative investigation of particle formation of a model pharmaceutical formulation using single droplet evaporation experiments and X-ray tomography. *Adv. Powder Technol.* **29**(12), 2996–3006 (2018)
20. S. Santesson, S. Nilsson, Airborne chemistry: acoustic levitation in chemical analysis. *Anal. Bioanal. Chem.* **378**(7), 1704–1709 (2004)
21. Y. Cerenius et al., Preliminary tests on the use of an acoustic levitator for liquid X-ray diffraction experiments. *J. Appl. Crystallogr.* **36**, 163–164 (2003)
22. J. Leiterer et al., The use of an acoustic levitator to follow crystallization in small droplets by energy-dispersive X-ray diffraction. *J. Appl. Crystallogr.* **39**, 771–773 (2006)
23. S. Tsujino, T. Tomizaki, Ultrasonic acoustic levitation for fast frame rate X-ray protein crystallography at room temperature. *Sci. Rep.* **6** (2016)
24. V. Cristiglio et al., Combination of acoustic levitation with small angle scattering techniques and synchrotron radiation circular dichroism. Application to the study of protein solutions. *Biochim. Et Biophys. Acta. Gen. Subj.* **1861**(1), 3693–3699 (2017)

25. S. Tsujino, A. Shinoda, T. Tomizaki, On-demand droplet loading of ultrasonic acoustic levitator and its application for protein crystallography experiments. *Appl. Phys. Lett.* **114** (2019)
26. Y.N. Samara et al., Using sound pulses to solve the crystal-harvesting bottleneck. *Acta Crystallogr. Sect. D. Struct. Biol.* **74**, 986–999 (2018)
27. B. Hadimioglu, R. Stearns, R. Ellson, Moving liquids with sound: the physics of acoustic droplet ejection for robust laboratory automation in life sciences. *Jala* **21**(1), 4–18 (2016)
28. W.J. Xie et al., Levitation of iridium and liquid mercury by ultrasound. *Phys. Rev. Lett.* **89**, 104304 (2002)
29. Z.Y. Hong et al., The liquid phase separation of Bi–Ga hypermonotectic alloy under acoustic levitation condition. *Chin. Sci. Bull.* **52**, 1446–1450 (2007)
30. Y.J. Lv, B. Wei, Supercooling of aqueous NaCl and KCl solutions under acoustic levitation. *J. Chem. Phys.* **125**, 144503 (2006)
31. D. Geng et al., Containerless solidification of Ag–Cu eutectic alloy under acoustic levitation condition. *Sci. Sinica. Phys. Mech. Astron.* **41**, 227–235 (2011)
32. N. Yan et al., Rapid solidification of acoustically levitated Al–Cu–Si eutectic alloy under laser irradiation. *Chin. Sci. Bull.* **56**, 912–918 (2011)
33. W.J. Xie et al., Interaction of acoustic levitation field with liquid reflecting surface. *J. Appl. Phys.* **107**, 014901 (2010)
34. Z.Y. Hong et al., Acoustic levitation with self-adaptive flexible reflectors. *Rev. Sci. instrum.* **82**, 074904 (2011)
35. W.J. Xie et al., Temperature dependence of single-axis acoustic levitation. *J. Appl. Phys.* **93**, 3016–3021 (2003)
36. J. Ren, W.J. Xie, Evaporation induced solidification of cyclohexane drops under acoustic levitation condition. *Acta Phys. Sin.* **60**, 114302 (2011)
37. C.P. Lee, A.V. Anilkumar, T.G. Wang, Static shape and instability of an acoustically levitated liquid drop. *Phys. Fluids A* **3**, 2497–2515 (1991)
38. R.G. Holt, E.H. Trinh, Faraday wave turbulence on a spherical liquid shell. *Phys. Rev. Lett.* **77**, 1274–1277 (1996)
39. Z.L. Yan et al., Surface capillary wave and the eighth mode sectorial oscillation of acoustically levitated drop. *Acta Phys. Sin.* **60**, 064302 (2011)
40. Z.Y. Hong et al., Surface wave patterns on acoustically levitated viscous liquid alloys. *Appl. Phys. Lett.* **104**, 154102 (2014)
41. W.J. Xie et al., Eutectic growth under acoustic levitation conditions. *Phys. Rev. E. Stat. Nonlin. Soft Matter Phys.* **66**, 061601 (2002)
42. N. Yan et al., A comparison of acoustic levitation with microgravity processing for containerless solidification of ternary Al–Cu–Sn alloy. *Appl. Phys. A* **120**, 207–213 (2015)
43. N. Yan et al., Phase separation and structure evolution of ternary Al–Cu–Sn immiscible alloy under ultrasonic levitation condition. *J. Alloy. Compd.* **544**, 6–12 (2012)

Chapter 9

Applications of Acoustic Levitation in Chemical Analysis and Biochemistry



Soichiro Tsujino and Takashi Tomizaki

Abstract The acoustic levitation is a versatile tool that can be used to study physical, chemical, or biochemical characteristics of liquid samples. By acoustically levitating samples in single droplets, their chemical or biochemical analysis and reactions can be investigated in the container-less condition in the absence of interactions between samples and container walls in ambient air as well as in controlled environments. In this chapter, we describe experiments on the single-droplet chemical/biochemical analysis, a recently proposed application for protein crystallography experiments, and relate instrumentation developments.

9.1 Application in Chemistry and Biochemistry

9.1.1 Introduction

Handling small particles or droplets to conduct container-less experiments by levitation in ambient air have been attracting researchers. Reported levitation experiments most often applied methods utilizing the electric or magnetic field, the focused laser beam, or the acoustic radiation [10, 11, 113]. Among these, while the so-called laser tweezers are powerful for manipulating micron to submicron size particles, methods using the electric or magnetic field have less restriction on the sample size. The acoustic radiation force can levitate samples with the size normally smaller than the sound wavelength, but it does not rely on special sample characteristics such as conductivity, magnetic susceptibility, or optical absorption. This advantage makes the acoustic levitation a versatile tool for studying physical, chemical, or biochemical characteristics of liquid samples in single-droplet and in container-less conditions without interactions between samples and container walls. The acoustic levitation experiments have been conducted in ambient air as well as in controlled environments at low temperature, high pressure, or under small gravity [34, 99, 116]. Several

S. Tsujino (✉) · T. Tomizaki

Paul Scherrer Institute, Forschungsstrasse 111, 5232 Villigen PSI, Switzerland
e-mail: soichiro.tsujino@psi.ch

works have been reported in the literature that conducted single-droplet chemical or biochemical analysis by taking advantage of these unique properties of the acoustic levitation. In this section, we describe such applications of the acoustic levitation for chemistry and biochemistry in single droplets.

9.1.2 *Chemistry in Single Droplets*

In most of the reported experiments, acoustic levitation experiments were conducted by using single-axis acoustic levitators, wherein an acoustic standing wave is excited in the acoustic cavity of the levitator and a droplet is levitated near one of the pressure nodes of the standing wave (see Chap. 1–3). In the case of a single-axis acoustic levitator operating at the ultrasound frequency of 20–40 kHz, the loading of liquid droplets with the volume of 0.5–6 μl (diameters of a few mm) can be achieved, e.g., by dispensing droplets from a syringe while placing the tip of the syringe at around one of the pressure nodes [51, 113]. This allows for handling of μl -volume samples without contaminations from containers and loss of analytes by absorption/reaction on/with container walls [75, 81, 113]. When combined with spectroscopic tools, samples can be studied without parasitic background signals from absorption and scattering of the light by containers [48].

When the acoustic levitation is applied for the analysis of chemical reactions, triggering of the chemical reactions can be easily done by dispensing the reactants to the solution of the levitated droplets. One of the first such experiments was conducted by Rohling et al. by combining a single-axis acoustic levitator with piezoelectric micropumps for the determination of analytes in the levitated single droplets [75]. Using the micropumps, reagent solutions and solvents with the volume of 0.25–1.5 nl were added to a levitated droplet with the volume below 5.6 μl . By measuring the optical absorption or fluorescence by a VIS/UV spectrometer, they monitored the progress of the microtitration in the levitated droplet. The reduction of the liquid during the experiment was monitored and compensated by the micropump dispenser.

In the experiments reported in [53, 54, 79, 82], the acoustic levitator was coupled with a flow-through microdispenser [46, 93] that was capable to dispense a well-defined sequence of picoliter reagents to the levitated droplet solution. Lopez-Pastor et al. reported an experiment that monitored the Knoevenagel condensation reaction in levitated droplets utilizing a system as shown in Fig. 9.1. By Raman spectroscopy, they monitored the reactions in the levitated droplet online. For that, they added several types of reagents to the levitated droplet in a well-defined sequence [54]. In another system of the chemical reaction experiments using the acoustically levitated droplet that was reported by Schneeline et al., a bundle of two inlet capillaries connected to reactant reservoirs and a capillary connected to a vacuum was added to the single-axis acoustic levitator [68, 86]. This way, they were able to study chemical reactions while remotely controlling the generation of μl droplets, the introduction of reactants into levitated droplets, and the removal of the levitated fluid after the chemical reaction. Experiments conducted in such a system include the kinetic

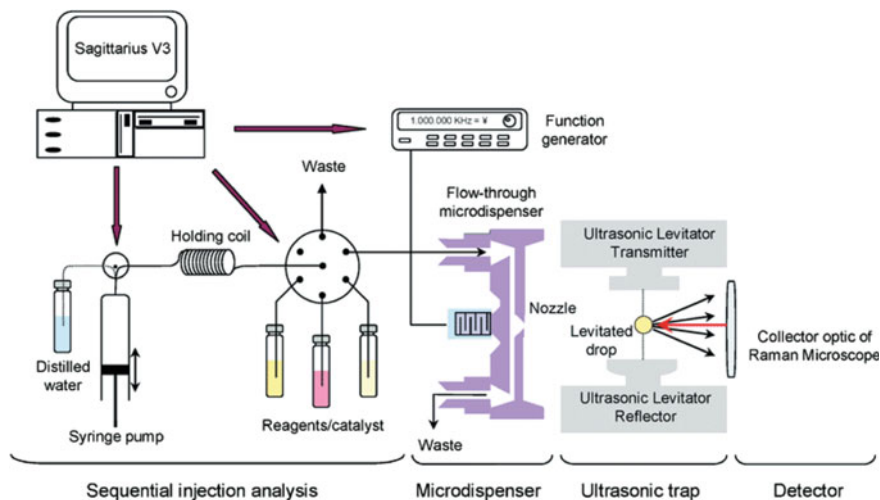


Fig. 9.1 Experimental setup consisting of flow system for liquid handling, microdispenser, ultrasonic levitator, and Raman microscope. From [54]

measurements of the luminol chemiluminescence and the reaction of pyruvate with nicotinamide adenine dinucleotide catalyzed by lactate dehydrogenase [68]. These single-droplet chemical reaction experiments demonstrated the feasibility of using an acoustically levitated droplet as a microreactor in conjunction with an appropriate instrument for handling sample and reactant.

The time resolution of such single-droplet chemical reactions is partly limited by the mixing time of the reactant solution with the levitated droplet. Chainani et al. studied the progress of a solution mixing between a levitated droplet of $3.7 \mu\text{l}$ of 0.058 M HCl (pH: 1.24) with a droplet of 370 nl of 0.25 M KOH (pH: 13.4) via the change of phenolphthalein absorption [15]. There, an electrostatic droplet launcher ejected KOH droplets. The subsequent mixing of the ejected KOH droplets with the levitated HCl droplet upon collision and coalescence was monitored by recording the color change of the levitated droplet using a high-speed camera. After the coalescence, the momentum of the dispersed KOH droplets induced positional oscillation and orbiting of the droplet with the period in the order of a few hundred milliseconds and with the oscillation amplitude as large as $\sim 10 \text{ mm}$. Therefore, the evaluation of the mixing time in such experiments required the analysis of the moving droplet. From the analysis, they found the mixing time equal to 2 s .

The collided and coalesced droplets induced the internal circulation of liquid in the levitated droplet by their momentum and was reduced the mixing time substantially. Other processes that contribute the mixing time includes the inter-diffusion of the two liquid and the convective flow inside the levitated droplet [14]. The latter is induced by acoustic streaming [1, 65, 74, 83, 100, 121, 124]. Further acceleration of the mixing is possible by exciting the Rayleigh surface mode [67] of the levitated droplets to shake the liquid by their shape oscillation [15, 107]. Chainani

et al. demonstrated an order of magnitude reduction of the mixing time by the shape oscillation that was induced by applying an amplitude modulation of the ultrasound acoustic pressure at the corresponding resonance frequency equal to ~150 Hz [15].

9.1.3 *Chemistry in Ionic Liquid and Liquid Marbles*

To design a single-droplet experiment using the acoustic levitation, one should be aware of the evaporation of the liquid contents, since it can change the reaction chemistry. This may be the case when the reaction under study takes longer than a few minutes: in the case of a water droplet in ambient air (at 20 °C and the relative humidity of ~40%), when the initial droplet diameter is 1 mm, it decreases to 0.5 mm in ~300 s by evaporation. The evaporated liquid can be compensated by continuous or intermittent dispensing using on-demand dispensers [75], although it can cause positional oscillations of the levitated droplet [9, 15, 54, 102].

Use of ionic liquids is an interesting way to overcome the liquid evaporation [53, 54, 85]. Ionic liquids have a low melting point and are liquid at room temperature in contrast to typical ionic compounds such as sodium chloride. Because of the strong ionic interactions between cation and anion, ionic liquids have a negligible vapor pressure in ambient condition. This property makes those ideal solvents for single-droplet experiments in ambient air that demand duration much longer than a few minutes.

Another interesting way to avoid the liquid evaporation is to use liquid marbles produced by encapsulating an aqueous droplet with a hydrophobic powder [3, 17, 122]. Zang et al. conducted an experiment to acoustically levitate liquid marbles prepared from 20 µl water droplets encapsulated by polytetrafluoroethylene (PTFE) particles with 5 µm diameters [122]. They found that increasing the ultrasound pressure selectively exposed the liquid at the top and the bottom polar areas of the levitated liquid marbles, that again closed by decreasing the ultrasound pressure. By utilizing this property, they added a block of KMnO₄ into the water within the liquid marble and changed the droplet color, see Fig. 9.2.

9.1.4 *Analysis of Biochemical Reactions, Cells, and Living Animals in Single Droplets*

The container-less sample delivery of the acoustic levitation is also advantageous for the analysis of biological macromolecules because of the absence of possible contaminations from containers and the influence of the container walls on the samples and their reactions. The substantial ultrasound pressure (2–3 kPa-rms) required to levitate a droplet in air is often a concern for handling fragile samples. However, the high ultrasound pressure appears to have no adverse effect on biological

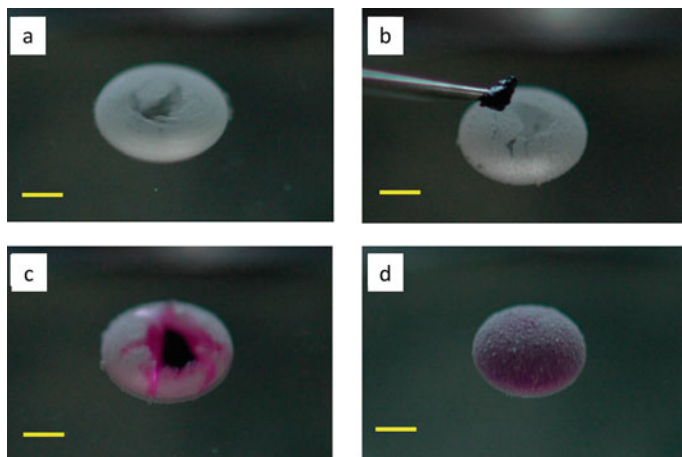


Fig. 9.2 Liquid marble acting as a microreactor: **a** once the cavity emerges, **b** a block of KMnO_4 is added to the liquid marble, **c** KMnO_4 dissolves, and **d** particle shell of the liquid marble recovers to the initial state upon decreasing the sound intensity. Scale bar = 1 mm. Adapted from [122]

specimens in levitated droplets as indicated by several successfully conducted experiments described below. This can be ascribed to the fact that the transmission of the ultrasound into the droplet liquid through the air–liquid interface is normally small (below $\sim 0.1\%$) because of the large acoustic impedance mismatch between air and liquid.

In the experiments reported in [112], Weis and Nardozzi studied the enzyme kinetics in acoustically levitated droplets; the authors measured the rate of the alkaline phosphatase-catalyzed hydrolysis of 4-methylumbellifluorone phosphate in acoustically levitated droplets of aqueous tris (50 mM) at pH 8.5 at $22 \pm 2^\circ\text{C}$ by monitoring the variation of the fluorescence spectra of the levitated solution. As a result, they found that the rate of the product formation was in excellent agreement with the rate observed in bulk solution in a cuvette, indicating that the acoustic levitation does not alter the enzyme activity. In the same work, the authors lowered the droplet temperature down to $-6 \pm 2^\circ\text{C}$ in a supercooled solution by taking advantage of the absence of the sample container. This way, they were able to observe that the rate of the same reaction decreased sixfold at $-6 \pm 2^\circ\text{C}$ from that at $22 \pm 2^\circ\text{C}$ in the solution environment.

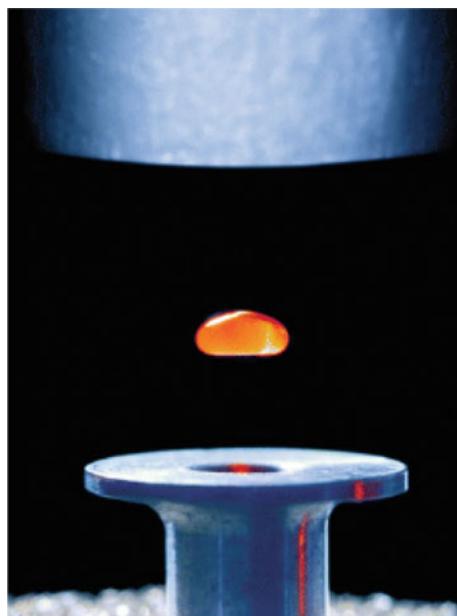
Santesson et al. reported another example of biochemical reactions study using the acoustic levitation. In the experiments described in [79, 82], the authors studied the biochemical reactions in single cells and the biochemical communications between cells that were contained in levitated droplets for investigating processes related to Type-2 diabetes. In particular, hormone-mediated regulation of adipocyte lipolysis and the regulation of adipocyte lipolysis by cell-cell communication between adipocytes and β -cells were observed at the few-cell level. Their results demonstrated

the potential for future analysis based on the acoustically levitated single drops as the “wall-less” test tubes for human cells obtained from clinical biopsies.

For probing and analyzing the chemistry and biochemistry in the acoustically levitated droplet samples, several groups have reported the combination of Raman spectroscopy as a direct molecular probe of the sample chemistry [4, 9, 20, 53, 54, 69, 70, 97, 104, 118]. In the work reported in [69], the heme dynamics of red blood cells in a levitated 5 μl suspension (Fig. 9.3) was monitored. In addition, the detection of hemozoin in malaria infected cells was demonstrated. In yet another experiment conducted by Wood et al., a portable Raman acoustic levitation spectroscopic system for environmental monitoring was developed [118]. They demonstrated that the combination of the Raman spectrometer with the acoustic levitation enabled the analysis of living algal cells in a contactless environment resulting in a 15-fold increase in signal-to-noise ratio, as compared to spectra of samples containing a similar number of cells in a microcuvette.

The work by Xie et al. demonstrated the acoustic levitation of small living animals, such as ant, ladybug, and small fish [120]. The authors found that there was no apparent influence of the ultrasound on the vitality of ant and ladybug, but the vitality of young fish was reduced because of the inadequacy of water supply. In the work reported in [92], Sundvik et al. studied the influence of the acoustic levitation on living animals extensively. In particular, the authors explored if zebrafish embryos can be levitated without causing any effects on their early developments and observed no statistically significant effect for the duration less than 2000s. The result indicated that acoustic levitation can be used as a non-contacting wall-less platform for characterizing and manipulating vertebrae embryos without causing major adverse effects to their development.

Fig. 9.3 A 5 μl drop containing red blood cells in phosphate buffered saline (PBS) levitated in a node of a standing wave created between an ultrasonic transducer (bottom) and a concave reflector (top). From [69]



9.1.5 High Sensitivity Analysis with the Combination of Mass Spectroscopy, Raman Spectroscopy, and Other Methods

Coupling of the acoustic levitation with the mass spectroscopy, which is yet another highly sensitive method for chemical analysis, has been explored by several groups [19, 52, 61, 91, 106, 114]. One of the advantages of the acoustic levitation is in eliminating the interference of the sample support [106] at the step of interfacing fragile samples (such as protein), for example, in the case of the matrix-assisted laser desorption/ionization (MALDI) [94].

Mass spectrometry experiments utilizing other sample ionization methods have been successfully conducted with acoustically levitated single droplets. In [19], the authors demonstrated the real-time reaction monitoring of acid-catalyzed degradation in a levitated 6 μl droplet using the direct ionization in real-time (DART) ionization. In [61], the field-induced droplet ionization mass spectrometry (FIDI-MS) was demonstrated. Using the equipment shown in Fig. 9.4, the authors investigated the details and consequences of the reactions between the photosensitizer-generated singlet oxygen and substrate molecules that are relevant to the photodynamic cancer therapy. By conducting experiments with the levitated droplets with 4 μl in volume, they were able to probe the highly reactive and easily degrading product of lipid oxidation without the extensive sample handling and transfer required for standard methods.

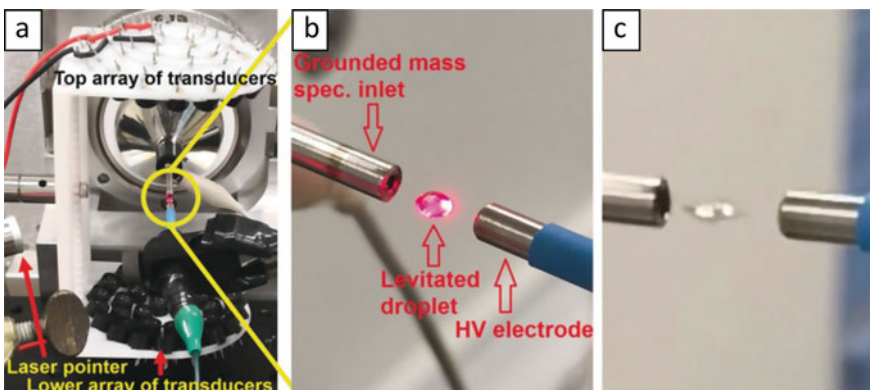


Fig. 9.4 The experimental setup of acoustic levitation coupled with field-induced droplet ionization mass spectrometry (FIDI-MS). **a** The overall arrangement of the levitator, FIDI electrodes, and mass spectrometer. **b** A levitated and illuminated droplet sandwiched by the two FIDI electrodes, one of which is the atmospheric pressure sampling input of the mass spectrometer and the other is the high voltage electrode. **c** Bipolar Taylor cones form upon triggering the FIDI voltage. Adapted from [61]

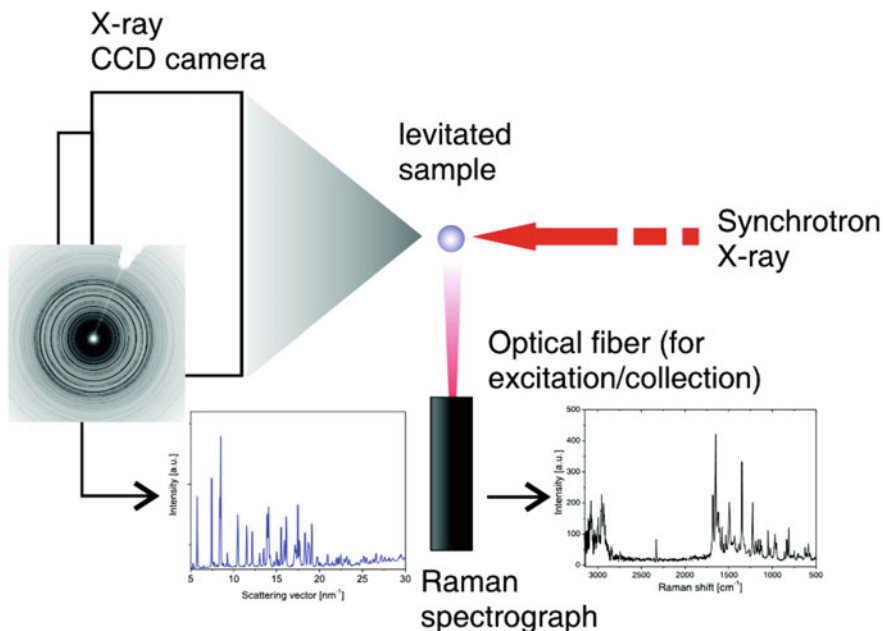


Fig. 9.5 Setup of the XRD/Raman experiment used to follow the crystallization of nifedipine in levitated droplets. From [43]

Several groups have reported the application of the acoustic levitation for preparation and processing of amorphous pharmaceuticals and biological macromolecules [6, 7, 26, 84, 108, 109, 88, 73], and crystallization/agglomeration of proteins and other molecules [8, 16, 18, 23, 41, 43, 47–50, 71, 80, 117] upon drying the levitated solution droplets. Some of those works combined the acoustic levitation with *in situ* X-ray characterization methods and/or Raman spectroscopy, see Fig. 9.5. Such single-droplet drying experiments in acoustic levitators [33, 50, 94] are also relevant to investigate the spray drying behavior of foods [84, 85].

9.2 Application of Acoustic Levitation for Protein Crystallography

9.2.1 Introduction

The application of the acoustic levitation for protein crystallography experiments has been proposed recently [22, 98, 101–103]. One of the development targets of the instrument, the acoustic levitation diffractometer (ALD), is to realize a high-throughput fully automated protein crystallography pipeline at room temperature.

Such an instrument will have a significant impact on the screening efficiency and throughput of drug developments. Another important target of ALD is to conduct experiments to study conformational dynamics and biochemical processes in single-crystals at room temperature that are difficult to conduct in conventional cryo-X-ray diffraction or cryo-electron microscopy (EM) measurements. Using ALD, room temperature protein structure dynamics can be studied in the time-scale of seconds to minutes. This is complementary to the serial femtosecond crystallography (SFX) and synchrotron serial crystallography (SSX) methods covering the femtosecond to millisecond timescales using X-ray-free electron lasers (XFELs) and synchrotron sources. In this section, we describe the background and the current status of the ALD development.

9.2.2 *Background and Motivation*

X-ray diffraction is one of the most established methods for the structural analysis of biological macromolecules. It is essential to determine the atomic configuration of biological crystalline specimens and to investigate the three-dimensional structure of synthetic molecules. The atomic structure of a protein crystal can be solved from the intensities of Bragg reflections from 10^4 to 10^6 that are reconstructed from a dataset consisting of 10^2 to 10^4 or more X-ray diffraction images. Datasets are collected by irradiating an X-ray beam to single protein crystals from various crystal orientations while limiting the total X-ray dose per crystal to avoid the radiation damage.

By combining a highly brilliant X-ray beam available at synchrotron facilities with a high-frame-rate two-dimensional pixelated X-ray image detector with the single-photon sensitivity [25, 35], the collection time of a complete dataset of X-ray diffraction images per sample has been reduced to a few tens of seconds. Acquisition rates that are now routinely above 10 Hz enable the continuous rotation of the protein crystal maintained at *cryogenic* temperatures. Such technological advancements have been constantly improving the throughput of the instruments. Nevertheless, further improvement of the throughput is demanded for applications related to drug developments: In the case of the structure-based drug discovery (SBDD), the high-throughput is of particular importance. The goal of SBDD is to find certain ligand molecules that bind to a target protein and hence can be used as the starting points of the drug development. For this search, a large number of ligand–protein complexes have to be screened. This often requires multiple ligand binding structures with a structurally diverse set of compounds to investigate the interaction with the target protein in all detail. Not only the combination of the ligand–protein complexes but also various conditions (concentration of the ligand solution, duration, temperature, as well as the condition for the crystal growth, etc.) have to be tested to increase the hit rate of the structure determinations. Such screening of compound libraries of several thousand molecules by the application of X-ray crystallographic methods requires substantial experimental efforts, since it will demand the collection of several thousand datasets

[36, 42]. In comparison, the typical throughput on the state-of-the-art protein crystallography beamlines at synchrotrons, such as I04–1 of the Diamond Light Source [58], is limited to a few hundred datasets per day.

The prerequisite of successful crystallography experiments is the preparation of high-quality sample; the optimal condition of crystallization is carefully searched and chosen to prepare samples with sufficient qualities to solve the structure at atomic resolution, that is, to solve the structure at a resolution better than ~ 2 Å. Protein crystals are typically prepared on a multi-well (e.g., 12×8) crystallization plate. The sample size can be small, in the order of $10\text{--}20$ μm , or in the order of $100\text{--}500$ μm , especially for crystallography experiments of the conformational dynamics or ligand-binding screening experiments, where the crystal structures of samples should be well established.

To conduct a conventional cryo-X-ray diffraction experiment from these samples, firstly, a sample is manually harvested from one of the wells of a crystallization plate using a sample holder that also acts as the sample holder for the X-ray diffraction experiment. The harvested sample is then frozen and eventually delivered to the X-ray beam. The overall throughput of the X-ray diffraction experiments is limited not only by the efficiency of the data collection but also by these preparation steps. In fact, the time-consuming manual steps, the preparation of sample holders and the manual harvesting of crystals, are the bottleneck of the overall throughput. Therefore, when fast and efficient methods of automated crystal harvesting and delivery, utilizing, e.g., on-demand acoustic droplet ejection, are combined with ALD, the overall throughput of X-ray diffraction experiments might be several orders of magnitude larger than the state of the art.

In contrast to conventional experiments at cryo-conditions, room-temperature experiments will not only enable the rapid screening of crystals but also facilitate the investigation of the conformation diversity of biological macromolecules that are difficult to study with cryo-cooled specimens [30, 40]. At room temperature, the protein crystals are closer to physiological conditions. Therefore, faster data acquisition will open up a range of possible experiments that are difficult with the standard instruments. These include *in situ* structural dynamics studies of the conformational variation of proteins and binding of proteins with small molecules (ligands).

With the recent advent of the high-resolution EM, the application of the cryo-EM for the structural analysis of large protein molecules has been rapidly increasing. In cryo-EM, protein samples are dispensed on a TEM grid and frozen, and a large number of ($>10^5\text{--}10^6$) real-space images of single molecules orienting various directions are collected. From such a dataset, the three-dimensional structure of the protein molecules is reconstructed by tomographic synthesis. The cryo-EM has an advantage of eliminating the crystal growth step, which is normally the critical step in the X-ray diffraction experiments. However, high-throughput data collections for the binding of target proteins with small ligand molecules, as required for SBDD, are still difficult with cryo-EM. Also, because of the requirement of vacuum and cryo-cooling, it is difficult to conduct dynamical studies of proteins in physiological conditions. Differently from cryo-EM, the structural analysis of proteins by X-ray diffraction is not only capable to solve the static structure of samples with unknown structures, but

also able to investigate the time-dependent biochemical processes such as enzymic reactions and the conformation dynamics of molecules induced by pH stimulus or light excitation. Recently, ultrafast conformational dynamics has been successfully studied by femtosecond SFX using the X-ray-free electron lasers down to femtosecond timescales at room temperature. Complementary to such studies, experiments on slower timescales (millisecond and slower) have been rapidly advanced using synchrotron X-ray sources in combination with two-dimensional pixelated X-ray image detectors.

From these backgrounds, the development of the ALD instrument is underway at the Paul Scherrer Institut, Switzerland, with the purpose of realizing a high-throughput automated crystallography pipeline at room temperature. To achieve this goal, one has to surmount the throughput bottleneck due to the manual sample harvesting and delivery at the state-of-the-art synchrotron beamlines. This will be achieved by combining the ALD with an automated sample ejector. The ejector may be based on, e.g., acoustic droplet ejection [27, 28] of a sample with the crystallization liquid. The ejected droplet is subsequently captured by the acoustic levitator. This way, the sample harvesting and delivery will be achieved in one automated step without using sample holders.

Another purpose of developing ALD is to conduct experiments on the room-temperature dynamics of single-crystal protein samples. For this, we take advantage of the fact that the crystal is in the levitated droplet at room temperature. By exciting the sample optically or adding a ligand solution to change the chemical content of the levitated droplet, it will be possible to study the conformational dynamics or ligand-binding process in seconds-to-minutes timescales using single-crystal sample that is difficult with conventional crystallography experiments. The possibility to observe slow processes makes ALD a complementary method to the ultrafast experiments using the XFELs and synchrotrons.

9.2.3 Acoustic Levitation Diffractometer

In the ALD instrument, a highly brilliant X-ray beam that is available at synchrotron facilities is combined with a single-axis acoustic levitator and a high-frame-rate pixelated X-ray image detector, see Fig. 9.6. Single protein crystal samples are inside the acoustically levitated droplets loaded at the middle node of the levitator. In the reported ALD experiments, the acoustic levitator was excited by an ultrasound with the frequency of ~39 kHz (with the corresponding wavelength λ of 8.7 mm in air at 20 °C).

The top right panel in Fig. 9.6 displays the typical time-averaged pressure distribution (the high- and low-pressure regions are dark and light, respectively) imaged by Schlieren method at ultrasound pressure amplitude nominally in the range of 2.6–3 kPa-rms. By exciting an ultrasound standing wave in the acoustic cavity of the levitator, the time-averaged pressure and velocity are induced via the nonlinearity

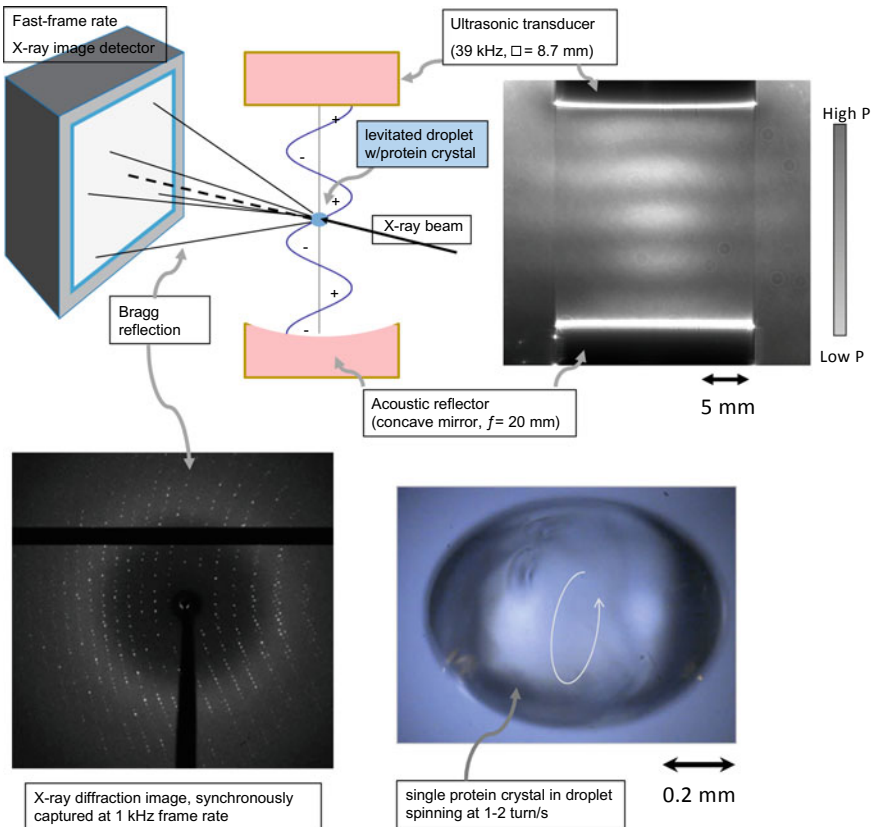


Fig. 9.6 Schematic of the acoustic levitation diffractometer. The top right panel displays the time-averaged pressure in the acoustic levitator imaged by Schlieren method. The bottom right panel shows an example of a levitated droplet with a single protein crystal therein. The bottom left panel shows one of the X-ray diffraction images from the crystal collected during the experiment.

of air and the resultant acoustic radiation force can levitate droplets (see Chap. 1–3) with high positional stabilities [103]. The levitator acoustic cavity is typically adjusted to the fifth resonance (the distance between the transducer and the reflector approximately equal to $n\lambda/2$ with n equal to 5). This way, a large stereo angle from the sample to the detector screen is secured to collect Bragg reflections up to 1.5–2.5 Å resolution without being shadowed by the transducer or mirror.

In ALD experiments conducted at the Paul Scherrer Institut on the beamline X06SA of the Swiss Light Source, a highly brilliant X-ray beam with the beam size in the range of 100–200 μm (depending on the sample type and sample size) irradiated a protein crystal sample in an acoustically levitated droplet while the sample rotated inside the droplet. The sample (lysozyme, with the size of ~0.5 mm) depicted in the right bottom panel of Fig. 9.6 was in the levitated droplet of the crystallization liquid (water with PEG) with the diameter of ~0.8 mm. Bragg reflections from the sample at

various crystal orientations were collected by a high-frame-rate X-ray image detector EIGER X 1M or 16M [25], which captured diffraction signals with the frame rate up to 3 kHz when the crystal was rotated at \sim 1 turn/s. The bottom left panel in Fig. 9.6 shows one of the frames of the collected X-ray diffraction images recorded at 1 kHz. The crystal rotation speed of \sim 1 turn/s matched well with the crystal rotation angle per frame (below \sim 1°) for the frame rate of the available detectors as well as the typical photon flux of the X-ray beam (\sim 10¹² photon/s) to secure the necessary dose to record high-resolution Bragg reflections.

Inside the acoustically levitated droplet, acoustic streaming creates the internal circulation of the liquid [1, 65, 74, 83, 100, 121, 124]. This in turn induces the spinning and orbiting of the crystal therein. The crystal rotation, that was \sim 1 turn/s in the above example, can be increased to several tens of turn/s. Therefore, data collection speed/time is not limited by the levitator but by the detector frame rate and the X-ray photon flux. Orbiting of samples in the levitated droplets can cause displacement of the sample from the X-ray beam when the crystal is much smaller than the levitated droplet. Nevertheless, the positional stability of a crystal with the size of 100–200 μ m inside a levitated droplet with the diameter of 1 mm within 10–50 μ m has been possible for the duration of \sim 30 s. This allowed for collecting more than 10⁴ to 10⁵ images within 2–30 s to record the ligand-binding processes of protein crystals [98] (see Sect. 9.2.4).

By applying the recently developed data processing methods for SFX [115], individual X-ray diffraction images were indexed, i.e., the lattice unit-cell dimension, the crystal orientation, and the corresponding lattice indices of the observed Bragg reflections were analyzed. Figure 9.7d–f shows the evolution of the crystal orientation obtained from the indexing of X-ray diffraction images such as those depicted in Fig. 9.7a–c recorded at 130 Hz. Such parameters evaluated from the entire dataset were integrated and used to solve the crystal structure of the sample at atomic resolution as shown in Fig. 9.8. The electron density that was solved and refined from the ALD dataset is shown in Fig. 9.8a. To study the potential influence of the acoustic pressure on the crystal structure, the electron density was compared with the electron density shown in Fig. 9.8b. This was solved from a dataset acquired by a conventional method (oscillation method) for another samples but simultaneously prepared on the same crystallization plate. It was found that the two structures were nearly identical. In particular, both densities exhibited similar coordinate bonding of the water molecules (blue) and the metal atoms (sodium in red and chloride in cyan). In addition, the disulphide bridge lengths that are normally used as a measure of the crystal damage caused by radiation [12] were compared for the two structures and were found to be identical within 0.02 Å. These results indicate that the crystal structured remained intact during the ALD experiment in the ultrasonic acoustic radiation.

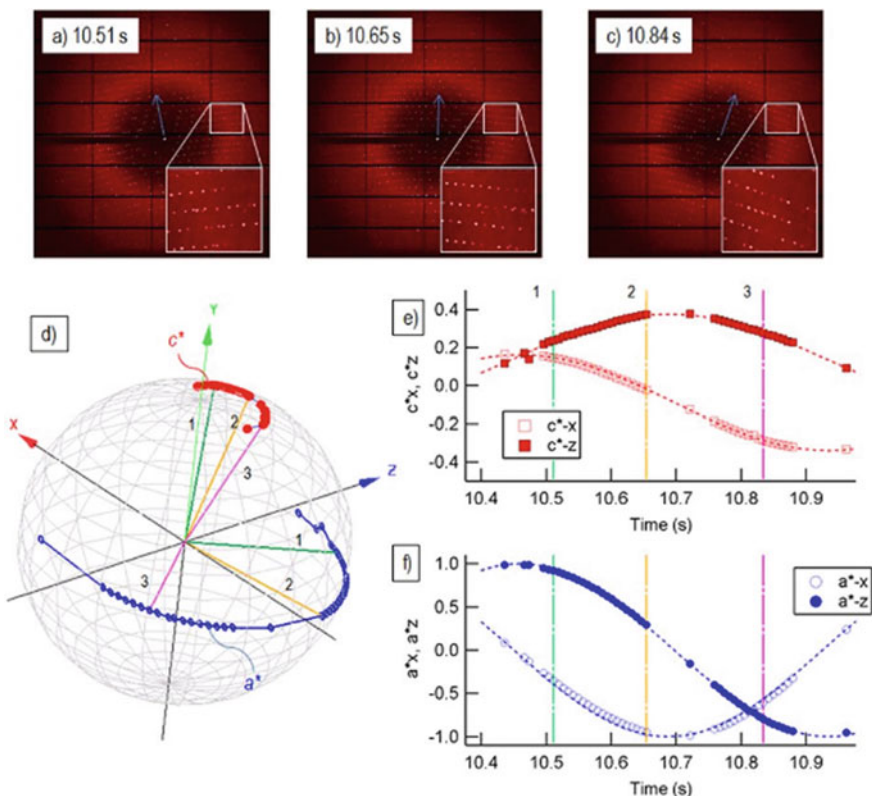


Fig. 9.7 Snapshots of the X-ray diffraction images from one of the datasets. (a–c) were acquired, respectively, at 10.51, 10.65, and 10.84 s after the start of data acquisition. (d–f) The time evolution of the crystal orientation evaluated from the indexed diffraction spots. The directions of a^* and c^* are indicated on the Gauss plot (d), together with the evolution of a^* and c^* for the time between 10.4 and 10.9 s: the crystal spins with c^* direction as the spin axis about ~ 1 rotation per second, corresponding to $1\text{--}2^\circ$ per frame. In this example, c^* was nearly along the y-direction. (e, f), respectively, show the x- and z-component of the unit vectors parallel to a^* and c^* within this time interval. The time marked as 1, 2, and 3 in (d–f), respectively, corresponds to the acquisition time of the images (a–c). From [101]

9.2.4 Single-Crystal Time-Lapse Measurement in Levitated Droplets

Investigation of dynamical characteristics of biological macromolecules has been reported in the literature by conducting time-resolved X-ray diffraction experiments using XFELs and synchrotrons by using various sample delivery methods [13, 38, 64, 110, 111]. Some of the drawbacks of these experiments include the requirement of a large number of crystals and the limited timescales of observations below 100 milliseconds. The latter also limits the flexibility of the type of the stimuli that trigger

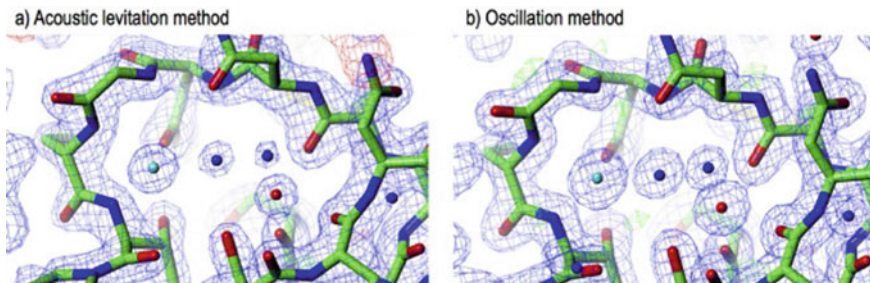


Fig. 9.8 Comparison of the electron density solved and refined from the acoustic levitation method (a) and from the conventional oscillation method (b). The figures depict a part of $2F_o-F_c$ electron density maps rendered by CCP4MG [59]. The electron density maps were calculated at 1.5σ . The contour level of the F_o-F_c map is at $\pm 3\sigma$. Sodium (red) and chloride (cyan) atoms and water molecules (blue) are also shown. From [101]

the protein dynamics to those that act quickly, such as optical excitations, as in the ultrafast experiments. In ALD, the crystal in the levitated droplet at room temperature can be kept stably for the duration of seconds to several minutes. Therefore, one can study slow protein reactions triggered not only by fast stimuli but also by other methods that require longer time until they act on the crystal. These include the soaking of ligand solution, i.e., modifying the chemical content of the levitated droplet by dispensing solution of small molecules that can bind the host protein crystal.

A pilot ALD experiment to observe such a ligand-soaking process was reported in [98]. There, a ligand-binding process between lysozymes and *p*-Toluenesulfonic acid was studied. In the experiment, first a test sample with the size of $\sim 300 \mu\text{m}$ was loaded (rotated at a few turn/s) in a levitated droplet with the diameter of $\sim 0.5 \text{ mm}$. Then, X-ray diffraction images from the sample were collected before/during/after $0.5\text{--}1 \mu\text{l}$ droplets of *p*-Toluenesulfonic acid solution at a concentration of 500 mM were dispensed to the levitated droplet. To dispense the solution, multiple (5–10) droplets of the solution were ejected from both sides of the levitated droplets using two dispensers. This way, the positional fluctuation of the levitated droplet upon dispensing the solution was subsided within 1 s. The mixing time of the solution with the levitated droplet was also minimized to $\sim 1 \text{ s}$ at the same time.

Datasets consisting of 6000 diffraction images were collected every 30 s at 3 kHz, and the crystal structure was solved from each time period. In Fig. 9.9a, b, the solved electron density maps ($2F_o-F_c$ maps) before and 30 s after soaking the crystal with the ligand solution were shown. The comparison of the two clearly indicates the emergence of the *p*-Toluenesulfonic molecule bound to a specific side chain, asparagine 19 (ASN 19) as indicated by allowing inside the box, after the soaking. Close inspection of the electron density maps further revealed that the electron density of the side chain (ASN 19) that was unclear before the soaking became distinctly visible after the ligand binding. This observation was tentatively ascribed to the stabilization of the spatial movement of the side chain by the formation of hydrogen

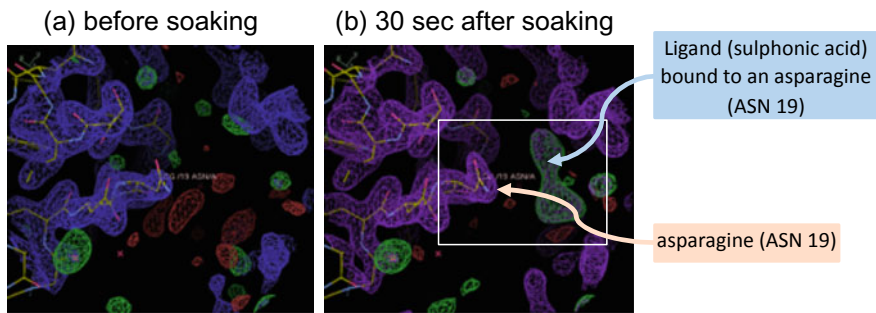


Fig. 9.9 Electron density maps (parts of $2F_o - F_c$ maps) of a lysozyme crystal solved and refined from the room-temperature ALD experiment. **a, b** show the electron density (**a**) before and (**b**) 30 s after dispensing the ligand solution to the levitated droplet with the test sample therein. Adapted from [98]

bonds by the ligand binding. This result demonstrates the feasibility of the room-temperature time-lapse experiment using ALD to detect the ligand-binding processes.

9.2.5 On-Demand Loading of Acoustic Levitator with Small Droplets

An on-demand droplet ejector for sample harvesting and delivery is particularly important for the high-throughput protein crystallography experiments using ALD as described in Sect. 9.2.2. As a first step toward this goal, the droplet loading was tested using a commercial drop-on-demand (DoD) dispenser (Pipejet nanodispenser, BioFluidix GmbH) in experiments reported in [102]. The experiments focused on the droplet capturing process in the acoustic levitator for droplets with the diameter below ~ 0.5 mm, that are difficult to achieve by using syringes with the same sizes (that is necessarily for loading crystals therein) because of the capillary force. Figure 9.10 shows snapshots from a high-speed-camera recording of a successful event of the ejection and the capture of a water droplet with the diameter of ~ 0.5 mm. Figure 9.10d depicts the trajectory of the droplet evaluated from the same recording, showing the relaxation oscillation of the captured droplet within the middle node. For stable and repetitive droplet ejection, setting the ejection velocity of the droplet to 0.5–1 m/s is required. At the same time, to capture the droplet by the levitator, the droplet velocity when it enters into the levitator has to be sufficiently low. To fulfill these requirements, the droplet with the velocity of ~ 0.5 m/s was ejected from afar (bottom right corner). Owing to the subsequent reduction of the velocity by the drag force and the gravity, the droplet velocity was reduced to ~ 0.3 m/s, that lead to the successful capture of the droplet by the levitator. Even though the loading was successful for this event, the required precise alignment and the sensitivity of the droplet trajectory to the disturbances of surrounding air, as well as the necessity to adjust the levitator

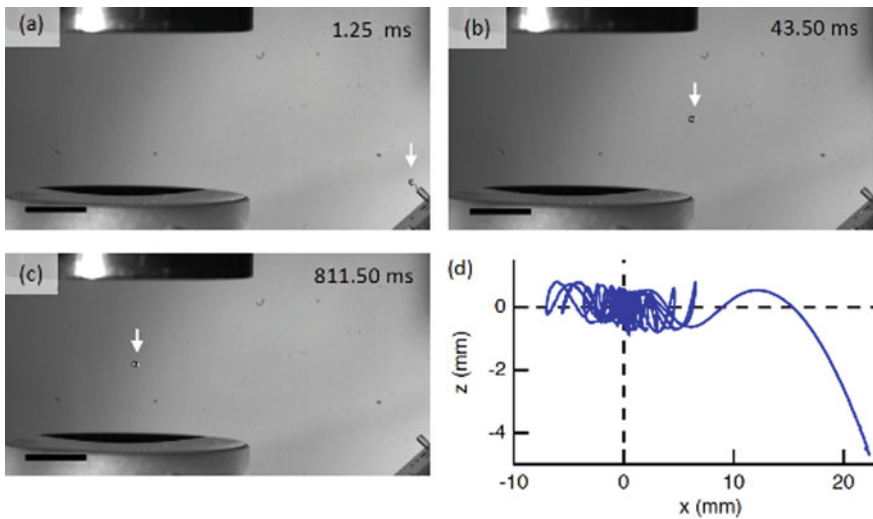
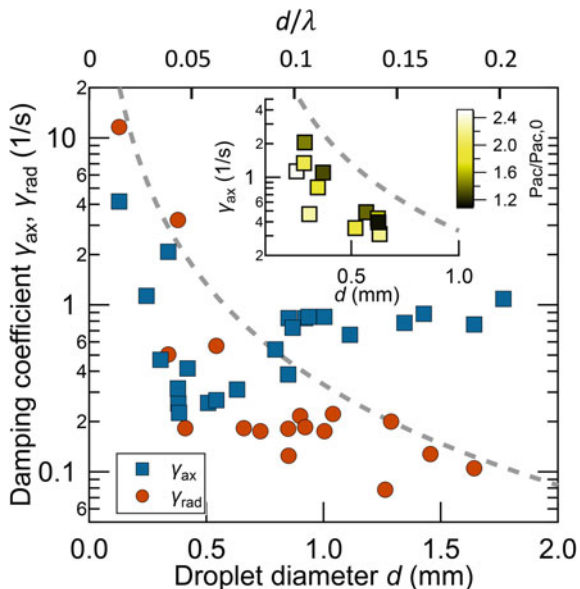


Fig. 9.10 On-demand loading of an acoustic levitator with a water droplet. **a–c** Selected time frames of the droplet loading to the acoustic levitator when the droplet was ejected from the drop-on-demand dispenser (right bottom corner). These were recorded using the high-speed camera at the frame rate of 4 kHz. The scale bar is 5 mm. **d** shows the droplet trajectory over 1 s (center-of-mass motion) evaluated from the recorded event. From [102]

to the third resonance instead of fifth (to increase the ultrasound pressure) were not optimal for practical applications. Further, it was desirable to shorten the relatively long (1–10 s) settling time of the droplet oscillation.

The damping coefficient γ of the relaxation oscillation of a spherical particle/droplet in acoustic levitators such as the one shown in Fig. 9.10d is normally assumed to be given by the ratio γ_S of the Stokes coefficient equal to $6\pi\mu(d/2)$ to the particle mass $(4\pi/3)\rho(d/2)^3$, where $\mu = 1.85 \times 10^{-5}$ Pa·s is the viscosity of ambient air at 20 °C, d is the particle diameter, and ρ is the density of the particle/droplet. However, it was found that γ evaluated from Fig. 9.10d largely deviated from γ_S . This phenomenon was studied in detail in [103]. The result summarized as the relationship between γ and d for d in the range of 0.1–2 mm is shown in Fig. 9.11. It was found that while γ_S is isotropic, the observed γ was highly anisotropic and different in axial and radial motion nearly an order of magnitude for large droplets ($d > 1$ mm) for the axial motion. Although the d -dependence of γ in the radial motion was approximately similar to that of γ_S , the value of γ was smaller than γ_S . The deviation of γ from γ_S diminished as the ultrasound pressure was reduced as shown in the inset of Fig. 9.11. The precise physical origin of these observations has not been elucidated yet. Nevertheless, this phenomenon has consequences for applications that utilize the capture of ejected droplets as an automated method of sample loading: Firstly, the maximum repetition time of the experiment will be limited by $1/\gamma$, and secondly, the loading of small droplets (of 0.1–0.5 mm that are relevant

Fig. 9.11 Relationship between droplet diameter d and the damping coefficient of the axial and radial oscillation measured at $P_{\text{ac}}/P_{\text{ac},0}$ in the range of 2–2.5, where $P_{\text{ac},0} = 1.35 \text{ kPa-rms}$ is the threshold pressure for levitating a water droplet. The inset shows the axial damping coefficients measured for $P_{\text{ac}}/P_{\text{ac},0}$ in the range of 1.2–2.4. The dashed curve shows the calculated damping coefficient expected from the Stokes coefficient. From [103]



to experiments for crystals of 50–100 μm in size) will become comparatively more challenging since small γ makes the droplet capture more difficult.

These issues of the single-dispenser loading can be partly resolved by using two DoD dispensers with the setup shown in Fig. 9.12a. In this case, as depicted in Fig. 9.12b–g, two counter-propagating droplets were aligned to collide at the middle node of the levitator cavity adjusted to the fifth resonance, and their subsequent coalescence resulted in the droplet loading. Comparing to the DoD loading using single dispenser, the droplet velocities (0.75 and 0.90 m/s for the left and the right droplet) could be set at high values to achieve stable droplet trajectories and stable droplet ejection. The settling time of the captured droplet was shortened by an order of magnitude. Further, the alignment procedure of the dispensers was much simplified.

9.2.6 Application of On-Demand Droplet Loading for Protein Crystallography Experiments

The double-dispenser droplet loading method was applied to the ALD installation on the X06SA beamline at the Swiss Light Source, Paul Scherrer Institut, to conduct X-ray diffraction experiments for the on-demand loaded protein crystals [102]. Figure 9.13a shows the experimental setup. One DoD dispenser was filled with samples (lysozyme crystals with the size in the range of 100–200 μm) in the crystallization buffer, and another dispenser was filled only with the crystallization buffer.

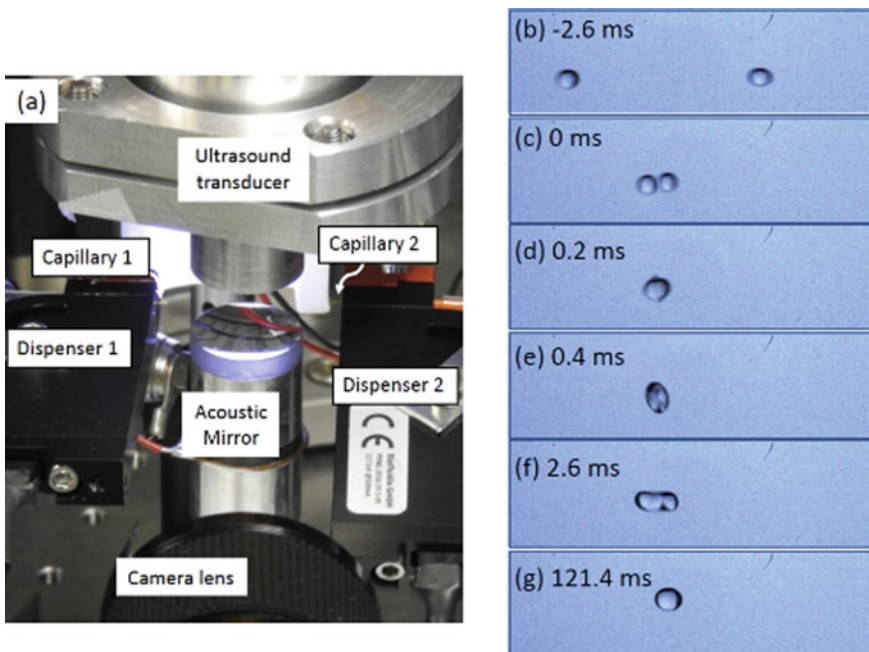


Fig. 9.12 **a** The experimental configuration of the on-demand loading of the acoustic levitator with water droplets using two drop-on-demand dispensers. **b–g** show the selected time frames of a droplet loading event recorded using the high-speed camera at the frame rate of 5000 Hz. The droplet radii were equal to 0.26 mm, and the relative velocity of the droplets was equal to 1.65 m/s. From [102]

After loading the samples by the double-dispenser method, datasets consisting of 3000 X-ray diffraction images were collected at 1 kHz frame rate.

As shown in the inset of Fig. 9.13a, the recorded diffraction spots were sharp. This indicated the absence of crystal damage, that is, the sample dispensing method and the data collection caused neither the increase in crystal mosaicity nor the changes in unit-cell parameters [21]. The hit rate (the fraction of the images that recorded the diffraction from a sample) of one of the datasets reached 30%, and the index rate (the fraction of images of which Bragg reflection indices were successfully assigned) was 10%. The same dataset was used to solve the crystal structure by the molecular replacement method at the achieved resolution equal to 2.65 Å. Figure 9.13b, c shows selected parts of the solved electron density. It was found that the bond lengths including those of the disulfide bridges of the solved electron density agreed well with the results of the previous experiments shown in Fig. 9.8. Therefore, together with the observed sharp diffraction spots, these results indicated the absence of any crystal damage by the drop-on-demand sample loading method as well as by the acoustic levitation. The lack of the sample damage concluded here was in-line with the literature reporting the crystallography experiments for ejected crystals from drop-on-demand dispensers [31, 57, 76, 79, 90].

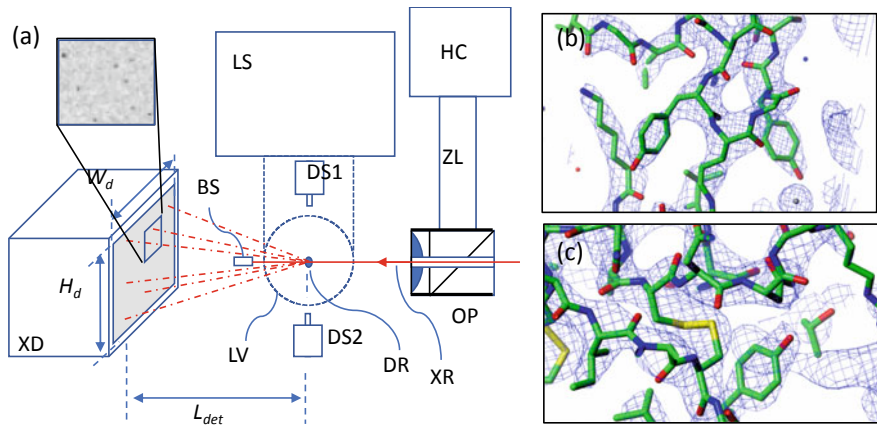


Fig. 9.13 **a** Schematic experimental setup of the ALD combined with the on-demand sample loading equipment. The schematics in the middle show the top view of the acoustic levitator (LV), drop-on-demand dispensers (DS1 and 2). DR: droplet, XR: X-ray beam, XD: fast-frame-rate X-ray image detector, OP: objective lens–prism assembly, ZL: zoom lens, HC: high-speed camera for droplet observation, BS: beam stop for the direct X-ray beam, LS: support for the acoustic levitator with the XYZ translation stage, Ldet: distance between the sample in the levitating droplet and the detector equal to 85 mm, and Wd: width of the X-ray detector active area equal to 77.2 mm (the height was equal to 79.9 mm). The inset shows the sharp diffraction spots observed in the experiment. **b, c** show two parts of the electron density of the solved lysozyme structure, rendered by CCP4MG [59]. From [102]

9.2.7 Outlook ~ Toward Fully Automated Crystallography Pipeline Using the Acoustic Levitation

Combining the crystal harvesting and delivery steps in single on-demand step will be a significant advancement to realize a high-throughput and fully automated crystallography pipeline using the acoustic levitation as shown in Fig. 9.14. For a fully automated system without the requirement of manual steps, it is highly desirable to further develop a sample loading method such as the acoustic ejection of samples, e.g., by focused acoustic radiation [27, 28] from standard crystallization plates [78] for ALD. The absence of sample damage by such sample harvesting methods and ALD data collection show the feasibility of such an instrument. The prospective order(s) of magnitude improvement of the overall throughput will be highly beneficial for screening of large ligand libraries for drug discovery [32, 42, 77], enabling the fully experimental X-ray screening of compound libraries consisting of several thousands of fragment molecules or compounds selected by structure-based in silico methods.

The application of ALD for the protein crystallography so far has been focusing on relatively large samples ($>50 \mu\text{m}$) grown from water-soluble proteins. However, the recent advent of ultrafast SFX experiments has been highlighting the experiments with smaller ($<10 \mu\text{m}$) crystals that might simplify the effort to prepare high-quality

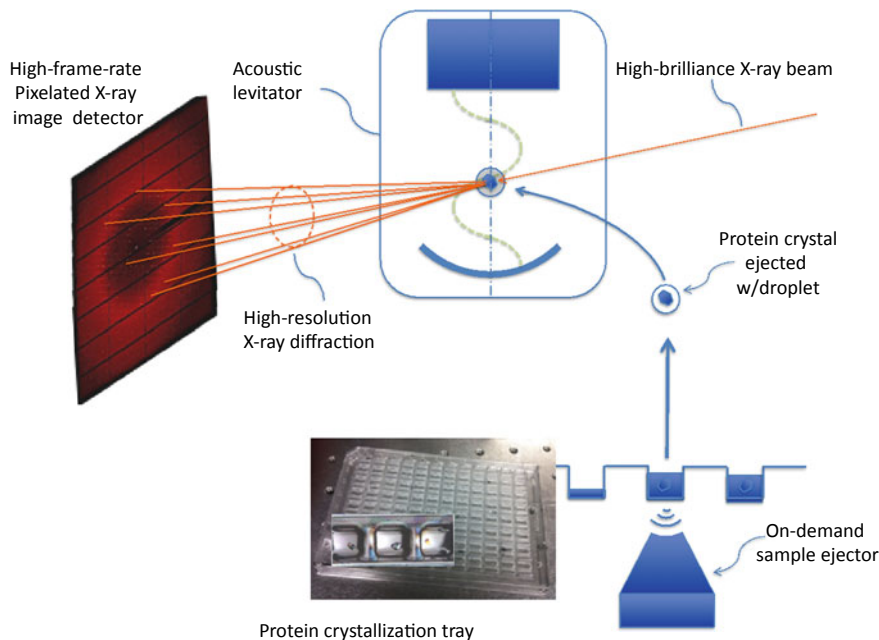


Fig. 9.14 Schematic diagram of an envisioned fully automated room-temperature protein crystallography pipeline using the acoustic levitation diffractometer combined with the on-demand sample harvesting and delivery mechanism using the acoustic ejection from a standard protein crystallization plate

crystals. At synchrotrons with the photon flux of 10^{12} to 10^{13} photon/s, data collection with 10–20 μm size crystals is straightforward. Therefore, it seems likely that high-throughput serial crystallography experiments for such samples using ALD will become possible when a dedicated sample delivery method targeting small samples is available. Another important class of samples is membrane proteins that are attached to the cell membranes and act as the regulator to control the chemical environment within the cell. High-quality crystals of membrane proteins have been normally prepared in a lipidic cubic phase (LCP), a highly viscous crystallization medium that is difficult to eject with typical acoustic ejectors. Therefore, to increase the applicability of ALD, it is an urgent task to develop a sample harvesting and delivery strategy for LCP samples with the size in the order of 10–20 μm .

9.3 Development of Acoustic Levitator Toolkit for Container-Less Transport and Mixing Experiments

Adding capabilities such as the spatial transportation of droplets and the simultaneous handling of multiple droplets will broaden the scope of the acoustic levitation experiment to those that combine multiple tasks in one package in an airborne container-less liquid processing instrument. To realize such an instrument, developing additional levitation tools and/or levitators that are beyond the conventional single-axis levitators will be necessary. Several works have been reported that advanced the acoustic levitation technology in this direction. In a system envisioned by Nakamura group at Tokyo Institute of Technology, Japan, the apparatus consisted of a linear droplet transporter [24, 37, 44], directional switching [39, 45, 62], droplet mixer [63], and dispensers [95, 96] that have been developed based on modified acoustic cavities or acoustic traveling wave field on a plate or a disk. In another approach, Poulikakos group at ETH Zürich, Switzerland, developed an acoustophoretic device based on a planar acoustic cavity excited by closely spaced array of ultrasound transducers. By synchronous amplitude switching of neighboring ultrasound transducers, they demonstrated continuous spatial shift of pressure nodes that was used for the planar transportation of multiple levitated droplets [29]. Contactless droplet coalescence and mixing, solid–liquid encapsulation, absorption, dissolution, and DNA transfection [29, 105] have been demonstrated using such a device. Figure 9.15 shows a semi-automated acoustophoretic system utilizing such a planar acoustic cavity tool used for DNA transfection experiments [105]. The T-shaped planar acoustic levitator

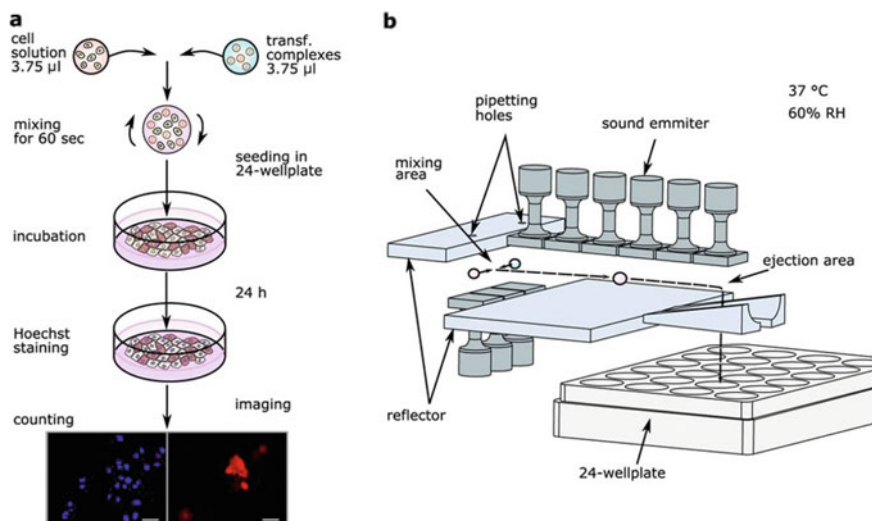


Fig. 9.15 **a** Illustration of the protocol of the experiment in the acoustophoretic DNA transfection system. **b** Illustration of the acoustophoretic setup. Adapted from [105]

was designed to mix a droplet containing mammalian cells with another droplet of the transfection complex solution, both pipetted from nozzles into the levitator, then to eject the merged droplets into one of the well of a 24-well plate. The successful demonstration of the viability of the contactless procedure and its comparison with standard methods reported in [105] shows the potential of the acoustic levitation for the application of high-throughput acoustophoretic biological reactors.

Recently, holographic synthesis of acoustic field has been actively studied. Flexible acoustic field has been produced either by using a phase mask to modulate the phase of the ultrasound emission from transducer arrays [60] or by directly modulating the phases of individual element of a phased-array emitter [56, 66]. This way, advanced acoustic field such as the self-bending and bottled beam [123] and the acoustic vortex beam that is instrumental to realize single-beam acoustic tweezers [5, 67, 119] can be synthesized. Further, by dynamically controlling the focal point of this synthesized acoustic field by controlling the phases of the voltages driving the array emitters, one can move a levitated particle or droplet along a desired path. For the further detail, readers are referred to Chap. 1–3. In the field of droplet manipulation, recently published works in [2, 107] have demonstrated the droplet mixing, transportation, and ejection of levitated droplets by driving the array elements with synthesized phase patterns computed from the designed droplet trajectories. Further advancement of the holographic acoustic levitation technology in the field of bio/chemical applications is foreseen.

References

1. Y. Abe, D. Hyuga, S. Yamada, K. Aoki, Study of internal flow and surface deformation of large droplet levitated by ultrasonic wave. *Ann. NY. Acad. Sci.* **1077**, 49 (2006)
2. M.A.B. Andrade, T.S.A. Camargo, A. Marzo, Automatic contactless injection, transportation, merging, and ejection of droplets with a multifocal point acoustic levitator. *Rev. Sci. Instrum.* **89**, 125105 (2018)
3. P. Aussillous, D. Quere, *Liquid Marbles* **411**, 924 (2001)
4. S. Baer, C. Esen, A. Ostendorf, Phase equilibrium measurements of acoustically levitated squalene-CO₂ mixtures by Raman spectroscopy. *J. Raman spectrosc.* **45**, 680 (2014)
5. D. Baresch, J.-L. Thomas, R. Marchiano, Observation of a single-beam gradient force acoustical trap for elastic particles: acoustical tweezers. *Phys. Rev. Lett.* **116**, 024301 (2016)
6. C.J. Benmore, J.K.R. Weber, Amorphization of molecular liquids of pharmaceutical drugs by acoustic levitation. *Phys. Rev. X* **1**, 011004 (2011)
7. C.J. Benmore, J.K.R. Weber, A.N. Tailor, B.R. Cherry, J.L. Yarger, Q. Mou, W. Weber, J. Neuwein, S.R. Byrn, Structural characterization of aging of glassy pharmaceuticals made using acoustic levitation. *J. Pharma. Sci.* **102**, 1290 (2013)
8. S. Biedasek, M. Abboud, H.-U. Moritz, A. Stammer, Online-analysis of acoustically levitated droplets. *Macromol. Symp.* **259**, 390 (2007)
9. A. Biswas, Solidification of acoustically levitated o-terphenyl crystals: a Raman study. *J. Cryst. Growth* **147**, 155 (1995)
10. E.H. Brandt, Levitation in physics. *Science* **243**, 349 (1989)
11. E.H. Brandt, Suspended by sound. *Nature* **413**, 474 (2001)
12. W.P. Burmeister, Structural changes in a cryo-cooled protein crystal owing to radiation damage. *Acta Cryst.* **D56**, 328 (2000)

13. D. Bourgeois, T. Ursby, M. Wulff, C. Pradervand, A. Legrand, W. Schildkamp, S. Labouré, V. Srager, T.Y. Teng, M. Roth, K. Moffat, Feasibility and realization of single-pulse laue diffraction on macromolecular crystals at ESRF. *J. Synchrotron Rad.* **3**, 65 (1996)
14. E.T. Chaniani, K.T. Ngo, A. Scheeline, Electrochemistry in an acoustically levitated drop. *Anal. Chem.* **85**, 2500 (2013)
15. E.T. Chaniani, W.-H. Choi, K.T. Ngo, A. Scheeline, Mixing in colliding, ultrasonically levitated droplets. *Anal. Chem.* **86**, 2229 (2014)
16. V. Cristiglio, I. Grillo, M. Fomina, F. Wien, E. Shalaev, A. Novikov, S. Brassamin, M. Réfrégiers, J. Pérez, L. Hennet, Combination of acoustic levitation with small angle scattering techniques and synchrotron radiation circular dichroism. Application to the study of protein solutions. *Biochimica et Biophysica Acta (BBA)* **1861**, 3693 (2017)
17. Z. Chen, D. Zang, L. Zhao, M. Qu, X. Li, X. Li, L. Li, X. Geng, Liquid marble coalescence and triggered microreaction driven by acoustic levitation. *Langmuir* **33**, 6232 (2017)
18. Y. Cerenius, Å. Oskarsson, S. Santesson, S. Nilsson, L. Kloof, Preliminary tests on the use of an acoustic levitator for liquid X-ray diffraction experiments. *J. Appl. Cryst.* **36**, 163 (2003)
19. E.A. Crawford, C. Esen, D.A. Volmer, Real time monitoring of containerless microreactions in acoustically levitated droplets via ambient ionization mass spectrometry. *Anal. Chem.* **88**, 8396 (2016)
20. A.N. Davies, P. Jacob, A. Stockhaus, R. Kuckuk, W. Hill, R. Hergenröder, A. Zybin, D. Klockow, Acoustic trap for simplified micro-sample handling in laser spectroscopy, *Appl. Spectrosc.* **54**, 1831 (2000)
21. K. Diederichs, Simulation of X-ray frames from macromolecular crystals using a ray-tracing approach. *Acta. Cryst. D* **65**, 535 (2009)
22. P. Docker, R. Morris, M. Newton, E. Dye, J. Kay, J. Beale, D. Axford, A. Orville, D. Stuart, The development of acoustic levitation for time resolved protein crystallography experiments at XELS. *TechConnect Briefs* **4**, 100 (2017)
23. F. Delissen, J. Leiter, R. Beinert, F. Emmerling, A.F. Thünemann, Agglomeration of proteins in acoustically levitated droplets. *Anal. Bioanal. Chem.* **392**, 161 (2008)
24. M. Ding, D. Koyama, K. Nakamura, Noncontact ultrasonic transport of liquid using a flexural vibration plate. *Appl. Phys. Express* **5**, 097301 (2012)
25. R. Dinapoli, A. Bergamaschi, B. Henrich, R. Horisberger, I. Johnson, A. Mozzanica, E. Schmid, B. Schmitt, A. Schreiber, X. Shi, G. Theidel, EIGER: next generation single photon counting detector for X-ray applications. *Nucl. Instrum. Methods Phys. Res., Sect. A* **650**, 79 (2011)
26. F.J.S. Doerr, I.D.H. Oswald, A.J. Florence, Quantitative investigation of particle formation of a model pharmaceutical formulation using single droplet evaporation experiments and X-ray tomography. *Adv. Powder Technol.* **29**, 2996 (2018)
27. S.A. Elrod, B. Hadimioglu, B.T. Khuri-Yakub, E.G. Rawson, E. Richley, C.F. Quate, N. Mansour, T.S. Lundgren, Nozzleless droplet formation with focused acoustic beams. *J. Appl. Phys.* **65**, 3441 (1989)
28. R. Ellson, Picoliter: enabling precise transfer of nanoliter and picoliter Volumes. *Drug Discovery Today* **7**, S32 (2002)
29. D. Foresti, M. Nabavi, M. Klingauf, A. Ferrari, D. Poulikakos, Acoustophoretic contactless transport and handling of matter in air. *Proc. Natl. Acad. Sci. U S A* **110**, 12549–12554 (2013)
30. J.S. Fraser, H. van den Bedem, A.J. Samelson, P.T. Lang, J.M. Holton, N. Echols, T. Alber, Accessing protein conformational ensembles using room-temperature X-ray crystallography. *PNAS* **108**, 162347 (2011)
31. F.D. Fuller, S. Gul, R. Chatterjee, E.S. Burgie, I.D. Young, H. Lebrette, V. Srinivas, A.S. Brewster, T. Michels-Clark, J.A. Clinger, B. Andi, M. Ibrahim, E. Pastor, C. de Lichtenberg, R. Hussein, C.J. Pollock, M. Zhang, C.A. Stan, T. Kroll, T. Fransson, C. Weninger, M. Kubin, P. Aller, L. Lassalle, P. Bräuer, M.D. Miller, M. Amin, S. Koroidov, C.G. Roessler, M. Allaire, R.G. Sierra, P.T. Docker, J.M. Glownia, S. Nelson, J.E. Koglin, D. Zhu, M. Chollet, S. Song, H. Lemke, M. Liang, D. Sokaras, R. Alonso-Mori, A. Zouni, J. Messinger, U. Bergmann, A.K. Boal, J.M. Bollinger Jr., C. Krebs, M. Hogbom, G.N. Phillips Jr., R.D. Vierstra, N.K.

- Sauter, A.M. Orville, J. Kern, V.K. Yachandra, J. Yano, Drop-on-demand sample delivery for studying biocatalysts in action at X-ray free-electron lasers. *Nat. Methods* **14**, 443 (2017)
32. M. Grimes, D.R. Hall, A.W. Ashton, G. Evans, R.L. Owen, A. Wagner, K.E. McAuley, F. von Delft, A.M. Orville, T. Sorensen, M.A. Walsh, H.M. Ginna, D.I. Stuart, Where is crystallography going? *Acta Crystallogr. Sect. D* **74**, 152 (2018)
33. C. Groenewold, C. Möser, H. Groenewold, E. Tsotsas, Determination of single-particle drying kinetics in an acoustic levitator. *Chem. Eng. J.* **86**, 217 (2002)
34. H. Hatano, Y. Kanai, Y. Ikegami, T. Fujii, K. Saito, Ultrasonic levitation and positioning of samples. *Jpn. J. Appl. Phys.* **21**, 202 (1982)
35. B. Henrich, A. Bergamaschi, C. Broennimann, R. Dinapoli, E.F. Eikenberry, I. Johnson, M. Kobas, P. Kraft, A. Mozzanica, B. Schmitt, PILATUS: a single photon counting pixel detector for X-ray applications. *Nucl. Instrum. Methods Phys. Res., Sect. A* **607**, 247 (2009)
36. F.U. Huschmann, J. Linnik, K. Sparta, M. Ühlein, X. Wang, A. Metz, J. Schiebel, A. Heine, G. Klebe, M.S. Weiss, U. Mueller, Structures of endothiapepsin-fragment complexes from crystallographic fragment screening using a novel, diverse and affordable 96-compound fragment library. *Acta Cryst.* **F72**, 346 (2016)
37. Y. Ito, D. Koyama, K. Nakamura, High-speed noncontact ultrasonic transport of small objects using acoustic traveling wave field. *Acoust. Sci. Tech.* **31**, 420 (2010)
38. J.A. Jamsen, W.A. Beard, L.C. Pedersen, D.D. Shock, A.F. Moon, J.M. Krahn, K. Bebenek, T.A. Kunkel, S.H. Wilson, Time-lapse crystallography snapshots of a double-strand break repair polymerase in action. *Nat. Commun.* **8**, 253 (2017)
39. R. Kashima, S. Murakami, D. Koyama, K. Nakamura, M. Matsukawa, Design of a junction for a noncontact ultrasonic transportation system. *IEEE Trans. UFFC* **61**, 1024 (2014)
40. D.A. Keedy, L.R. Kenner, M. Warkentin, R.A. Woldeyes, J.B. Hopkins, M.C. Thompson, A.S. Brewster, A.H. Van Benschoten, E.L. Baxter, M. Uervirojnangkoorn, S.E. McPhillips, J. Song, R. Alonso-Mori, J.M. Holton, W.I. Weis, A.T. Brunger, S.M. Soltis, H. Lemke, A. Gonzalez, N.K. Sauter, A.E. Cohen, H. van den Bedem, R.E. Thorne, J.S. Fraser, Mapping the conformational landscape of a dynamic enzyme by multitemperature and XFEL crystallography. *eLife* (2015). <https://doi.org/10.7554/elife.07574>
41. N. Keil, S. Will, G. Lee, Correlation of the kinetics of aggregation and inactivation of L-glutamate dehydrogenase during drying and particle formation of a levitated microdroplet. *Dry. Technol.* **37**, 164 (2018)
42. G.M. Keserue, D.A. Erlanson, G.G. Ferenczy, M.M. Hann, C.W. Murray, S.D. Pickett, Design principles for fragment libraries: maximizing the value of learnings from pharma fragment-based drug discovery (FBDD) programs for use in academia. *J. Med. Chem.* **59**, 8189 (2016)
43. M. Klimakow, J. Leiterer, J. Kneipp, E. Rössler, U. Panne, K. Rademann, F. Emmerling, Combined synchrotron XRD/Raman measurements: in situ identification of polymorphic transitions during crystallization processes. *Langmuir* **26**, 11233 (2010)
44. D. Koyama, K. Nakamura, Noncontact ultrasonic transportation of small objects over long distances in air using a bending vibrator and a reflector. *IEEE Trans. UFFC* **57**, 1152 (2010)
45. D. Koyama, K. Nakamura, Noncontact ultrasonic transportation of small objects in a circular trajectory in air by flexural vibration of a circular disc. *IEEE Trans. UFFC* **57**, 1434 (2010)
46. T. Laurell, L. Wallman, J. Nilsson, Design and development of a silicon microfabricated flow-through dispenser for on-line picolitre sample handling. *J. Micromech. Microeng.* **9**, 369–376 (1999)
47. J. Leiterer, W. Leitenberger, F. Emmerling, A.F. Thünemann, U. Panne, The use of an acoustic levitator to follow crystallization in small droplets by energy-dispersive X-ray diffraction. *J. Appl. Cryst.* **39**, 771 (2006)
48. J. Leiterer, F. Delissen, F. Emmerling, A.F. Thünemann, U. Pann, Structure analysis using acoustically levitated droplets. *Anal. Bioanal. Chem.* **391**, 1221 (2008)
49. J. Leiterer, F. Emmeling, U. Panne, W. Christen, K. Rademann, Tracing coffee tabletop traces. *Langmuir* **24**, 7970 (2008)
50. J. Leiterer, F. Emmerling, J. Radnik, U. Bentrup, A. Brückner, Flying droplets as model system for spray drying—an in situ synchrotron X-ray scattering study on complex oxides catalyst precursors. *Catal. Today* **155**, 326 (2010)

51. E.G. Lierke, Acoustic levitation a comprehensive survey of principles and applications. *Acta Acustica United Acustica* **82**, 220 (1996)
52. J. Leiterer, U. Panne, A.F. Thünemann, S.M. Weidner, Container-less polymerization in acoustically levitated droplets: an analytical study by GPC and MALDI-TOF mass spectroscopy. *Anal. Methods* **3**, 70 (2011)
53. N. Leopold, M. Haberkorn, T. Laurell, J. Nilsson, J.R. Baena, J. Frank, B. Lendl, On-line monitoring of airborne chemistry in levitated nanodroplets: in situ synthesis and application of SERS-active Ag-Sols for trace analysis by FT-Raman spectroscopy. *Anal. Chem.* **75**, 2166 (2003)
54. M. Lopez-Pastor, A. Dominguez-Vidal, M.J. Ayora-Canada, T. Laurell, M. Vakcarcek, B. Lendl, Containerless reaction monitoring in ionic liquids by means of Raman microscopy. *Lab Chip* **7**, 126 (2007)
55. M. Lucas, S.J. Brotton, S.K. Shukla, J. Yu, S.L. Anderson, R.I. Kaiser, Oxidation of a levitated droplet of 1-allyl-3-methylimidazolium dicyanamide by nitrogen dioxide. *J. Phys. Chem. A* **123**, 400 (2019)
56. A. Marzo, S.A. Seah, B.W. Drinkwater, D.R. Sahoo, B. Long, S. Subramanian, Holographic acoustic elements for manipulation of levitated objects. *Nat. Commun.* **6**, 8661 (2015)
57. F. Mafune, K. Miyajima, K. Tono, Y. Takeda, J. Kohno, N. Miyauchi, Y. Joti, J. Kobayashi, E. Nango, S. Iwata, M. Yabashi, Microcrystal delivery by pulsed liquid droplet for serial femtosecond crystallography. *Acta Crystallogr., Sect. D* **72**, 520 (2016)
58. P. McEwan, P. Collins, A. Dias, M. Mazanetz, B. Brandao-Neto, A. Douangamath, J. Ng, N. Wright, T. Krojer, J. Barker, F. von Delft, Routine fragment screening by crystal structure, in *Proceedings of Fragments 2015: Fifth RSC-BMCS Fragment-Based Drug Discovery Meeting* (2015)
59. S. McNicholas, E. Potterton, K.S. Wilson, M.E.M. Noble, Presenting your structures: the CCP4mg molecular-graphics software. *Acta Crystallogr., Sect. D* **67**, 386 (2011)
60. K. Melde, A.G. Mark, T. Qiu, P. Fischer, Holograms for acoustics. *Nature* **537**, 518 (2016)
61. C. Mu, J. Wang, K.M. Barraza, X. Zhang, J.L. Beauchamp, Mass spectrometric study of acoustically levitated droplets illuminates molecular-level mechanism of photodynamic therapy for cancer involving lipid oxidation. *Angew. Chem.* **58**, 8082 (2019)
62. S. Murakami, D. Koyama and K. Nakamura, Ejection of small objects in a noncontact ultrasonic transporter. *AIP Conf. Proc.* **1433**, 783 (2012)
63. R. Nakamura, Y. Mizuno, K. Nakamura, Demonstration of noncontact ultrasonic mixing of droplets. *Jpn. J. Appl. Phys.* **52**, 07HE02 (2013)
64. E. Nango, A. Royant, M. Kubo, T. Nakane, C. Wickstrand, T. Kimura, T. Tanaka, K. Tono, C. Song, R. Tanaka, T. Arima, A. Yamashita, J. Kobayashi, T. HosakaI, E. Mizohata, P. Nogly, M. Sugahara, D. Nam, T. Nomura, T. Shimamura, D. Im, T. Fujiwara, Y. Yamanaka, B. Jeon, T. Nishizawa, K. Oda, M. Fukuda, R. Andersson, P. Båth, R. Dods, J. Davidsson, S. Matsuoka, S. Kawatake, M. Murata, O. Nureki, S. Owada, T. Kameshima, T. Hatsui, Y. Joti, G. Schertler, M. Yabashi, A.-N. Bondar, J. Standfuss, R. Neutze, S. Iwata, A three-dimensional movie of structural changes in bacteriorhodopsin. *Science* **354**, 1552 (2016)
65. W.L.M. Nyborg, in *Physical Acoustics*, Vol. 2B, Chap. 11, ed. by W.P. Mason (Academic Press, Cambridge, MA, 1965), p. 265
66. Y. Ochiai, T. Hoshi, J. Rekimoto, Pixie dust: graphics generated by levitated and animated objects in computational acoustic potential field. *ACM Trans. Graph. (TOG)* **33**, 85 (2014)
67. A. Ozcelik, J. Rufo, F. Guo, Y. Gu, P. Li, J. Lata, T.J. Huang, Acoustic tweezers for the life sciences. *Nat. Methods* **15**, 1021 (2018)
68. Z.N. Pierre, C.R. Field, A. Scheeline, Sample handling and chemical kinetics in an acoustically levitate drop microreactor. *Anal. Chem.* **81**, 8496 (2009)
69. L. Puskar, R. Tuckermann, T. Frosch, J. Popp, V. Ly, D. McNaughton, B.R. Wood, Raman acoustic levitation spectroscopy of red blood cells and *Plasmodium falciparum* trophozoites. *Lab Chip* **7**, 1125 (2007)
70. J. Quino, T. Hellwig, M. Griesing, W. Pauer, H.-U. Moritz, S. Will, A. Braeuer, One-dimensional Raman spectroscopy and shadowgraphy for the analysis of the evaporation behavior of acetone/water drops. *Int. J. Heat Mass Transf.* **89**, 406 (2015)

71. J. Radnik, U. Bentrup, J. Leiterer, A. Brückner, F. Emmerling, Levitated droplets as model system for spray drying of complex oxides: a simultaneous in situ X-ray diffraction/Raman study. *Chem. Mater.* **23**, 5425 (2011)
72. L. Rayleigh, VI, On the capillary phenomena of jets. *Proc. R. Soc. Lond.* **29**, 71 (1879)
73. S. Rehder, J.X. Wu, J. Laackmann, H.-U. Moritz, J. Rantanen, T. Rades, C.S. Leopold, A case study of real-time monitoring of solid-state phase transformations in acoustically levitated particles using near infrared and Raman spectroscopy. *Eur. J. Pharm. Sci.* **48**, 97 (2013)
74. N. Riley, in *Encyclopedia of Acoustics*, vol. 1, ed. by M.J. Crocker (Wiley, Hoboken, NJ, 1997), p. 321
75. O. Rohling, C. Weitkamp, B. Neidhart, Experimental setup for the determination of analytes contained in ultrasonically levitated drops. *Fresenius J. Anal. Chem.* **368**, 125 (2000)
76. C.G. Roessler, R. Agarwal, M. Allaire, R. Alonso-Mori, B. Andi, J.F. Bachega, M. Bommer, A.S. Brewster, M.C. Browne, R. Chatterjee, E. Cho, A.E. Cohen, M. Cowan, S. Datwani, V.L. Davidson, J. Defever, B. Eaton, R. Ellson, Y. Feng, L.P. Ghislain, J.M. Glownia, G. Han, J. Hattne, J. Hellmich, A. Heroux, M. Ibrahim, J. Kern, A. Kuczewski, H.T. Lemke, L.M.P. Liu, W.M. McClintock, S. Myers, S. Nelsen, J. Olechno, A.M. Orville, N.K. Sauter, A.S. Soares, S.M. Soltis, H. Song, R.G. Stearns, R. Tran, Y. Tsai, M. Uervirojnangkoorn, C.M. Wilmot, V. Yachandra, J. Yano, E.T. Yukl, D. Zhu, A. Zouni, Acoustic injectors for drop-on-demand serial femtosecond crystallography. *Structure* **24**, 631 (2016)
77. P. Rucktooa, R.K. Y. Cheng, E. Segala, T. Geng, J.C. Errey, G.A. Brown, R. M. Cooke, F.H. Marshall, A.S. Doré, Towards high throughput GPCR crystallography: In Meso soaking of Adenosine A2A receptor crystals. *Sci. Rep.* **8**, 41 (2018)
78. Y.N. Samara, H.M. Brennan, L. McCarthy, M.T. Bolland, D. Laspina, J.M. Wlodek, S.L. Campos, R. Natarajan, K. Gofron, S. McSweeney, A.S. Soares, L. Leroy, Using sound pulses to solve the crystal-harvesting bottleneck. *Acta Crystallogr., Sect. D* **74**, 986 (2018)
79. S. Santesson, M. Andersson, E. Degerman, T. Johansson, J. Nilsson, S. Nilsson, Airborne cell analysis. *Anal. Chem.* **72**, 3412 (2000)
80. S. Santesson, E.S. Cedergren-Zeppezauer, T. Johansson, T. Laurell, J. Nilsson, S. Nilsson, Screening of nucleation conditions using levitated drops for protein crystallization. *Anal. Chem.* **75**, 1733 (2003)
81. S. Santesson, S. Nilsson, Airborne chemistry: acoustic levitation in chemical analysis. *Anal. Bioanal. Chem.* **378**, 1704 (2004)
82. S. Santesson, E. Degerman, P. Rorsman, T. Johansson, S. Lemos, S. Nilsson, Cell–cell communication between adipocytes and pancreatic β-cells in acoustically levitated droplets. *Integr. Biol.* **1**(10), 595 (2009). <https://doi.org/10.1039/b907834g>
83. H. Schlichting, Berechnung ebener periodischer grenzschichtstromungen. *Phys. Z.* **33**, 327 (1932)
84. M.A.I. Schutyser, J. Perdana, R.M. Boom, Single droplet drying for optimal spray drying of enzymes and probiotics. *Trends Food Sci. Technol.* **27**, 73 (2012)
85. M.A.I. Schutyser, E.M. Both, I. Siemons, E.M.J. Vaessen, L. Zhang, Gaining insight on spray drying behavior of foods via single droplet drying analyses. *Drying Technol.* **37**, 525 (2019)
86. A. Schneeline, R.L. Behrens, Potential of levitated drops to serve as microreactors for biophysical measurements. *Biophys. Chem.* **165–166**, 1 (2012)
87. J. Schenk, U. Panne, M. Albrecht, Interaction of levitated ionic liquid droplets with water. *J. Phys. Chem. B* **116**, 14171 (2012)
88. R. Sedelmayer, M. Griesing, A.H. Halfar, W. Pauer, H.-Ul Moritz, Experimental investigation of the morphology formation of polymer particles in an acoustic levitator. *Macromol. Symp.* **333**, 142 (2013)
89. J. Sloth, S. Kiila, A.D. Jensen, S.K. Andersen, K. Jørgensen, H. Schiffter, G. Lee, Model based analysis of the drying of a single solution droplet in an ultrasonic levitator. *Chem. Eng. Sci.* **61**, 2701 (2006)
90. A.S. Soares, M.A. Engel, R. Stearns, S. Datwani, J. Olechno, R. Ellson, J.M. Skinner, M. Allaire, A.M. Orville, Acoustically mounted microcrystals yield high-resolution X-ray structures. *Biochemistry* **50**, 4399 (2011)

91. A. Stindt, M. Albrecht, U. Panne, J. Riedel, CO₂ laser ionization of acoustically levitated drops. *Anal. Bioanal. Chem.* **405**, 7005 (2013)
92. M. Sundvik, H.J. Nieminen, A. Salmi, P. Panula, E. Häggström, Effects of acoustic levitation on the development of zebrafish, *Danio rerio*, embryos. *Sci. Rep.* **5**, 13596 (2015)
93. I. Surowiec, J.R. Baena, J. Frank, T. Laurell, J. Nilsson, M. Trojanowicz, B. Lendl, Flow-through microdispenser for interfacing μ-HPLC to Raman and mid-IR spectroscopic detection. *J. Chromatogr. A* **1080**, 132 (2005)
94. K. Tanaka, H. Waki, Y. Ido, S. Akita, Y. Yoshida, T. Yoshida, Protein and polymer analyses up to m/z 100,000 by laser ionization time-of-flight mass spectrometry. *Rapid Commun. Mass Spectrom.* **2**, 151 (1988)
95. H. Tanaka, Y. Wada, Y. Mizuno, K. Nakamura, Behavior of ultrasonically levitated object above reflector hole. *Jap. J. Appl. Phys.* **52**, 100201 (2013)
96. H. Tanaka, Y. Wada, Y. Mizuno, K. Nakamura, Effect of holed reflector on acoustic radiation force in noncontact ultrasonic dispensing of small droplets. *Jap. J. Appl. Phys.* **55**, 067302 (2016)
97. Y.A. Tobon, S. Seng, L.A. Picone, Y.B. Bava, L.C. Juncal, M. Moreau, R.M. Romano, J. Barbillat, S. Sobanska, Photochemistry of single particles using acoustic levitation coupled with Raman microspectrometry. *J. Raman Spectrosc.* **48**, 1135 (2017)
98. T. Tomizaki, A. Shinoda, S. Tsujino, Single crystal time-lapse measurement using ultrasonic acoustic levitation. *AIP Conf. Proc.* **2054**, 060072 (2019)
99. E.H. Trinh, Compact acoustic levitation device for studies in fluid dynamics and material science in the laboratory and microgravity. *Rev. Sci. Instrum.* **56**, 2059 (1985)
100. E.H. Trinh, J.L. Robey, Experimental study of streaming flows associated with ultrasonic levitators. *Phys. Fluids* **6**, 3567 (1994)
101. S. Tsujino, T. Tomizaki, Ultrasonic acoustic levitation for fast frame rate X-ray protein crystallography at room temperature. *Sci. Rep.* **6**, 25558 (2016)
102. S. Tsujino, A. Shinoda, T. Tomizaki, On-demand droplet loading of ultrasonic acoustic levitator and its application for protein crystallography experiments. *Appl. Phys. Lett.* **114**, 213702 (2019)
103. S. Tsujino, Y. Sato, Y. Takeda, T. Tomizaki, Oscillation resonances and anisotropic damping of the motion of acoustically levitated droplets in single-axis acoustic levitators. *Appl. Phys. Lett.* **115**, 053702 (2019)
104. R. Tuckermann, L. Puskar, M. Zavabeti, R. Sekine, D. McNaughton, Chemical analysis of acoustically levitated droplets by Raman spectroscopy. *Anal. Bioanal. Chem.* **394**, 1433 (2009)
105. T. Vasileiou, D. Foresti, A. Bayram, D. Poulikakos, A. Ferrari, Toward contactless biology: acoustophoretic DNA transfection. *Sci. Rep.* **6**, 20023 (2016)
106. C. Warschat, A. Stindt, U. Panne, J. Riedel, Mass spectrometry of levitated droplets by thermally unconfined infrared-laser desorption. *Anal. Chem.* **87**, 8323 (2015)
107. A. Watanabe, K. Hasegawa, Y. Abe, Contactless fluid manipulation in air: droplet coalescence and active mixing by acoustic levitation. *Sci. Rep.* **8**, 10221 (2018)
108. J.K.R. Weher, C.J. Benmore, A.N. Tailor, S.K. Tumber, J. Neufeld, B. Cherry, J.L. Yarger, Q. Mou, W. Weber, S.R. Byrn, A neutron-X-ray, NMR and calorimetric study of glassy Probuloc synthesized using containerless techniques. *Chem. Phys.* **424**, 89 (2013)
109. J.K.R. Weher, C.J. Benmore, K.J. Suthar, A.J. Tamalonis, O.L.G. Alderman, S. Sendelbach, V. Kondev, J. Yarger, C.A. Rey, S.R. Byrne, Using containerless methods to develop amorphous pharmaceuticals, *Biochimica et Biophysica Acta (BBA)—General Subjects*, **1861**, 3686 (2017)
110. T. Weinert, N. Olieric, R. Cheng, S. Brünle, D. James, D. Ozerov, D. Gashi, L. Vera, M. Marsh, K. Jaeger, F. Dworkowski, E. Panepucci, S. Basu, P. Skopintsev, A.S. Doré, T. Geng, R.M. Cooke, M. Liang, A.E. Prota, V. Panneels, P. Nogly, U. Ermler, G. Schertler, M. Hennig, M.O. Steinmetz, M. Wang, J. Standfuss, Serial millisecond crystallography for routine room-temperature structure determination at synchrotrons. *Nat. Commun.* **8**, 542 (2017)
111. T. Weinert, P. Skopintsev, D. James, F. Dworkowski, E. Panepucci, D. Kekilli, A. Furrer, S. Brünle, S. Mous, D. Ozerov, P. Nogly, M. Wang, J. Standfuss, Proton uptake mechanism in bacteriorhodopsin captured by serial synchrotron crystallography. *Science* **365**, 61 (2019)

112. D.D. Weis, J.D. Nardozzi, Enzyme kinetics in acoustically levitated droplets of supercooled water: a novel approach to cryoenzymology. *Anal. Chem.* **77**, 2558 (2005)
113. E. Welter, B. Neidhart, Acoustically levitated droplets—a new tool for micro and trace analysis. *Fresenius' J. Anal. Chem.* **357**, 345 (1997)
114. M.S. Westphall, K. Jorabchi, L.M. Smith, Mass spectrometry of acoustically levitated droplets. *Anal. Chem.* **80**, 5847 (2008)
115. T.A. White, R.A. Kirian, A.V. Martin, A. Aquila, K. Nass, A. Barty, H.N. Chapman, CrystFEL: a software suite for snapshot serial crystallography. *J. Appl. Cryst.* **45**, 335 (2012)
116. R.R. Whymark, Acoustic field positioning for containerless processing. *Ultrasonics* **13**, 251 (1975)
117. S.E. Wolf, J. Leiterer, M. Kappl, F. Emmerling, W. Tremel, Early homogeneous amorphous precursor stages of calcium carbonate and subsequent crystal growth in levitated droplets. *J. Am. Chem. Soc.* **130**, 12342 (2008)
118. B.R. Wood, P. Heraud, S. Stojkovic, D. Morrison, J. Beardall, D. McNaughton, A portable Raman acoustic levitation spectroscopic system for the identification and environmental monitoring of algal cells. *Anal. Chem.* **77**, 4955 (2005)
119. J. Wu, Acoustical tweezers. *J. Acoust. Soc. Am.* **89**, 2140 (1991)
120. W.J. Xie, C.D. Cao, Y.J. Lü, Z.Y. Hong, B. Wei, Acoustic method for levitation of small living animals. *Appl. Phys. Lett.* **89**, 214102 (2006)
121. A.L. Yarin, G. Bren, O. Kastner, D. Rensink, C. Tropea, Evaporation of acoustically levitated droplets. *J. Fluid Mech.* **399**, 151 (1999)
122. D. Zang, J. Li, Z. Chen, Z. Zhai, X. Geng, B.P. Binks, Switchable opening and closing of a liquid marble via ultrasonic levitation. *Langmuir* **31**, 11502 (2015)
123. P. Zhang, T. Li, J. Zhu, X. Zhu, S. Yang, Y. Wang, X. Yin, X. Zhang, Generation of acoustic self-bending and bottle beams by phase engineering. *Nat. Commun.* **5**, 4316 (2014)
124. H. Zhao, S.S. Sadhal, E.H. Trinh, Internal circulation in a drop in an acoustic field. *J. Acoust. Soc. Am.* **106**, 3289 (1999)